NORTHWESTERN UNIVERSITY

Development and Validation of Scalable Nanoplatforms for Anti-Inflammatory Immunotherapy

A DISSERTATION

SUBMITTED TO THE GRADUATE SCHOOL IN PARTIAL FULFILLMENT OF THE REQUIREMENTS

for the degree

DOCTOR OF PHILOSOPHY

Field of Interdisciplinary Biological Sciences

By
Sean David Allen

EVANSTON, ILLINOIS

March 2019

ABSTRACT

Development and Validation of Scalable Nanoplatforms for Anti-Inflammatory Immunotherapy
Sean David Allen

Nanocarriers are nanometer-sized (1-1000 nm) structures capable of encapsulating cargo. This encapsulation can drastically alter the pharmacokinetic properties of the cargo, while also allowing for the rational design and engineering of the nanocarrier itself. Poly(ethylene glycol)-block-poly(propylene sulfide) is an amphiphilic diblock copolymer capable of self-assembling into diverse nanocarriers. The purpose of this work was to investigate the utility of PEG-*b*-PPS nanocarriers for anti-inflammatory usage as therapeutic nanocarriers, particularly with regard to the sterile scale-up of their production and their efficacy in ameliorating the inflammatory conditions in atherosclerosis. This work covers the production of PEG-*b*-PPS nanocarriers, encapsulation of compounds within said nanocarriers, their safety and biodistribution in mice and non-human primates, and their utility as anti-inflammatory therapeutic nanocarriers.

To assess these characteristics of the nanocarriers, several quantitative methodologies were utilized. Size and morphological nanocarrier characterization was performed, along with *in vitro* examination of immunogenicity, compound encapsulation efficiency, delivery and subcellular localization, and assessment of cell viability. Finally, *in vivo* work, centered firstly around intravital fluorescent imaging and flow cytometric analysis of uptake in organs and cell populations and secondly in assessment of therapeutic efficacy in the ldlr-/- mouse model of atherosclerosis, was performed.

I have found that flash nanoprecipitation, a novel method of forming soft polymeric nanostructures, is capable of recapitulating all of the previously formed nanostructures using PEG-*b*-PPS polymer in addition to a previously unavailable nanostructure called a bicontinuous nanosphere. I have characterized these four different nanostructures and have demonstrated their ability to encapsulate different compounds, particularly the ability of polymersomes and bicontinuous nanospheres to simultaneously encapsulate both hydrophilic and hydrophobic compounds. Flash nanoprecipitation is scalable to production volumes relevant for non-human primate experimentation and is easily performed under sterile conditions. PEG-*b*-PPS nanocarriers formed by flash nanoprecipitation are non-immunogenic, non-toxic, are taken up primarily

by the spleen and liver after IV administration and are taken up primarily by phagocytic cells such as macrophages, monocytes, and dendritic cells. Encapsulation of celastrol, an inhibitor of the inflammatory NF-κB pathway, in these nanocarriers results in the reduction of inflammatory cells in the blood and atherosclerotic plaques of atherosclerotic mice and additionally results in the reduction of plaque staining area.

I conclude therefore that PEG-*b*-PPS nanocarriers are an effective drug delivery platform for the encapsulation and *in vivo* delivery of anti-inflammatory compounds for therapeutic biomedical applications. Additionally, I have demonstrated that flash nanoprecipitation is a rapid, scalable, and sterile method of forming these nanocarriers for future translational use.

ACKNOWLEDGEMENTS

There are many, many people that have played critical roles in helping me get to this point. I would not have been able to accomplish this alone, and I am indebted to you all.

I'd like to first acknowledge the support of my parents Natalie and Bryan, who have always believed in me and always sought to fuel my curiosity. You guys raised me to work hard and ask questions, and that's basically the core of what I've been trying to do these past five years. I want to thank my younger brother Nathan, who has been one of my best friends and closest companions. It blows me away how lucky I've been to have had a best friend living with me since I was four years old. You're all grown up now and married and all that, but sometimes you're still just my little younger brother, playing with Legos. I want to thank my wife, Liliana, who has supported me through all the years of my higher education, and moved halfway across the country with me, away from our friends and family, while I pursued my goal of earning a PhD. You've always been so considerate of me and my aspirations. I hope that I am a good enough husband to make it up to you.

I also want to say thank you to my friends, who have helped me stay grounded and sane through this whole process. Dan – ever since you gave me a spot in the high school newspaper to help me rearrange my classes, you've always had my back. I consider myself very lucky that I've gotten to spend so many formative years with you as my confidant and roommate. Ryan – I think we come from drastically different backgrounds, country gentry vs. city slicker, but I think we share a lot of core values. Especially our sense of humor. Any time I'm feeling down, I can just imagine what strange thing you'd have to say, and it makes me feel better. Anna – unlike some people, you just won't quit keeping in regular contact. While some normal humans might be fine with infrequent communication, you always make sure I remember that you're out there somewhere, cross-stitching. Also, yes, I remember that you introduced Lily and I. I'd ask you to stop bringing it up all the time, but I don't think that'd help. Shirley – every time we get to meet up, it is just like picking up where we left off. Kenny – thanks for basically being another younger brother to me. You're obviously a lot weirder than Nathan, but all the same I know that I can trust you the same way I trust family. I know you'll always be there for me, no matter what.

I'd like to give a shout out to my extended family, both those in the US and in Korea. I've always been blown away with how earnestly my family has rooted for me through the years. I don't get to see you all as often as I'd like, especially since we are spread out all over the world, but I want you all to know that you're in my thoughts and have my sincere appreciation.

As this work was done in the Scott lab, it is pretty clear that it could not have been performed otherwise. However, it would have been a painful and difficult process if I had not been blessed with kind, intelligent, fun, and helpful coworkers. I want to especially thank the starting cohort of the Scott Lab: Nicholas, Dina, Diana, and Fanfan. Nick: it has been a wild time turning into a real scientist with you. I'm glad you decided to pursue your PhD in the lab, and I'm glad I got to be around to see you become a dad, all responsible-like. We're graduating at pretty much the same time, so I know you're going on a similar journey that I am, and I wish you all the best. Dina: thanks for all the cat GIFs. I know you're having a great time out in Portland, and I hope you continue to enjoy science and life out West. Diana: everyone in lab owes you a great deal of gratitude for basically teaching us everything we knew about PEG-*b*-PPS. Fanfan: I appreciate all of the really impressive work you've accomplished in the lab and feel like I've gradually come to earn your respect and trust. That means a lot to me, coming from the resident Scott Lab chemistry guru! It was a lot of hard work to get the lab up and running, but we managed to do it by working together and supporting each other. Sharan, thanks for all of your advice and help over the years – you feel like a friend I can count on over the coming years. All of my ideas were workshopped with everyone in lab that would listen to me: Trevor, Molly, Mike, Sophia, and Mallika, thank you so much for helping me figure things out!

There were several individuals outside of the Scott Lab that provided an outsized amount of help with gathering data. Jonathan Remis, thank you for your work taking the cryoTEM pictures for the entire Scott Lab for the entire time that it has been in existence. Without you, a really considerable part of the nanoparticle characterization would have been excruciatingly difficult. Keith MacRenaris, thank you for all your help with ICP-MS and MRI work. Steven Weigand, thank you for your attentive training on the use of the small angle x-ray scattering beamline at the Argonne National Lab.

I'd like to thank my committee: Thomas Meade, Guillermo Ameer, and Vadim Backman. These professors served on my qualifying exam committee and have stuck it out through the yearly updates to now, years later, as the members of my thesis committee. They have their own labs to run, and other committees to sit on, but these men have always been interested in my work and have provided essential feedback. I don't know when or in what form this research would have been completed without their input, but it would definitely be for the worse.

Finally, I need to thank my PI, Evan Scott. Evan has been the best boss I could have possibly hoped for. I am naturally inclined to be inquisitive and impulsive, but also prone to losing interest as things become difficult or as they slow down. Evan has helped me strengthen my good qualities while supporting my development as I got used to hunkering down and powering through the slower and more annoying parts of science. Science (and biology in particular) is filled with disappointments as experiments that seemed so straightforward return strange or contradictory results. Through it all, Evan has remained positive and easy to approach. I never felt afraid to come to him for help, or worried about how he would react to bad news. I also appreciate how quick on his feet Evan is – I can come up with some pretty strange and out-there ideas, but Evan has always rolled with the punches and could help refine some of the wilder pitches I've made. The thing I'm most appreciative of is that Evan has given me extremely wide latitude to pursue my interests and try things out. I have felt very fulfilled in my research, a feeling that I think is rare for PhD students. I owe that feeling to Evan.

LIST OF ABBREVIATIONS

PEG-*b*-PPS	Poly(Ethylene Glycol)-Block-Poly(Propylene Sulfide)
LDLR	Low Density Lipoprotein Receptor
IV	Intravenous
NF-κB	Nuclear Factor Kappa-Light-Chain-Enhancer of Activated B Cells
PSs	Polymersomes
DPPE	1,2-Dipalmitoyl-sn-Glycero-3-Phosphoethanolamine
CMC	Critical Micelle Concentration
CAC	Critical Aggregation Concentration
Tg	Glass Transition Temperature
PPO	Poly(Propylene Oxide)
LogP	Octanol:Water Partition Coefficient
MCs	Micelles
FMs	Filomicelles
MW	Molecular Weight
FDA	Food and Drug Administration
PRRs	Pattern Recognition Receptor
TLR	Toll-Like Receptor
PAMPs	Pathogen-Associated Molecular Patterns
DAMPs	Damage-Associated Molecular Patterns
IFN	Interferon
TGF	Transforming Growth Factor
IL	Interleukin
TNF	Tumor Necrosis Factor
DCs	Dendritic Cells
cDCs	Classical Dendritic Cells

APCs	Antigen Presenting Cells
MHC	Major Histocompatibility Complex
CD	Cluster of Differentiation
pDCs	Plasmacytoid Dendritic Cells
RNA	Ribonucleic Acid
LPS	Lipopolysaccharide
MDSCs	Myeloid Derived Suppressor Cells
DNA	Deoxyribonucleic Acid
NK	Natural Killer
MPS	Mononuclear Phagocyte System
FNP	Flash Nanoprecipitation
PBS	Phosphate Buffered Saline
THF	Tetrahydrofuran
TF	Thin Film
SD	Solvent Dispersion
PDI	Polydispersity Index
CIJ	Confined Impingement Jets
MIVM	Multi-Inlet Vortex Mixer
DCM	Dichloromethane
DMF	Dimethylformamide
HPLC	High Performance Liquid Chromatography
DLS	Dynamic Light Scattering
NTA	Nanoparticle Tracking Analysis
CryoTEM	Cryogenic Transmission Electron Microscopy
SAXS	Small Angle X Ray Scattering
LAL	Limulus Amebocyte Lysate
DiI	1.1’-Dioctadecyl-3,3,3’,3’-Tetramethylindocarbocyanine Perchlorate

BCN	Bicontinuous Nanosphere
MLP	Multilamellar Polymersome
TP	Tubular Polymersome
SEAP	Secreted Alkaline Phosphatase
SC	Subcutaneous
ICG	Indocyanine Green
NIR	Near Infrared
DMEM	Dulbecco's Modified Eagle's Medium
FBS	Fetal Bovine Serum
Penstrep	Penicillin Streptomycin
TMR	Tetramethylrhodamine
DiD	1,1'-Dioctadecyl-3,3,3',3'-Tetramethylindodicarbocyanine
FITC	Fluorescein Isothiocyanate
BSA	Bovine Serum Albumin
MPLA	Monophosphoryl Lipid A
Cel	Celastrol
BMDCs	Bone Marrow Derived Dendritic Cells
HBSS	Hank's Balanced Salt Solution
RPMI	Roswell Park Memorial Institute
ACK	Ammonium-Chloride Potassium
OVA	Ovalbumin
PE	Phycoerythrin
APC	Allophycocyanin
Dy	DyLight
Cy	Cyanine
LN	Lymph Node
RCF	Relative Centrifugal Force

BV	Brilliant Violet
GFP	Green Fluorescent Protein
Dex	Dextran
CB	Cascade Blue
AUC	Area Under Curve
BCIP	5-Bromo-4-Chloro-3-Indolyl-Phosphate
NBT	Nitrotetrazolium Blue
TR	Texas Red
MFI	Median Fluorescence Intensity
SD	Standard Deviation
SEM	Standard Error of the Mean
ASF	Acid Sensitive Fluorophore
DAPI	4’,6’-Diamidine-2’-Phenylindole
TDB	Trehalose Dibenhenate
PMA	Phorbol 12-Myristate 13-Acetate
ELISA	Enzyme Linked Immunosorbent Assay
NHP	Non-Human Primate
PLGA	Poly(Lactide-co-Glycolide)
MRI	Magnetic Resonance Imaging
cMo	Classical Monocyte
ncMo	Nonclassical Monocyte
IVIS	Intravital Imaging System
LD50	50% Lethal Dose
RT-PCR	Reverse Transcriptase Polymerase Chain Reaction
RNAseq	Ribonucleic Acid Sequencing
HRP	Horseradish Peroxidase
CBC	Complete Blood Count

CH50	50% Hemolytic Complement
BUN	Blood Urea Nitrogen
AST	Aspartate Aminotransferase
ALT	Alanine Aminotransferase
RBC	Red Blood Cell
WBC	White Blood Cell
CTLA	Cytotoxic T-Lymphocyte-Associated Protein
LDL	Low Density Lipoprotein
MyD88	Myeloid Differentiation Primary Response 88
AP-1	Activator Protein 1
IKK	Inhibitor of Kappa B Kinase
JNK	C-Jun N-Terminal Kinase
MAPK	Mitogen-Activated Protein Kinase
TRIF	TIR-Domain-Containing Adapter-Inducing Interferon Beta
IRF	Interferon Regulatory Factor
JAK	Janus Kinase
STAT	Signal Transducer and Activator of Transcription
oxLDL	Oxidized Low Density Lipoprotein
acLDL	Acetylated Low Density Lipoprotein
MARCO	Macrophage Receptor with Collagenous Structure
LOX	Lectin-Type Oxidized Low Density Lipoprotein Receptor
mTOR	Mammalian Target of Rapamycin
mTORC	Mammalian Target of Rapamycin Complex
AKT	Protein Kinase B
ERK	Extracellular Signal-Regulated Kinase
TSC	Tuberous Sclerosis Complex
TKR	Tyrosine Kinase Receptor

IGF	Insulin-Like Growth Factor
TRAF	Tumor Necrosis Factor Receptor Associated Factor
PI3K	Phosphoinositide 3-Kinase
HSP	Heat Shock Protein
HSF	Heat Shock Factor
IP	Intraperitoneal
DMSO	Dimethyl Sulfoxide
OCT	Optimal Cutting Temperature
ORO	Oil Red O
DN	Double Negative
R-PS	Rapamycin Polymersomes
EC50	Half Maximal Effective Concentration
NET	Neutrophil Extracellular Trap

DEDICATION

I dedicate this dissertation to my 할머니, 허연옥. When I was young, I promised I would grow up to try to find a way to make your arthritis go away. I hope that this work, in its small way, will help fulfill a part of that promise. Without your love and support, none of this would have been possible.

TABLE OF CONTENTS

LIST OF FIGURES

LIST OF TABLES

CHAPTER 1

Introduction: Overview and Review of Literature

1.1. Dissertation Overview

1.1.1. Motivations and Objectives

Many diseases and disorders have, as a component of their etiology, an inflammatory component. In diseases such as these (e.g. atherosclerosis) anti-inflammatory compounds would likely serve a complementary role to already-used therapeutics but are rarely investigated, often due to off-target effects or poor bioavailability. This work details the development of poly(ethylene glycol)-block-poly(propylene sulfide) (PEG-*b*-PPS) based nanocarriers to serve as drug delivery vehicles to enhance the bioavailability and specificity of anti-inflammatory therapeutics.

1.1.2. Dissertation Outline

The remainder of Chapter 1 will serve as a comprehensive literature review of polymeric nanoparticles in general, PEG-*b*-PPS nanocarriers in particular, and the use of either as drug delivery vehicles. The *in vivo* fate of nanoparticles and their toxicology will be discussed, along with a primer on immunobiology, which is relevant to the biodistribution of nanoparticles. Finally, Chapter 1 will close with a discussion of the current state of anti-inflammatory nanoparticle therapeutic research. Chapter 2 will discuss my introduction of a new method of forming PEG-*b*-PPS nanocarriers called flash nanoprecipitation and my efforts to validate it against currently used methods of forming nanocarriers. Chapter 3 will discuss my development of PEG-*b*-PPS nanocarriers as drug delivery vehicles, particularly with regard to their loading of cargo, subcellular localization, cellular biodistribution, and *in vivo* organ biodistribution. Chapter 4 will cover my work demonstrating the safety of these PEG-*b*-PPS nanocarriers in mice and non-human primates. Chapter 5 concerns the anti-inflammatory applications of these nanocarriers I have developed, specifically their use as a treatment for murine atherosclerosis. Chapter 6 serves as a summary of my work and an outline of future directions for the continued development of PEG-*b*-PPS nanocarriers.

1.2. Review of Literature

Many of the micro- and nano-sized supramolecular structures in biology are formed from amphiphilic lipids (e.g. phospholipids), which feature a hydrophilic head group and a hydrophobic lipid tail(s) [1]. The thermodynamically driven self-assembly of these amphiphiles in aqueous solution leads to aggregate formations, often with defined shapes such as bilayer membranes or micellar spheres [2, 3]. Inspired by these lipids, materials scientists have explored the synthesis and application of amphiphilic polymers that self-assemble into analogous structures under aqueous conditions [4-6], a comparison of which is shown in **Figure 1-1**. As with their lipid counterparts, these polymers possess a hydrophilic and hydrophobic portion, typically as separate polymers (i.e. blocks) covalently attached to one another [7]. These polymer amphiphiles are often of a considerably higher molecular weight than their lipid counterparts, however, which imparts their aggregate structures with occasionally different properties. For example, lipid bilayer vesicles, otherwise known as liposomes [8], have been demonstrated to be less stable to shear forces than polymersomes (PSs) [6], the equivalent structure formed of amphiphilic polymers. This trend holds generally true, with the polymers generally featuring lower critical micellar concentrations than lipids and imparting greater stability to the assembled nanoparticles [9].

1.2.1. Self-Assembled Polymeric Nanocarriers

The use of polymer for the formation of self-assembled nanostructures is also beneficial due to their synthetic nature. As many of the commonly used polymers for this purpose are synthesized through a polymerization process (rather than being isolated from natural sources), rational engineering decisions can be made with regard to the choice of monomers and the inclusion of reactive groups or stimuli-responsive elements. More diverse chemical architectures than simple headgroup-tail are commonly synthesized, e.g. multi-arm block copolymers, dendrimers, tri- and ter-block copolymers. In all, the usage of polymers instead of phospholipids allows for the engineering of materials properties that allow for more complex control over the behavior of the aggregate morphologies that are formed. With the number of

variables available, this section will explicate the relationship between polymer properties and the properties of the resulting polymeric nanoparticles.

The formation of nanoscale aggregates in a solution of block copolymers where at least one block is insoluble in the solvent is driven by the solvophobic 'burying' of these insoluble blocks from the

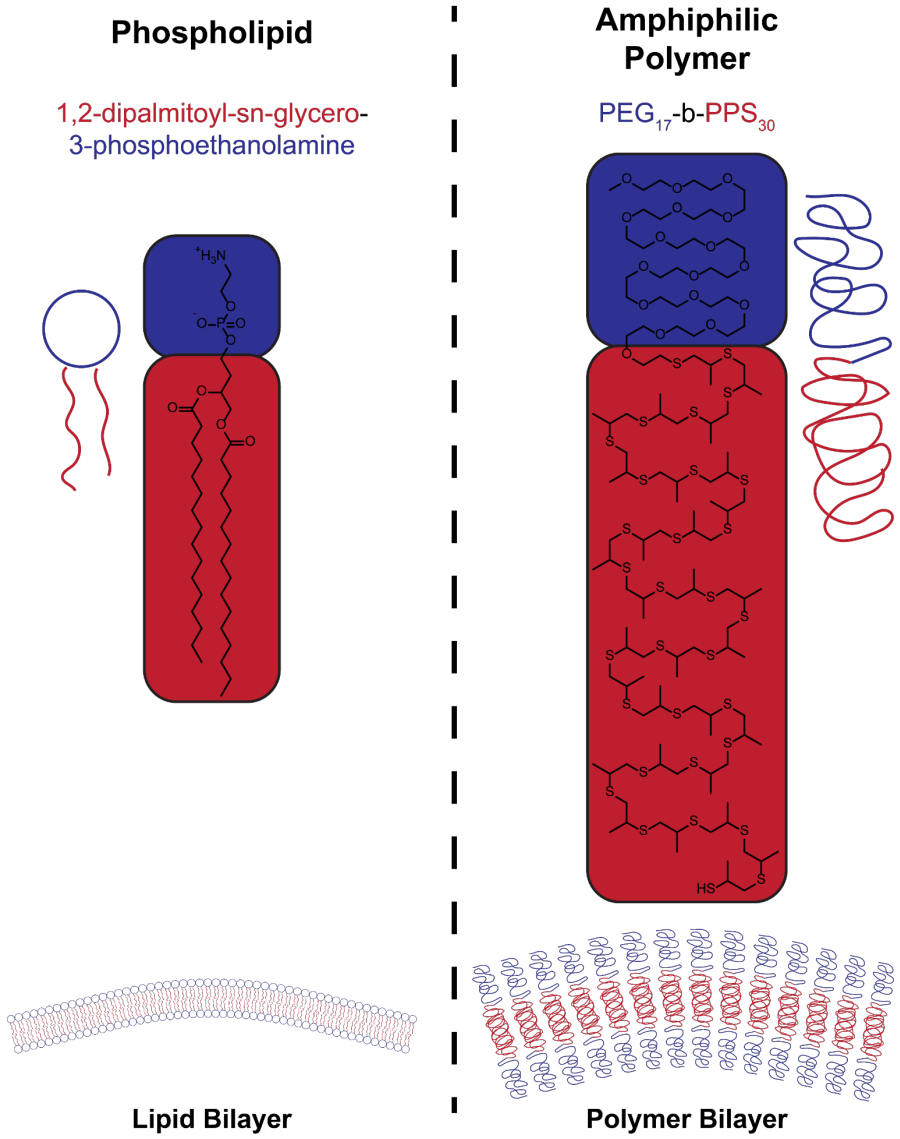

Figure 1-1. Comparison of an example phospholipid and amphiphilic polymer. DPPE, a common lipid used in liposomes, is displayed on the left. PEG-*b*-PPS, the primary polymer used in the studies covered by this dissertation, is shown on the right. Hydrophilic portions are shown in purple and hydrophobic in red. A bilayer formed from each molecule shown below.

surrounding solvent. As this dissertation relates to the biomedical applications of these nanoparticles, the solvent is aqueous, and therefore the solvophobic block is correspondingly hydrophobic. This ability to form aggregates requires a sufficient concentration of the block copolymer in solution. At too low a concentration, individual polymer molecules exist in solution without aggregating. At a particular concentration, sufficient polymer exists in solution such that aggregate structures can begin to form, a concentration known as the critical micelle concentration (CMC, sometimes also conceptualized as the critical aggregation concentration or CAC) [10, 11]. The relationship between the size of the hydrophobic block of the polymer and the polymer CMC is:

$$\log CMC = aN_i^{1/3} + b$$

Where *a* and *b* are constants specific to the polymer used and N_i is the number of repeat monomer units in the hydrophobic block [12]. The thermodynamic stability of polymeric nanoparticles is fundamentally related to the CMC, and as polymer chains have more points of interaction with one another compared to lipids, they have a lower energy of micellization [13].

Glass transition temperature of a polymer is the temperature at which there is a switch between a hard or 'glassy' state and a soft or 'rubbery' state for the polymer. These two states represent, conceptually, a difference in the degree of interaction between polymer molecules, where at temperatures below the glass transition temperature (Tg) the polymer demonstrates reduced fluidity and increased intermolecular interaction and at temperatures above the Tg the polymer has increased fluidity and flexibility [14]. When polymers are organized into membranes, the relationship between the temperature of the system and the Tg of the polymer can result in stiff crystalline membranes or more fluid membranes [15]. This, in turn, can result in differences in the plasticity and deformability of the nanostructure at different temperatures, or in the presence of plasticizing agents [16]. The Tg of a polymer can also influence its ability to be properly hydrated during nanoparticle formation, as polymers with higher Tg values may require higher temperatures during nanoparticle formation in order to ensure proper aggregate formation [17, 18].

The molecular weight of the hydrophobic block of the polymer is directly related to the CMC of the polymer, as discussed above. Additionally, molecular weight is directly related to the size of the nanoparticle aggregate, with larger molecular weights corresponding to larger radii [19, 20]. In the case of membranes,

this can result in reduced porosity [21] and reduced fluidity [22]. Additionally, increased hydrophobic volume can allow for higher loading capacities for hydrophobic cargo [23]. Higher molecular weight for the hydrophilic block can allow for greater coverage of the hydrophobic phase of the particle. In a biological context, larger hydrophilic blocks can more effectively reduce adsorption of hydrophobic domains of compounds (e.g. proteins) to the nanoparticles, reducing non-specific uptake and increasing circulation time [24].

Amphiphilic block copolymers can form a variety of aggregate morphologies in aqueous solvent. Disregarding strong interactions between polymer molecules, which can significantly complicate prediction of aggregate morphology [25], the main determinant of the aggregate morphology that a polymer will form is the molecular packing parameter of the polymer [26]. The packing parameter, p, is defined as:

$$p = \frac{v}{a_o l_c}$$

Where v is the volume of the hydrophobic block, a_o is the surface area of the hydrophilic block, and l_c is the length of the hydrophilic block [27]. When p > 1, inverted aggregate morphologies are formed, akin to cubosomes [28]. When p = 1, planar lamellae are formed, while 1/2 < p < 1 leads to vesicular formations, 1/3 < p < 1/2 form cylindrical structures, and p < 1/3 forms spherical micelles [29]. As these terms can be

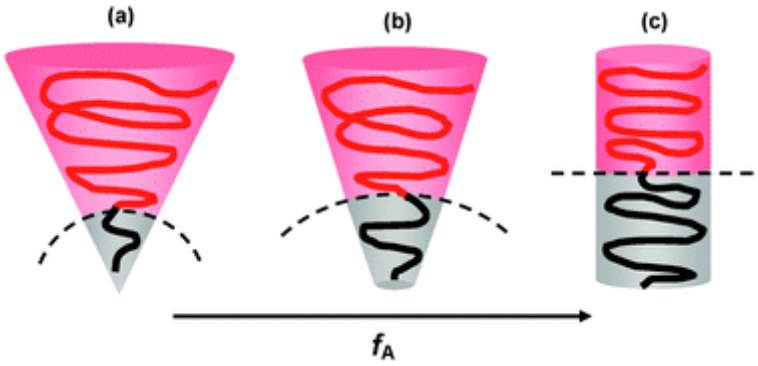

Figure 1-2. Illustration of the packing parameter of a diblock copolymer. Red represents the hydrophilic block and black the hydrophobic, with the dashed line representing the interface between the two. Represented are the polymer packing geometries to form (a) spherical micelles, (b) cylindrical micelles, and (c) vesicles. f_A in this figure represents the hydrophobic mass fraction, equal to 1-$f_{Hydrophilic}$. Reproduced from [29] with permission from The Royal Society of Chemistry.

related to the molecular weight of the hydrophilic and hydrophobic blocks of the copolymer, for a given copolymer it is possible to rationally choose sizes for the blocks to achieve a particular aggregate morphology (**Figure 1-2**).

1.2.2. Poly(ethylene glycol)-block-poly(propylene sulfide)

The polymer used in the studies covered by this dissertation is poly(ethylene glycol)-block poly(propylene sulfide) (PEG-*b*-PPS). This polymer, first synthesized in the Hubbell Lab in 2001 [30], was inspired by Pluronic polymers, which are di- and tri-block polymers made up of PEG and poly(propylene oxide) (PPO) capable of forming aggregate nanoscale morphologies such as micelles and polymersomes, driven by the hydrophobicity of the PPO block [31-33]. Observing that PPS is similar to PPO atomically, differing only by a substitution of an oxygen with a sulfur, but also recognizing that PPS, as a homopolymer, is significantly more hydrophobic than PPO, researchers in the Hubbell Lab surmised that PEG-*b*-PPS may have a similar ability to form nanoparticles as Pluronics, but may have increased stability driven by the increased hydrophobicity of PPS [34, 35]. As demonstrated in **Table 1-1**, while PPO, PPS, and PEG all have similar glass transition temperatures, they have considerably different calculated octanol:water partition coefficients [36]. PEG is the most hydrophilic, with a negative logP value demonstrating its preferential partition into water over octanol. While both PPO and PPS have positive logP values, PPS far outstrips the hydrophobicity of PPO. As mentioned in section 1.2.1., the hydrophobicity of the polymer block in aqueous media is the driving force behind the formation of aggregate supramolecular structures. Additionally, hydrophobicity is an important variable for the stability of the aggregate structures, as it

Table 1-1. Structures and characteristics of selected polymers.

Polymer	Structure	Calculated logP at 30 Monomer Units	Glass Transition Temperature (°C)
Poly(ethylene glycol)	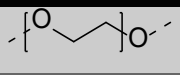	-4.95	-67
Poly(propylene oxide)	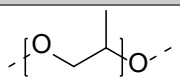	4.24	-74
Poly(propylene sulfide)	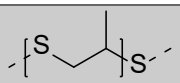	26.82	-46

minimizes the movement of single polymer chains out of the aggregate structure and into solution. Given the importance of stability for biomedical applications (further discussed in section 1.2.3.), PPS seemed like a good hydrophobic block to explore. The choice of PEG is straightforward, as it is the most commonly utilized hydrophilic block for amphiphilic block copolymers [37, 38]. Following the 1977 demonstration by Abuchowski et al. that PEGylation (i.e. the covalent attachment of PEG to another molecule) of catalase reduced the immunogenicity and prolonged the circulation half-life of the catalase after intravenous (IV) administration [39], PEG has seen expansive adoption in a number of biomedical applications for its perceived ability to limit biofouling and clearance *in vivo* [40-42].

As had been previously demonstrated with other block copolymers made up of a hydrophilic and hydrophobic block, PEG-*b*-PPS demonstrated the ability to form different aggregate morphologies depending on the hydrophilic mass fraction of the polymer (f_{PEG}), i.e.:

$$\frac{MW_{Hydrophilic}}{MW_{Hydrophilic} + MW_{Hydrophobic}}$$

Work by Cerritelli et al. identified three aggregate morphologies that could be achieved using PEG-*b*-PPS at different f_{PEG}: micelles (MCs), filamentous micelles with a high aspect ratio i.e. filomicelles (FMs), and vesicles i.e. polymersomes (PSs) [35] (**Figure 1-3**). Aside from increased hydrophobicity, PPS has an additional characteristic that differentiates it from the poly(propylene oxide), namely the ability of the sulfur group to be oxidized to a sulfoxide and sulfone group. As the PPS becomes oxidized, it becomes less hydrophobic. This shift in hydrophobicity was found to be sufficient to destabilize the aggregate morphology of the PEG-*b*-PPS nanocarriers by shifting the f_{PEG} upward. For example, oxidation of PEG-*b*-PPS that forms polymersomes resulted in the destabilization of the polymersomes and the release of cargo loaded within the polymersomes [43]. Oxidation of the PPS block of PEG-*b*-PPS can also drive the shift from one aggregate morphology to another, e.g. from filomicelles into spherical micelles [44]. This oxidation-responsive nature of PEG-*b*-PPS has biological implications, as oxidative species can be found in some specific biological contexts, such as within the endolysosomal pathway of cells. Oxidation of PEG-*b*-PPS nanocarriers within the endolysosomal pathway can result in cargo release, including escape of cargo from the lysosomes into the cytoplasm [45].

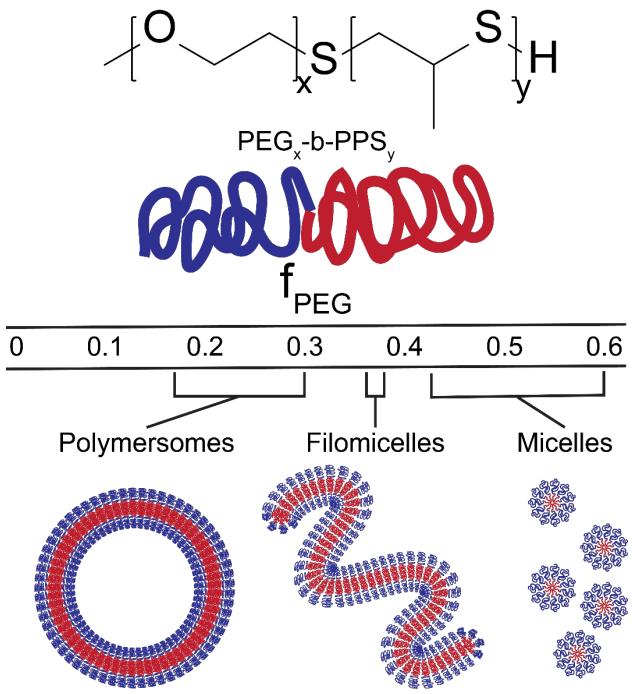

Figure 1-3. Relationship between hydrophilic mass fraction and aggregate morphology. The hydrophilic mass fraction, f_{PEG}, determines what aggregate morphology PEG-*b*-PPS will form, for a given formation technique. Polymersomes form at f_{PEG} values from 0.17 to 0.3, filomicelles from 0.37 to 0.39, and micelles from 0.42 to 0.6, when formed by thin film rehydration.

1.2.3. Polymeric Nanocarriers as Drug Delivery Vehicles

Nanoparticles may be used as delivery vehicles (i.e. as *nanocarriers*) in biomedical contexts to enhance or alter properties of the cargo compared to administration in free form. There are five primary ways by which cargo encapsulation within nanocarriers can alter its properties (**Figure 1-4**). **1)** Nanocarriers can help improve the solubility and hence bioavailability of hydrophobic compounds, some of which are only sparingly soluble in biological fluids and are often cleared from circulation by adsorbing to serum albumin. As many currently used and potential drug candidates are hydrophobic or suffer from poor bioavailability, nanocarriers are a promising formulation-based method of expanding the utility of classes of compounds that may otherwise see reduced use in clinical applications. **2)** Nanocarriers can protect sensitive cargo from degradation. Some cargoes demonstrate short *in vivo* half-lives due to rapid turnover

or degradation through enzymatic (e.g. protease, lipase, esterase) and other processes (e.g. hydrolysis, oxidation). Encapsulation in nanocarriers can offer some protection for these cargoes through physical isolation of the cargo from the degradative process. **3)** Nanocarriers allow for targeted delivery, both passive/intrinsic and active, which can simultaneously enhance the amount of cargo that reaches the target tissue or cell type while reducing off-target effects due to delivery to non-target cells. **4)** Nanocarriers allow for control over combinatorial delivery. Under normal circumstances, combinatorial drug therapies result in systemic administration of multiple compounds that have different pharmacokinetics, resulting in differential

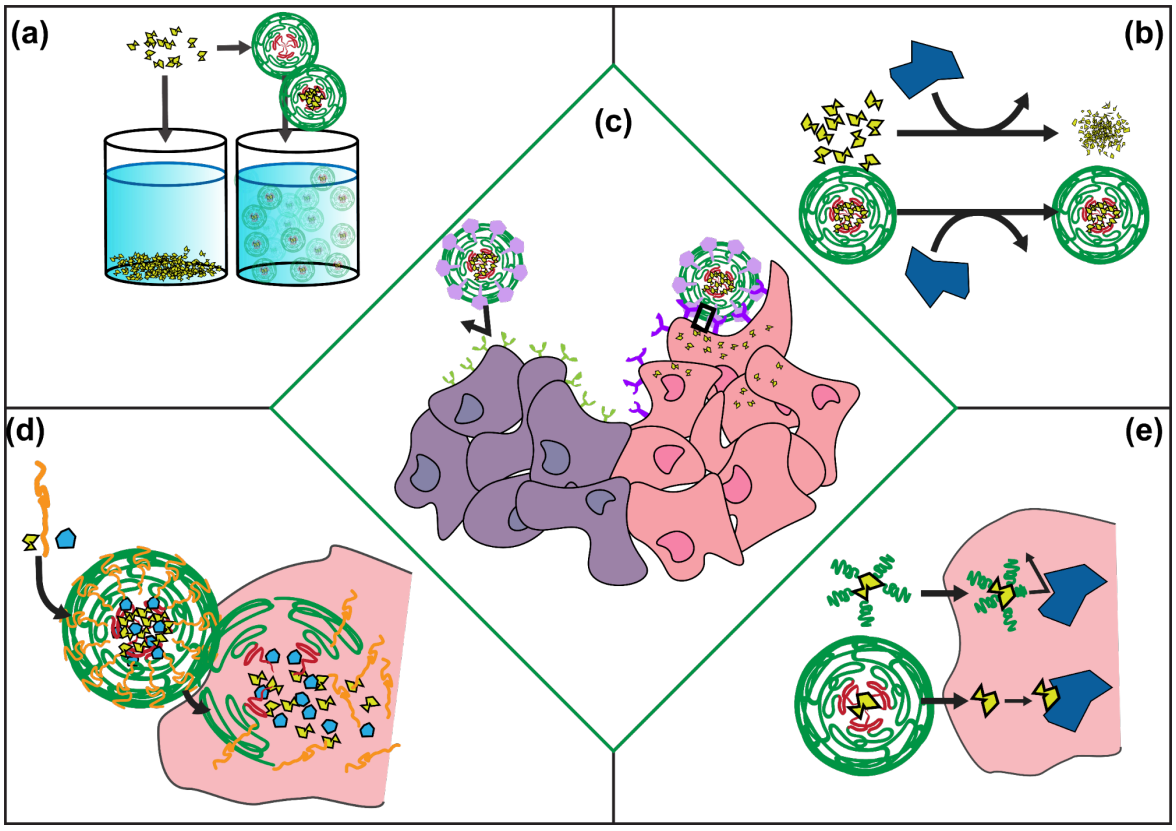

Figure 1-4. Illustration of drug delivery benefits of nanocarriers. (a) Encapsulation of hydrophobic or otherwise poorly water-soluble cargo within nanocarriers can improve aqueous solubility. (b) Encapsulation of cargo can protect cargo from degradation. (c) Nanocarriers can be functionalized to allow for targeted delivery. (d) Co-encapsulation of several cargoes into a nanocarrier can allow for simultaneous and controlled delivery to a target. (e) Nanocarriers can be engineered independently of the cargo, preventing situations where engineering of the cargo results in a reduction or loss of activity.

spatiotemporal distribution of the compounds in the body. In contrast, compounds co-encapsulated within a nanocarrier will be delivered to the same tissue or cell. In cases where it is important that both compounds reach the same cell, such as in vaccination where the antigen and adjuvant are both required to mount a robust response from antigen presenting cells, encapsulation in nanocarriers can reduce the stochasticity and increase the effectiveness of the formulations. **5)** Nanocarriers may be rationally designed independent of the cargo, allowing for changes to be made to the delivery vehicle without altering the potential therapeutic efficacy or properties of the cargo (e.g. PEGylation may reduce the inhibitory effectiveness of a drug; nanocarriers may be PEGylated instead, and the unmodified drug may be loaded inside). This allows for modifications that include the aforementioned addition of active targeting moieties such as peptides or antibodies. This also allows for the engineering of stimuli responsive cargo release, such as upon a change of pH, oxidative environment, ultrasound, etc.

There are a number of FDA-approved nanocarriers available in the clinic, which are listed in **Table 1-2**. With the exception of Abraxane, a simple conjugation of the drug paclitaxel to the protein albumin, all of the currently approved nanocarriers are lipid-based, with nearly all being liposomal [46-49]. The primary benefit from liposomal formulation has been a reduction in toxicity due to reduced non-specific uptake. Most of these treatments (6 of the 9 liposomal formulations) are treatments for cancer. All of these currently approved treatments are reformulations of previously approved drugs, which aided in the approval process. Liposomes possess a number of limitations as effective drug delivery vehicles, as was discussed in the introductory paragraph of section 1.2. Though there have been some successes, the number of approved liposomal formulations is dwarfed by the number that failed to be approved [50]. This failure is largely due to an inability to demonstrate an increase in effectiveness compared to free drug, potentially due to clearance of the liposomes by the immune system [51].

In light of these limitations and the success of polymersomes in outperforming liposomes in terms of stability and *in vivo* efficacy in preclinical studies, the result of increased circulation time and greater potential for the cargo to be delivered to the intended target [52], the question arises of why there has not been increased translational application of polymeric nanocarriers. The first answer is simply a consideration of time. Liposomes were first characterized by Alec Bangham and Robert W. Horne in 1964

[53] but were only successfully translated into the clinic in 1995, over 30 years later. Polymersomes, best characterized in the Eisenberg Lab in 1995 [54, 55] and the Discher Lab in 1999 [6], thus have only had 20 years of research. It is to be expected that polymersomes would have a somewhat easier path forward toward translation, with liposomes alleviating some of the concerns about use of therapeutic nanoparticles in humans. However, liposomes, made up of highly biocompatible lipids, are considered less potentially

Table 1-2. Current list of FDA-approved nanocarrier formulations for clinical use.

Name	Formulation Type	Disease/Disorder	Date Approved	Improvement Over Traditional Formulation
Doxil	Liposomal Doxorubicin	Kaposi's Sarcoma, Ovarian Cancer	1995	Increased targeting, reduced toxicity
Abelcet	Liposomal Amphotericin B	Fungal Infection	1995	Reduced toxicity
Visudyne	Liposomal Verteporfin	Age-Related macular Degeneration	2000	Increased stability
Estrasorb	Lipid Micelle Estrogen	Hot Flashes	2003	Increased delivery, increased solubility
DepoDur	Liposomal Morphine Sulfate	Pain Management	2004	Sustained release
Abraxane	Albumin Bound Paclitaxel	Breast, Pancreatic, and Lung Cancers	2005	Increased solubility, increased targeting
DepoCyt	Liposomal Cytarabine	Lymphomtous Meningitis [Discontinued]	2007	Increased targeting, reduced toxicity
Exparel	Liposomal Bupivacaine	Pain Management	2011	Reduced dosage, improved efficacy
Marquibo	Liposomal Vincrisitine	Acute Myelogenous Leukemia	2012	Increased targeting, reduced toxicity
Onivyde	Liposomal Irinotecan	Advanced Pancreatic Cancer	2015	Increased targeting, reduced toxicity
Vyxeos	Liposomal Cytarabine and Daunorubicin	Acute Myeloid Leukemia	2017	Increased targeting, reduced toxicity, dual delivery

toxic or dangerous compared to synthetically produced polymers, some of which do not have clear routes of degradation or elimination from the body. These concerns, coupled with continued skepticism about the consistent production of liposomal formulation, have led to some headwinds against the translation of polymeric nanoparticles into the clinic. The second answer to the current absence of FDA-approved polymeric nanoparticle therapeutics is that there are a number that are currently in clinical trials [56-58]. This includes Genexol-PM, a polymeric nanoparticle formulation of paclitaxel that, while not approved by the FDA, is currently approved for use in South Korea [59].

Table 1-3. Current list of FDA-approved PEGylated formulations for clinical use.

Name	Formulation Type	Disease/Disorder	Date Approved
Pegadamase	11-17 PEG 5k, adenosine deaminase	Severe Combined Immunodeficinecy	1990
Pegaspargase	69-82 PEG 5k, L-Asparaginase	Leukemia	1994
Pegvisomant	4-6 PEG 5k, human growth hormone	Acromegaly	2002
Pegloticase	9 PEG 10k, urate oxidase	Chronic Gout	2010
PEG-Interferon α2b	1 PEG 12k, Interferon α2b	Hepatitis C	2001
Pegfilgrastim	1 PEG 20k, granulocyte colony stimulating factor	Neutropenia	2002
PEG-EPO	1 PEG 30k, erythropoietin	Chronic Renal Failure	2007
Pegaptanib	1 PEG 40k Branched, nucleotide aptamer	Macular Degeneration	2004
PEG-Interferon α2a	1 PEG 40k Branched, Interferon α2a	Chronic Hepatitis C	2002
Certolizumab Pegol	1 PEG 40k Branched, anti-TNF Antibody Fab	Chronic Rheumatoid Arthritis	2009
PEG-Interferon β1	1 PEG 20k, Interferon β1	Relasping Multiple Sclerosis	2014

Ultimately, adoption of polymeric nanocarriers for clinically-relevant treatments will require them to outperform traditional formulation methods through improvement of solubility, stability, and bioavailability of the therapeutic. The polymeric nanocarriers will also need to have a compelling utility over lipid nanoparticles, most likely due to increased stability and engineerable characteristics, while maintaining or improving upon the biocompatibility of lipid nanoparticles. Polymeric nanocarriers will need to be fabricated rapidly, consistently, sterilely, and at volumes relevant for human use. The work represented in this dissertation attempts to address several of these concerns for the advancement of polymeric nanocarriers to the clinic.

1.2.4. Inflammation and Immunobiology

Further discussion of *in vivo* applications of nanoparticles will first require a primer on the main group of cells, tissues, and organs that take up the nanoparticles after administration: the immune system. The immune system can be grouped functionally into collections of cells: innate vs adaptive immune cells, phagocytic vs non-phagocytic immune cells, professional antigen presenting cells vs non-antigen presenting cells, inflammatory vs anti-inflammatory immune cells, lymphoid vs myeloid cells, etc. The major immune cell types are grouped based on these functional categories in **Figure 1-5,** and a subset of these cell types along with their subpopulations have their properties summarized in **Table 1-3**. These cell types are particularly important with regard to nanoparticle interactions with the immune system and therefore will be discussed in greater detail. These immune cells are produced in primary lymphoid organs (fetal liver, bone marrow, thymus) and mature in secondary lymphoid organs (spleen, lymph nodes [60]). It is within these secondary lymphoid organs that a significant amount of antigen presentation and cell activation occurs.

Macrophages are phagocytic cells, some of which are embryonic in origin and others of which are derived from monocytes. There are a number of tissue specific macrophage subpopulations (e.g. red pulp macrophages, Kupffer cells, alveolar macrophages, etc.), and given both their phenotypic and ontogenetic diversity, the categorization of macrophages is somewhat controversial. Generally speaking, it can be said that macrophages are mononuclear cells that are highly phagocytic [61]. This broad functional definition,

devoid of ontogeny, underscores the variety of different specialized tasks that tissue-specific macrophages perform. Macrophages are critical for tissue maintenance and regularly phagocytose senescent and apoptotic cells. In some tissues, such as the lungs, macrophages highly express pattern recognition receptors (PRRs), such as the Toll-like receptor (TLR) family [62]. Alveolar macrophages utilize these receptors to actively phagocytose and clear bacteria and debris from the lungs [63]. Signaling through TLR and other PRR pathways results in active secretion of pro-inflammatory cytokines, resulting in robust immune responses [64]. In contrast, gut resident macrophages, which are also highly phagocytic, demonstrate significantly reduced inflammatory cytokine production, even after phagocytosis of bacteria [65]. This demonstrates that a focus on delivering to a particular cell type, with no regard to tissue or organ, is not an effective strategy for delivery to macrophages. Aside from the highly diverse category of tissue-resident macrophages, there also exist a group of macrophages that typically appear at the site of tissue damage or infection. These macrophages are derived from Ly-6C^{hi} monocytes and typically exist

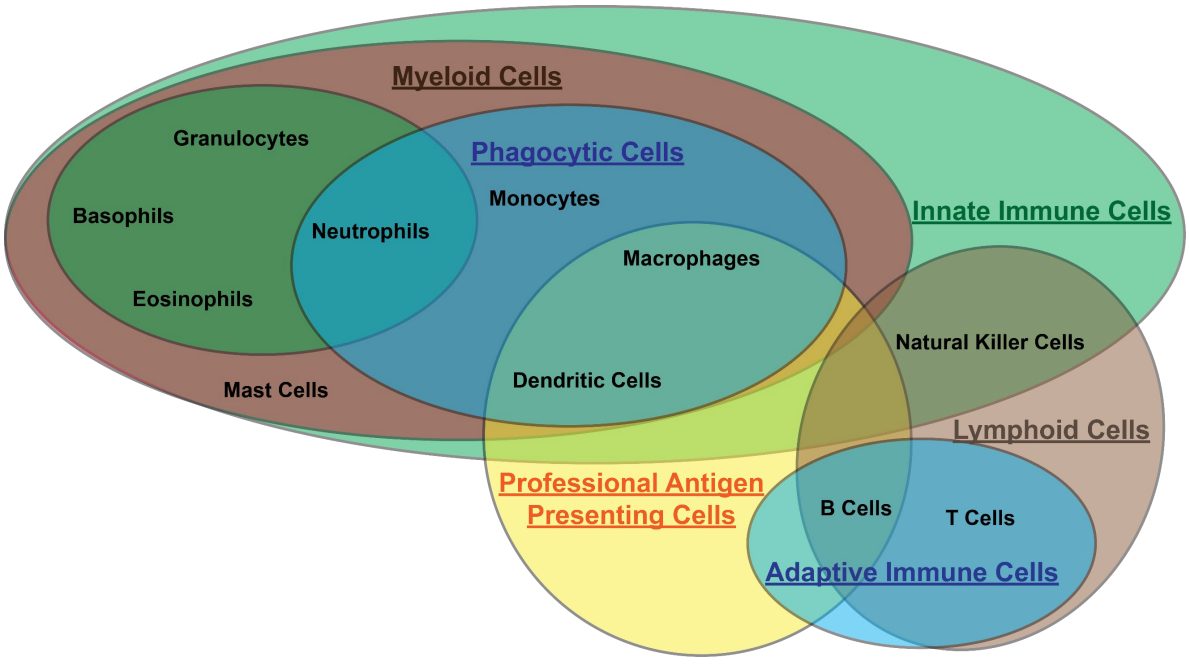

Figure 1-5. Groupings of the major immune cell populations. Group names are underlined. Cells belong within each grouping (i.e. circle) within which they fall.

Table 1-4. Selected immune cell populations of particular importance in the following studies.

Cell Type	Lineage	Inflammatory Contribution	Phagocytic Capacity	Antigen Presentation Capacity
Macrophages	Embryonic, Myeloid	Typically pro-inflammatory	High	Moderate
-M1		Strongly pro-inflammatory	High	Moderate
-M2		Often resolves inflammatory state	Moderate	Moderate
Monocytes	Myeloid	Typically pro-inflammatory	Moderate	Low
-Ly-6C High		Pro-inflammatory	Moderate	Low
-Ly-6C Low		Unclear	Low	Low
Dendritic Cells	Myeloid	Can be pro- or anti-inflammatory	Moderate	High
-Classical		Typically pro-inflammatory, unless induced to be tolerogenic	Moderate	High
-Plasmacytoid		Can modulate adaptive immune responses	Low	Low
Neutrophils	Myeloid	Very pro-inflammatory	High	Low
Natural Killer Cells	Lymphoid	Pro-inflammatory	Low	Low
B Cells	Lymphoid	Pro-inflammatory	Low	Moderate
T Cells	Lymphoid	Typically pro-inflammatory	Low	Low
-CD4+		Pro-inflammatory	Low	Low
-CD8+		Pro-inflammatory	Low	Low
-Regulatory		Anti-inflammatory, reduces T cell responses	Low	Low

somewhere on a spectrum of polarization between two states, termed ‘M1’ and ‘M2’. Originally, these two states were considered to be distinct and discrete, but more recent work has demonstrated that they are indeed much more of a continuum, with nuanced and identifiable subsets [66]. ‘M1’ macrophages are predominantly pro-inflammatory and react to pathogen-associated molecular patterns (PAMPs) and IFN-γ

by generating nitric oxide from arginine. On the other hand, ‘M2’ macrophages, which focus primarily on tissue repair and the resolution of inflammatory response, react mainly to damage-associated molecular patterns (DAMPs) and TGF-β1 and produce ornithine from arginine. ‘M1’ macrophages are microbicidal, recruit other immune cells through the secretion of cytokines such as IL-1β and TNF-α, and can cause damage to tissues through the release of reactive oxygen species. ‘M2’ macrophages release IL-10, a tolerogenic and anti-inflammatory cytokine, and play an important role in tissue remodeling after damage and angiogenesis [67]. Both types of macrophages can be pathogenic, and it is generally important to note that macrophages can switch polarizations if needed. In fact, macrophages display surprising plasticity, a trait that can make them potentially very interesting targets for immunomodulatory treatments [68].

Dendritic cells, like macrophages, have a complex and debatable ontogeny. Characterized originally by their cell morphology (i.e. mononuclear and possessing dendrites) [69], many of the cells now considered to be dendritic cells have diverse enough morphological character such that cell shape is no longer sufficient to group the cells [70]. Monocytes can be induced to phenotypically transform into dendritic cell-like or macrophage-like cells. As these cells are often functionally indistinguishable from ‘real’ dendritic cells or macrophages, there is significant disagreement on how to classify them [71]. Dendritic cells, not of monocyte origin, are derived from a committed dendritic cell precursor in the bone marrow. Dendritic cells can be subdivided into two categories: classical dendritic cells and plasmacytoid dendritic cells. Classical dendritic cells (cDCs) are phagocytic cells that are highly effective antigen presenting cells (APCs), most likely the foremost APCs in the body. They are able to perform cross-presentation, which involves the loading of endocytic-origin peptides onto MHCI complexes. This is particularly important for viral infections, as the loading of viral antigens onto MHCI complexes would normally require a cell to be already infected. In the case of dendritic cells, they can endocytose virus particles and break them down within their endolysosomal pathway, presenting their antigens on both MHCII and MHCI molecules to activate and mature CD4+ and CD8+ T cells, respectively [72]. Plasmacytoid dendritic cells (pDCs) are not effective at endocytosis or antigen presentation when in their naïve state. They are, however, primed to respond to viral signals – pDCs express TLR7 and TLR9, receptors for single stranded RNA and CpG oligonucleotides respectively. They do not, however, strongly express TLR2 or TLR4, much more common PRRs for

bacterial pathogenic markers peptidoglycan and lipopolysaccharide (LPS). Upon stimulation by viruses, pDCs strongly secrete interferon and other cytokines to activate other immune cells. They additionally improve their capacity to present antigens through MHCII [73, 74]. pDCs are also capable of promoting tolerogenic responses and can induce regulatory T cells while simultaneously inducing anergy in activated T cells [75]. This ability to induce anergy in active T cells and promote a tolerogenic response is not specific to pDCs but does appear to function through different pathways in cDCs [76, 77].

Monocytes are bone marrow derived mononuclear cells that are categorized into two groups based on their expression level of the cell surface marker Ly-6C: high or low. Ly-6C^{hi} monocytes can be found in both blood and tissues, particularly in damaged or inflamed tissues [62]. In these sites, Ly-6C^{hi} monocytes can be activated, secrete pro-inflammatory cytokines, and can differentiate into dendritic cell-like or macrophage-like lineages [71]. Ly-6C^{low} monocytes are found primarily in the blood and do not typically exit the vasculature to enter tissue. It is not clear whether Ly-6C^{low} monocytes differentiate into Ly-6C^{hi} monocytes *in vivo* in the presence of inflammatory stimuli. Ly-6C^{hi} monocytes are more phagocytic than Ly-6C^{low} monocytes [78]. Ly-6C^{low} monocytes may themselves be pro-inflammatory under certain conditions [79]. While pro-inflammatory under most circumstances, Ly-6C^{hi} monocytes associated with tumors can take on an immunosuppressive phenotype, termed a monocytic myeloid derived suppressor cell (mMDSC) [80]. This cell population is poorly characterized but appears to be very similar to a Ly-6C^{hi} monocyte with regard to its cell surface protein expression [81]. Transcriptionally, however, mMDSCs express nitric oxide synthase and arginase 1, both of which appear to suppress T cells in the tumor microenvironment and potentially systemically [82].

Neutrophils are multi-lobed myeloid cells that are often the first recruited cell type to damaged and infected tissue. Neutrophils, in the presence of stimuli, rapidly release proteases, reactive oxygen species, signaling molecules, and antimicrobial compounds and peptides [83]. Neutrophils may also release some or all of their own DNA as an extracellular ‘trap’ for microbes, a process known as NETosis [84]. Neutrophils are highly pro-inflammatory and often cause destructive tissue remodeling during the process of releasing the cargo of their cytoplasmic granules. After their initial peak, neutrophils are typically replaced by recruited monocytes [85]. Neutrophils are highly phagocytic cells, though they are poor antigen presenters [86, 87].

In humans, neutrophils often account for a majority of the white blood cells in peripheral blood, 50-70% of circulating white blood cells [87]. In mice, however, neutrophils account for only 20-30% of peripheral white blood cells [88]. It is not clear why there is such a drastic difference between humans and mice in this regard, but it does suggest that caution would be wise when attempting to extrapolate murine results into humans relating to neutrophil-dependent immune processes [89].

T Cells are lymphoid adaptive immune cells responsible for antigen specific immune response. They can be divided into three main groups: helper T cells, cytotoxic T cells, and regulatory T cells. Helper T cells (CD4+ T cells) interact with antigen presenting cells to become activated, after which they can aid in the recruitment and activation of other immune cells, serving as an antigen-specific immune signal amplifier [90]. There are a number of helper T cell subsets, but in-depth discussion of their traits and functions are outside the scope of this dissertation. Cytotoxic T cells (CD8+ T cells) kill cells based on antigen presented on MHCI molecules, representing the cytoplasmic presence of foreign or misfolded proteins [91]. Cytotoxic T cells themselves can be aided by interactions with helper T cells [92] and can in turn also activate and recruit other cells through cytokine secretion [93]. Regulatory T cells are anti-inflammatory cells that, in the response to a specific antigen presented by an antigen presenting cell, reduce immune cell responses, typically through direct receptor engagement or through the secretion of anti-inflammatory cytokines, particularly TGF-β and IL-10 [94]. As T cells are capable of forming long-lived memory subsets, which retain the antigen-specificity of a parent T cell that successfully mounted an immune response, T cells are critically important in vaccination [95].

B Cells are the antibody producing cells of the immune system and are the only cell type to perform this function [96]. The B cell receptor, which is antigen-specific, reacts to the binding of antigen by internalizing the antigen and preparing it for presentation on MHCII. As such, B cells are able to activate T cells and function as professional antigen presenting cells [97]. This interaction with antigen primarily occurs in secondary lymphoid organs and may be significantly enhanced by follicular dendritic cells and macrophages, which can present the antigen on their surface for recognition by B cells [98]. B cells are also stimulated by helper T cells, in an antigen-specific manner, to stimulate their production of antigen-specific antibodies [99]. B cells are also able to form memory cells, which can be re-stimulated by antigen at a later

date, leading to proliferation and the production of antibodies. As such, memory B cell formation is a goal of vaccination for the purposes of long lasting immunity [100].

NK Cells are innate immune cells that are nonetheless lymphoid in origin. Like cytotoxic T cells, NK cells serve mainly to kill cells. Unlike cytotoxic T cells, which are antigen-specific, NK cells primarily recognize cells that have aberrantly reduced their MHCI production [101]. As MHCI is the complex which presents cytoplasmic antigens to cytotoxic T cells in the case of virus infection, some viruses cause a reduction in MHCI production to prevent recognition by cytotoxic T cells. NK cells are able to recognize this change and kill these infected cells. NK cells are able to produce IFN-γ after stimulation and are thus able to activate other immune cells [102]. NK cells are poorly phagocytic and are not antigen presenting cells [103].

1.2.5. Nanoparticle Uptake by Immune Cells

Nanoparticles are of a similar size to a number of biological molecules and complexes that the immune system regularly interacts with. For example, IgG antibodies are 14.2 nm in diameter [104] and viruses can range in size from tens to hundreds of nanometers in diameter [105, 106]. The immune system regularly binds to and internalizes particles of this size range through receptor mediated endocytosis, macropinocytosis, and phagocytosis. Of these three internalization mechanisms, macropinocytosis is the only one that is not strictly receptor-mediated and is typically used by antigen presenting cells for environmental sampling [107]. Nanoparticles are, therefore, macropinocytosed non-specifically by cells, particularly antigen presenting cells. Nanoparticles that are surface-functionalized with ligands for endocytosis or phagocytosis receptors, either intentionally or through protein adsorption to the surface of the nanoparticle, are also internalized through these other pathways [108]. There are size limitations for the internalization of nanoparticles *via* these different routes, with endocytosis being rare for particles > 200 nm and macropinocytosis being rare for particles > 500 nm (**Figure 1-6**) [109]. As evident by these ranges, many nanoparticles are able to be internalized *via* all three pathways. Mononuclear phagocytic cells, i.e. monocytes, macrophages, and dendritic cells, are capable of performing all three of these routes of internalization and are the main cell types that internalize nanoparticles within the body [110].

Mononuclear phagocyte system (MPS) is a term used to describe the clearance of materials in the body by monocytes, macrophages, and dendritic cells [111]. Macrophages are typically considered to be the primary cell type of the MPS [112]. While most tissues contain some resident macrophages, there are certain organs that contain macrophages and other MPS cells that act as major uptake and clearance sites

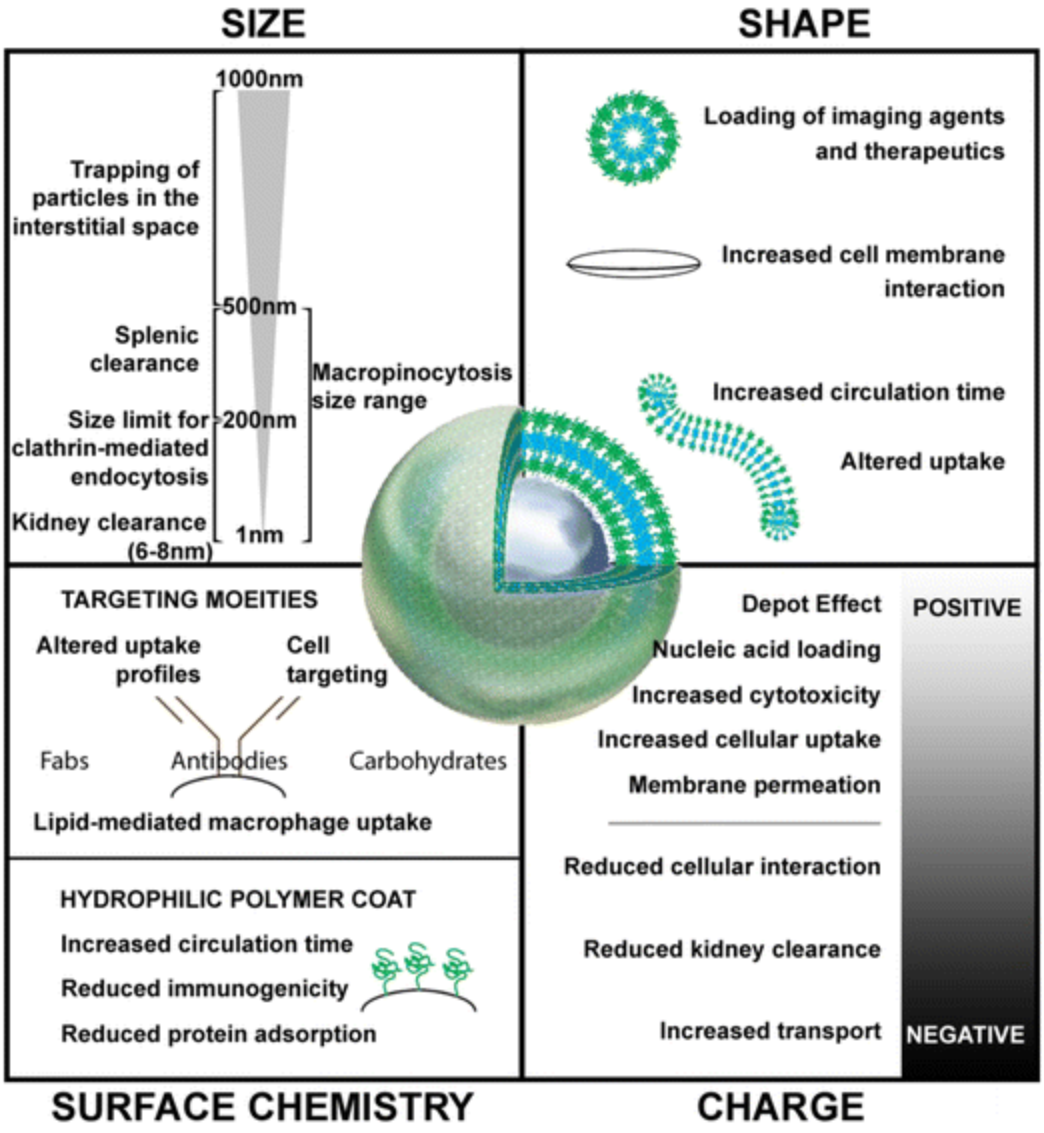

Figure 1-6. Design considerations for uptake of nanoparticles by immune cells. Size, shape, charge, and surface chemistry are important variables to consider when designing nanomaterials for the modulation of inflammatory cells. Reprinted with permission from [109] © 2016 American Chemical Society.

for nanoparticles, namely the liver, spleen, lymph nodes, and kidneys (**Figure 1-7**) [110]. Nanoparticles administered intravenously first enter systemic circulation. From there, some nanoparticles, traveling through the celiac artery, will be delivered to the liver and spleen. As the spleen is a secondary lymphoid organ, it contains nearly all of the main immune cell types and a significant number of nanoparticles will be internalized by phagocytic cells in the spleen. Nanoparticles exiting the spleen *via* the splenic vein will drain into the portal vein, which is routed through the liver prior to returning to systemic circulation. As is apparent, the liver is a very important MPS organ, with significant uptake of nanoparticles by Kupffer cells (tissue-resident macrophages), dendritic cells, other macrophage subpopulations, hepatocytes, and liver

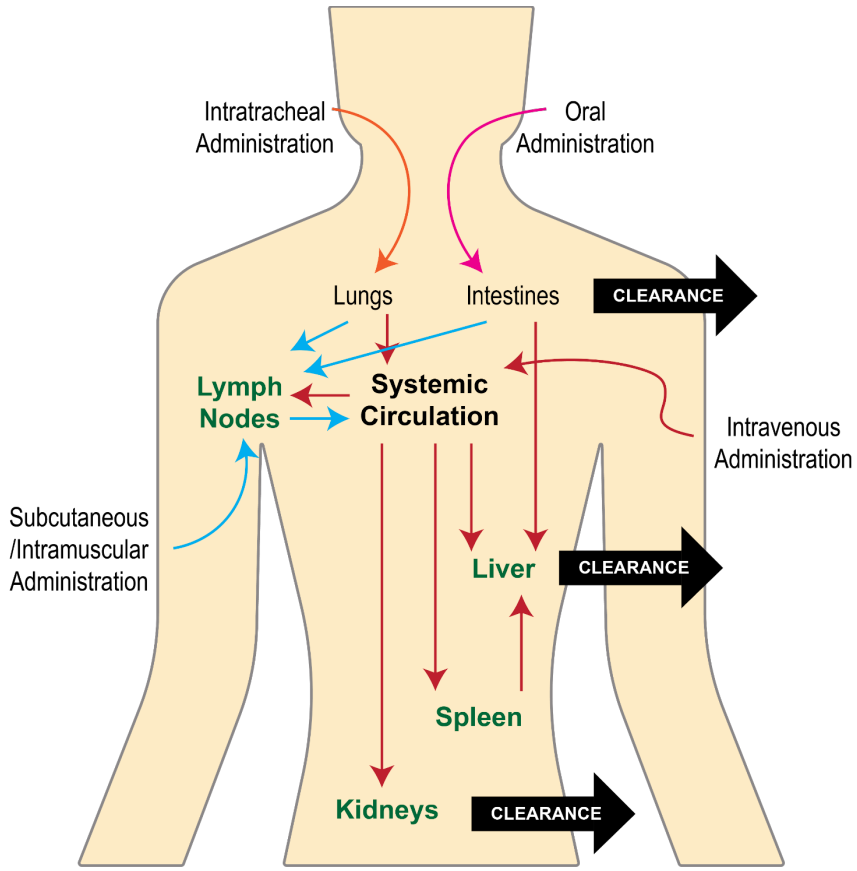

Figure 1-7. Routes of administration, uptake, and clearance of administered nanoparticles. Nanoparticles may be administered intravenously (red arrow), subcutaneously/intramuscularly (blue arrow), intratracheally (orange arrow), or orally (pink arrow). Organs in green font are major MPS organs. Large black arrows denote organs that clear large numbers of nanoparticles from the body.

Table 1-5. Current list of anti-inflammatory or immunosuppressive nanocarriers undergoing clinical trials.

Name	Formulation Type	Disease/Disorder	Phase	Company
Nanocort	Liposomal Prednisolone	Rheumatoid Arthritis	IIb	Enceladus
Oncocort	Liposomal Dexamethasone	Progressive Multiple Myeloma	I-IIa	Enceladus
L-CsA	Liposomal Cyclosporin A	Bronchiolitis Obliterans Syndrome	III	Breath Therapeutics
SEL-212	Polymeric Nanocarrier Rapamycin	Gout	III	Selecta

sinusoidal endothelial cells. For nanoparticles to be cleared from the liver, they either need to be broken down in Kupffer cells or excreted through the biliary pathway *via* hepatocytes [113]. Nanoparticles broken down into sufficiently small pieces can be cleared renally through the kidneys, though these pieces will need to be less than 6 nm in diameter [114]. For polymeric nanoparticles, such as PEG-*b*-PPS nanocarriers, individual polymer molecules are sufficiently small to be filtered out of blood renally. Other routes of administration of nanoparticles can result in different initial biodistribution, though ultimately many of the nanoparticles are still cleared through the liver. Oral administration first delivers nanoparticles to the gut, which contains MPS cells. In the gut, some nanoparticles can pass through lymphatics to lymph nodes, while others can enter into the portal vein and travel to the liver [115]. Intratracheal administration delivers nanoparticles to the lung, which contains a number of MPS cells, such as alveolar macrophages [116]. Nanoparticles that are not internalized by MPS cells directly may pass into lymphatics or into circulation. Subcutaneous or intramuscular injection of nanoparticles primarily deliver nanoparticles to the nearest draining lymph nodes, though some nanoparticles may be internalized by tissue-resident MPS cells [117].

1.2.6. Anti-Inflammatory Nanotherapeutics

There are currently no FDA-approved anti-inflammatory nanocarrier treatments. This is perhaps unsurprising, given the paucity of nanocarrier treatments in general. There are currently four anti-inflammatory nanotherapeutics in clinical trials, summarized in **Table 1-4** [49]. As nanoparticles are taken up in such significant numbers by MPS cells, it would appear that there would be significant benefit to the encapsulation of immunomodulatory compounds within nanocarriers for the delivery to immune cells. Target selectivity conferred by nanocarriers may alter the breadth and depth of immune suppression by drugs or may allow for the use of anti-inflammatory and immunosuppressive drugs that were previously considered unusable due to poor pharmacokinetics and bioavailability.

1.3. Scope of This Work

Nanocarriers have current utility as drug delivery vehicles, but a number of challenges remain that hinder their wide adoption into the standard formulation arsenal of the pharmaceutical industry. The PEG-*b*-PPS polymer is well-suited to address some of the current issues with loading and stability. As a hypothesized 'blank slate' system capable of being used for both pro- and anti-inflammatory applications, PEG-*b*-PPS nanocarriers could be used in a sector of pharmaceutical treatments that is relatively underserved by nanoparticle formulation techniques – immunomodulation. However, before PEG-*b*-PPS nanocarriers can be successfully translated into the clinic, critical questions need to be addressed. Can PEG-*b*-PPS nanocarriers be loaded with hydrophobic and hydrophilic cargo at high encapsulation efficiency in a rapid, scalable, and sterile way? Are PEG-*b*-PPS nanocarriers safe when administered *in vivo*? Can PEG-*b*-PPS nanocarriers be formulated and loaded in such a way that they can function as an anti-inflammatory therapeutic platform? These are the questions that drove the research covered in this dissertation and that have been addressed by the studies described within.

1.4. Publication Information

Sections of this chapter have been published with the following citation information:

S. Allen, Y.G. Liu, and E. Scott. Engineering Nanomaterials to Address Cell-Mediated Inflammation in Atherosclerosis. Regenerative Engineering and Translational Medicine 2(1), pp 37-50. 2016. **[109]**

CHAPTER 2

Rapid and Scalable Production of Soft Nanocarriers

2.1. Abstract

Clinical translation of nanocarriers is hindered by difficulties in scaling up the production of nanocarrier formulations. These formulations will need to be sterile and pyrogen-free and rapid prototyping would be beneficial for preclinical optimization of the formulations. Current methods for forming PEG-*b*-PPS nanocarriers are not sufficiently scalable or have too much batch-to-batch variability to be relied upon for clinical applications. Reduction of variability, particularly for polymersomes, involves the process of extrusion. The extrusion step is often rate-limiting, can reduce sterility, and can result in the loss of product. To address these issues, I utilized a method of nanoparticle formation known as flash nanoprecipitation (FNP). To date, FNP had not been utilized to fabricate complex soft polymeric nanocarriers but had instead been used for forming solid core drug nanoparticles. I found that FNP was indeed able to form PEG-*b*-PPS nanocarriers and could be used to remove the need for extrusion of PEG-*b*-PPS polymersomes.

2.2. Introduction

2.2.1. Formulation Methods for PEG-*b*-PPS Nanocarriers

PEG-*b*-PPS nanocarriers were formed primarily by two different methods since the initial characterization of the polymer, thin film rehydration (**Figure 2-1a**) and solvent dispersion (**Figure 2-1b**) [35]. In thin film rehydration, the polymer is dissolved in a volatile organic solvent and is evenly coated onto glass, e.g. the inner surface of a round bottom flask or a glass vial, through evaporation of the organic solvent. After removal of the organic solvent, the thin film of polymer is rehydrated with an aqueous solvent, such as water or 1x phosphate buffered saline (1xPBS). This rehydration is often sped up through agitation of the solution (e.g. shaking, stirring, sonication) and/or heating [118]. Nanocarriers formed by thin film rehydration are already dispersed in aqueous solvent, and therefore do not need to have any organic solvent removed (in contrast to solvent dispersion). Micelles (MCs) and polymersomes (PSs) are both able

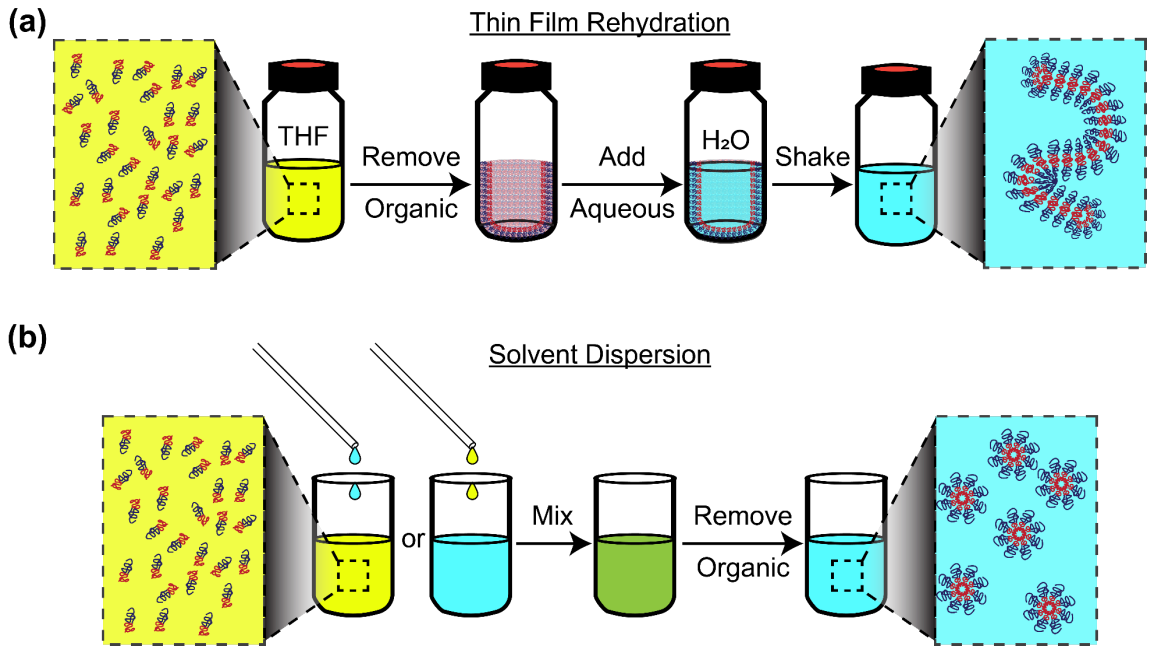

Figure 2-1. Illustration of the two formulation methods for PEG-*b*-PPS nanocarriers. (a) Thin film rehydration begins with the dissolution of polymer in a good (i.e. organic) solvent, such as THF. The solvent is removed, typically through vacuum desiccation, leaving behind a thin film of polymer deposited on the glass of the container. Aqueous non-solvent is added, and the container is shaken until nanocarriers form. (b) Solvent dispersion involves the dropwise addition of aqueous non-solvent to a vial of polymer dissolved in organic solvent or the inverse, with polymer and organic solvent added dropwise to aqueous solvent. This system is mixed, typically through stirring of a magnetic bar (not pictured). This mixed solvent system is purified to remove the organic solvent, typically through vacuum desiccation, buffer exchange columns, or dialysis.

to be formed by thin film rehydration. Filomicelles (FM) were exclusively formed by thin film rehydration [35]. The drying process to remove organic solvent takes several hours, occasionally overnight. Rehydration time depends on the polymer and conditions, but generally ranges from short (< 1 hour) for MCs to long (> 24 hours) for FMs, with PSs typically requiring several hours [44]. PSs formed by thin film rehydration are polydisperse and require extrusion in order to be a monodisperse population [43].

Solvent dispersion, often also referred to as nanoprecipitation or cosolvent dispersion, involves the gradual addition of polymer dissolved in organic solvent to aqueous nonsolvent. In the normal addition

process, the polymer/organic solution is added dropwise to a stirring aqueous solution [119]. In reverse addition, it is the aqueous solution that is gradually dripped into the stirring polymer/organic solvent solution [120]. The rate of addition of the two solvents is typically slow, to allow for the dispersion of each drop into the stirring solution before the addition of the next drop, usually requiring an hour or longer. MCs and PSs can be formed using solvent dispersion, but polymer that forms FMs under thin film rehydration form a heterogenous population of FMs, PSs, and MCs when formed using solvent dispersion, making this formation method unsuitable for FMs [35, 119]. The organic solvent must be removed from the solution prior to use in biological contexts. This can be achieved through a buffer exchange column, through dialysis, or through vacuum desiccation (if the solvent is sufficiently volatile). Removal of the organic solvent can take several hours up to several days, depending on the method of removal. PSs made by solvent dispersion are similarly polydisperse to those made by thin film rehydration and must also be extruded prior to use [43, 121].

As mentioned, PSs formed by either of these processes require the use of an extruder to make them suitably monodisperse for use in biomedical applications, particularly those involving *in vivo* applications. Extrusion is a process by which membrane bound vesicles are forced through a membrane with a defined pore size, with the effect of forcing the vesicles to adopt diameters able to pass through the membrane. This requires the application of considerable force, achieved either through hand-driven syringes or positive pressure from a nitrogen gas tank [122]. Samples typically need to be passed through the extruder multiple times in order to achieve a monodisperse population, typically understood to mean a polydispersity index (PDI) of < 0.3. Extrusion is a difficult and time-consuming process that often results in the loss of sample mass/volume and loss of sterility.

An additional method of preparing PEG-*b*-PPS polymersomes was developed after the initial characterization of PEG-*b*-PPS nanoparticles, termed ‘direct hydration’. Direct hydration works by first dissolving the PEG-*b*-PPS polymer in a 1:1 w:w ratio of PEG 500, which acts as a solvent for both the PEG and PPS blocks, at 95 °C for 20 minutes. After mixing, a very small amount of aqueous buffer is added, sequentially, with mixing performed in between additions. In the original paper, the volumes of aqueous buffer added were 10, 20, 70, and 900 μL, for a total of 1 mL of aqueous buffer added by the end of the

process [123]. While PEG 500 is not particularly toxic, removal may be desired, which would involve chromatography or dialysis. PSs formed by this method are polydisperse and the method itself is time-consuming and difficult to scale.

2.2.2. Flash Nanoprecipitation

The origin of FNP relates to the methods of formation for solid core drug nanoparticles [124]. Solid core drug nanoparticles are nanoparticulate aggregates of a hydrophobic small molecule, often stabilized with polymer. The principle behind the formation of these nanoparticles was the transition of the small molecule from an environment in which it was freely soluble to one where it is no longer soluble. This was typically achieved by dissolving the small molecule in an organic solvent in which it was soluble and adding a nonsolvent (i.e. a solvent in which it is not soluble), typically an aqueous solution [125]. This addition process was often akin to solvent dispersion. Upon reaching a point where it is no longer soluble, the small molecule would begin forming aggregates through a process called nucleation. After a period of initial nucleation, where small molecule response to supersaturation is to form a new aggregate, follows a period of growth, where small molecules not already in an aggregate are added to already existing ‘seeds’ [126].

A common goal in the creation of nanoparticles is to have control over the size and polydispersity of the nanoparticles. In order to achieve uniformity in size, nucleation should begin relatively uniformly, so that individual aggregates have similar amounts of time to proceed through the growth phase. Achieving uniform nucleation requires that there is rapid molecular mixing of the two solvents, such that the small molecules stop being soluble in the mixed solvent system at approximately the same time throughout the entire volume of the system. Macro- and mesoscale mixing processes are not sufficiently uniform to achieve this, which introduces some inherent polydispersity to nanoparticles formed through nucleation and growth [127].

In 2003, a formulation technique was developed that utilized confined jets of solvent and non-solvent that, upon impingement would result in microscale mixing [124]. This rapid mixing would produce highly uniform solutions of the two miscible solvents to form. If a small molecule compound were dissolved in an organic solvent and were impinged against an aqueous non-solvent, the homogenous mixture formed

would produce a supersaturated environment for the compound, leading to nucleation. Due to the uniform nature of the mixing, nucleation would be rapid, leading to many nucleation points. This process was termed ‘flash nanoprecipitation’. This development of reproducible microscale mixing resulted in monodisperse solid core nanoparticles. These nanoparticles often still required the addition of a small amount of stabilizing polymer, which would sit at the nanoparticle-aqueous solvent interface [127]. This polymer could help prevent further particle aggregation and/or Ostwald ripening, in which smaller nanoparticles would gradually lose molecules and larger nanoparticles would gradually gain them, leading to a gradual increase in the size of the nanoparticles over time [128]. The process would also typically utilize relatively large aqueous reservoirs, which would serve to dilute the organic solvent used in the mixing process and to dilute the nanoparticles to reduce the chance of inter-particle interactions, i.e. aggregation. Dilution may also arrest particle growth and finalize particle formation.

Multiple designs exist for FNP devices. The first design utilized two impingement streams that, when powered with equal force, would collide within a mixing chamber before exiting into a reservoir [124]. This original design was subsequently adapted to a form that could be hand-driven, simplifying the conditions needed to utilize the mixer [129]. This design is commonly known as the confined impingement jets (CIJ) mixer, which was used for studies in this work (**Figure 2-2**). Other more complex geometries exist. The two-jet design requires that equal volumes of aqueous and organic solvent are used, which may be limiting under some applications. A newer design utilizes a vortex mixing process, which allows for four jets to be utilized. This design is called the multi-inlet vortex mixer (MIVM), and allows for additional parameters to be tweaked, such as more complex mixtures of solvents and different addition speeds [130].

2.3. Materials and Methods

2.3.1. Chemicals

Unless specifically denoted, all chemicals and reagents were purchased from Sigma Aldrich.

2.3.2. Synthesis of Functionalized Poly(Ethylene Glycol)

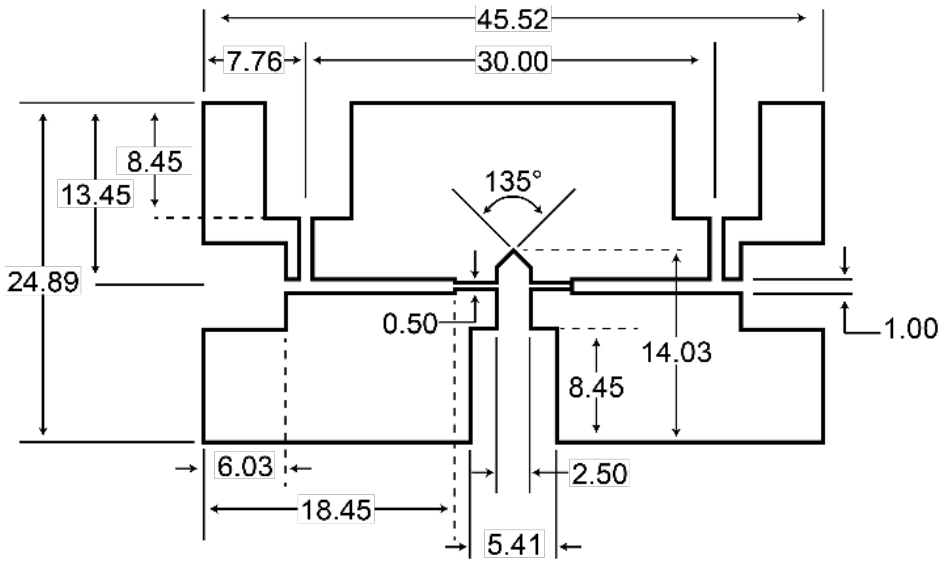

Figure 2-2. Design schematic of the CIJ mixer used in this study. All measurements are in millimeters. Reprinted with permission from [172].

PEG was functionalized as described previously [45, 131, 132]. 10 g of methyl ether PEG, MW 750, (1 molar equivalent) was dissolved in 200 mL toluene (ThermoFisher Scientific) in a three neck round bottom flask. The flask was then outfitted with a Dean Stark trap and azeotropic distillation was performed, with the solution heated to 165 °C under nitrogen gas. Once 100 mL of water/toluene had been removed, the PEG solution was cooled to room temperature, then was moved into an ice bath. 3 molar equivalents of triethylamine were added to the PEG solution. 3 molar equivalents of mesyl chloride was diluted in toluene 1:10 prior to gradual addition to the distilled PEG solution, dropwise *via* drip funnel with rapid stirring. The reaction was stirred vigorously overnight under nitrogen gas. The resulting product was filtered through Celite diatomaceous earth in a Buchner funnel to remove salt precipitate. Toluene was removed from product using a rotary evaporator. Product was brought up in 100 mL of dichloromethane (DCM), filtered through a basic alumina column, and was returned to the rotary evaporator to remove nearly all of the DCM. Product in DCM was then precipitated dropwise in cold diethyl ether. Ether was decanted and the product, PEG mesylate, was collected for drying in a vacuum desiccator. The same process was performed for methyl ether PEG, MW 2000.

5 g of PEG mesylate was dissolved in anhydrous tetrahydrofuran (THF) in a 3 neck round bottom flask under nitrogen. 3 molar equivalents of potassium carbonate were added to the reaction, followed by 3 molar equivalents of thioacetic acid. The reaction was vigorously stirred overnight at room temperature. The product was filtered through Celite diatomaceous earth in a Buchner funnel to remove salt precipitate. THF was removed by rotary evaporation and the product was brought up in 100 mL of dichloromethane (DCM), filtered through a basic alumina column, and was returned to the rotary evaporator to remove nearly all of the DCM. Product in DCM was then precipitated dropwise in cold diethyl ether. Ether was decanted and the product, PEG thioacetate, was collected for drying in a vacuum desiccator.

2.3.3. Synthesis of Poly(Ethylene Glycol)-Block-Poly(Propylene Sulfide)

PEG-b-PPS polymer was synthesized as described previously [45, 121, 131, 132]. Summarized syntheses are described in the following paragraphs. Degree of polymerization was assessed *via* ^{1}H NMR (3H methyl ether, 3.36 singlet; 4H PEG -CH_2-CH_2-, wide peak 3.60–3.64; 1H -CH_2-CH-CH_3 wide peak 2.56–2.65; 2H -CH-CH_2-CH-CH_3, wide peak 2.82–2.95, 3H -CH_2-CH_3 wide peak 1.30–1.38).

Polymersome polymer: 1 molar equivalent of PEG thioacetate (MW 750) was dissolved in 10 mL anhydrous DMF under argon in a 25 mL Schlenk flask. 1.1 molar equivalents of 0.5 M sodium methoxide solution in methanol was added, and the solution was stirred for 5 minutes to allow for the deprotection of the thiolate anion. The reaction was moved into a water bath at room temperature and 35 equivalents of propylene sulfide was added. The reaction was stirred for an additional 10 minutes. If the polymer was to possess a free terminal thiol, 15 equivalents of glacial acetic acid were added to protonate the thiolate anion. If the polymer was to be end-capped with another molecule to impart different functionality (e.g. bromoethyl phthalimide) or to quench the reactivity of a free thiol (e.g. benzyl bromide), 15 equivalents of the end-capping molecule was added to the reaction, which was allowed to proceed for 8 hours before working up the reaction. In all cases, work up of the polymer proceeded by precipitating the product in 100 mL of methanol in 50 mL conical tubes, followed by centrifugation at 10,000 rcf for 5 minutes to pellet the precipitate. Methanol was decanted and the product, PEG_{17}-*b*-PPS_{35} polymer, was dried overnight in a vacuum desiccator.

Filomicelle polymer: 1 molar equivalent of PEG thioacetate (MW 2000) was reacted as described for the polymersome polymer, with the exception of the number of molar equivalents of propylene sulfide added, which was instead 45 molar equivalents.

Micelle polymer: Micelle polymer was synthesized as described for the filomicelle polymer, with the exception of the number of molar equivalents of propylene sulfide added, which was instead 20 molar equivalents.

Bicontinuous nanosphere polymer: Bicontinuous nanosphere polymer was synthesized as described for polymersome polymer, with the exception of the number of molar equivalents of propylene sulfide added, which was instead 75 molar equivalents.

2.3.4. Formation of Nanocarriers by Thin Film Rehydration, Cosolvent Dispersion, and Flash Nanoprecipitation

Thin film rehydration: 20 mg of polymer was weighed into a 1.8 mL glass HPLC vial and dissolved in 750 µL of DCM, which was subsequently removed by vacuum desiccation for 6 h. 1 mL of 1xPBS was then added to the HPLC vial, which was shaken at 1500 rpm overnight on a Multi-Therm shaker (Heidolph) at room temperature. When noted in the text, polymersomes formed by this method were extruded through a 200 nm pore size disposable extruder (T&T Scientific) 15 times.

Cosolvent dispersion: 20 mg of polymer was dissolved in 500 µL of THF, which was dripped into a stirring reservoir of 3 mL of 1xPBS. This resulted in an identical THF:1xPBS ratio as used for the FNP fabrication method. THF was removed *via* vacuum dessication.

Flash nanoprecipitation: Nanocarriers were formed using the confined impingement jets (CIJ) mixer described by Han et al. [129]. PEG-*b*-PPS copolymers were dissolved in 500 µL of tetrahydrofuran (THF) and placed into a 1 mL plastic disposable syringe. 500 µL of phosphate buffered saline (1xPBS) was prepared in a second 1 mL syringe. The two solutions were impinged against one another within the CIJ mixer by hand, at a rate of approximately 1 mL/s. The supersaturated solution exited the mixer into a 20 mL glass scintillation vial containing a 2.5 mL reservoir of 1xPBS. This product was then separated from THF on a sepharose 6B size exclusion column. For multiple impingement samples, the glass scintillation

reservoir was left empty. Following each impingement, the resulting solution containing 1:1 THF:1xPBS and 20 mg of polymer was split evenly into two 1 mL syringes and was reintroduced into the CIJ mixer. The process was repeated between one and four times, with the final impingement emptying into a reservoir containing 2.5 mL 1xPBS.

2.3.5. Size and Morphological Characterization of Nanocarriers

Nanoparticle tracking analysis (NTA) and dynamic light scattering (DLS): Hydrodynamic diameters of nanostructures were measured using nanoparticle tracking analysis (NTA) on a Nanosight NS300 (Malvern). Measurements were taken using samples at a 1:1000 dilution in 1xPBS, resulting in approximately 0.1 mg/mL polymer concentrations. Readings were performed using a 633 nm laser. Five 1-minute videos were recorded per sample, with results averaged across the five readings. For micellar samples, typically < 30 nm in diameter, dynamic light scattering measurements were performed using a Zetasizer (Malvern) to accurately measure the size distribution, due to the limitations of NTA for smaller diameter aggregates.

Cryogenic transmission electron microscopy (cryoTEM): Specimens for cryoTEM were prepared by applying 4 µL of 1 mg/mL sample on a pretreated, holey carbon 400 mesh TEM grids and were plunge-frozen with a Gatan Cryoplunge freezer. Images were collected in vitreous ice using a JEOL 3200FSC transmission electron microscope operating at 300 keV at 4000x nominal magnification. A total dose of ~ 10 $e^{-}/Å^{2}$ and a nominal defocus range of 2.0–5.0 µm were used. Micrographs were acquired using a Gatan 3.710 × 3838-pixel K2 Summit direct electron detector operating in counting mode. Each micrograph was acquired as 20-frame movies during a 5 s exposure. After data acquisition, the individual frames of each micrograph were aligned using Digital Micrograph software (Gatan) to compensate for stage and beam-induced drift, and the aligned images were summed for further image processing.

Small angle X-ray scattering (SAXS): SAXS studies were performed at the DuPont-Northwestern-Dow Collaborative Access Team (DND-CAT) beamline at Argonne National Laboratory's Advanced Photon Source (Argonne, IL, USA) with 10 keV (wavelength λ = 1.24 Å) collimated X-rays. All the samples were analyzed in the q-range (0.001 to 0.5 $Å^{-1}$), with a sample-to-detector distance of approximately 7.5 m and

an exposure time of 1 s. The diffraction patterns of silver behenate was utilized to calibrate the q-range. The momentum transfer vector q is defined as $q = 4\pi \sin\theta/\lambda$, where θ is the scattering angle. The data collected was then analyzed using PRIMUS 2.8.2 software, where the solvent buffer scattering was subtracted, and the final scattering curve was obtained. Model fitting was performed using SASView software.

2.3.6 Endotoxin Testing

Assessment of endotoxin level was performed qualitatively with a LAL get clot assay (PYROGENT Plus Gel Clot LAL Assay, Lonza), with a 0.125 EU/mL sensitivity level. Samples were considered endotoxin-free if a 1:4 dilution of the sample passed the clot test, making them < 0.5 EU/mL. Endotoxin level was also tested using RAW Blue cells and the Quanti-Blue assay (Invivogen). RAW Blue cells were seeded into wells of a 96-well plate at 50,000 cells per well and 180 μL per well, in addition with 20 μL of the sample to be tested. As a positive control, a stock solution of LPS in endotoxin free water (5 ng/mL, ~5 EU/mL) was tested as described above, representing a concentration of 0.5 EU/mL in the well. As a negative control, endotoxin free water was tested.

2.4. Results

2.4.1. Formation of Polymersomes, Filomicelles, and Micelles by FNP

FNP was initially developed for the formation of solid core nanoparticles, not the formation of polymeric ‘soft’ nanoparticles [124]. Given the principles governing the formation of polymeric nanoparticles and those governing the FNP process, it was reasonable to hypothesize that FNP would be able to form polymeric nanoparticles using PEG-*b*-PPS [127]. However, it was not clear whether all nanoparticle morphologies accessible by PEG-*b*-PPS would be able to be formed by FNP. After all, solvent dispersion, a process similar to FNP, was found to not be able to form homogenous formulations of FMs, despite using PEG-*b*-PPS polymer that easily formed FMs by thin film rehydration [35]. Given the potential for formation technique-dependent morphological restrictions, it was clear that thorough investigation was required to

examine what PEG-*b*-PPS nanoparticle morphologies could be formed by FNP, and how similar the f_{PEG} rules were between traditional formation techniques and FNP.

Determination of the morphology of the PEG-*b*-PPS nanoparticles formed by FNP would ultimately require cryogenic transmission electron microscopy (cryoTEM). However, as the process is rate-limiting, I sought to develop an assay that could help discriminate between the one morphology capable of loading hydrophilic compounds (PSs) and the two morphologies only able to load hydrophobic compounds (MCs and FMs). I settled on simultaneously encapsulating a hydrophobic compound (ethyl eosin) and a hydrophilic compound (calcein). Both molecules are fluorescent, aiding in quantification. Different PEG-*b*-PPS polymers, with different f_{PEG} values, were dissolved in tetrahydrofuran (THF) along with ethyl eosin and were impinged against an aqueous solution containing calcein (generalized schematic **Figure 2-3**) at a rate of 1.2×10^{-6} m^3/s. After column purification to remove unencapsulated dye, nanoparticle formulations could be analyzed for fluorescence. Polymers that formed PSs would display fluorescence from both the calcein and ethyl eosin, while polymers that formed FMs or MCs would only display ethyl eosin fluorescence.

14 polymers were tested for this initial morphological characterization of formation by FNP (**Table 2-1**). Previous work using FNP for forming solid core drug nanoparticles found that solvent and non-solvent selection is important for the formation of stable nanoparticles [133]. Given the Hildebrand solubility parameter (δ) of PPS (δ = 17.9 $MPa^{1/2}$), I utilized THF as the organic solvent for the polymer (δ = 18.6 $MPa^{1/2}$). For the aqueous non-solvent, 10 mM phosphate buffered saline (1xPBS) was used, as it is both biological compatible and also a kosomotropic salt solution. The kosmotropic nature of the buffer reduces PEG solubility, which should increase the steric stabilization of the particles [134]. Normal FNP procedure involves the use of large aqueous reservoirs that dilute the sample post impingement to help prevent Ostwald ripening. As this dilution is undesirable for biomedical applications, where better control over the concentration is required and concentration of the sample after formation could reduce loading, cause a loss of cargo and product, and could reduce sterility, I sought to reduce the volume of the reservoir to a final solution of 1:6 ratio of organic:aqueous [129]. A polymer which forms polymersomes by thin film and solvent dispersion, PEG_{17}-*b*-PPS_{30} was used for preliminary studies into the suitability of FNP for forming PEG-*b*-PPS nanoparticles under different reservoir sizes and solvent conditions. PEG_{17}-*b*-PPS_{30} polymer

was able to form polymersomes using FNP when originally dissolved in THF, but not when dissolved in a

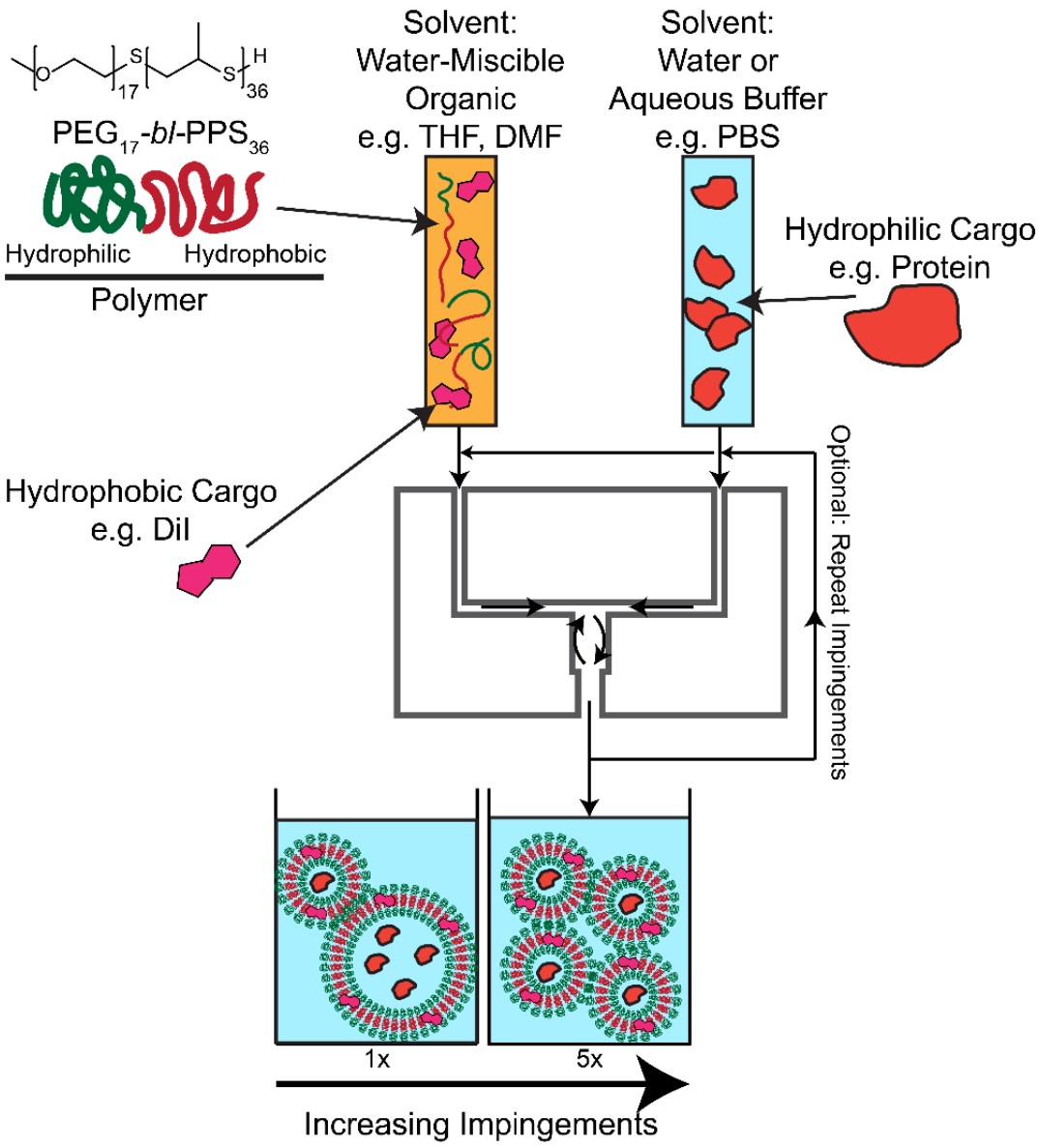

Figure 2-3. Production of nanocarriers *via* FNP in a hand-driven CIJ mixer. Diagram of the formation of polymersomes using FNP. The PEG-*b*-PPS polymer is dissolved in organic solvent along with hydrophobic cargo and is impinged against aqueous solvent with dissolved hydrophilic cargo. Rapid mixing occurs within the CIJ mixer, and efflux can be repeatedly impinged or allowed to complete the formation process through dilution in a reservoir of aqueous solvent. Reprinted with permission from [172].

different organic solvent in which it is soluble, dimethylformamide (DMF) (**Figure 2-4**). Instead, the polymer

#	PEG DoP	PPS DoP	f_{PEG}	End capping	Com/Aq Solv	D (nm)	PDI	Morphology
1	17	75	0.119	Thiol	THF/PBS	143.13	0.62	**BCN**, M, P
2	17	44	0.187	Benzyl	THF/PBS	116.53	0.24	**P**
3	17	38	0.21	Thiol	THF/PBS	115.29	0.63	**P**, MLP[a], **TP**[a]
3‡					THF/Water	N/A	N/A	**FM**
4	17	36	0.219	Thiol	THF/PBS	80.51	0.37	**P**, MLP[a], **TP**[a]
4†					DMF/PBS	41.53	0.31	**M**, P[b]
5	45	96	0.219	Benzyl	THF/PBS	20.54	0.25	**M**
6	17	35	0.224	Pyridyl sulfide	THF/PBS	68.58	0.22	**P**, MLP[a], **TP**[a]
7	17	33	0.235	Thiol	THF/PBS	95.06	0.55	**P**, MLP[a]
8	17	30	0.252	Thiol	THF/PBS	97.96	0.52	**P**, MLP[a]
9	17	23	0.305	Thiol	THF/PBS	29.78	0.43	**M**, P, FM
10	45	44	0.38	Benzyl	THF/PBS	14.28	0.33	**FM**
11	45	38	0.415	Phthalimide	THF/PBS	19.03	0.29	**M**
12	45	24	0.529	Benzyl	THF/PBS	10.13	0.38	**M**
13	45	20	0.574	Benzyl	THF/PBS	12.75	0.3	**M**
14	45	12	0.692	Benzyl	THF/PBS	15.43	0.43	**M**

Table 2-1. Relationship between PEG weight fraction (f_{PEG}) and morphology.

Com/Aq Solv = Common/Aqueous Solvents used during the impingement process. M = Micelles, FM = Filomicelles, BCN = Bicontinuous Nanospheres, P = Polymersomes, MLP = Multilamellar Polymersomes, TP = Tubular Polymersomes. Predominant population(s) shown in bold. [a] Population only found after multiple impingements. [b] Very rare population. DLS diameter and polydispersity data not available for samples predominantly composed of filomicelles, i.e. sample 3‡. Reprinted with permission from [164] © 2017 Elsevier.

formed micellar aggregates, with this different in structure most likely driven by the different δ of DMF, at 24.8 $MPa^{1/2}$. This solubility parameter is much higher than that of PPS and THF, which would lower chain flexibility and produce different kinetics for nanostructure formation. Similarly, the attempted formation of polymersomes using the same polymer but different aqueous non-solvents resulted in changes in the aggregate structure diameter (**Figure 2-5**). The chaotropic solution of 154 mM urea resulted in a significant drop in diameter of the aggregate morphology, most likely indicating a shift from polymersome to micelle morphology. All kosmotropic salt solutions matched the size of polymersomes formed by 1xPBS and water. Reservoir size also impacted the formation of different structures, suggesting that the concentration of organic solvent immediately after impingement is an important parameter for the types of structures formed (**Figure 2-6**). The same polymer formed polymersomes at reservoir volumes ranging from 1.5 to 3.5 mL but formed filomicelles instead at reservoir volumes ranging from 0 to 0.5 mL.

I found that FNP recapitulated, by and large, the same relationship between f_{PEG} and morphology as thin film rehydration: MCs formed at $f_{PEG} > 0.45$, FMs formed at $f_{PEG} \approx 0.38$, and PSs formed at $f_{PEG} < 0.3$ and >0.2 [35, 121]. By the fluorescence assay, I found that FNP formed hydrophilic-loading nanoparticles within the f_{PEG} range expected to form PSs (**Figure 2-7**). CryoTEM micrographs of different samples demonstrated that polymer that formed FMs by thin film rehydration could also form FMs by FNP (polymer 10), and that MCs were easily formed by a number of polymers by FNP. Intriguingly, FNP made

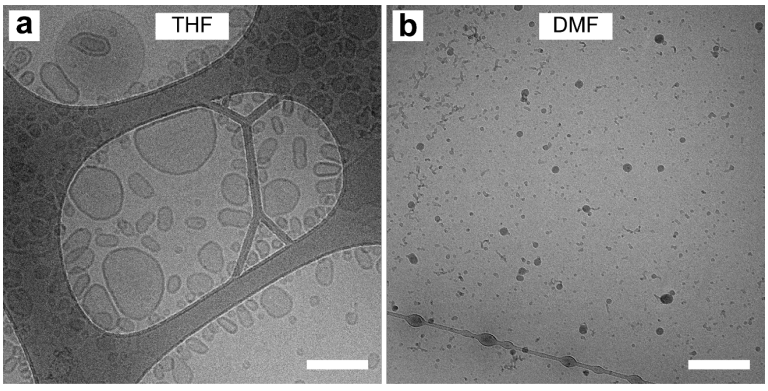

Figure 2-4. Organic solvent effects on polymersome formation by FNP. Representative cryoTEM micrographs of nanoparticles formed from PEG_{17}-*b*-PPS_{30} polymer by FNP when the organic solvent used during impingement was (a) THF or (b) DMF. Scale bars represent 100 nm.

a diverse range of vesicular structures, ranging from the typical PS structure (**Figure 2-7d**) to large tubular vesicles (**Figure 2-7b**) and multilamellar PSs (**Figure 2-7e**). The latter two structures are not seen in cryoTEM micrographs of PSs formed by thin film rehydration or solvent dispersion, suggesting that FNP has access to morphological populations that the other two formulation methods do not.

Also visible in **Figure 2-7** is a hereto unmentioned morphology, formed at an f_{PEG} that typically is unused. This morphology (**Figure 2-7c**) is called a bicontinuous nanosphere (BCN) in the literature [135] and is a morphology that had not previously been formed using PEG-*b*-PPS.

2.4.2. Formation of Bicontinuous Nanospheres by FNP

BCNs are the polymeric analog of lipid-based liquid crystalline nanostructures such as those with an internal bicontinuous cubic phase (cubosomes) or reversed hexagonal phase (hexosomes), which have been investigated as drug and vaccine delivery vehicles [136]. **Figure 2-8** illustrates the internal organization of cubosomes and hexosomes compared to liposomes. Cubosomes are cubic organized systems formed by a folding of lipid bilayers to create non-intersecting and bicontinuous aqueous channels

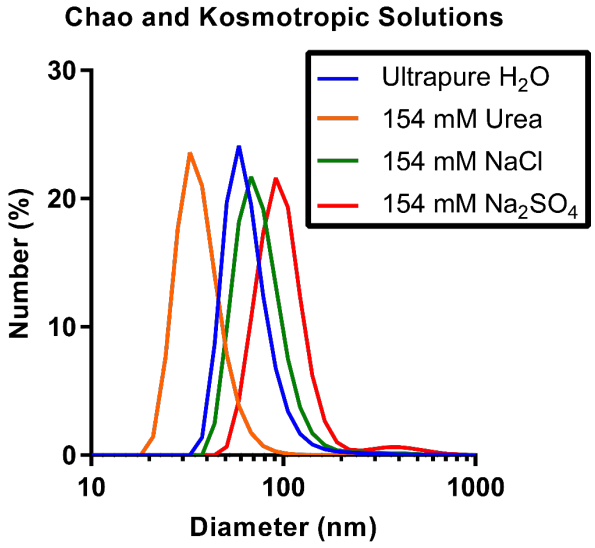

Figure 2-5. DLS size distribution measurements of FNP formulations formed using different aqueous solvents. Nanoparticle size distributions in water, urea (chaotrope), NaCl, or Na_2SO_4 (both kosmotropes). Lines represent the averages of n=3 formulations.

[137]. Hexosomes are hexagonally packed, rod-shaped inverse micelles, resulting in stacked aqueous channels [138]. Cubosomes and hexosomes are most commonly formed from glyceryl monooleate and phytantriol [139-141]. These nanoparticles have enhanced loading of hydrophilic, amphiphilic and hydrophobic payloads compared to liposomes, and possess sustained release capabilities. They have potential use as controlled delivery vehicles as alternatives to liposomes [142-144].

The pioneering work on the formation and characterization of cubosomes and hexosomes was performed using lipids. Analogous to how liposome research preceded polymersome research, there is now active research on developing similar nanostructures using block copolymers to replace lipids as the aggregate-forming molecule. As mentioned in Section 2.1., lipid-based nanoparticles possess some characteristics that are undesirable for biomedical applications. Some of these characteristics are

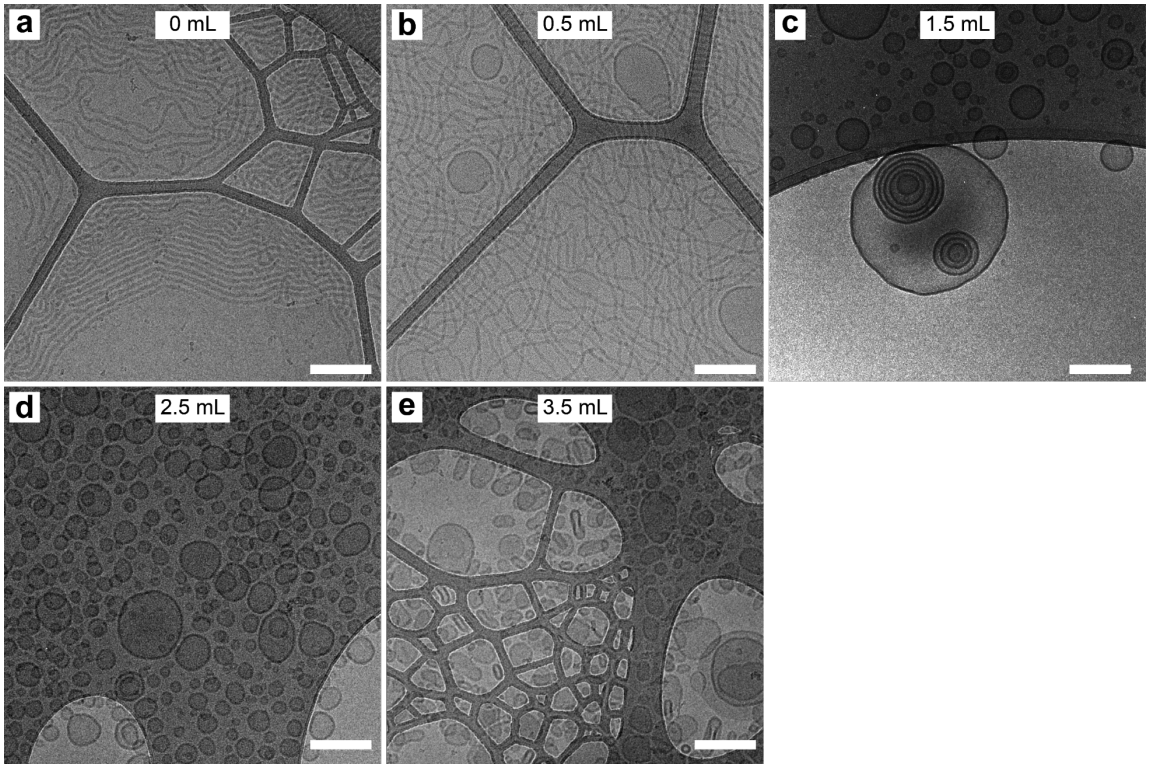

Figure 2-6. Relationship between aqueous reservoir volume and nanoparticle aggregate morphology. Representative cryoTEM micrographs using the same PEG_{17}-*b*-PPS_{30} and FNP conditions, changing only the volume of the 1xPBS reservoir to (a) 0 mL, (b) 0.5 mL, (c) 1.5 mL, (d) 2.5 mL, and (e) 3.5 mL. Scale bar is 100 nm in all images.

addressed through the use of block copolymers and those cases will be briefly remunerated here as they apply to cubosomes and hexosomes. Cubosomes and hexosomes suffer from stability issues, and often

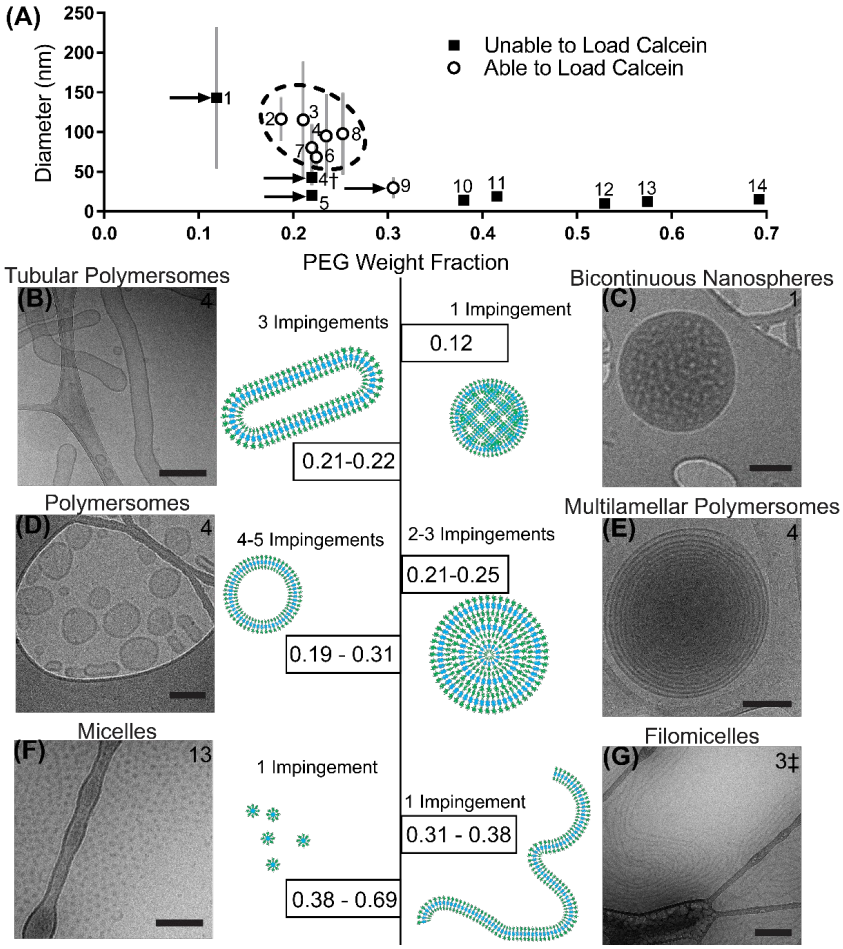

Figure 2-7. Relationship between PEG weight fraction and morphology. (A) Diameter of nanostructures formed *via* FNP from PEG-*b*-PPS copolymers of varying block lengths. Error bars represent the standard deviation of the nanostructure populations (PDI × Mean Diameter). Dotted area represents polymersome-forming samples. Arrows point out samples of note. †Sample formed using DMF as the organic solvent, rather than THF. ‡Sample formed using water instead of 1xPBS. (B–G) Weight fractions of PEG responsible for forming specific nanostructures *via* flash nanoprecipitation, paired with cartoon and representative cryoTEM images. All scale bars = 100 nm, except for scale bars within (B) and (E), which are 300 nm. Sample number is listed in the upper corner of each image. See Table 2-1 for details of copolymers. Reprinted with permission from [164] © 2017 Elsevier.

require the addition of block copolymers to their lipid structures during or after formation to prevent further aggregation [137]. Also, lipid nanoparticles are susceptible to degradation *in vivo* due to the number of extracellular esterases and lipases [145]. This reduces the ability to control when and where cubosomes and hexosomes degrade and release their cargo *in vivo*. Aside from addressing their particular issues, polymeric cubosomes (i.e. bicontinuous nanospheres) and hexosomes can also take advantage of the amenability of block copolymers to rational engineering of their properties. For example, PEG-*b*-PPS is highly stable, but becomes destabilized under oxidative conditions, particularly those in the endolysosomal pathway [43].

Polymeric bicontinuous nanospheres (BCNs) are the polymeric analogs of the lipid-based cubosomes [120]. They are more stable than cubosomes and, due to their polymeric composition, do not require the further addition of stabilizers [146-148]. As with cubosomes, BCNs have been categorized into gyroid (Ia3d), diamond (Pn3m) and primitive (Im3m) phases depending on their internal cubic organization (**Figure 2-8**) [149]. In contrast to the simple diblock copolymers that form PSs, self-assembly of BCNs in aqueous solutions often requires polymers with more complex molecular structures such as comb-like, semi-crystalline, or dendrimeric organizations [120, 149-164]. These polymers typically require multi-step and often difficult syntheses, which has posed challenges for the scalable fabrication of BCNs. Additionally, since identification of a nanoparticle as a BCN requires confirmation of its internal organization, structural confirmation of the BCNs requires analysis by electron microscopy and small angle X-ray scattering (SAXS), neither of which are easily accessible. Additionally, self-assembly of BCNs is highly dependent on the method of formation, concentration of the polymer, manufacturing conditions and solvents employed. As a result of this difficulty in uniform scalable fabrication and the existences of a numbers of potential complicating variables, polymeric BCNs have not been explored for various medical and non-medical applications, in contrast to their lipid-analogues. To address the issues with complex chemical synthesis, several recent studies have shown that simple amphiphilic linear block copolymers could also be utilized to form BCNs [135, 148, 165-167]. **Table 2-2** summarizes the polymers and formation methods used to make BCNs, as of December 2018.

As per my finding with FNP, PEG-*b*-PPS is now an additional polymer that has been found to form BCNs, as characterized by their cryoTEM micrographs and SAXS Bragg peak ratios (**Figure 2-9**). As PEG-*b*-PPS polymer of this f_{PEG} had not previously been reported in the literature, I sought to investigate whether it was able to form BCNs through the more traditional formulation methods. Working with a postdoctoral investigator in lab, Sharan Bobbala, we found that TF and SD were unsuitable for forming BCNs, in contrast

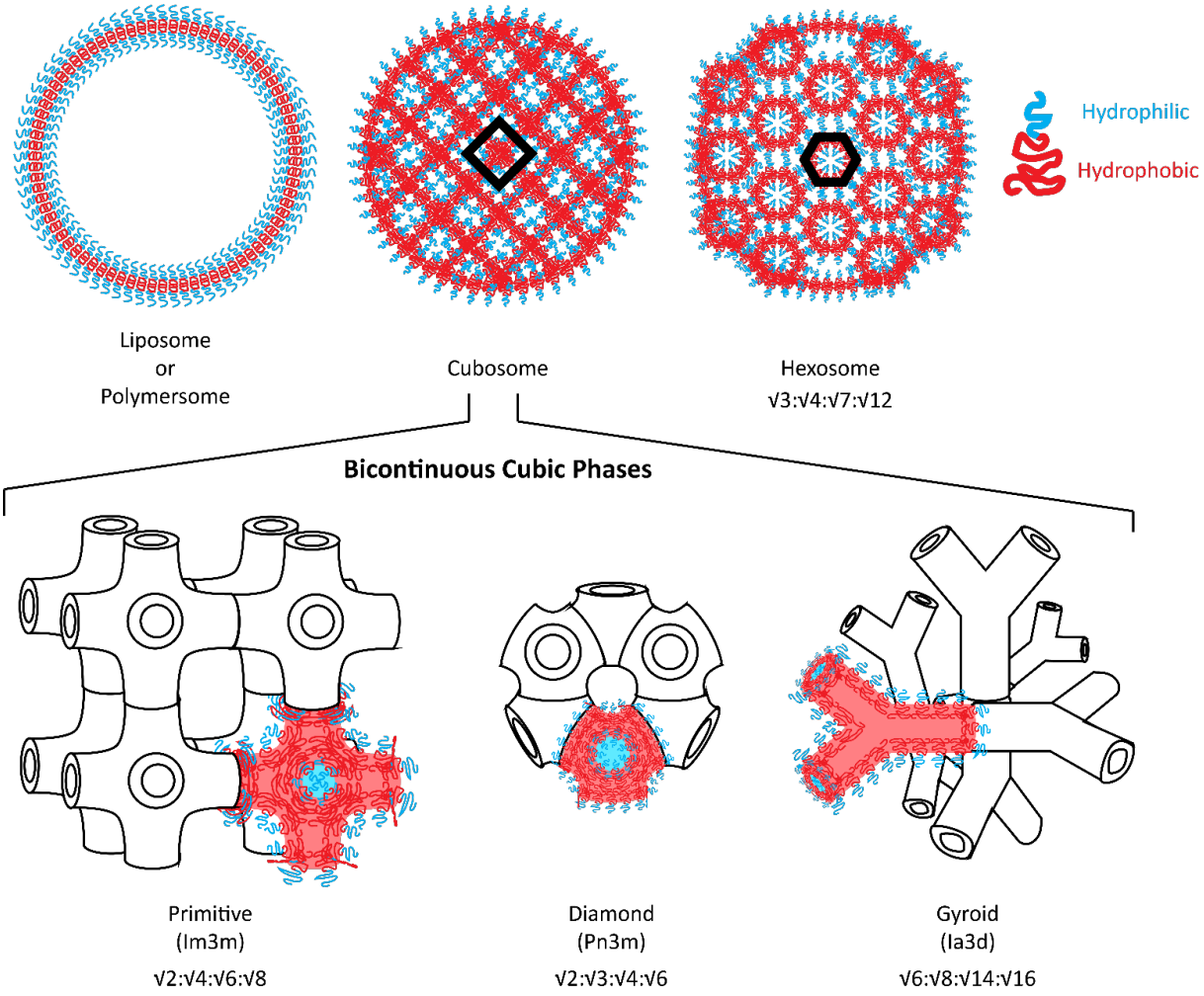

Figure 2-8. Structure of cubosomes and hexosomes with a liposome/polymersome shown for comparison. Nanoarchitectures are drawn as polymeric nanocarriers, but lipid nanocarriers possess analogous internal structures. Blue regions are hydrophilic, while red regions are hydrophobic. Schematic representations of the different bicontinuous cubic phases are included with typical Bragg peak ratios listed below. Reproduced from [174] with permission from The Royal Society of Chemistry.

with the ease at which FNP was able to form these nanostructures. Rather, BCNs formed by TF or SD in

Polymer	Solvent	Non-Solvent	w% Non-Solvent	mL/h	Ref
PEO-*b*-PTMSPMA [a]	Methanol	Water	39	n.s.	[104]
PAA-*b*-PMA-*b*-PS [b]	THF [q]	Water	16 to 44	15	[156]
PNOEG-PNGLF [c]	DMSO [r]	Water	70	5.6	[154]
PEO-*b*-PODMA [d]	THF [q]	Water	60	4	[163]
PEO-*b*-PBMA [e]	THF [q]	Water	60	4	[133]
PEO-*b*-PODMA [d]	THF [q]	Water	20	1.3	[152]
3xbPEG-*b*-PS [f]	Dioxane	Water	50	1	[147]
3xbPEG-*b*-PS [f]	Dioxane	Water	50	1	[157]
Norbornene Block Copolymer [g]	DMSO [r]	Water	50	1	[148]
3xbPEG-PS [f]	Dioxane	Water	50	1	[149]
PEO-*b*-PODMA [d]	THF [q]	Water	n.s.	4	[145]
3xbPEG-3xbPS [h]	Dioxane	Water	50	1	[151]
POEGMA-*b*-Poly(nucleobase) [i]	DMF [s], DMSO [r]	Water	89	1	[160]
PEO-*b*-POMDA [d]	THF [q]	Water	5 to 63	4	[165]
3xbPEG-*b*-PS [f]	Dioxane	Water	50	1	[158]
3xbPEG-*b*-P(styrene-ran-TMS-indanolylstyrene) [j]	THF [q]	Water	n.s.	0.5	[159]
PS209-*b*-PEG45 [k]	Dioxane/DMF [s]	Water	50	1	[150]
PEG-*b*-(PODMA-co-PDSMA) [l]	THF [q]	Water	40	5.15	[153]
PEG-*b*-PMPCS [m]	THF [q]	Water	100	1	[161]
POSS-OL-POM [n]	Acetone	N-Decane	40	N/A	[162]
PAA-*b*-P4VB [o]	THF [q]	Water	62	288	[155]
PEG-*b*-PPS [p]	THF [q]	Water and PBS [t]	86	1800	[164]
PEG-*b*-PPS [p]	THF [q]	Water and PBS [t]	86	1800	[146]

Table 2-2. Polymers and corresponding formulation parameters for forming BCNs.
Notes: [a] poly(ethylene oxide)-*block*-poly(3-(trimethoxysilyl)propyl methacrylate), [b] poly(acrylic acid)-*block*-poly(methyl acrylate) *block*-polystyrene, [c] poly(norborene-oligo(ethylene glycol))-poly(norborene-lysine-leucine-phenylalanine), [d] poly(ethylene oxide)-*block*-poly(octadecyl methacrylate), [e] poly(ethylene oxide)-*block*-poly(n-butyl methacrylate), [f] branched poly(ethylene glycol)-*block*-polystyrene, [g] Norbornene Block Copolymer, [h] branched poly(ethylene glycol)-*block*- branched polystyrene, [i] poly(oligo(ethylene glycol) methyl ether methacrylate)-*block*-poly(nucleobase), [j] branched poly(ethylene glycol)-*block*- trimethylsilylindanolylstyrene, [k] polystyrene-*block*-poly(ethylene glycol), [l] poly(ethylene oxide)-*block*-(poly(octadecyl methacrylate)-*co*-poly(docosyl methacrylate)), [m] poly(ethylene glycol)-*block*-poly(2,5-bis[(4-methoxyphenyl)-oxycarbonyl]styrene), [n] polyoxometalate-organic linker- polyhedral oligomeric silsesquioxane, [o] poly(acrylic acid)-*block*-poly(4-vinylbenzyl)-3-butyl imidazoliumbis (trifluoromethylsulfonyl)imide, [p] poly(ethylene glycol)-*block*-poly(propylene sulfide), [q] tetrahydrofuran, [r] dimethyl sulfoxide, [s] dimethylformamide, [t] phosphate buffered saline. Reproduced from [174] with permission from The Royal Society of Chemistry.

water formed large insoluble polymer aggregates (**Figure 2-10**). We particularly found that there was a strong dependence on the aqueous non-solvent for whether the BCN structures could form using SD, and that BCNs were unable to form by TF regardless of whether water or 1xPBS was used (**Table 2-3**). While SD could form some BCNs when water was utilized as the aqueous non-solvent, only some of the polymer formed these structures, with some polymer lost to large aggregates during the formation process. FNP, by contrast was able to form BCNs in both water and 1xPBS, though the BCNs formed in 1xPBS were larger and were more polydisperse (**Table 2-3**).

2.4.3. Reduction of Diameter and PDI of Polymersomes Without Extrusion Using FNP

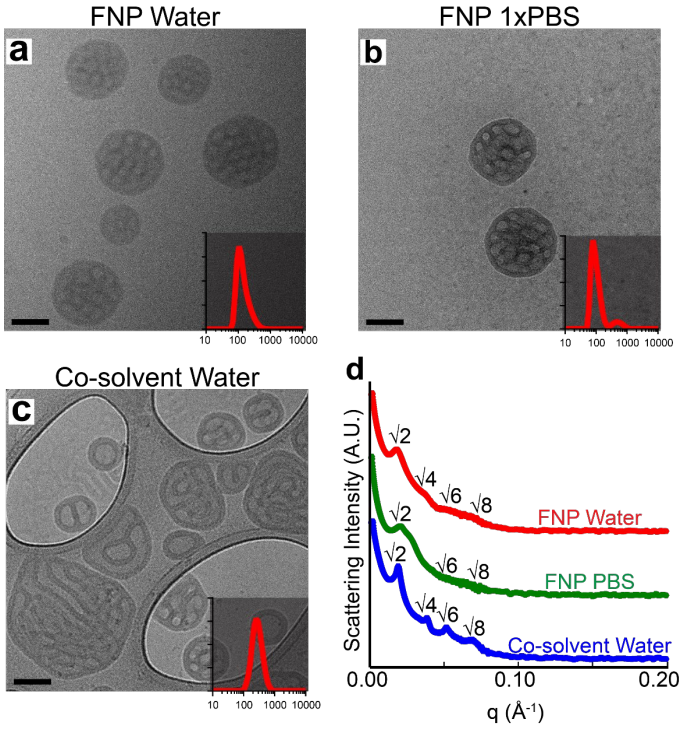

Figure 2-9. PEG_{17}-*b*-PPS_{75} BCNs displayed primitive Im3m cubic phases. CryoTEM images and overlaid DLS size distributions of BCNs formed by flash nanoprecipitation using water (a) or 1xPBS (b) as the aqueous solvent. BCNs formed using co-solvent dispersion (c) with water as the aqueous solvent is also shown. (d) SAXS data with labeled Bragg peaks for BCN formulations shown in images from (a)–(c). In (a)–(c), scale bars represent 100 nm. Adapted from [146] with permission from The Royal Society of Chemistry.

One barrier to the translation of polymersomes into the clinic is the polydispersity of the nanocarriers after formation by traditional methods. Polydispersity of nanocarriers impact their biomedical applications by altering their biodistribution and cellular uptake. There are a number of biological barriers (e.g. fenestrations) which block supramolecular assemblies of certain size ranges from passing through. Additionally, the size and shape of nanocarriers can affect the ability of cells to internalize the structures. Nanocarriers used in biomedical applications are therefore expected to have a low polydispersity for therapeutic reproducibility and consistency. The PSs formed by FNP (**Table 2-1**) demonstrated a PDI that ranged from 0.220 to 0.634, which is similar to the PDI of PSs formed by solvent dispersion (SD) and thin film rehydration (TF) (**Figure 2-11**). Both SD and TF require extrusion, which can be time-consuming, result in the loss of product, potentially reduce loading efficiency, and presents an opportunity for the introduction of contaminants and endotoxin. Shear flow has been demonstrated to be a viable and underexplored mechanism to influence the shape and polydispersity of metastable aggregate states. Since vesicle uniformity has been found to improve with increasing shear rate [168, 169], I hypothesized that repeated impingement of polymersomes within the CIJ mixer (i.e. repeated mixtures of the nascent polymersome

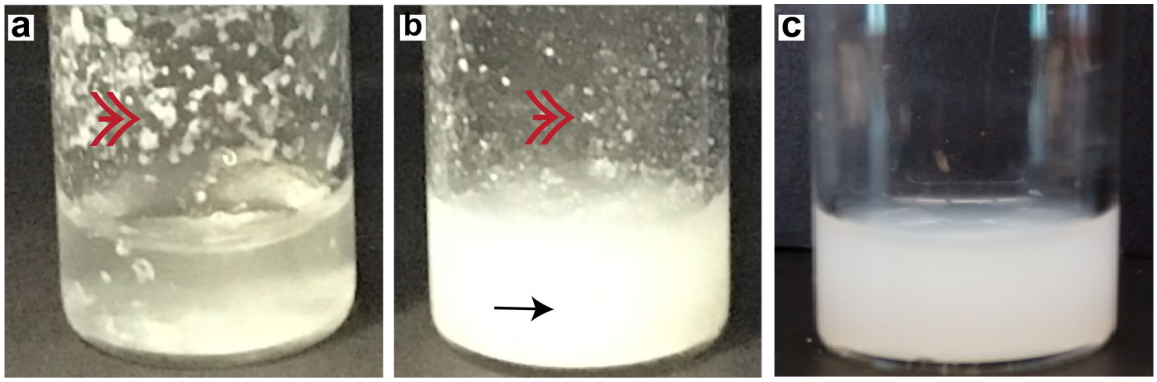

Figure 2-10. Insoluble aggregates of PEG_{17}-*b*-PPS_{75} polymer after TF and SD. PEG-*b*-PPS polymer that forms BCNs *via* FNP fails to form soluble nanostructures when the formulation method is changed to (a) thin film rehydration or (b) solvent dispersion compared to (c) FNP in 1xPBS. Representative images are shown. Red double arrows point to large insoluble polymer aggregates collected on the walls of the scintillation vial. Black arrow points to the suspension of some successfully formed BCN nanostructures. Adapted from [146] with permission from The Royal Society of Chemistry.

solution against itself) in the continued presence of organic solvent, promoting continued fluidity of the PPS membrane, may decrease vesicle polydispersity without the need for subsequent extrusion.

I found that multiple impingements through the CIJ mixer both decreased the mean PS diameter and lowered the PDI to levels to those achievable by extrusion (**Figure 2-11**). To maintain high levels of the common solvent within hydrophobic PPS membranes for continued chain flexibility, I impinged a PEG-*b*-PPS solution in THF against 1xPBS as I would for normal FNP. However, rather than allowing the

Table 2-3. Formulation conditions for BCNs by FNP.

Formation Method	Aqueous Solvent	Diameter (nm)	PDI
FNP	Water	210.5	0.166
FNP	1xPBS	392.8	0.287
SD	Water	319.8	0.169
SD	1xPBS	Insoluble Aggregates	N/A
TF	Water	Insoluble Aggregates	N/A
TF	1xPBS	Insoluble Aggregates	N/A

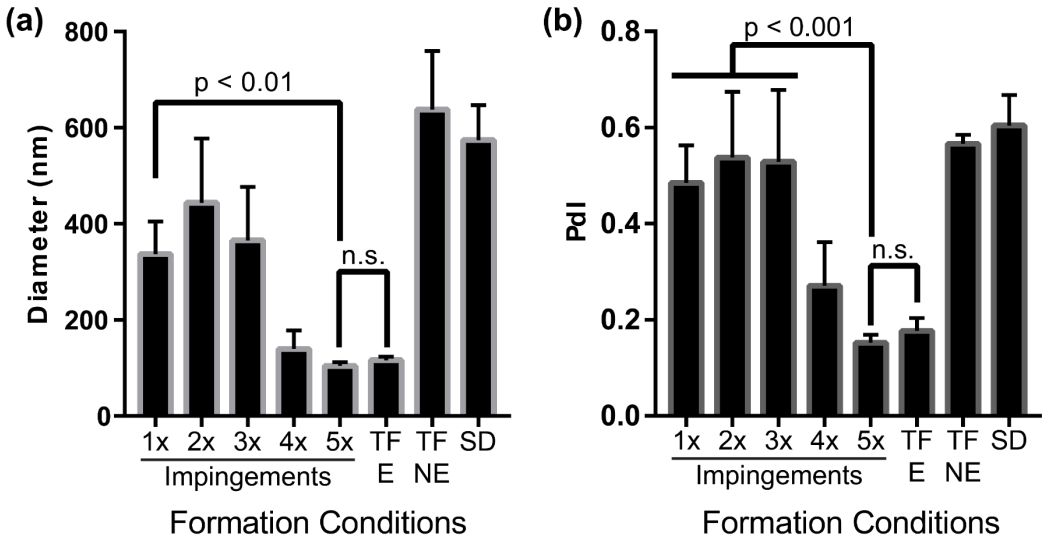

Figure 2-11. Diameter and PDI of polymersomes after multiple impingements. (a) DLS mean diameter and (b) PDI of polymersomes formed after multiple impingements (1x-5x) or formed by thin film (TF) or solvent dispersion (SD) with (E) or without (NE) extrusion. Error bars are standard error, n = 5. Figure adapted from [164] with permission © 2017 Elsevier.

resultant crude mixture to dilute in an aqueous reservoir, I instead took the mixture without dilution, divided it between two syringes, and repeated the impingement. As no reservoir was used, the volume remained constant, and the impingement could be repeated multiple times over the course of several minutes without sample loss. By the fifth impingement, there was no statistical difference in the diameter or PDI between FNP PSs and PSs formed by thin film rehydration that were subsequently extruded through a 0.1 μm filter. 5x-impinged PSs were stable for four days and demonstrated no significant change in PDI (**Figure 2-12a**). This change in the distribution of sizes from 1x-5x impingements (**Figure 2-12b**) can be observed by cryoTEM (**Figure 2-13**). While the first impingement generated primarily unilamellar and some rare multilamellar polymersomes ranging between 50 nm to nearly a micron in diameter, the 5x-impinged polymersomes were monodisperse (PDI < 0.15) and all possessed a single bilayer (**Figure 2-13e**). The 2x and 3x polymersome populations were composed of large, multilamellar, and/or tubular polymersomes (**Figure 2-7b,e; Figure 2-13b,c; and Figure 2-14a,b**). Tubular polymersomes have been predicted in simulations of polymersome formation under conditions of shear flow [168]. Multilamellar vesicles are a common liposomal structure [170], may be a result of multiple fusion events induced by increased polymersome collisions under conditions of turbulent flow while PPS chains remain fluid and swollen with

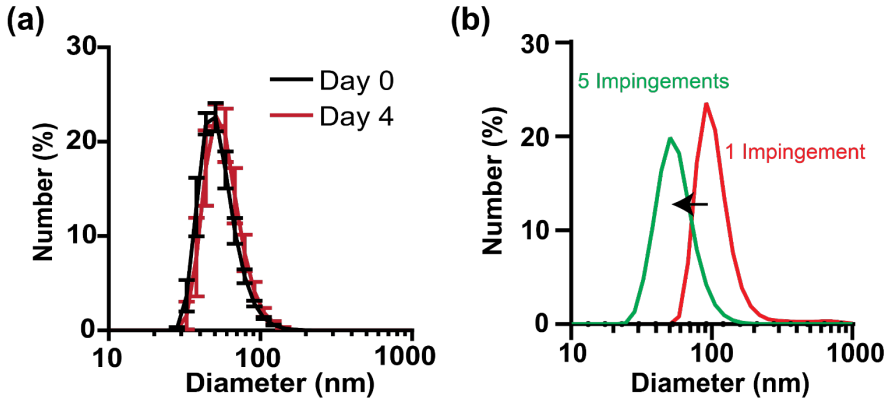

Figure 2-12. Stability and size change of multiply-impinged polymersomes. (a) DLS size distribution of 5x impinged polymersomes on the day of formation or after storage at room temperature for four days. Error bars = S.E.M., n=3. (b) DLS size distribution of 1x and 5x impinged polymersomes overlaid for comparison. Figure edited and adapted with permission from [164] and [172] © 2017, 2018 Elsevier.

THF. I found this protocol of repeated impingements to support the gram-scale production of monodisperse polymersomes within a matter of minutes, which is a task that could require days to weeks to achieve by thin film hydration and extrusion.

2.4.4. Formation of Large, Sterile Batches of Monodisperse PSs by FNP

Primate studies require the production of larger volumes of nanocarrier formulations than murine studies but require the same (if not greater) level of attention to consistency and sterility. I wanted to investigate whether FNP could be utilized, using multiple impingements with PEG-*b*-PPS (**Figure 2-15a**) to produce monodisperse polymersome formulations at larger volumes. Performing FNP with a CIJ mixer as

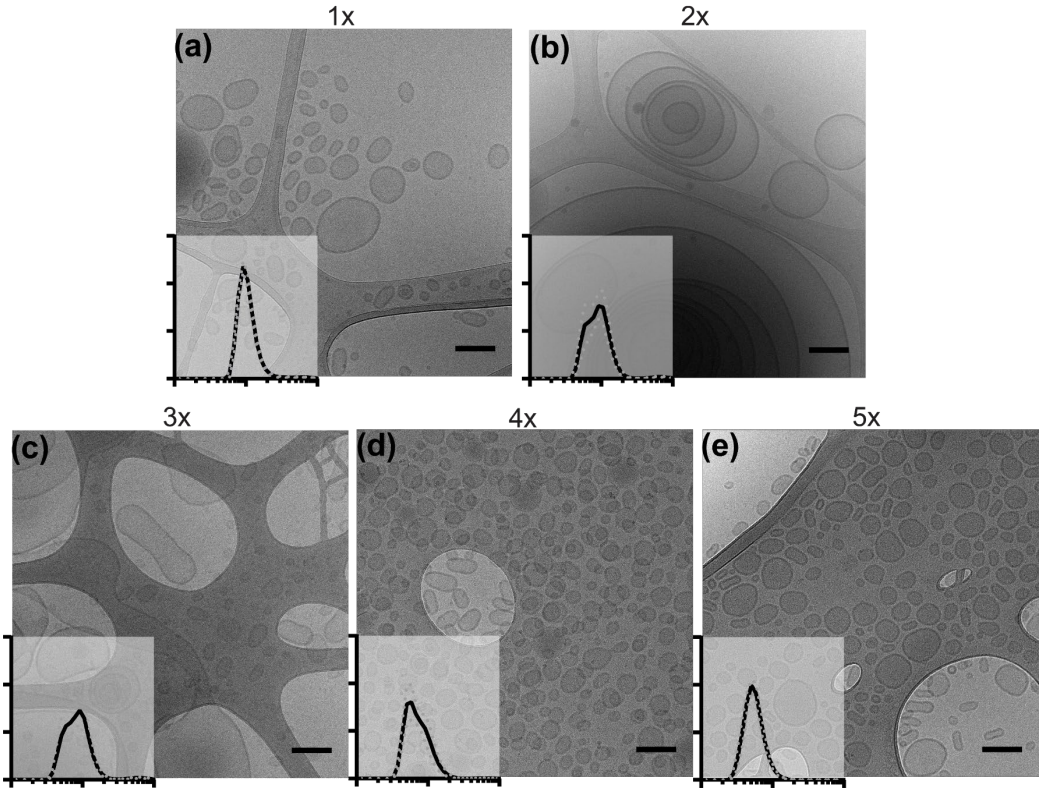

Figure 2-13. CryoTEM micrographs of multiply-impinged polymersomes. (a)-(e) CryoTEM micrographs of multiply-impinged polymersomes after increasing numbers of impingements (1x-5x, respectively). Insets of DLS size distributions are included for each representative micrograph, with x- and y- axes corresponding to the same scale as for **Figure 2-8**. Figure adapted with permission from [164] © 2017 Elsevier.

before, I were able to form monodisperse populations of polymersomes at 10 times the volume that I had previously attempted (30 mL formulation at 20 mg/mL of polymer). Nanoparticle tracking analysis (NTA)-based size distribution (**Figure 2-15b**) and corresponding cryoTEM image (**Figure 2-15c**) show a monodisperse population of vesicular nanostructures, with distinctly visible bilayers. The polymersomes were 93.7 ± 8.6 nm in diameter, and their aggregate morphology, as assessed by SAXS, is represented well by a vesicular model (**Figure 2-15d**).

As sterility is important for general *in vivo* applications and minimized endotoxin levels are crucial for controlled immunomodulation, I sought to produce sterile PS formulations by FNP. By soaking the CIJ mixer used to perform the flash nanoprecipitation in 0.5 N NaOH overnight, and washing thoroughly with

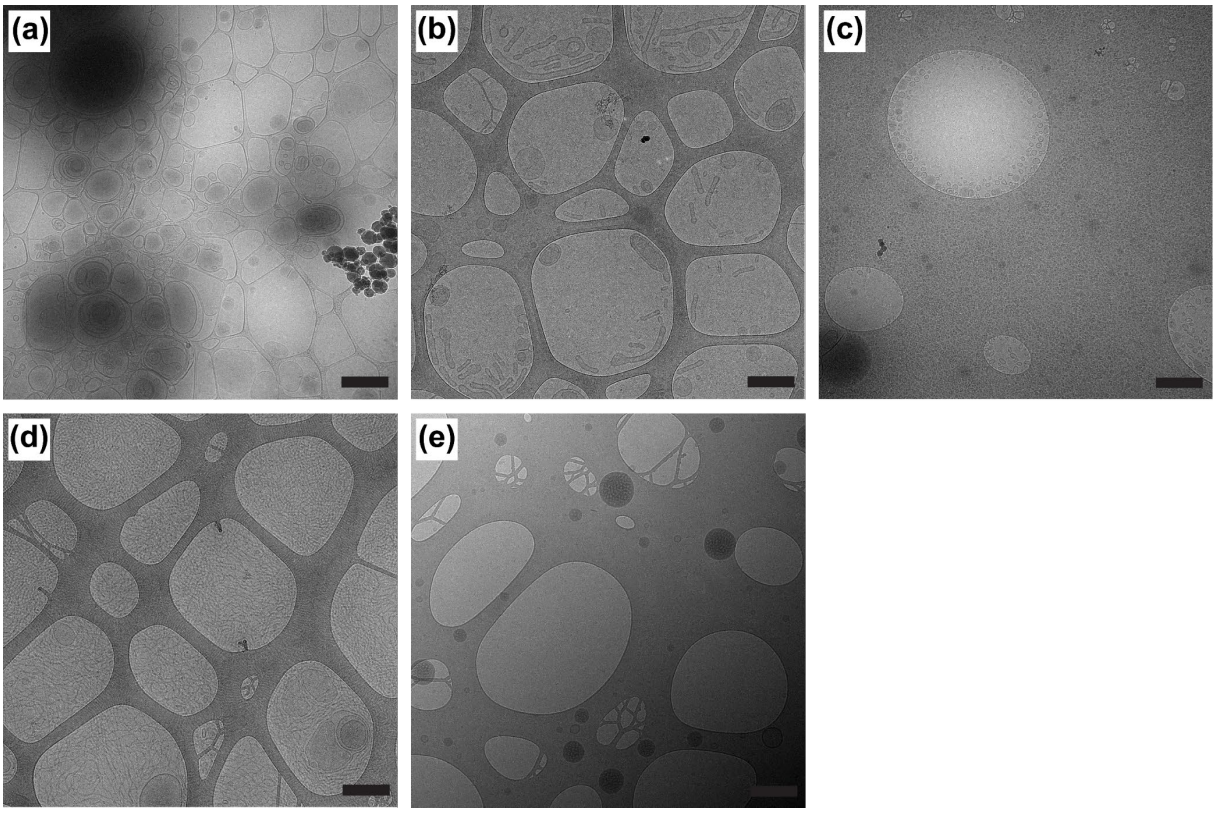

Figure 2-14. Low magnification cryoTEM micrographs of nanostructures formed by FNP. CryoTEM micrographs of (a) multilamellar polymersomes, (b) tubular polymersomes, (c) small monodisperse polymersomes, (d) filomicelles, and (e) bicontinuous nanospheres. Scale bar represents 1500 nm for (a) and 500 nm for (b)-(e). Figure adapted with permission from [164] © 2017 Elsevier.

endotoxin-free water, I was able to create formulations of polymersomes with endotoxin levels < 0.5 EU/mL using the FDA-mandated Limulus Amebocyte Lysate (LAL) gel clot assay [171]. This level is an order of magnitude lower than the safety cutoff for human testing [172]. To further quantify and compare the ability to control endotoxin levels in FNP fabricated PSs, I utilized the RAW Blue assay. The RAW Blue assay is a cell-based assay which utilizes RAW 264.7 cells that have been stably transfected with an NF-κB-driven

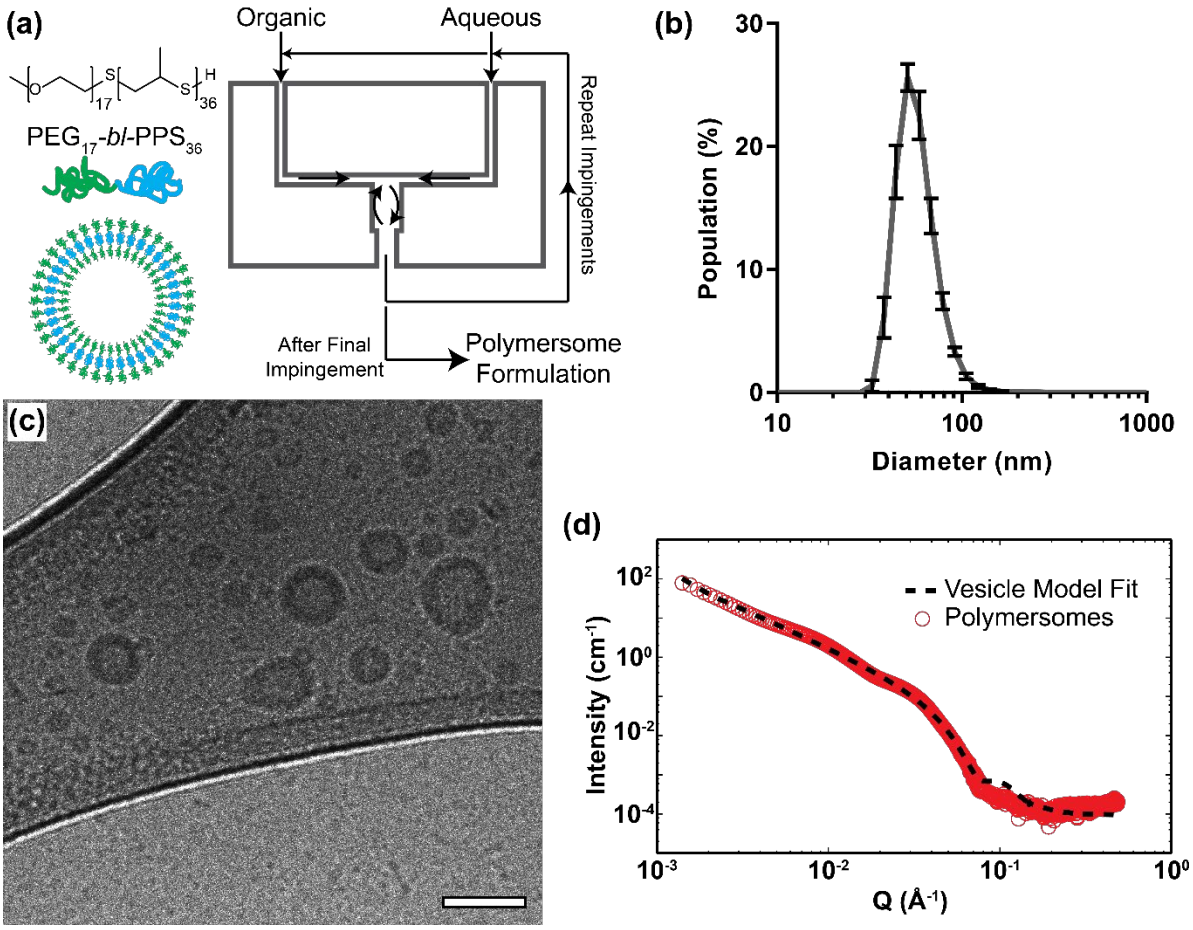

Figure 2-15. Characterization of polymersomes formed by scaled up FNP. (a), PEG_{17}-*b*-PPS_{36} diblock copolymer structure, PS morphology, and schematic of the CIJ mixer used for FNP formation of PSs in this study. **(b)**, NTA size distribution data for PSs formed *via* FNP, n = 3, error bars = S.E.M. **(c)**, Representative cryoTEM image of PSs formed *via* FNP, scale bar = 150 nm. **(d)**, SAXS data and vesicular model fit (SASView) of polymersome formulation, confirming vesicular aggregate morphology. Figure reprinted with permission from [173] © 2018 Springer.

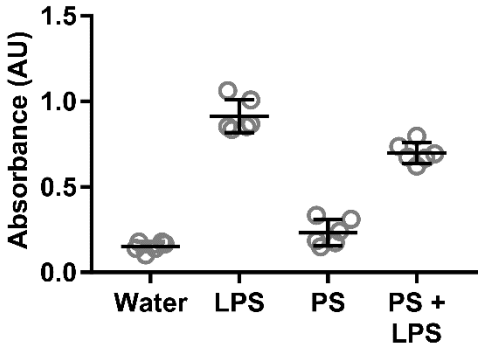

Figure 2-16. Endotoxin characterization of PSs formed by FNP. RAW Blue LPS assay of polymersomes formed by sterile FNP, n=6, error bars represent standard deviation. Reprinted with permission from [172].

secreted alkaline phosphatase (SEAP) construct [173]. Upon stimulation by a number of PAMPs, RAW Blue cells secrete SEAP, which can be detected and quantified by an enzyme-based colorimetric assay. **Figure 2-16** demonstrates that PSs formed by sterile FNP are not significantly more stimulatory toward RAW Blue cells than endotoxin-free water. Polymersome formulations that met this criterion were used in the subsequent *in vivo* studies, such as those in chapters 3, 4, and 5.

2.5. Discussion

FNP using PEG-*b*-PPS was able to form all three of the standard morphologies (micelles, filomicelles, polymersomes) at approximately the same f_{PEG} fractions as have been previously demonstrated for thin film and solvent dispersion: 0.18-0.3 for polymersomes, 0.38 for filomicelles, and 0.41-0.69 for micelles. Given the speed at which FNP forms nanostructures (<1 minute), this represents a significant improvement in how quickly PEG-*b*-PPS nanoparticles can be formulated. The relationship between f_{PEG} and aggregate morphology was most closely aligned between TF, SD, and FNP when the following parameters were used for FNP: organic solvent THF, aqueous solvent kosmotropic solution e.g. 1xPBS, aqueous reservoir size 1.5-3.5 mL. Using a different organic solvent (i.e. DMF) resulted in formation of micelles when using polymersome-forming polymer and using a chaotropic aqueous solvent resulted in a decrease in diameter of the nanostructures, most likely as a result of forming micelles instead of PSs.

Decreasing the reservoir size to 0.5 mL or less resulted in the formation of filomicelles instead of polymersomes. There are a significant number of FNP parameters that require further exploration, to be delved into further in Chapter 6.

Micelles, filomicelles, and standard spherical polymersomes were not the only nanostructures that were found to form during the FNP process. More exotic vesicular structures were formed, namely multilamellar and tubular polymersomes. Neither of these structures are seen when PEG-*b*-PPS polymersomes are formed by TF or SD and are rare structures when polymersomes are formed by a single impingement of FNP. They become a much larger share of the polymersome population after the second and third impingements of a multi-impingement protocol, suggesting that their formation is a complex process involving the additional shear forces and aqueous:organic solvent mixture present during multiple impingements. Better control over the shear forces or solvent mixtures, e.g. through the use of an MIVM instead of CIJ mixer, may elucidate the physical parameters involved in the formation of these exotic vesicular structures.

An additional unusual nanostructure that was found is the bicontinuous nanosphere. BCNs have not previously been reported using PEG-*b*-PPS polymer. This is due to the high hydrophobicity of the PPS block used to achieve the f_{PEG} required for this structure, i.e. PEG_{17}-*b*-PPS_{75}, f_{PEG} = 0.12. The extreme hydrophobicity and molecular weight of the PPS block leads to rapid aggregation into large and unstable structures. At the time scales of formation involved in both TF and SD, aggregation occurs more rapidly than stable BCNs are able to form, reducing or eliminating the BCN population. This is exacerbated by the solvent quality of the aqueous non-solvent – water is better able to form BCNs than 1xPBS, in which the presence of kosmotropic salts reduce the solubility of PEG. FNP, with its rapid microscale mixing, is able to form stable BCNs before larger scale aggregation occurs and is able to do so in both water and 1xPBS. These BCNs have cubic internal organization of aqueous pores/channels, as identified by cryoTEM and SAXS.

Polymersomes formed by SD or TF require extrusion in order to reduce their PDI. As hinted upon by the reservoir size data and the exotic vesicular structure data, shear forces and extended mixture time in the presence of high levels of organic solvent appear to play an important role in aggregate morphology

formation. Multiple impingements beyond the first 3 impingements results in a drop in vesicle size and polydispersity. This decrease is not significantly different from the decrease in diameter and polydispersity seen when thin film polymersomes are extruded, suggesting that multiple impingements can replace extrusion. As the multiple impingement process takes less than 10 minutes, can be easily performed sterilely, and does not result in the loss of polymer or cargo, it is a significant improvement over extrusion. FNP formation of polymersomes was scaled up to 10 times the volume of polymersomes formed, to 30 mL of polymersomes formed in a single batch. This volume is a much more applicable size for use in preclinical studies in non-human primates and eventually in clinical trials in humans. This scalability of FNP would be meaningless for clinical applications if it were not matched by the ability to keep the formulations sterile and endotoxin-free. Simple sodium hydroxide treatment of the CIJ mixer, along with rapid washes with endotoxin free water in a biological safety cabinet, resulted in a decrease of contaminating endotoxin far below the limits set by the FDA for human use.

Having demonstrated the usefulness of FNP for forming PEG-*b*-PPS nanoparticles of all known morphologies accessible by the polymer, the next step was to ensure that FNP was also capable of forming nanocarriers, i.e. that PEG-*b*-PPS nanoparticles can be efficiently loaded with hydrophilic and/or hydrophobic cargo.

2.6. Acknowledgements

I would like to acknowledge the help of Sharan Bobbala for his help with the characterization of bicontinuous nanospheres. After my initial characterization of their formation, it was his aid that allowed for the continued pursuit of understanding the formation conditions that drove BCN aggregation. I also want to acknowledge the hard work of Omar Osorio, the undergraduate who helped perform a great deal of the initial work on flash nanoprecipitation. Also important was the cryoTEM work of Jonathan Remis and the help of Steven Weigand with SAXS.

2.7. Publication Information

Sections of this chapter have been published with the following citation information:

S. Allen, O. Osorio, Y.G. Liu, E. Scott. Facile assembly and loading of theranostic polymersomes *via* multi-impingement flash nanoprecipitation. Journal of Controlled Release, 262 91-103. 2017. [166]

S. Bobbala, S.D. Allen, E.A. Scott. Flash nanoprecipitation permits versatile assembly and loading of polymeric bicontinuous cubic nanospheres. Nanoscale 10 (11), 5078-5088. 2018. [148]

S. Allen, M. Vincent, E. Scott. Rapid, Scalable Assembly and Loading of Bioactive Proteins and Immunostimulants into Diverse Synthetic Nanocarriers *via* Flash Nanoprecipitation. Journal of Visualized Experiments 138, (e57793). 2018. [174]

S.D. Allen, Y.G. Liu, S. Bobbala, L. Cai, P.I. Hecker, R. Temel, E.A. Scott. Polymersomes scalaby fabricated *via* flash nanoprecipitation are non-toxic in non-human primates and associate with leukocytes in the spleen and kidney following intravenous administration. Nano Research 11(10), 5689-5703. 2018. [175]

S.D. Allen, S. Bobbala, N.B. Karabin, E.A. Scott. On the advancement of polymeric bicontinuous nanospheres toward biomedical applications. Nanoscale Horizons, Advance Article. 2019. [176]

CHAPTER 3

Development of Complex Soft Nanocarriers as Delivery Vehicles

3.1. Abstract

Flash nanoprecipitation is capable of forming micelles, filomicelles, polymersomes, and bicontinuous nanospheres from PEG-*b*-PPS polymer. For this formulation process to be useful in drug delivery applications it needs to be able to efficiently load cargo into the nanoparticles it forms. This cargo could potentially include hydrophilic and/or hydrophobic compounds of a variety of molecular weights. Once loaded, nanocarriers formed by FNP will need to be successfully internalized by cells. In this chapter, I investigate the encapsulation efficiency of a number of hydrophilic and hydrophobic compounds using FNP, and furthermore investigate the *in vitro* and *in vivo* uptake of these nanocarriers. This work provides the conceptual basis for creating nanocarrier therapeutics for *in vivo* use.

3.2. Introduction

3.2.1. Encapsulation Efficiency and Loading Capacity of Nanocarriers

The driving force behind the formation of aggregate nanostructures by amphiphilic block copolymers is the hydrophobic block and the thermodynamic favorability of 'burying' the hydrophobic block from aqueous solvent [177]. An added consequence of this is the generation of a hydrophobic volume within the nanoparticle, which can be loaded with hydrophobic cargo. Hydrophobic molecules will preferentially partition into the hydrophobic volume, provided the partition coefficient of the molecule allows for sufficient preference for the hydrophobic polymer over the surrounding aqueous solution [178]. The amount of cargo that is successfully loaded (i.e. encapsulated) in the nanocarrier is often described by the encapsulation efficiency [179], calculated as:

$$Encapsulation\ Efficiency\ (\%) = \frac{mg\ of\ cargo\ encapsulated}{mg\ of\ cargo\ added\ to\ initial\ formulation}\ x\ 100\%$$

A separate but related concept is that of the loading capacity of a nanocarrier. Nanocarriers possess a hydrophobic volume stabilized by the hydrophilic block of the polymer. At sufficiently high concentrations

of hydrophobic cargo, it is possible to saturate the hydrophobic volume of the nanocarrier. Loading capacity can therefore be considered the maximum amount of cargo that can be loaded into a set number of nanoparticles [180], calculated here as:

$$Loading\ Capacity\ (\%) = \frac{maximum\ mg\ of\ cargo\ encapsulated}{mg\ of\ polymer\ used}\ x\ 100\%$$

When attempting to encapsulate cargo at concentrations above the loading capacity of the nanoparticle, encapsulation efficiency will appear to decrease due to the saturation of the hydrophobic volume of the nanoparticle. It is therefore instructive, especially in comparative cases, to determine both the loading capacity and encapsulation efficiency of a given cargo within a given polymer/nanocarrier.

3.2.2. Morphology and Loading of Hydrophobic and/or Hydrophilic Cargo

All nanoparticles formed from amphiphilic block copolymers are capable of encapsulating hydrophobic cargo. The same cannot be said for hydrophilic cargo, as it conceptually requires an internal hydrophilic volume in order to be successfully encapsulated. One caveat is that some hydrophilic cargoes have sufficiently intermediate partition coefficients (e.g. $0 < \log P < 1$) or contain hydrophobic domains (e.g. many proteins) [181]. These cargoes may either load inefficiently into the hydrophobic volume or may adsorb to the nanoparticle surface. Hydrophilic cargoes may also be covalently conjugated to polymer, often with a hydrolysable linker [182]. Additionally, while PEG-*b*-PPS, the polymer used in this dissertation, is neutral in charge, charged polymers may introduce effects that can attract cargo to the nanoparticles ionically [183].

Aside from these caveats, hydrophilic cargoes require aqueous interior volumes within the nanoparticles. This effectively rules out micelles and filomicelles, which only possess hydrophobic interior volumes. Both polymersomes and bicontinuous nanospheres, however, have hydrophilic interior volumes. It has been demonstrated that polymersomes can effectively encapsulate both hydrophilic and hydrophobic cargo [184]. Cubosomes, the lipid analogs of BCNs, can also encapsulate hydrophilic and hydrophobic cargo [185]. As BCNs are relatively new, their capacity to load hydrophilic and hydrophobic cargo is presumed but not definitively explored.

Despite the fact that all PEG-*b*-PPS morphologies are capable of loading hydrophobic compounds, it is not clear whether all morphologies have the same loading capacity. At sufficiently high concentrations of hydrophobic compounds, it is possible that micelles will convert to polymer-stabilized solid core nanoparticles, for example. Also, it is unclear if polymersomes or filomicelles will maintain their morphologies at saturating levels of hydrophobic cargo loading. As the morphology of nanocarriers is an important variable in their biodistribution and cellular uptake (to be further explored in 3.2.3 and 3.2.4), it is important to know if certain concentrations of hydrophobic cargo will cause morphological changes to the aggregate structure formed by PEG-*b*-PPS. As BCNs are a relatively unexplored polymeric nanoparticle morphology, their loading capacity and ability to transition between different morphologies requires significant exploration as well.

The loading of hydrophilic cargoes into PSs and BCNs is also a potentially complex process. Conceptually, in a simplified model of hydrophilic cargo encapsulation, the concentration of cargo within the aqueous volumes inside the nanocarriers would be equal to the concentration of the cargo outside the particles. Therefore, encapsulation efficiency would simply be a factor of how much of the total volume in the system is within a particle rather than outside a particle. In general, the fraction of the volume within nanoparticles is significantly lower than the aqueous volume outside of nanoparticles. As such, encapsulation efficiency for hydrophilic compounds is typically low when compared to that of hydrophobic compounds [186].

The encapsulation efficiency can be different for different nanoparticle formation methods. For example, when formed by TF, PSs begin as a polymer melt resembling a sponge, as the aqueous solvent gradually diffuses into the thin film of polymer and polymer chains begin reorganizing themselves [187]. The loading of hydrophilic cargo in this circumstance requires the diffusion of the cargo, which is typically significantly larger than water molecules, into the aqueous cavities before they are closed off during the formation of the polymersome vesicles. It is common, therefore, for hydrophilic cargo to encapsulate at concentrations lower than the concentration of cargo in the surrounding solution [188]. Hydrophilic cargo is typically not loaded by flash nanoprecipitation, as most of the nanoparticles formed by FNP are solid-core hydrophobic nanoparticles. As such, it is not clear how the rapid microscale mixing fundamental to FNP

affects the loading of hydrophilic cargoes into polymersomes. It is even less clear how well hydrophilic cargo loads into BCNs, by FNP or otherwise.

3.2.3. Delivery to Phagocytic Cell Types *in vitro* by Nanocarriers

Once loaded, nanocarriers are expected to deliver their cargo to a target location, often to a target cell population. As discussed in section 1.2.5. and highlighted in **Figure 1-6**, nanoparticles are overwhelmingly internalized by immune cells, particularly those of the MPS, when administered *in vivo*. There are a number of factors that influence cellular uptake of nanoparticles [189]. Prevention or alteration of protein adsorption to the nanoparticle surface can change what receptors on the cell surface engage with the nanoparticles (if at all), influencing whether the particle is internalized by endocytosis, macropinocytosis, or phagocytosis. Some nanoparticles may interact with the cell surface but fail to be internalized, which may or may not be the functional goal of the delivery system. As some cargo may be intended for delivery into the endolysosome or cytoplasm, internalization could be a critical step in the delivery process. Cellular uptake of nanoparticles can be altered by specifically incorporating targeting moieties to the nanoparticle surface. These targeting molecules be peptides, proteins (e.g. antibodies or receptor ligands), aptamers, etc [190]. Nanoparticle morphology plays a role in cellular uptake, although the relationship is complex. There is evidence that suggests that different cell types prefer different morphologies [121, 191]. Beyond this preference, there is also the consideration of the geometry of receptor-ligand engagement, and the relationship between nanocarrier surface area and protein adsorption.

3.2.4. *In vivo* Biodistribution of Nanocarriers *via* IV or SC Administration

Administration of nanocarriers *in vivo* results in the introduction of a staggering number of variables that determine what the biodistribution of the nanocarriers will be. Route of administration, nanocarrier morphology, and surface charge all play significant roles in both organ level and cell population level biodistribution. The PEG-*b*-PPS nanocarriers utilized in this work are of neutral charge and as such the numerous biological interactions that ensure from being positively or negatively charged do not apply in this situation. Charge will therefore be disregarded for this dissertation, though significant work is being

performed in our lab relating to positively and negatively charged PEG-*b*-PPS nanocarriers and their biodistribution.

As eluded to in **Figure 1-7**, route of administration can significantly affect biodistribution of nanocarriers as it determines which biological barriers the nanocarriers will face first. Nanocarriers administered by IV injection will enter systemic circulation and will collectively enter the lung first *via* the pulmonary vein, prior to returning to the heart *via* the pulmonary artery. From there, the nanocarriers will be transmitted *via* the aorta to different branches, traveling to different organs and tissues within the body. A large number of these nanocarriers will pass through the liver, spleen, and kidneys, all potential locations of MPS clearance [192]. As nanocarriers exit vasculature and enter into tissue, they can be internalized by tissue-resident cells or can gradually pass into the lymphatics, to be delivered to lymph nodes. Subcutaneous administration will instead first deposit nanocarriers into tissue, leading them to first encounter tissue-resident cells and eventually lymph nodes [193]. From there, nanocarriers that have not yet been internalized by cells can enter systemic circulation [191]. Some nanocarriers may be too large to easily diffuse through the extracellular space after subcutaneous injection and may form a nanocarrier depot at the site of injection or alternatively may interact with ECM and dwell in the extracellular space [193]. At each step along the way, for either route of administration, nanocarrier shape, size, and charge can influence whether nanocarriers are stopped by or pass through biological barriers.

Recent work in our lab has characterized the organ and cellular biodistribution of PEG-*b*-PPS micelles, filomicelles, and polymersomes after IV administration [121] and the cellular biodistribution of those same morphologies in the draining lymph node and spleen after SC administration [191]. A postdoc in our lab, Sijia Yi, found that IV injections of MC, FM, and PS had similar organ-level biodistributions. She investigated the uptake of these nanocarriers using indocyanine green (ICG), a near-infrared (NIR) fluorescent dye which allows for better fluorescent quantification through/in opaque tissues, at 1, 24, and 48 hours post-injection (**Figure 3-1**). One hour after injection, all nanocarriers saw uptake in the liver, kidneys, heart, and lungs. PS and MC both saw splenic uptake, while FM did not. In fact, FM saw the least uptake at 1H, suggesting superior retention in circulation and reduced clearance by MPS. This trend of low uptake for FM was maintained at 24H and 48H post-injection as well. PS uptake persisted the longest out

of the three morphologies, particularly in the spleen, where the other two morphologies no longer displayed signal at the 48H timepoint. MCs showed the most persistent uptake in the lungs, heart, and kidneys, out of the three morphologies, suggesting more non-MPS uptake than PSs. Uptake was also assessed on a cell population basis by flow cytometry (**Figure 3-2**). Macrophages and dendritic cells generally showed the most uptake of all three morphologies in the spleen, lymph nodes, and liver. In the blood, dendritic cells, monocytes, granulocytes, and neutrophils all showed uptake of nanocarriers, though the uptake was particularly high for FMs, suggesting they are internalized by circulating leukocytes instead of organ-resident cells. Macrophages and dendritic cells in the liver demonstrate dynamic changes in the morphology they preferentially took up, with MCs overtaking PSs and FMs after 48H. In other work from our lab, uptake by specific cell populations was assessed in the lymph nodes and spleen after SC injection of all three morphologies (**Figure 3-3**). The general trend was that MCs possessed the broadest uptake by different phagocytic cell types, while filomicelles possessed the least uptake. PSs were moderately selective, and

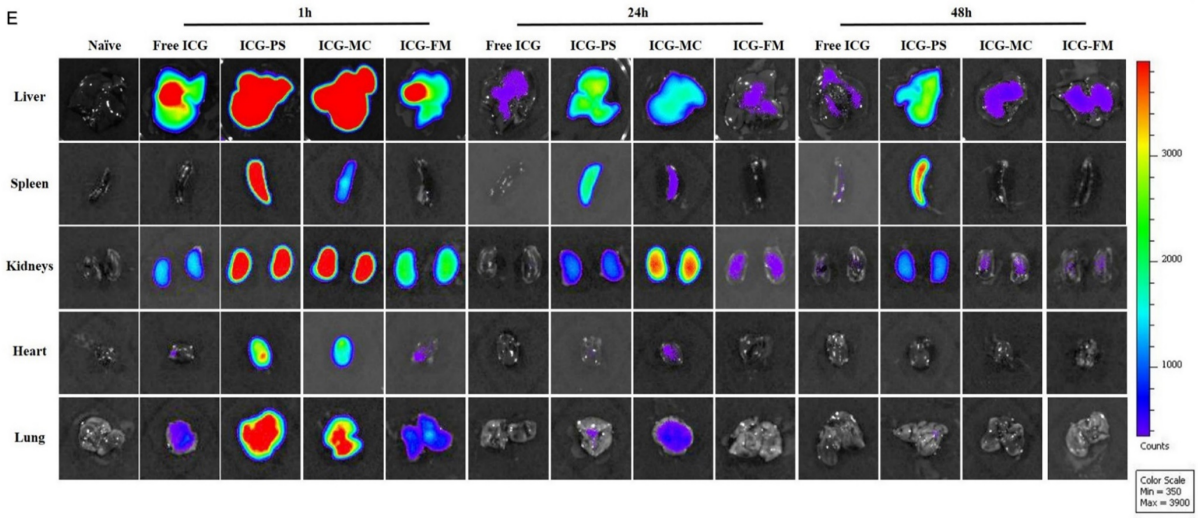

Figure 3-1. Organ-level biodistribution of intravenously administered MC, PS, and FM. Intravital imaging (IVIS) of ICG fluorescence. Organs were imaged from mice that were administered either 1xPBS, free ICG, or ICG loaded into either MC, PS, and FM. Mice were injected with formulations and were sacked at 1H, 24H, or 48H post-injection. All organs (liver, spleen, kidneys, heart, and lungs) are placed on the same scale of radiant efficiency. N=3-6 mice per formulation. Adapted with permission from [121] © 2016 American Chemical Society.

were taken up by monocytes and dendritic cells, particularly in the spleen. FMs were generally only found in monocytes. In all, this data demonstrates that there are organ- and cell-level biodistribution differences between different nanocarrier morphologies. As all morphologies were made of PEG-*b*-PPS polymer, with the same surface chemistry and charge, the predominant variable accounting for their differential

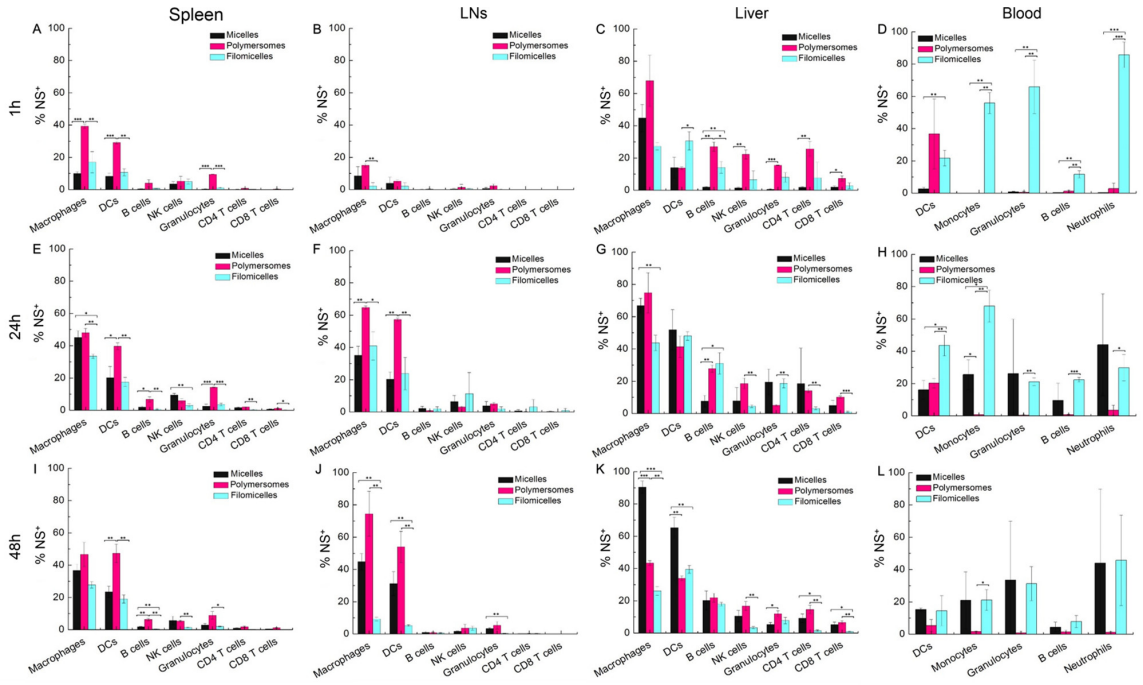

Figure 3-2. Cellular-level biodistributions of MC, PS, and FM. Flow cytometric analysis of the association of MC, PS, and FM with immune cells isolated from spleen (A, E, I), lymph nodes (LNs) (B, F, J), liver (C, G, K), and blood (D, H, L) of C57BL/6 mice after time points of 1 h (A–D), 24 h (E–H), and 48 h (I–L) following tail vein injection. Histograms show the average percentages ± standard deviation (SD) of nanostructure positive (NS+) cells for each indicated cell type in different tissue. Macrophages: CD11b+F4/80+; dendritic cells (DCs): CD11c+; B cells: CD45+CD19+; natural killer (NK) cells: CD45+CD49b+; granulocytes: Gr-1+CD11b+; CD4 T cells: CD45+CD3+CD4+; CD8 T cells: CD45+CD3+CD8+; monocytes: Ly6G–CD11c–CD11b+; and neutrophils: CD11b+Ly6G+. Data were obtained from two independent experiments and contain N = 6–8 for each group. Statistical significance: *p ≤ 0.01, **p ≤ 0.005, ***p ≤ 0.0001. Adapted with permission from [121] © 2016 American Chemical Society.

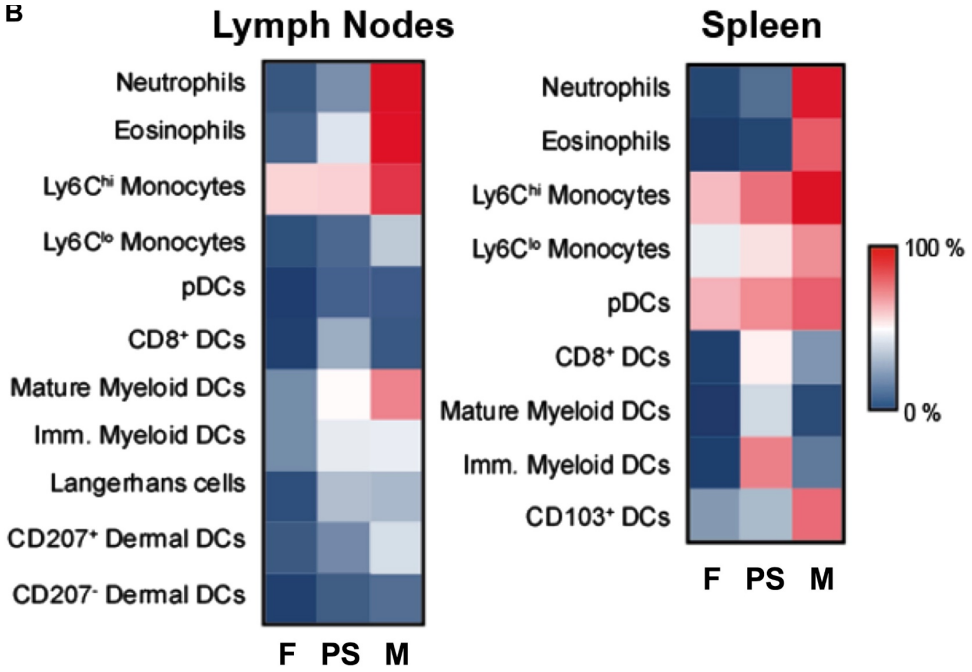

Figure 3-3. Cellular-level biodistribution of MC, FM, and PS after subcutaneous administration. Flow cytometric analysis of single-cell suspensions from mouse lymph nodes and spleens was conducted 24 hours after subcutaneous injection of fluorescent nanocarriers into the footpad (n = 5-8). A heat map demonstrates percentages of key phagocyte populations that associated with PEG-*b*-PPS filomicelles (F), vesicular polymersomes (PS), and spherical micelles (M). Amine-functionalized PEG17-bl-PPS30 block copolymers were conjugated to fluorescent Dy647-N-hydroxysuccinimide and assembled in the presence of block copolymers engineered to generate filamentous, vesicular, or spherical morphologies. Reproduced from [189] Creative Commons License.

biodistribution is there size and shape, which can be exploited to allow for passive (i.e. non-receptor mediated) targeting of the nanocarriers to cell types and tissues.

3.3. Materials and Methods

3.3.1. Animal Use

C57BL/6J female mice, 6-8 weeks old, were purchased from Jackson Laboratories. All mice were housed and maintained in the Center for Comparative Medicine at Northwestern University. All animal experimental procedures were performed according to protocols approved by the Northwestern University Institutional Animal Care and Use Committee (IACUC). Female cynomolgus monkeys *(Macaca fascicularis*) were used for the nonhuman primate study conducted at the University of Kentucky (UK). The four monkeys originated from Mauritius and were on average 4.8 years of age (range 4.5-4.9). The animals were housed in an AAALAC accredited facility under the care of the UK Division of Laboratory Animal Resources. All experiments were approved by the UK Institutional Animal Care and Use Committee.

3.3.2. Chemicals

Unless explicitly stated below, all reagents and chemicals were purchased from Sigma-Aldrich.

3.3.3. Mammalian Cell Culture

RAW 264.7 macrophages were obtained from the American Type Culture Collection (ATCC, Rockville, MD, USA). These cells were cultured in Dulbecco's Modified Eagle's Medium (DMEM) supplemented with 10% fetal bovine serum (FBS), penicillin (100 IU/mL) and streptomycin (100 µg/mL) at 37 °C and 5% CO_2.

3.3.4. Loading of Hydrophilic and Hydrophobic Cargo into Nanocarriers

For FNP PS loading experiments, PEG_{17}-*b*-PPS_{36}-Thiol polymer (20 mg) was dissolved in THF and impinged against aqueous nonsolvent using the CIJ mixer described in Chapter 2. For calcein and ethyl eosin co-loading experiments, the aqueous solvent consisted of 0.4 mM calcein in 1xPBS. 10 µL of a 5 mg/mL ethyl eosin solution in ethanol was added to 490 µL of THF and 20 mg of polymer. For the TMR-dextran and ICG co-loading experiments, 2 mg of TMR-dextran (70 kDa, Thermo Fisher) was dissolved in 500 µL 1xPBS. 50 µL of a 1 mg/mL ICG solution in ethanol was added to 450 µL of THF and 20 mg of polymer. For alkaline phosphatase – ethyl eosin co-loading experiments, alkaline phosphatase was loaded at a concentration of 1 mg/mL within the reservoir, while 10 µL of a 5 mg/mL ethyl eosin solution in ethanol

was added to 490 µL of THF and 20 mg of polymer. For calcein and DiI co-loading experiments, the aqueous solvent consisted of a 0.4 mM calcein solution in 1xPBS, which was impinged against 490 µL THF with 10 µL DiI (as supplied, Thermo Fisher) and 20 mg of polymer. For the experiments examining the relative loading of fluorescein-dextran and cascade blue-dextran, both were used from stock solutions of 1 mg/mL in 1xPBS (both supplied by Thermo Fisher). For the GFP loading experiments, 50 µL of a 200 µg/mL stock solution (GFP generously supplied by Weston Kightlinger in the Jewett Lab at Northwestern University) was dissolved in 450 µL of 1 × PBS (for syringe loading) or 2.45 mL 1xPBS (for reservoir loading), while 20 mg of polymer was dissolved in 500 µL of THF. Fluorescence and absorbance measurements were taken on a SpectraMax M3 microplate reader (Molecular Devices). All readings were taken in black-walled clear bottom 96-well plates (Corning 07-200-567), at 100 µL volumes. All readings were normalized to a 100 µL 1xPBS blank control. The following settings were used for fluorescence measurements for each fluorophore (excitation/emission, filter used): calcein: 470/509, 495 filter, ethyl eosin: 525/560, 550 filter, tetramethylrhodamine: 555/580, 570 filter, fluorescein: 494/524, 515 filter, cascade blue: 400/425, 420 filter, indocyanine green: 780/820, no filter, DiI: 549/565, 550 filter, DiD: 644/670, 665 filter, ovalbumin Texas red: 594/615, 610 filter, and GFP: 485/535, 495 filter. NBT diformazan was detected *via* absorbance at 620 nm.

FNP of PSs and BCNs was performed as previously described. Briefly, PEG-*b*-PPS co-polymer (10 mg) was dissolved in 500 µL of THF along with the hydrophobic cargo and was loaded into a 1 mL syringe. Another 1 mL syringe was loaded with 500 µL of 1x PBS (for PSs) or water (for BCNs). These two solutions were impinged against one another in a hand-driven CIJ mixer. For PSs, the impinged solution was redivided between the two syringes for an additional four more impingements before finally being introduced to a reservoir of 1.5 mL of 1× PBS to decrease polydispersity as described previously in Chapter 2. For BCNs, the impinged solution was immediately diluted with 1.5 mL of water. Unloaded formulations were dialyzed overnight in a 100 kDa Float-A-Lyzer G2 device (Repligen, Waltham, MA) in 1xPBS to remove residual organic solvent. For dual-loaded PS and BCN formulations, hydrophobic DiD (5 µL from 2.5 mg/mL in THF, Thermo Fisher) and hydrophilic fluorescein isothiocyanate-bovine serum albumin (FITC-BSA) (100 µL from 2 mg/mL in water or PBS) were added to the THF and aqueous phase, respectively, prior to the impingement. To ensure removal of both unloaded hydrophobic and hydrophilic dyes,

formulations were column filtered using a Sepharose CL-6B column with PBS as an eluent. For *in vivo* experiments, PSs or BCNs were covalently labeled with maleimide-functionalized fluorescent dye (DyLight 755-maleimide). Solutions of PSs or BCNs (5 mg/mL) were added with 0.07 mM of DyLight 755-maleimide (Fisher), vortexed overnight at room temperature, and excess unreacted dye was then removed by dialyzing against sterile PBS. Ethyl eosin-loaded formulations were created as described for the FNP PS loading experiments.

Hydrophilic molecules calcein (4 mM, 50 µL), Texas Red-dextran (10 kDa, Thermo Fisher) (10 mg/mL, 20 µL), tetramethylrhodamine dextran (70 kDa, Thermo Fisher) (5 mg/mL, 20 µL) and Texas Red-ovalbumin (Thermo Fisher) (5 mg/mL, 25 µL) were separately loaded inside BCNs. Hydrophobic molecules ethyl eosin (5 mg/mL, 10 µL), and DiD (20 mg/mL, 5 µL) were loaded inside BCNs. For each individual loading experiment, hydrophilic or hydrophobic molecules were added to water or THF, respectively to attain a final volume of 500 µL before impingement. For co-loading of ovalbumin and MPL, the aqueous phase containing ovalbumin (5 mg/mL, 25 µL) and the THF phase containing MPL (1 mg/mL, 20 µL) were impinged against each other to form BCNs. For control experiments, PEG_{17}-bl-PPS_{32} was utilized to form polymersomes using FNP and loaded with Ovalbumin and MPL as described above. The loading efficiency was determined by fluorescence measurements using the following wavelengths: (excitation/emission, filter used): calcein: 470/509, 495 filter, ethyl eosin: 525/560, 550 filter, tetramethylrhodamine: 555/580, 570 filter, DiD: 644/670, 665 filter, and Texas Red-ovalbumin: 594/615, 610 filter.

PEG-*b*-PPS micelles were formed *via* thin film hydration, as described previously in section 2.2.1. To summarize, 15 mg of PEG_{45}-*b*-PPS_{20}-Benzyl was weighed into a glass HPLC vial (Thermo Fisher). If the formulation was to contain celastrol, celastrol was added to the vial at this point from a stock solution of 1 mg/mL in tetrahydrofuran (THF). The mixture was dissolved in 1 mL of THF and was left in a vacuum desiccator overnight to remove the THF and coat the walls of the vial in polymer. After desiccation, 1 mL of sterile phosphate buffered saline (1xPBS) was added to each vial. Vials were then shaken for 2 hours at 1000 rpm. Formulations were used immediately or were stored at 4 °C.

3.3.5. Confocal Microscopy

Cel-MC were formed, as described above, using 10 mg polymer, 10 µg celastrol, and 10 µg DiI with hydration in 1 mL of 1xPBS. DiI is a lipophilic dye that stably loads within PEG-*b*-PPS nanocarriers [44]. RAW 264.7 cells (supplied by ATCC, TIB-71) were added to an 8-chamber coverslip-bottom slide at $2x10^5$ cells per chamber. Cells were either left untreated or treated with 1 mg/mL micelles (1 µg/mL celastrol) overnight. Cells were then washed twice with 1xPBS and returned to complete media for an additional 24 hours. Cells were incubated with 100 nM LysoTracker Green DND-26 (ThermoFisher Scientific) and 8 µM Hoechst 33342 (ThermoFisher Scientific) in 1xPBS for 30 minutes prior to being washed twice and returned to complete media. Cells were then imaged using an SP5 Leica confocal microscope at 63x objective magnification. Hoechst nuclear staining was detected using a 405 nm laser with emission detected using a HyD detector set to a 440/470 band. Lysotracker Green was detected using a 488 nm laser and a HyD detector set to a 500/530 band. DiI was detected using a 561 nm laser and a HyD detector set to a 570/630 band.

Bone marrow derived dendritic cells were generated from bone marrow collected from the tibias and femurs of C57BL/6 mice, in a protocol slightly modified from those described previously [194]. Tibias and femurs of C57BL/6 mice were cleaned of tissue, cut, and flushed through with 10% FBS in Hank's balanced salt solution (HBSS, Thermo Fisher). Cells were centrifuged, supernatant was removed, and they were then treated with ammonium-chloride-potassium (ACK) lysis buffer for 5 min. Lysis was stopped with the addition of excess HBSS, and cells were centrifuged again, resuspended in 10 mL cell culture medium (10% FBS and 1xPenstrep in RPMI), and were plated in 100 mm petri dishes. Every three days, 200 ng of GM-CSF and 100 ng of IL-4 were added to culture. On the 8th day of maturation, cells were collected and plated into a FluoroDish at $3x10^5$ cells/mL, along with 15 µL of dual-loaded GFP ethyl eosin polymersomes. Lysotracker Blue (lysosome stain) and SYTO 61 (nuclear stain) were added at 1:10,000 dilutions. Plated cells were imaged within a humidified chamber using a 63x oil-immersion objective on a SP5 Leica Confocal Microscope using HyD detectors and four lasers: 415 nm diode laser for Lysotracker Blue, 488 nm argon laser for GFP, 514 nm argon laser for ethyl eosin, and 633 nm HeNe laser for SYTO 61.

RAW 264.7 macrophages ($2x10^5$ cells per ml, 150 µL) were plated in each well of an 8-well chamber slide and cultured overnight. Texas Red dextran-loaded BCNs (5 mg/mL in PBS, 10 µL) were

added to each well and incubated for 2, 4 and 8 h. After incubation, the cells were washed with DMEM, and stained with LysoTracker green (lysosome stain) and DAPI (nuclear stain). The cells were then fixed and imaged using a 63x oil-immersion objective on a SP5 Leica confocal microscope.

3.3.6. BMDC Generation and Activation Assay

Bone marrow derived dendritic cells (BMDCs) were obtained after processing of bone marrow from the tibias and femurs of C57BL/6 mice as described in the previous section. These cells were plated in 100 mm petri dishes with GM-CSF and IL-4, refreshed every three days. After 8 days, matured dendritic cells were collected and utilized for the assay. A functional assay to demonstrate *in vitro* delivery of antigen (ovalbumin) and adjuvant (MPL) to BMDCs was performed using BCNs. In this study, BMDCs were plated into a non-tissue culture treated 48-well plate at 1 × 105 cells per well. After 6 hours of acclimation, cells were incubated with 20 µL of OVA-MPL-loaded BCNs or PSs (5 mg/mL polymer, 20 µg/mL OVA, 10 µg/mL MPL), OVA-loaded BCNs or PSs (5 mg/mL polymer, 20 µg/mL OVA), Blank BCNs or PSs (5 mg/mL polymer), free OVA (20 µg/mL) with or without free MPL (10 µg/mL), or 1xPBS. After 14 h of incubation, BMDCs were blocked with anti-mouse CD16/32 antibody and stained with: BV421 anti-mouse CD11c, PE/Cy7 anti-mouse MHCI-SIINFEKL, APC anti-mouse CD80, APC/Cy7 anti-mouse CD86, PerCP/Cy5.5 anti-mouse CD40, and Zombie Aqua viability dye. Cells were analyzed using a LSRII flow cytometer (BD Biosciences) and data was analyzed by Cytobank online software [195]. Gating strategy demonstrated in appendix **Figure A-1**. Results were analyzed for statistical significance with GraphPad Prism 7 using two-way ANOVA followed by Tukey's multiple comparison tests.

3.3.7. Cell Uptake and Viability Studies

RAW 264.7 macrophages ($2x10^5$ cells per ml, 500 µL) were seeded in each well of a 24-well plate and cultured overnight. DiD loaded BCNs (5 mg/mL in PBS, 20 µL) were added to each well and incubated for 2, 4, 8 and 24 h. After incubation, cells were washed thrice with PBS and harvested in 0.5 mL PBS. Samples were then stained with Zombie Aqua™ (live/dead stain) and analyzed using a LSRII flow cytometer (BD Biosciences), and data were analyzed by Cytobank online software

(https://www.cytobank.org/). DiD was analyzed using the APC filter set and 633-laser in the LSRII flow cytometer.

For the comparative uptake study between PSs and BCNs, RAW 264.7 cells were seeded in non-tissue culture-treated plastic 48-well plates at 100,000 cells per well. To these cells were added BCNs and PSs at equal polymer concentrations (0.5 mg/mL). Cells were incubated with FITC-BSA and DiD dual-loaded BCNs or PSs for 0.5, 1, 2, 3, 4, 5, 6, 7, and 8 h before cells were collected for uptake analysis using flow cytometry. Cells were stained with Zombie Aqua cell viability dye (BioLegend) for 15 min at a 1:100 dilution in cell staining buffer (eBioscience), washed with 1× PBS, and briefly fixed with 2% paraformaldehyde prior to analysis on a BD LSRFortessa. Flow cytometry data were analyzed using the online Cytobank analysis suite.

3.3.8. Intravital Fluorescent Imaging

Formulations of BCNs and PSs (100 µL, 5 mg/mL) were injected *via* the tail vein into C57BL/6J mice. After 4 or 24 h injection, 500 µL of blood was collected retro-orbitally, and mice were euthanized. Liver, kidneys, lungs, and spleens were collected and imaged with an IVIS Spectrum *in vivo* imaging system (PerkinElmer, Waltham, MA). Organs were imaged using the preset filter combination for DyLight 755 and automated acquisition settings at the “B” field of view and 0.5 mm height. Total radiant efficiency was calculated using Living Image software. Liver, blood, and spleens were retained for processing into single-cell suspensions for flow cytometry.

3.3.9. Cellular Biodistribution Flow Cytometry

Liver, blood, and spleen from mice, 4 and 24 h post intravenous (IV) administration of BCNs and PSs, were processed for flow cytometry. Livers were mechanically dissected into 1 mm^3 pieces, which were incubated in a digestion solution of 0.1 mg/mL DNase I (Roche) and 1.6 mg/mL Collagenase D (Roche) in serum-free RPMI (Thermo Fisher) at 37 °C for 45 min while shaking at 500 rpm, with breaks every 15 min for rapid vortexing of the samples. The liver cells were then passed through a 70 µm nylon mesh. Cells were spun at 100 rcf for 2 min twice, retaining the supernatant each time, which consisted of a single-cell

suspension of liver immune cells. Blood was spun at 3000 rpm for 25 min, and serum was removed from the cell pellet. Blood cells were lysed using ACK lysis buffer (Gibco) three times. Remaining cells were used for staining. Spleens were mechanically disrupted and passed through a 70 μm nylon mesh to make a single-cell suspension.

Single-cell suspensions were stained for viability using Zombie Aqua (Biolegend) and were blocked using an anti-CD16/32 blocking antibody. Cells were then stained with a panel of antibodies for immune cell populations, all antibodies were from Biolegend unless specified: BUV396 anti-CD45 (BD), BV650 anti-IA-IE, BV711 anti-Ly-6C, BV605 anti-F4/80, FITC anti-NK1.1, FITC anti-CD3, FITC anti-CD19, PerCP/Cy5.5 anti-CD11b, PE anti-B220, BV421 anti-CD11c, APC anti-CD8a, and Alexa Fluor 700 anti-Ly-6G. Flow cytometry was performed on a LSRFortessa 6-laser instrument (BD), and data were analyzed using the online Cytobank analysis suite, using a gating strategy demonstrated in appendix **Figure A-2**.

For primate studies, flow cytometry was performed using a BD LSRII. A portion of each primate organ was mechanically dissected into smaller pieces prior to being processed further. Liver and kidney samples were enzymatically digested in 0.4 mg/mL DNase I, 1.5 mg/mL collagenase A in 1xHBSS buffer, 5 mL per sample at 37 °C for 45 minutes, with samples vortexed every 15 minutes during the incubation process. All tissues were passed through a 70 μm nylon filter to produce single cell suspensions. Cells were first incubated in a viability and Fc blocking buffer, BioLegend Zombie Aqua and BD Pharmingen Human BD Fc Block, used at the vendor recommended concentrations. Cells were split into three groups to be stained with three separate antibody cocktail panels. Unless explicitly stated in parenthesis, antibody was acquired from BioLegend. Panel 1: BV450 CD45 (BD, D058-1282), APC/Cy7 HLA-DR (L243), PE CD1c (Miltenyi, AD5-8E7), FITC CD123 (ThermoFisher, 7G3), PerCP/Cy5.5 CD3 (BD, SP34-2) (lineage), PerCP/Cy5.5 CD20 (2H7) (lineage). Panel 2: BV450 CD45 (BD, D058-1282), APC/Cy7 CD45RA (Miltenyi, T6D11), PE CD8 (RPA-T8), FITC CD19 (Abcam, CB19), PE/Cy7 CD4 (OKT4), PerCP/Cy5.5 CD3 (SP34-2). Panel 3: BV450 CD45 (BD, D058-1282), APC/Cy7 CD14 (M5E2), PE CX3CR1 (K0124E1), PerCP/Cy5.5 CD16 (3G8), PE/Cy7 CD49d (9F10), FITC CD3 (BD, SP34-2) (lineage), FITC CD19 (Abcam, CB19) (lineage), FITC CD56 (Miltenyi, REA196) (lineage). Markers used for the identification of immune cell populations were adopted from previously published work, and are as follows: Plasmacytoid dendritic cells

(pDCs): CD45+ CD3- CD20- CD14- HLA-DR+ CD123+ CD1c-; classical dendritic cells (cDCs): CD45+ CD3- CD20- CD14- HLA-DR+ CD123-; T Cells: CD45+ CD3+, B Cells: CD45+ CD3- CD19+; NK Cells: CD45+ CD3- CD19- CD16+ CD56+; Neutrophils: CD45+ CD3- CD19- CD56- CD14 low CD49d-; classical monocytes (cMo): CD45+ CD3- CD19- CD14+ CD49d+ CD16-; non-classical monocytes (ncMo): CD45+ CD3- CD19- CD14+ CD49d+ CD16+ CX3CR1+; macrophages (Mφ): CD45+ CD3- CD19- CD14+ CD49d+ CD16+ CX3CR1-. cDC1s: cDC markers as listed above and CD1c-; cDC2s: cDC markers as listed above and CD1c+. T cells were gated as above, then gated as CD4+ or CD8+, then gated on CD45RA+ (effector) or CD45RA- (memory). Gating strategy is demonstrated in appendix **Figure A-3 and A-4** for panels 1 and 2, respectively.

3.4. Results

3.4.1. Encapsulation Efficiency of Polymersomes Formed by FNP for Hydrophilic and Hydrophobic Cargo

Polymersomes, in contrast to micelles and filomicelles, are able to load both hydrophilic and hydrophobic cargoes [45, 196]. PEG-*b*-PPS polymersomes had already been loaded with hydrophilic and hydrophobic cargoes, though not simultaneously, and not when formed by FNP. FNP has primarily been limited to the formation of solid core nanoparticles using hydrophobic molecules with a logP > 6 for stable nanoparticle formation [133, 197]. I sought to better understand cargo characteristics that influence encapsulation within polymersomes, particularly when loaded *via* FNP. I tested molecules ranging from < 1 kDa to > 100 kDa and with varying hydrophobicity and Stokes radius: calcein, ethyl eosin, indocyanine green, rapamycin, lipophilic dye DiD, dextran (10 and 70 kDa), green fluorescent protein (GFP), ovalbumin, and alkaline phosphatase (**Figure 3-4**). The first general trend is that small molecules, nearly all of which are hydrophobic, loaded with >50% encapsulation efficiency. The exception to the trend is calcein, which is relatively hydrophilic (logP = 1.6) and small (MW = 622.55 g/mol) [198]. As such, calcein actually demonstrates the lowest loading efficiency (5.25%), possibly due to its diffusion from the interior of assembling polymersomes into the exterior aqueous reservoir before vesicle stabilization. Alternatively,

calcein may have a partition coefficient denoting little preference between the hydrophobic interior of the polymersome membrane and the aqueous exterior, allowing it to diffuse through the membrane after encapsulation and removal of unencapsulated calcein. In contrast, ethyl eosin, rapamycin, DiD, and ICG presented very high loading efficiencies, as they can partition into the hydrophobic bilayers during polymersome assembly. All of these small molecules possessed higher logP values than calcein, suggesting that partition coefficient is an important characteristic of the cargo that can help predict its ability to load into polymersome membranes. The encapsulation efficiency of macromolecules was significantly higher than for calcein and ranged between 16 and 43%, depending on the macromolecule (**Figure 3-4**). This encapsulation efficiency is approximately as good, or is better, than other polymersome loading processes, such as solvent evaporation [199], thin film rehydration [131, 200-202], direct hydration [123], and electroporation [198].

Having demonstrated that polymersomes can be loaded with hydrophilic and hydrophobic cargo by FNP, I sought to demonstrate that they can be loaded with both simultaneously. There are a number of combinations of hydrophilic and hydrophobic cargo with potential biomedical relevance. For example, a protein therapeutic may be co-loaded with a hydrophobic fluorescent dye to track the delivery of the cargo

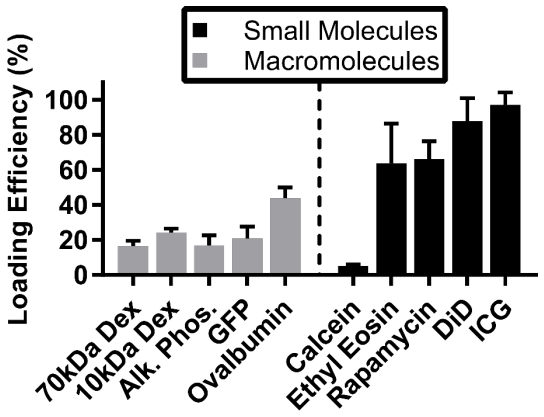

Figure 3-4. Loading of polymersomes with small molecules and macromolecules. (A) Loading efficiency of small molecules and macromolecules. Error bars represent standard deviation, n = 4. Dex = dextran, Alk. Phos. = alkaline phosphatase, GFP = green fluorescent protein, DiD = 1,1-Dioctadecyl-3,3,3,3-tetramethylindodicarbocyanine, ICG = indocyanine green. Figure adapted with permission from [164] © 2017 Elsevier.

Table 3-1. Encapsulation efficiency for dual-loading by FNP. Figure adapted with permission from [164] © 2017 Elsevier.

Dual Loaded Cargoes	Hydrophilic Loading (%)	Hydrophobic Loading (%)	LogP Values
TMR-Dextran 70 kDa, ICG	16.6 ± 3.0	97.1 ± 7.0	N/A, 9.06
Alkaline Phosphatase, Ethyl Eosin	19.0 ± 5.6	64.9 ± 5.4	N/A, 7.50
Calcein, Ethyl Eosin	5.1 ± 1.7	52.0 ± 2.6	1.61, 7.50
Calcein, DiI	2.5 ± 2.2	103.5 ± 12.1	1.61, 18.82
GFP, Ethyl Eosin	20.8 ± 6.7	63.7 ± 8.4	N/A, 7.50
Rapamycin, DiD	N/A	65.6 ± 7.2, 87.9 ± 13.1	6.18, 19.38

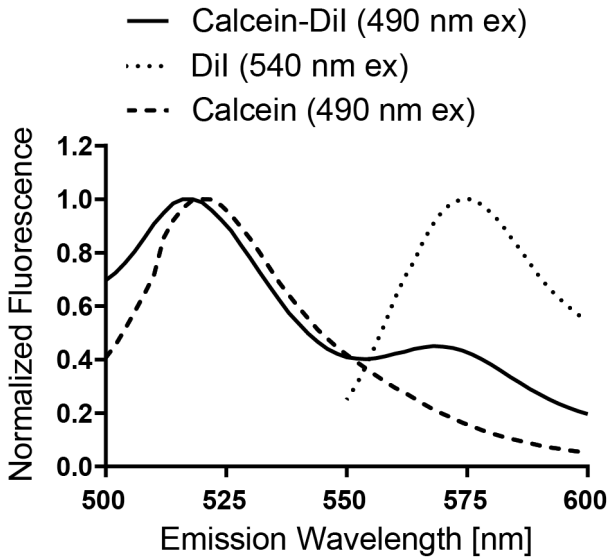

Figure 3-5. FRET between co-loaded calcein and DiI within polymersomes. Emission spectra of polymersomes loaded with calcein (dashed line), DiI (dotted line), or both (solid line). Calcein and dual-loaded formulations were excited with 490 nm light, the excitation wavelength for calcein. The DiI-only sample was excited with 540 nm light, the excitation wavelength for DiI. Figure adapted with permission from [164] © 2017 Elsevier.

to particular tissues or cells. Alternatively, vaccines typically consist of both an antigen and adjuvant, with most antigens being hydrophilic peptides or proteins and many adjuvants being hydrophobic pathogen-associated molecular patterns. Simultaneous co-loading of hydrophilic and hydrophobic molecules into

polymersomes was achieved simply by dissolving water soluble molecules in the aqueous stream and lipophilic molecules in the organic stream prior to impingement within the mixer. The co-loading efficiencies for hydrophilic-hydrophobic pairs of molecules are displayed in **Table 3-1**. Encapsulation of calcein (509 nm emission) and DiI (540 nm excitation) respectively within the polymersome lumen and membrane produced a FRET emission from DiI when exposed to a 490 nm light source (**Figure 3-5**), demonstrating the effective dual-loading of the fluorophores. The ease of this process demonstrates that FNP is a powerful tool for the formation of nanocarriers simultaneously loaded with diverse molecular payloads.

Three of the macromolecules I loaded into PSs *via* FNP were proteins. The folding of polypeptides into the tertiary structure of a functional protein is reversible and this denaturation can result in the loss of function of that protein. Denaturation of proteins can occur through a number of mechanisms, including the introduction of a sufficiently high concentration of organic solvent, which can cause hydrophobic portions of the protein to become soluble and the reverse for hydrophilic portions. Solvent dispersion and FNP both involve forming and loading nanoparticles in the presence of organic solvent and therefore there is some reasonable concern that these formulation techniques may be incompatible with protein cargo for which maintenance of function is important. In FNP, there are two sources of aqueous solution, either of which could potentially contain the hydrophilic cargo to be loaded. The encapsulation efficiencies in **Figure 3-4** and **Table 3-1** are based on the hydrophilic cargo being solubilized in the aqueous impingement syringe solution. A possible alternative is to solubilize the hydrophilic cargo within the reservoir. Nascent polymersomes would encounter the reservoir solution after the impingement has occurred but potentially before the vesicles have fully assembled. To determine the efficiency of this method, we attempted to simultaneously load polymersomes with two separate fluorescent dextrans of the same molecular weight by dissolving one in the impinged aqueous stream and one in the reservoir at the same concentration. The highly water-soluble macromolecule dextran (10 kDa) tagged with either cascade blue (CB) or fluorescein (F) was used. Dextrans are not proteins and therefore are not susceptible to solvent denaturation and whatever effects that might have on loading. To avoid any potential influences of the attached fluorophore on the loading efficiency, we conducted the experiments in pairs, with the dextran-CB in the syringe and dextran-F in the reservoir, and vice versa. I found there to be a statistically significant increase in loading

via syringe compared to reservoir, though loading by reservoir still occurred at detectable levels (**Figure 3-6a**).

After I found that reservoir-based loading was possible, I wanted to see whether a protein loaded in that manner would demonstrate less denaturation. I investigated whether loading *via* reservoir or syringe

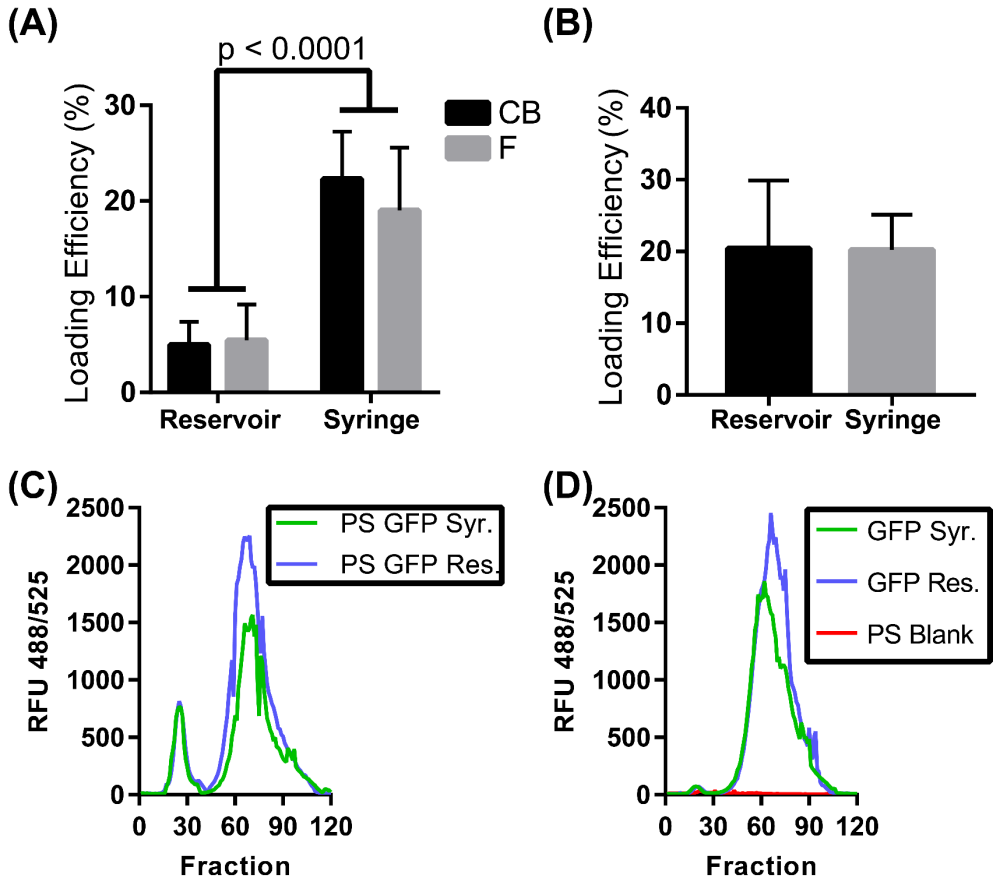

Figure 3-6. Hydrophilic loading by syringe or reservoir. (A) Encapsulation efficiency of fluorescently-labeled 10kDa dextrans (CB = cascade blue, F=fluorescein). Error bars represent standard deviation, n = 6. (B) Loading efficiency of GFP when loaded *via* either syringe or reservoir. Error bars represent standard deviation, n = 3. (C) Fluorescence of sepharose CL-6B column separated GFP-loaded polymersomes loaded *via* syringe or reservoir, 200 µL fractions. (D) Fluorescence of sepharose CL-6B column separated GFP processed *via* FNP through the syringe or reservoir without PEG-*b*-PPS copolymer, as a control. Included is a trace of blank polymersomes, for reference. Figure adapted with permission from [164] © 2017 Elsevier.

resulted in a greater amount of functional protein by loading GFP, which has a conformation-dependent fluorescence. I found that GFP fluoresced at equal levels whether loaded by syringe or reservoir within polymersomes (**Figure 3-6b**). I used size exclusion chromatography to separate non-encapsulated GFP from encapsulated GFP in polymersomes (**Figure 3-6c**). As controls, I also performed the same chromatography with unloaded polymersomes (Blank PS), and GFP that was processed by FNP without the presence of PEG-*b*-PPS polymer (solubilized in the syringe or reservoir) (**Figure 3-6d**). Blank polymersomes were not fluorescent and therefore did not interfere with area-under-curve (AUC) quantification of functional GFP. Analysis of the fluorescence AUC revealed that FNP decreased GFP fluorescence by 22.8 ± 5.4%. However, equal levels of fluorescence were again found for GFP-loaded polymersomes when the GFP was loaded from the syringe relative to the reservoir (recapitulating the results from **Figure 3-6b**), suggesting either that higher levels of loading occurred *via* the syringe or that GFP loaded equally either way and was equally protected from denaturation. These results therefore

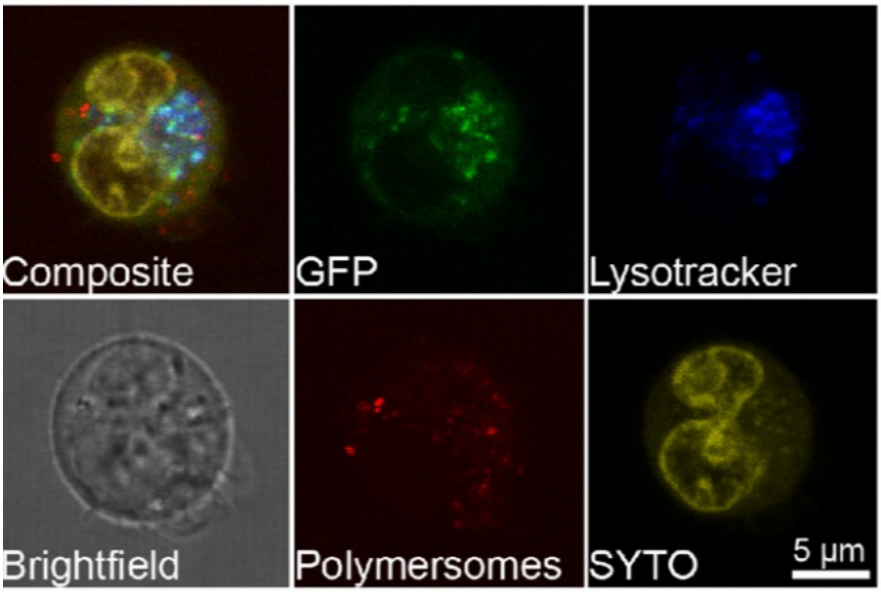

Figure 3-7. Subcellular localization of PSs in BMDCs. Live-cell confocal microscopy image of polymersome uptake and delivery of GFP in a bone marrow-derived dendritic cell. Polymersomes were loaded with the hydrophobic ethyl eosin (red) and hydrophilic GFP (green). Cells were additionally stained with SYTO 61 (yellow) and lysotracker (blue). Scale bar = 5 µm. Figure adapted with permission from [164] © 2017 Elsevier.

demonstrate that loading protein *via* the reservoir is preferable in cases where maintaining conformation is critical to macromolecule function, while loading *via* the syringe can achieve higher loading efficiencies at the expense of small decreases in protein bioactivity.

I sought to further validate the loading of active GFP by delivering GFP to cells *in vitro* and using confocal microscopy to determine if the delivered GFP was still fluorescent. Bone marrow derived dendritic cells (BMDCs) were generated from bone marrow freshly collected from C57BL/6 mice and after maturation were plated in the presence of polymersomes. The polymersomes were co-loaded with the hydrophobic dye ethyl eosin and GFP and the cells were further stained with nuclear stain SYTO 61 and lysosome stain Lysotracker Blue prior to imaging on a confocal microscope. Punctae of GFP and ethyl eosin were found within cells, demonstrating that conformationally-active GFP could be delivered to live cells *via* polymersomes (**Figure 3-7**). These results supported previously published confocal microscopy images and verify that FNP had no impact on the ability of PEG-*b*-PPS polymersomes to deliver payloads to the cytoplasm of BMDCs [131].

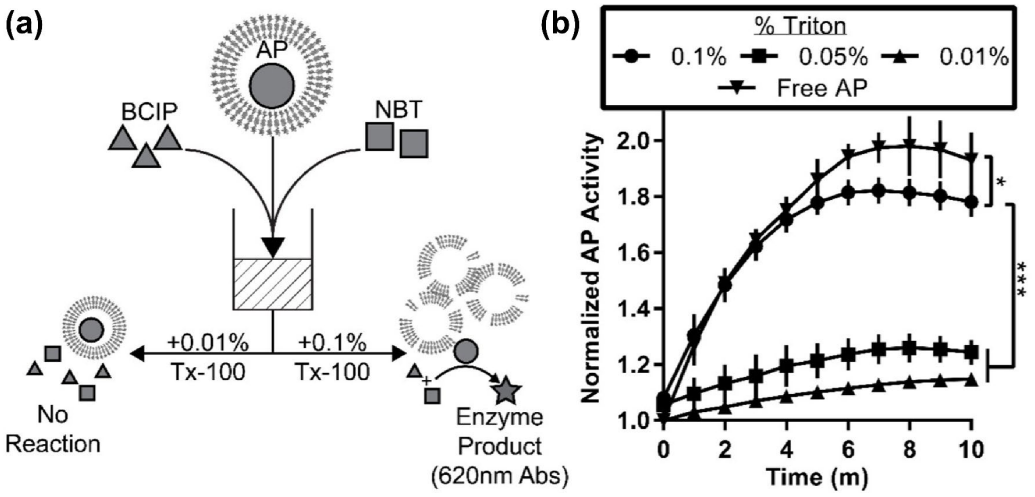

Figure 3-8. Loading of active enzyme into PSs by FNP. (a) Graphical representation of experimental setup. Alkaline phosphatase (AP) is represented by circles, BCIP by triangles, and NBT by squares. The product of the enzymatic reaction, formazan, absorbs strongly at 620 nm and is represented by a star. (b) Time-course of enzyme activity assay. Y-axis represents fold increase over original absorbance reading. Error bars represent standard deviation, n = 4. Statistical significance determined by 2-way ANOVA, *$p < 0.05$ and ***$p < 0.001$. Figure adapted with permission from [164] © 2017 Elsevier.

To further confirm the continued biological activity of loaded proteins, I chose an enzyme, alkaline phosphatase (AP), to encapsulated into polymersomes by FNP. AP removes phosphate groups from its substrates, including 5-bromo-4-chloro-3-indolyl-phosphate (BCIP), whose dephosphorylation is detectable by nitro blue tetrazolium (NBT) at an absorbance of 620 nm [203]. I encapsulated AP in PSs *via* syringe-loading and added the chromatography-purified AP-loaded PSs to a solution of BCIP and NBT. AP-PSs were lysed using Triton X-100 to allow the AP, BCIP and NBT to freely react in solution (**Figure 3-8a**). Low concentrations of Triton X-100 (0.01 v/v % and 0.05 v/v %) resulted in a low level of background reactivity, which was likely due to a burst effect resulting from the release of hydrophilic reagents trapped within the vesicle membranes, as there was no significant difference between the two low-concentration lysis treatments. The addition of 0.1% Triton X-100 resulted in the continued formation of significantly more product over a ten-minute period, verifying the maintenance of AP tertiary conformation and bioactivity following encapsulation within polymersomes by FNP. I also tested, as a control, free AP at a concentration matched to the amount of AP encapsulated within the PSs. I found the free AP to have a marginally greater activity than the polymersome loaded-AP after addition of 0.1% Triton X-100, differing by only 6.28% after 10 min (**Figure 3-8b**). This difference is likely the difference in denaturation caused by the FNP process.

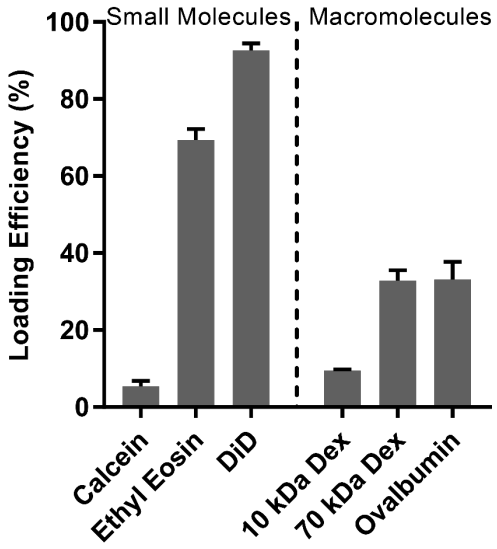

Figure 3-9. Encapsulation efficiency of cargoes into BCNs by FNP. Encapsulation efficiency of small and macromolecules into BCNs formed by FNP. Error bars represent SD, n = 3. Adapted from [146] with permission from The Royal Society of Chemistry.

3.4.2. Encapsulation Efficiency of Bicontinuous Nanospheres for Hydrophilic and Hydrophobic Cargo

After demonstrating the successful loading, dual-loading, and non-destructive loading of hydrophilc and hydrophobic molecules into PSs *via* FNP, Sharan Bobbala and I sought to examine whether BCNs could be loaded in a similar manner. The presence of hydrophobic volume and internal aqueous channels makes BCNs an attractive potential nanocarrier for both lipophilic and hydrophilic molecules [167]. To investigate their capacity to load diverse molecules into BCNs by FNP, FNP was performed using cargoes ranging in molecular weight and hydrophobicity: calcein, ethyl eosin, DiD, dextran (10 and 70 kDa), and ovalbumin. Loading efficiency of larger hydrophilic macromolecules ovalbumin and 70 kDa dextran (33%, each) were higher than that for smaller hydrophilic molecules calcein and 10 kDa dextran (5.3% and 9.46%, respectively) (**Figure 3-9**). The lower loading efficiency of small molecules may be due to their higher diffusion rate into the aqueous reservoir prior to completion of nanostructure assembly, similar to what was observed for polymersomes and calcein loading in section 3.4.1. After assembly, larger molecules may also

Table 3-2. Encapsulation efficiency by FNP for MCs, PSs, and BCNs.

			Encapsulation Efficiency (%)		
Compound	**MW (g/mol)**	**LogP**	**MC**	**PS**	**BCN**
DiD	1052.79	19.38	95.5	87.9	93.5
DiI	933.89	18.824	99.4	98.5	99.2
ICG	774.96	9.056	98.3	97.1	-
Ethyl Eosin	714.04	7.497	72.1	63.7	67.1
Celastrol	450.61	6.698	96.1	-	-
Rapamycin	914.17	6.181	-	65.6	-
Calcein	622.55	1.608	-	2.5	5.3
Dextran	10,000	-	-	21.2	9.5
	70,000	-	-	16.6	33.0
GFP	27,000	-	-	20.9	-
Ovalbumin	42,700	-	-	43.5	33.0
Alkaline Phosphatase	140,000	-	-	19.0	-

be more easily entrapped within the aqueous channels of the BCNs, potentially explaining why ovalbumin and 70kDa saw higher encapsulation. Hydrophobic molecules ethyl eosin and DiD demonstrated loading efficiencies >70% (**Figure 3-9**), likely due to partition into the large hydrophobic domains. These results demonstrate the ability of FNP to load both hydrophilic and hydrophobic cargoes into BCNs, as it had with polymersomes. Encapsulation efficiency of the various cargoes in micelles, polymersomes, and bicontinuous nanospheres is summarized in **Table 3-2**.

3.4.3. Oxidation-Responsive Release from Polymersomes and BCNs

Shelf-life of formulations is an important consideration for clinical adoption. Little is known about the gradual leakage of cargo from loaded BCNs, and I sought to investigate the topic. BCNs formed by FNP were loaded with calcein, 70 kDa dextran-tetramethylrhodamine, DiD, and ovalbumin-Texas Red. After these formulations were purified of unencapsulated cargo by size exclusion chromatography, formulations

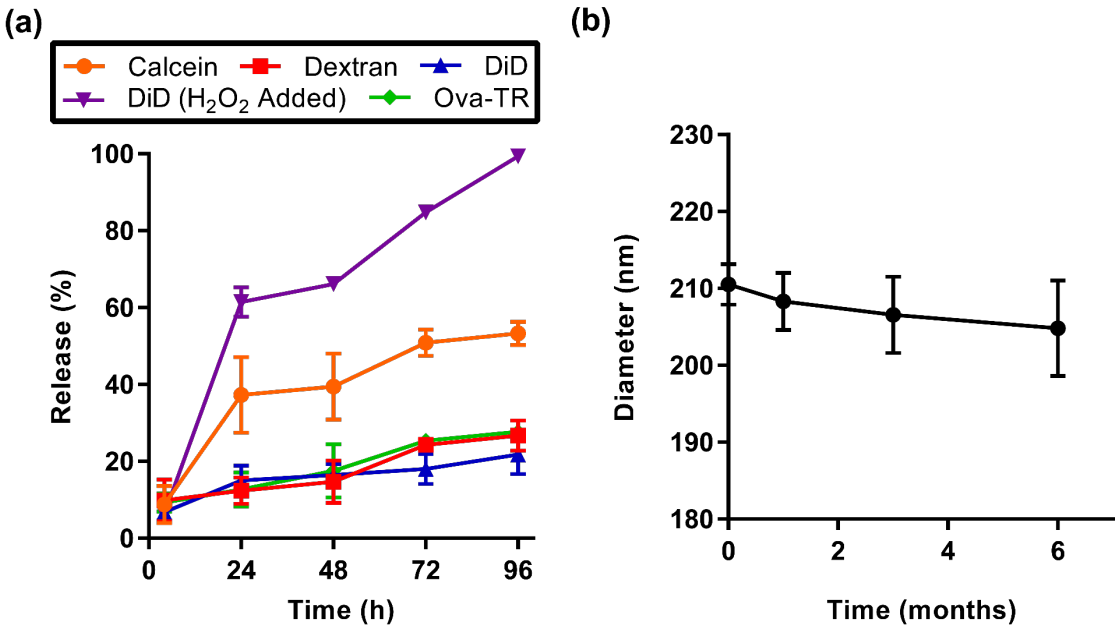

Figure 3-10. Release and stability characteristics of BCNs. (a) Release of hydrophilic and hydrophobic molecules from BCNs over 96 hours. Dextran used in this study was 70 kDa in molecular weight. (b) Diameter of BCN samples measured over the course of 6 months by DLS. In both cases, error bars represent SD, n = 3. Adapted from [146] with permission from The Royal Society of Chemistry.

were dialyzed for 96 hours, with fluorescence readings taken every 24 hours to measure the percentage of cargo that was released and dialyzed away (**Figure 3-10a**). Unsurprisingly, based on its low encapsulation efficiency, calcein was also the most rapidly released cargo, with 55% of the encapsulated calcein released after 96 hours. The two larger hydrophilic cargoes, dextran and ovalbumin, demonstrated 27% and 30% release, respectively. The lowest release was demonstrated by the highly hydrophobic DiD, with 21% released from BCNs in 96 hours. BCN formulations were very stable, demonstrating very little change in diameter over half a year of storage at room temperature (**Figure 3-10b**). This is in significant contrast to cubosomes, which are highly unstable in the absence of stabilizers.

PEG-*b*-PPS copolymers show oxidation responsive behavior due to the susceptibility of the sulfur atoms in the PPS chain to oxidation and resulting conversion to more hydrophilic sulfoxide and sulfone derivatives [204]. To assess the responsiveness of PEG-*b*-PPS BCNs to oxidation and the subsequent impact of this oxidation on controlled release of cargo, we performed degradation studies in the presence of a biologically relevant concentration of hydrogen peroxide (100 μM) [205] using DiD-loaded BCNs. In the presence of H_2O_2, 6% of DiD was released in the first 4 h, 61% by 24 h, and 100% by the end of the study (**Figure 3-10a**). The amount released in the first 4 hours is not significantly different from DiD release from BCNs in the absence of hydrogen peroxide, suggesting that the oxidation of BCNs within the first 4 hours is either negligible or has a negligible effect on release of hydrophobic cargo. To further confirm these results, BCNs were incubated with hydrogen peroxide and were observed for 4 days (**Figure 3-11a**). Incubation with hydrogen peroxide led to a noticeable loss of turbidity, typically indicative of a reduction in size of nanoparticles [43]. After 2 and 4 days of incubation, cryoTEM images revealed the majority of BCNs to have reassembled into micellar structures, which is consistent with an increase in the hydrophilic fraction of the copolymer and previously published results for oxidized PEG-*b*-PPS nanostructures (**Figure 3-11b,c**). This timescale matches up well with the oxidation-responsive DiD release observed in **Figure 3-10a**.

3.4.4. Loading Capacity of Polymersomes and Bicontinuous Nanospheres for Hydrophobic Cargo

The larger hydrophobic block length and aggregate volume of PEG_{17}-bl-PPS_{75} BCNs compared PEG_{17}-bl-PPS_{36} PS (75 propylene sulfide units compared to 36) led me to hypothesize that BCNs should be capable of loading larger quantities of hydrophobic cargo compared to PSs, on a per-particle basis. An additional consideration is that polymersomes maintain their morphology through the presence of a relatively thin single membrane. The stability of this membrane to the attempted loading of saturating concentrations of hydrophobic cargo has not been explored. BCNs, in contrast, appear to have a structure that is less susceptible to 'breaking' or 'popping' in the presence of more hydrophobic cargo. To test this,

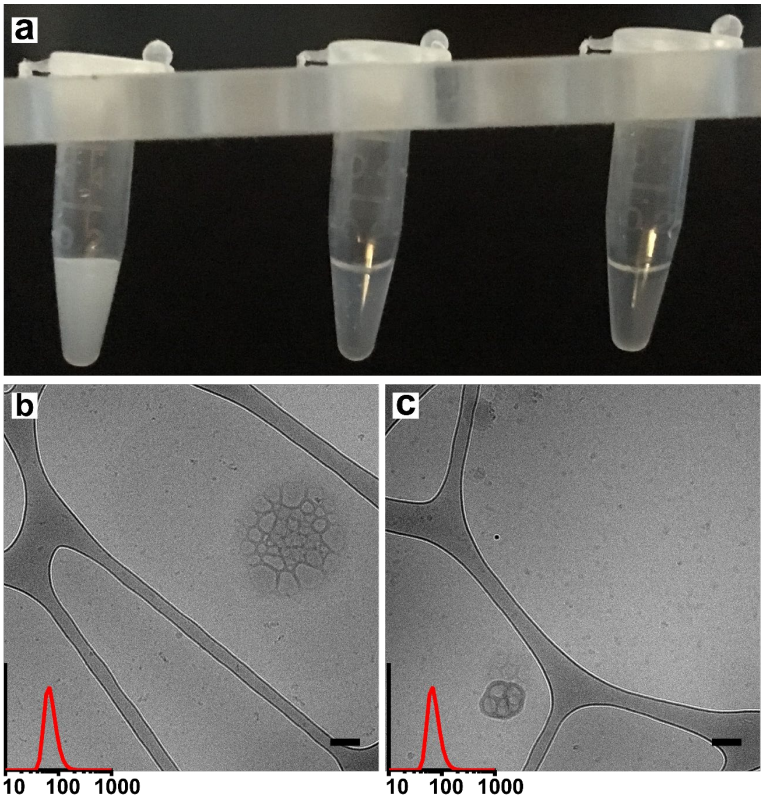

Figure 3-11. BCN degradation by hydrogen peroxide. (a) Macroscopic turbidity changes to BCN formulations after addition of hydrogen peroxide. BCNs incubated with hydrogen peroxide for 0 days (leftmost), 2 days (middle), and 4 days (rightmost). Included are cryoTEM micrographs of the oxidized BCN formulations after (b) 2 days and (c) 4 days of incubation. Scale bars are 100 nm, insets are DLS size distributions of the formulations. Adapted from [146] with permission from The Royal Society of Chemistry.

the hydrophobic loading and cellular internalization capacity of BCNs and PSs were compared using ethyl eosin, a hydrophobic fluorescent dye utilized in encapsulation efficiency experiment elsewhere in this chapter. In those encapsulation efficiency studies, I loaded ethyl eosin into PSs and BCNs at 0.25 and 0.5 weight % of the polymer mass, respectively. In this case, as I sought to compare the maximum hydrophobic loading capacity of PSs and BCNs, I chose a weight percentage of ethyl eosin 4-8 times greater than our previous work: 2 wt % ethyl eosin. Preliminary fluorescence measurements of BCN and PS formulations before and after removal of unencapsulated ethyl eosin suggested that both nanocarriers had similar levels of ethyl eosin encapsulation efficiency at 90-92%. However, the macroscopic turbidity of the 'polymersome' formulation was lower than usual, which lead me to suspect that the PS formulations were not forming the

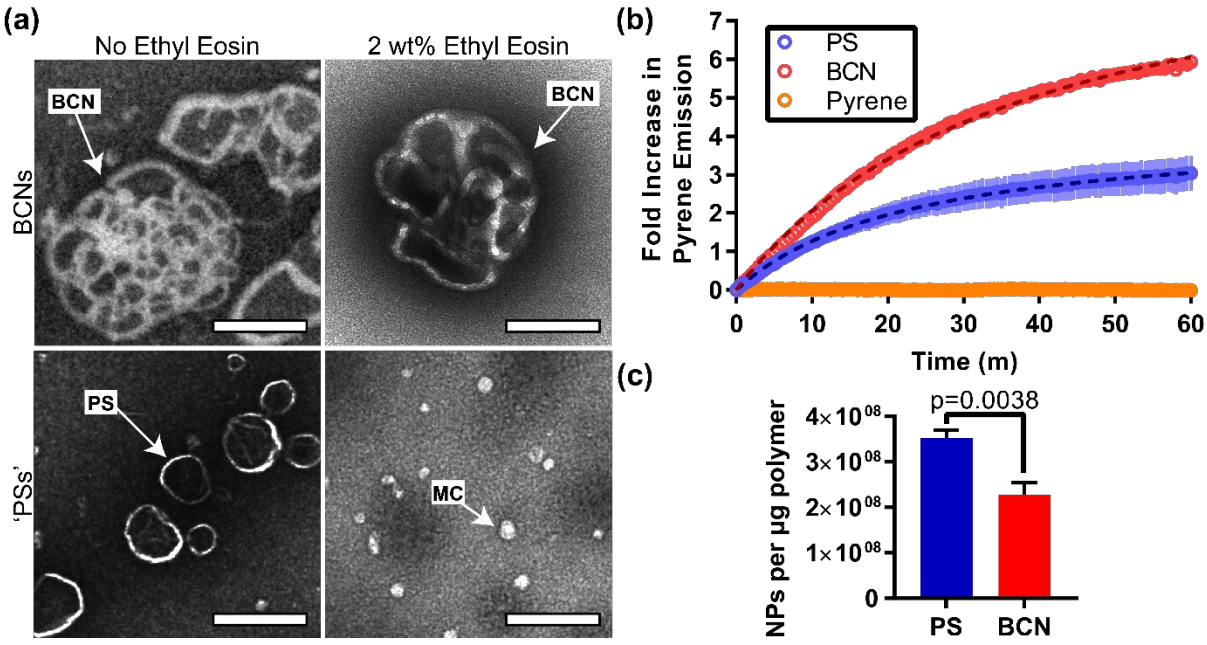

Figure 3-12. Comparative hydrophobic loading capacity of PSs and BCNs. (a) TEM images of PSs and BCNs with or without 2 wt % ethyl eosin loaded. The arrows and labels help identify example nanocarriers, MC = micelle. Scale bar = 200 nm. (b) Fold increase of pyrene fluorescence emission at 390 nm upon excitation at 331 nm in 1xPBS or in the presence of preformed BCNs or PSs. Error bars represent S.E.M., n = 3. (c) Particle number per microgram of polymer for PSs and BCNs, n = 3, Error bars = standard deviation (S.D.), p value determined by Welch's t-test. Adapted with permission from [222] © 2018 American Chemical Society.

typical PS morphology but were rather forming a disrupted morphology due to the overwhelming concentration of ethyl eosin. As ‘clear’ formulations have typically been micellar, I hypothesized that rather than forming ethyl eosin-loaded PSs, the high concentration of ethyl eosin forced the formation of micellar structures with PEG-*b*-PPS stabilized cores of ethyl eosin. To investigate my suspicions, I performed negative stain TEM on BCNs and PSs that were formed with or without ethyl eosin (**Figure 3-12a**). BCNs formed the same aggregate morphology with or without the presence of saturating concentrations of ethyl eosin, characterized by 200-300 nm structures with internal aqueous channels. PSs, however, demonstrated starkly different morphologies when comparing those loaded with ethyl eosin to those without. PSs formed in the absence of ethyl eosin demonstrate their characteristic vesicular morphology by TEM. PSs failed to form, however, in the presence of 2 wt % ethyl eosin. Rather, small micelle structures were found by TEM (**Figure 3-12a**), suggesting that the high concentration of ethyl eosin was sufficient to disrupt the proper formation of polymersomes, resulting instead in the formation of micelles. These results demonstrate that BCNs are capable of loading higher concentrations of hydrophobic compounds without altering their aggregate morphology in comparison to PSs.

It appeared that ethyl eosin, at high concentrations, interfered with PS formation during FNP. While this is in and of itself an interesting finding, it does not completely resolve the question of whether PSs or BCNs have differences in their hydrophobic loading capacity. To further investigate the comparative hydrophobic volume differences between BCNs and PSs, I adapted a standard assay for determining the critical micelle concentration (CMC) of amphiphiles using the hydrophobic fluorophore pyrene. The fluorescence emission intensity of pyrene changes depending on the surrounding solvent. At 390 nm, pyrene exhibits reduced emission intensity in aqueous environments and increased emission intensity in hydrophobic environments. This feature is useful for CMC measurements, as incremental amounts of the amphiphile can be added to aqueous pyrene until they reach their CMC and form micelles, loading the pyrene and increasing the fluorescent signal [206]. I reasoned that pyrene in aqueous solution would partition into the hydrophobic domains of assembled nanocarriers over time and that the process should be quantifiable by detecting an increase in fluorescence intensity. If BCNs do have increased capacity for hydrophobic compounds compared to PSs, exposing the nanostructures to a saturated pyrene solution

should result in a higher fluorescence intensity for the BCN-pyrene solution compared to the PS-pyrene solution over time, and both should outperform pyrene in the absence of added nanocarriers. Indeed, I found that BCNs saw a greater increase in fluorescence intensity in the pyrene solution by approximately twice as much as PSs (**Figure 3-12b**) after 1 h of mixing. This measurement was made at matching polymer concentrations in solution. However, per the same weight of polymer, PSs outnumber BCNs 1.5:1 (**Figure 3-12c**). This means that on a particle basis, BCNs were able to overcome a numerical disadvantage compared to PSs and still loading more pyrene in their extensive hydrophobic volume.

3.4.5. Codelivery of Hydrophobic and Hydrophilic Cargo to Cells *in vitro*

As demonstrated in section 3.4.1. (**Figure 3-7**), polymersomes are able to deliver both hydrophilic and hydrophobic cargoes simultaneously to cells *in vitro*. This advantage over micelles and filomicelles is hypothetically shared by BCNs, as they are able to load both classes of cargo as well. Due to the sparse literature on BCNs as delivery vehicles, there were no published reports on the *in vitro* simultaneous delivery of hydrophilic and hydrophobic cargo by BCNs. Since PSs are the polymeric standard for this type of dual delivery, I compared PSs and BCNs with regard to their loading and delivery of the hydrophilic protein fluorescein-tagged bovine serum albumin (FITC-BSA) and a hydrophobic dye, DiD (**Figure 3-13a**).

A comparison of the encapsulation efficiency of these two cargoes by BCNs and PSs demonstrated that BCNs were superior to PSs in loading both the hydrophilic and hydrophobic cargoes (**Figure 3-13b**). Differences in the hydrophilic encapsulation may be due to improved trapping of the protein within the aqueous pores of BCNs. These dual-loaded BCNs and PSs were incubated with RAW 264.7 cells. Cells were assessed for nanocarrier uptake after 30 minutes and once an hour every hour for 8 hours. Both BCNs and PSs were internalized rapidly by the cells, with clear signal present at the 30-minute mark. (**Figure 3-13c**). Also apparent from the contour plots is a correlation between DiD and FITC-BSA fluorescence. This is a consequence of stable ratiometric loading of the two cargoes within the nanocarriers, i.e. on average every nanocarrier internalized by a cell delivered a reliable ratio of DiD and FITC-BSA. Increasing amounts of nanocarriers were internalized over time, evidenced by the gradual increase in DiD MFI (**Figure 3-13d**). In contrast to that finding, FITC-BSA MFI peaked at 4 hours, a finding best explained

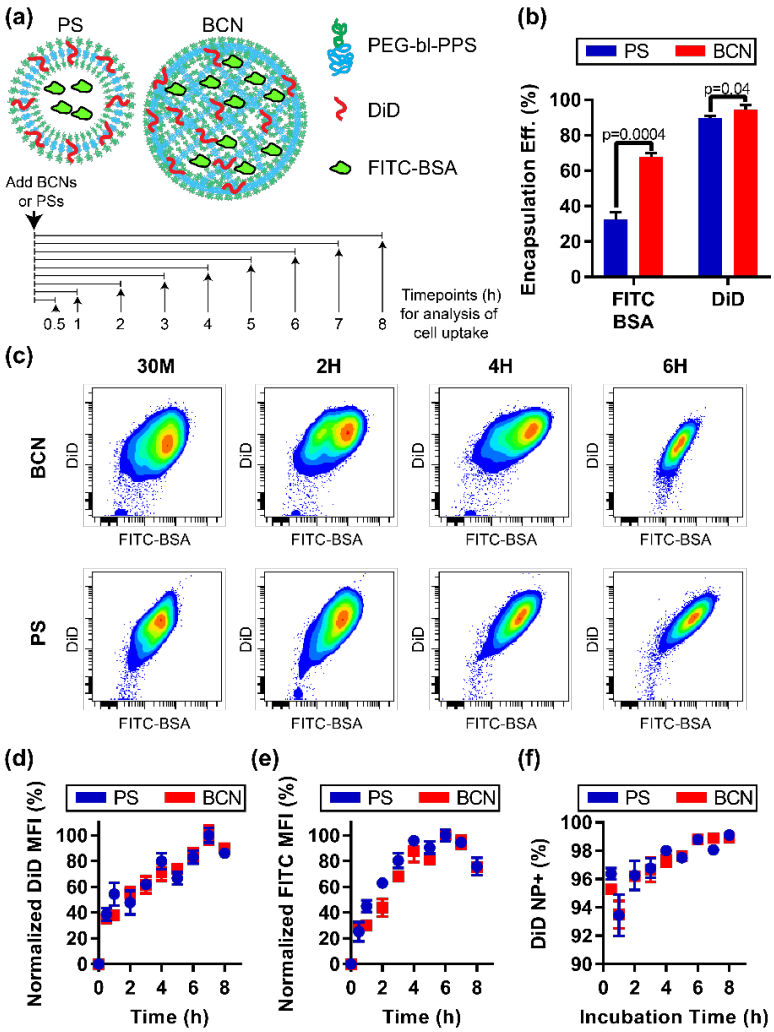

Figure 3-13. PS and BCN dual loading and in vitro uptake assay. (a) Overview of uptake assay of FITC-BSA/DiD dual-loaded PSs and BCNs by RAW 264.7 cells. (b) Encapsulation efficiency (percentage of cargo successfully loaded relative to total initial cargo) of FITC-BSA and DiD in PSs and BCNs when simultaneously loaded, n = 3 independent formulations, error bars = S.D. p values from the Holm–Sidak multiple t-test. (c) Representative contour plots from flow cytometry of RAW 264.7 cells incubated with PSs and BCNs for multiple timepoints. Normalized median fluorescence intensity (MFI) for (d) DiD and (e) FITC-BSA within cells after incubation with PSs and BCNs for increasing amount of time. (f) Percentages of cells that were PS or BCN positive, as determined by gating of the DiD channel. For (d)–(f), n = 6, error bars = S.D. Adapted with permission from [222] © 2018 American Chemical Society.

by a well-documented characteristic of FITC, which is its reduction in fluorescence as it traffics through the endolysosomal pathway [207] (**Figure 3-13e**). Cells continue to internalize more and more nanocarriers over the course of the 8 hours, but their initial uptake of nanocarriers is rapid and nearly ubiquitous. Over

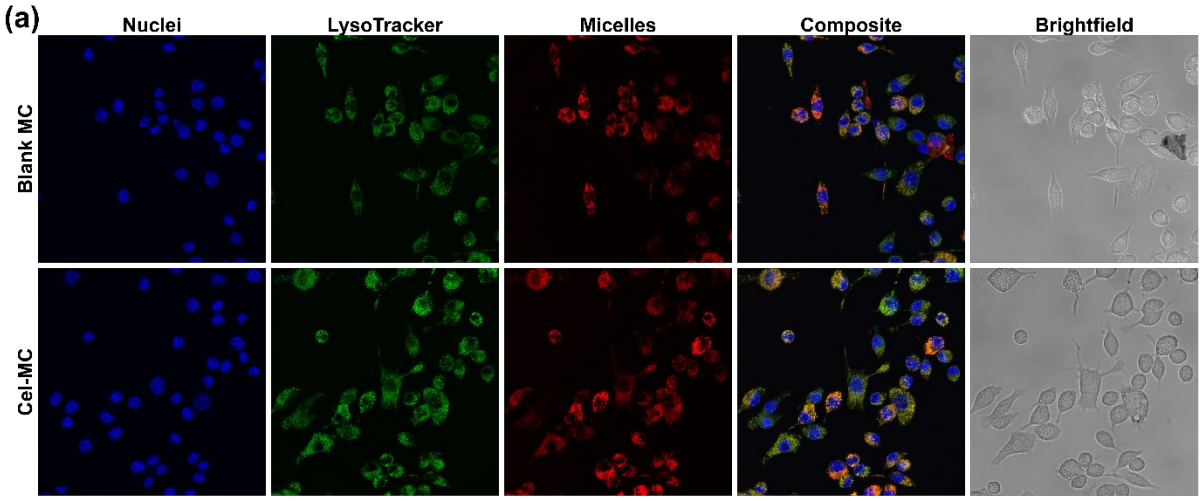

Figure 3-14. Subcellular localization of Cel-MC in RAW 264.7 cells. Confocal images of live RAW 264.7 cells incubated with a nuclear stain (blue) and a lysosomal stain (green). Cells were also incubated overnight with blank MC (top row) or Cel-MC (1 μg/mL celastrol, bottom row) labelled with DiI, a lipophilic dye. Composite and brightfield images are included to demonstrate colocalization of micelle and lysosome signal and cell morphology, respectively. Reproduced from [223] with permission from The Royal Society of Chemistry.

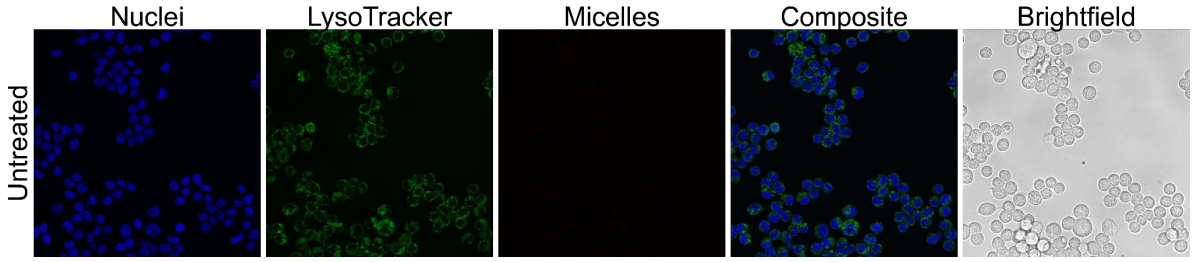

Figure 3-15. Control for fluorescent bleed through of lysotracker green. Confocal images of live RAW 264.7 cells incubated with a nuclear stain (blue) and a lysosomal stain (green). The red laser channel was utilized at the same power and filter set as for the DiI signal in micelles in Figure 3-14, to ensure there was no bleed through into the red channel by LysoTracker Green. Reproduced from [223] with permission from The Royal Society of Chemistry.

95% of cells were nanocarrier positive after just 30 minutes of incubation (**Figure 3-13f**). As such, the increase in MFI represents more uptake by cells that have already internalized nanocarriers, not the gradual uptake of nanocarriers by naïve cells. That said, by 8 hours of incubation nearly 100% of cells are nanocarrier-positive, demonstrating the ease with which PEG-*b*-PPS nanocarriers can deliver cargo to phagocytic cells *in vitro*.

3.4.6. Lysosomal Colocalization of Micelles, Polymersomes, and Bicontinuous Nanospheres

Some general subcellular localization data has been collected for PEG-*b*-PPS nanocarriers. PEG-*b*-PPS polymersomes are known to enter the endolysosomal pathway, where they can cause endosomal rupture and cytoplasmic release of cargo [45], albeit a triggered release by optical rupture. As demonstrated by Figure 3-7, I demonstrated that PEG-*b*-PPS polymersomes do indeed colocalize with lysosomal signal after internalization by BMDCs. Very recent work by another student in lab, Dina Kats, has demonstrated that PEG_{44}-*b*-PPS_{15}-ASF micelles colocalize with lysosomes after uptake by BMDCs [208].

The micelles that Kats et al. utilized were larger than typical PEG-*b*-PPS micelles (40 nm vs 20 nm in diameter) due to the presence of a covalently attached pH sensitive dye (ASF = acid-sensitive fluorophore). As micelles are the simplest PEG-*b*-PPS morphology and are the most promiscuously internalized by different cell types [121, 191], I sought to demonstrate their subcellular localization. My work with PEG-*b*-PPS micelles involved the loading of an anti-inflammatory small molecule, celastrol, which will be discussed in greater detail in Chapter 5. The subcellular localization of micelles was performed using celastrol-loaded micelles, as micellar delivery of celastrol was the primary focus of my micelle-related studies.

Celastrol-loaded and ‘blank’ micelles, both loaded with DiI for fluorescent detection of subcellular localization, were incubated with RAW 264.7 cells overnight and live confocal images were taken (**Figure 3-14**). Cells were labeled with LysoTracker Green and a nuclear stain (blue). The staining clearly demonstrates that micelles are co-localized with lysosomal signal. Some cells demonstrate no micelle signal but clear lysosomal signal, which shows that LysoTracker Green signal is not bleeding into the red channel, falsely contributing to the colocalization signal. To ensure that this is the case, a control set of

images was acquired using cells that were never incubated with micelles. These cells show no red fluorescent signal, despite the presence of LysoTracker Green (**Figure 3-15**).

Polymersomes and micelles of two sizes all appear to traffic through the endolysosomal pathway, ending up in lysosomes. The subcellular localization of BCNs had never been characterized, though it was highly likely that that morphology would also be localized similarly to the other PEG-*b*-PPS morphologies. BCNs were loaded with 10 kDa dextran conjugated to Texas Red and were incubated with RAW 264.7 cells. The cells and BCNs were incubated together for 2, 4, or 8 hours before confocal imaging. Cells were stained with LysoTracker Green and DAPI as a nuclear stain (**Figure 3-16**). As with the micelles, BCN

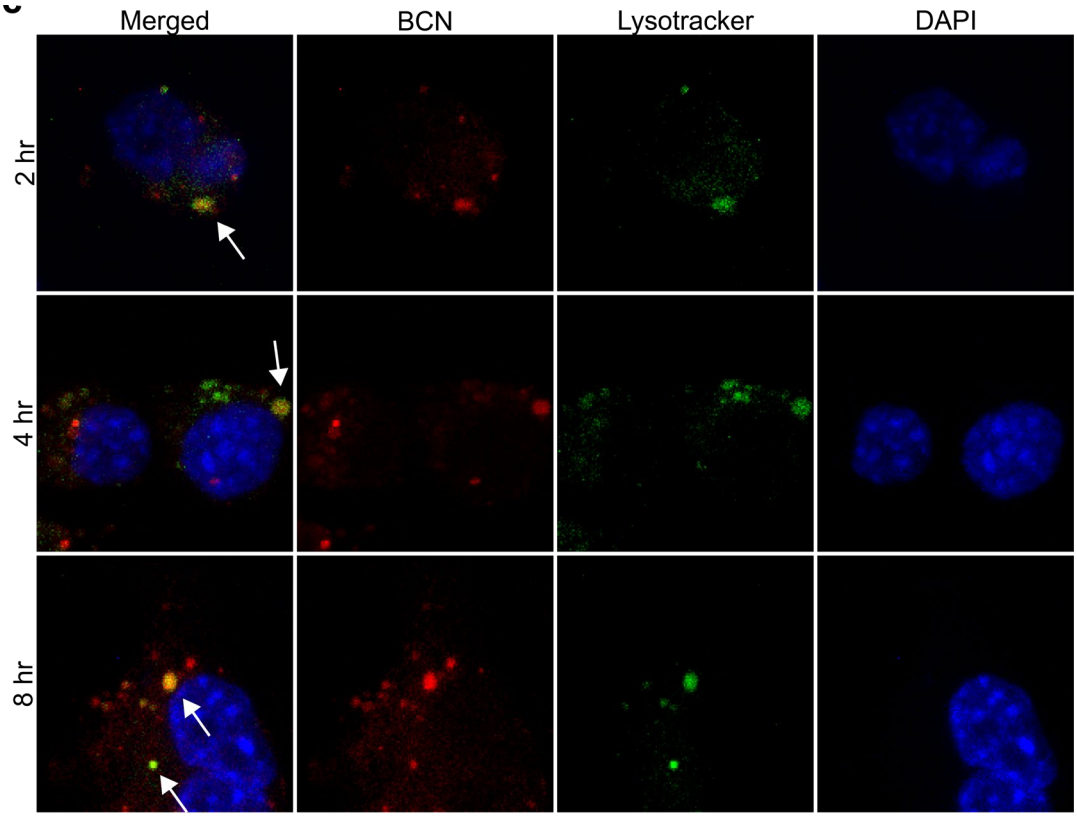

Figure 3-16. Subcellular localization of BCNs in RAW 264.7 cells. Confocal images of macrophages stained with lysosomal dye Lysotracker (green) and DNA dye DAPI (blue) following incubation with Texas Red labeled BCNs (red) for 2, 4, or 8 h. White arrows in the merged image point to examples of colocalization of Lysotracker and Texas Red signals, demonstrating endolysosomal uptake of BCNs. Adapted from [146] with permission from The Royal Society of Chemistry.

signal colocalized with lysosomes at all timepoints. There are, notably, punctae of both green and red fluorescence that are not colocalized. These represent lysosomes that do not contain BCNs and BCNs that are internalized but have not yet reached the lysosome. Most of the red (not colocalized) punctae are closer to the cell periphery, while matured lysosomes are typically perinuclear. The endolysosomal trafficking of PEG-*b*-PPS nanocarriers is beneficial for a number of delivery applications. For example, antigen display *via* MHCII requires the endolysosomal trafficking of antigen and adjuvant, both of which could potentially be loaded into PEG-*b*-PPS nanocarriers.

3.4.7. Loading and Delivery of Antigen and Adjuvant to BMDCs

To demonstrate the ability of BCNs to perform as delivery vehicles for antigen and adjuvant, I applied BCNs as a model nanoparticle vaccine formulation for the activation of bone marrow derived dendritic cells (BMDCs), which are phagocytes capable of initiating immune responses against antigenic molecular components of pathogens and thus key cellular targets during immunization. Activation of immunostimulation of pattern recognition receptors (PRRs) by pathogen associated molecular patterns (PAMPs) [209-211]. While protein and peptide antigens can be loaded within the aqueous channels of BCNs, common PAMPs, such as lipopolysaccharide (LPS) and the derivative monophosphoryl lipid A (MPL or MPLA), are well-suited for stable retention within the BCN hydrophobic volume. BMDCs are able to display peptide antigens on both MHCI and MHCII, with MHCI being loaded in the endoplasmic reticulum with peptides generated in the cytoplasm and MHCII being loaded in the endolysosome.

To demonstrate the functional dual delivery of hydrophilic and lipophilic payloads from PEG-*b*-PPS BCNs, an *in vitro* BMDC activation and antigen presentation assay was performed. In this study, BCNs were co-loaded with the model protein antigen ovalbumin (Ova) and TLR4 agonist MPL as an adjuvant using FNP and was incubated with BMDCs (**Figure 3-17a**). PEG-*b*-PPS polymersomes loaded with Ova and MPL was included in the study as a positive control. Dendritic cells, upon activation, produce several cell surface proteins to act as co-stimulatory signals for nearby T cells. Cell activation was quantified *via* flow cytometric assessment of expression level of these cell surface markers: CD80, CD86, and CD40. BMDCs were additionally analyzed for the surface presentation of the immunodominant antigenic peptide

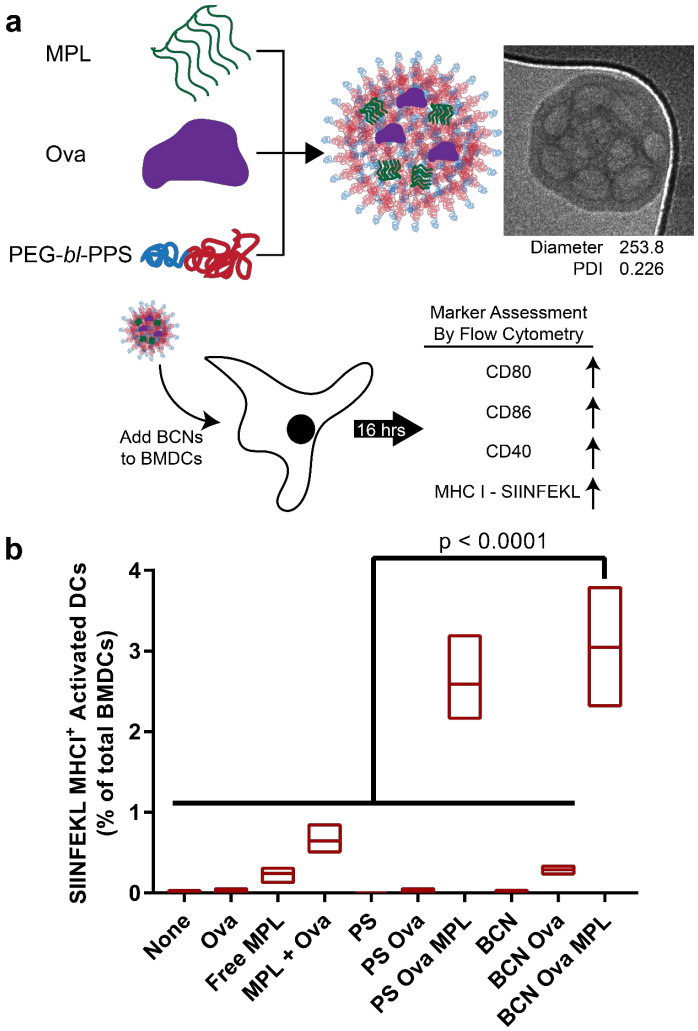

Figure 3-17. In vitro delivery of antigen and adjuvant to BMDCs using BCNs. (a) Schematic of the experimental process. TLR4 agonist MPL was loaded into BCNs with model protein antigen ovalbumin (Ova) by FNP. BCNs were incubated with BMDCs for 14 hours, which were then assessed for activation and antigen presentation by flow cytometry. (b) Activation of BMDCs by BCN formulations was determined by upregulation of cell surface markers CD80, CD86 and CD40. Antigen processing and presentation were determined using a fluorescent antibody specific for the SIINFEKL/MHCI complex. For comparison, polymersome (PS) formulations loaded with Ova and MPL were also tested. Floating bars represent min, mean, and max values, n = 3. Significance determined by 1-way ANOVA and Tukey's multiple comparisons test. Adapted from [146] with permission from The Royal Society of Chemistry.

fragment generated by the proteolytic cleavage of Ova by the proteasome within the cell cytosol. While BMDC activation is possible with just the delivery of adjuvant, the presentation of SIINFEKL occurs when Ova is successfully delivered into the cytosol for processing. In other words, delivery of ovalbumin protein to BMDCs is not sufficient to result in SIINFEKL presentation on MHCI. The only two ways that SIINFEKL can be produced and loaded onto MHCI is either 1) if ovalbumin protein 'escapes' from the endolysosomal pathway through some mechanism related to the destabilization of the PEG-*b*-PPS nanocarrier or 2) if SIINFEKL is 'cross-presented' by the BMDC, a poorly understood cell-specific mechanism by which endolysosomal antigens can be presented on MHCI [212].

Interestingly, BCNs loaded with Ova and MPL showed significantly greater SIINFEKL/MHCI surface presentation on BMDCs compared to all other control groups ($p < 0.0001$), outperforming free antigen and adjuvant added into the cell culture medium (**Figure 3-17b**). There was no statistical difference observed between Ova-MPL loaded BCNs and PSs. BCNs loaded with only Ova and no MPL neither activated cells nor resulted in antigen presentation, which agrees with literature signifying the requirement of adjuvant for improved activation of BMDCs. This also indicates that BCNs themselves are non-immunogenic and non-inflammatory *in vitro*. Furthermore, the enhanced SIINFEKL/MHCI expression demonstrates that BCNs can either promote endosomal escape of encapsulated payloads or allow for cross-presentation to occur. These results indicate FNP can be used to rapidly assemble BCNs and load them with antigen and adjuvant that in turn can be efficiently delivered to the cytosol of BMDCs. The presence of high internal surface area, extensive hydrophobic domains and aqueous internal channels allow BCNs to load and deliver molecules without the need for chemical conjugation that can modulate or decreases their activity.

3.4.8. *In vitro* Activation of RAW 264.7 Cells with Adjuvant-Loaded BCNs

MPL represents only one potential adjuvant that can be loaded in BCNs to stimulate immune cells. Different molecules can stimulate different PRRs, resulting in differential transcriptional activation and production of different cytokines. PEG-*b*-PPS nanocarriers themselves are non-immunogenic *in vitro*. To further explore the ability of BCNs to activate immune cells when loaded with PAMPs, I loaded BCNs *via*

FNP with hydrophobic molecules: trehalose dibenhenate (TDB), a synthetic mimic of a tuberculosis adjuvant; nigericin, a small molecule activator of the cytoplasmic NLRP3 inflammasome; MPLA, which was used in the ovalbumin BMDC experiment and which activates TLR4-MyD88 signaling; CL-429, a synthetic compound which activates both TLR and NOD signaling. I also tested unloaded BCNs and BCNs co-loaded with both MPLA and CL-429, but in half the amount of each compared to the singly loaded BCNs. RAW 264.7 cells or PMA-primed THP-1 cells were incubated with the BCN formulations for 16 hours or were treated with a positive control (endotoxin) or a negative control (endotoxin-free water). The supernatant of the cells was collected and tested *via* ELISA for the presence of two cytokines, TNF-α and IL-1β (**Figure 3-18**). Both cytokines are pro-inflammatory, but their production can be induced by independent pathways.

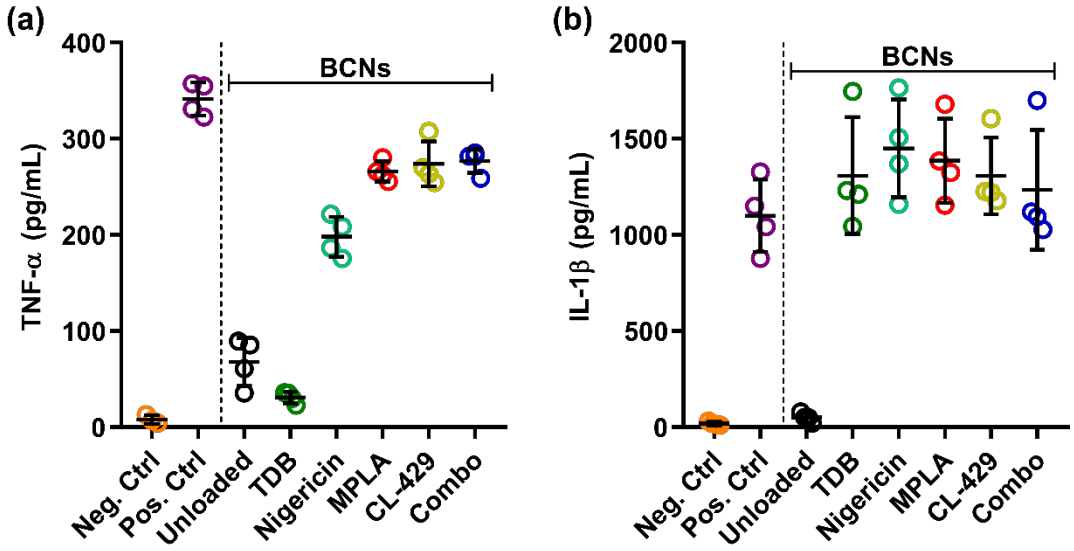

Figure 3-18. Cytokine secretion by myeloid cells after stimulation by adjuvant-loaded BCNs. (a) ELISA of TNF-α secretion from RAW 264.7 cells after a 16h incubation with BCNs loaded with: trehalose dibenhenate (TDB), nigericin, monophosphoryl lipid A (MPLA), CL-429, or a combination of MPLA and CL-429. As a positive control cells were treated with LPS and as a negative control cells were treated with endotoxin-free 1xPBS or were treated with BCNs that were not loaded with any adjuvant. (b) ELISA of IL-1β secretion from PMA-primed THP-1 cells after a 16h incubation with BCNs loaded as described for (a). All data points shown in the graphs, n=4. Horizontal bar marks the mean of the data, and error bars represent the s.d.

Unloaded BCNs did not induce cytokine secretion, confirming the results from the BMDC activation assay in **Figure 3-17**. All adjuvant-BCN formulations induced IL-1β secretion but, demonstrating the usefulness of careful selection of adjuvants for delivery, TDB did not induce TNF-α production and nigericin showed reduced production compared to MPLA and CL-429. The combination of MPLA and CL-429 displayed the same level of secretion of both cytokines as the two separate adjuvants (which were loaded at double the concentration). This preliminary study demonstrates that BCNs can be effectively used to deliver pro-inflammatory molecules, but also that the combinatorial selection of these molecules could result in complex and engineerable combinations of cytokine secretion profiles.

3.4.9. Cell Population Biodistribution in Non-Human Primates

The non-immunogenicity of PEG-*b*-PPS nanocarriers *in vitro* is an important finding for the eventual translation of the nanocarriers into the clinic. However, several findings *in vitro* and in mice first need to be recapitulated in a more closely applicable model, such as in non-human primates. As demonstrated in **Figure 2-15**, I was able to scale up the production of nanocarriers, particularly polymersomes, by utilizing FNP as the fabrication method. The cellular biodistribution of polymersomes after IV administration has been elucidated in mice, as discussed in the introduction of this chapter. However, there are many biological factors that differ between mice and primates, and it was critical that the cellular biodistribution be repeated in non-human primates.

Crab-eating macaques were administered polymersomes for a month, with the final injection occurring the day before sacking. Polymersomes were loaded with DiD for fluorescent tracking of their uptake by cell populations. After sacking, kidneys, livers, lymph nodes, and spleens were processed for flow cytometry. For all organs, saline controls were used to determine the baseline (background autofluorescence level) of the respective tissues. The lymph nodes (axillary, inguinal, and mesenteric) showed minimal uptake of polymersomes when comparing saline and polymersome injected primates. Only in the axillary lymph nodes were there specific cell populations that showed significant polymersome uptake, namely macrophages and NK cells (**Figure 3-19**). It is not unexpected that lymph node uptake would be low or undetectable 24 hours after injection, due to the intravenous route of administration.

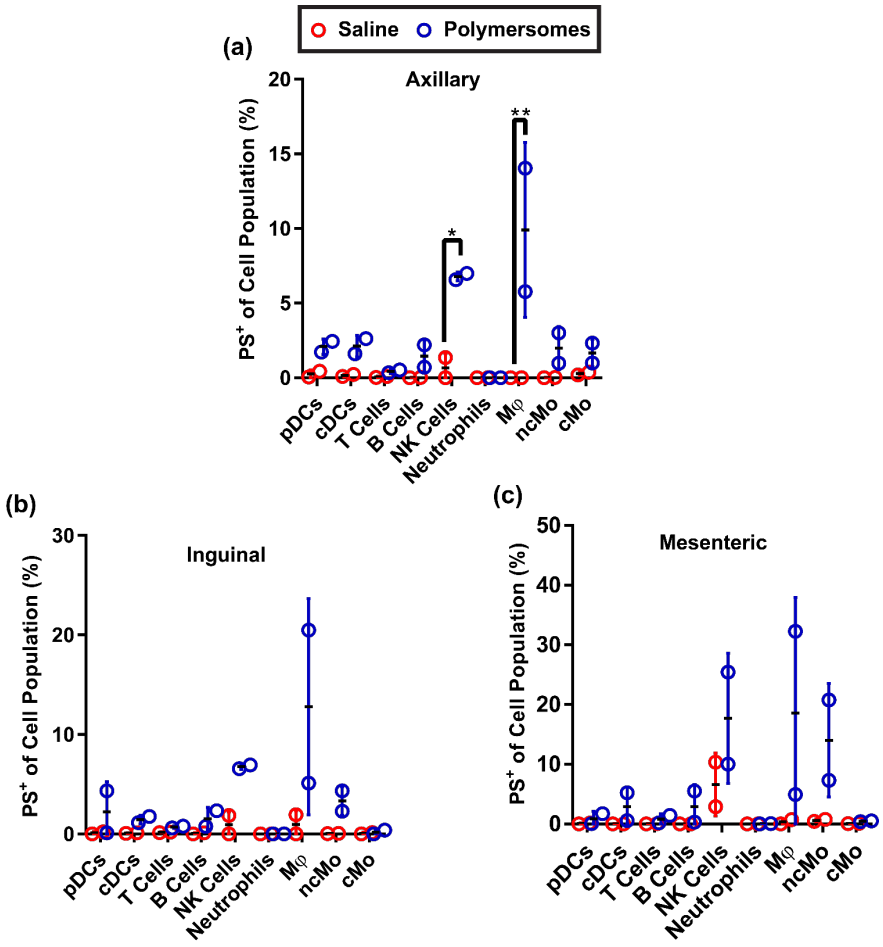

Figure 3-19. Flow cytometric analysis of polymersome uptake in *Macaca fascicularis* lymph nodes. PS uptake in cells as a percentage of that cell population within the (a) axillary, (b) inguinal, and (c) mesenteric lymph nodes of macaques after 4 weeks of administration, n=2 for each treatment error bars are s.d. * $p<0.01$, ** $p<0.001$, *** $p<0.0001$, significance determined by Tukey's multiple comparisons test. Plasmacytoid dendritic cells (pDCs): CD45+ CD3- CD20- CD14- HLA-DR+ CD123+ CD1c-; classical dendritic cells (cDCs): CD45+ CD3- CD20- CD14- HLA-DR+ CD123-; T Cells: CD45+ CD3+, B Cells: CD45+ CD3- CD19+; NK Cells: CD45+ CD3- CD19- CD16+ CD56+; Neutrophils: CD45+ CD3- CD19- CD56- CD14 low CD49d-; classical monocytes (cMo): CD45+ CD3- CD19- CD14+ CD49d+ CD16-; non-classical monocytes (ncMo): CD45+ CD3- CD19- CD14+ CD49d+ CD16+ CX3CR1+; macrophages (Mφ): CD45+ CD3- CD19- CD14+ CD49d+ CD16+ CX3CR1-. Figure reprinted with permission from [173] © 2018 Springer.

Yi et al demonstrated that IV administration of PSs resulted in uptake in the spleen and kidneys in mice [121]. I therefore performed flow cytometry to determine if similar cellular uptake of polymersomes by MPS cells in the spleen and kidneys also occurred in NHP. In both organs many cell populations saw high levels of uptake. Polymersome uptake was determined for each population of cells, and the percentage of cells of that population that were positive for polymersome fluorescent signal were: plasmacytoid dendritic cells (spleen – 68%, kidneys – 71%), classical dendritic cells (spleen – 40%, kidneys – 27%), macrophages (spleen – 96%, kidneys – 76%), non-classical monocytes (spleen – 72%, kidneys – 30%), and NK cells (spleen – 46%, kidneys – 89%) (**Figure 3-20**). In kidneys (**Figure 3-20b**), but not the spleen (**Figure 3-20a**), B cells showed significant uptake (56% of B cells positive for polymersome signal). In the spleen, of the three major subsets of dendritic cells, pDCs and cDC1s showed significant polymersome uptake (**Figure 3-20c**), while cDC2s were not. This high uptake of polymersomes by dendritic cells, particular plasmacytoid dendritic cells, is very similar to the uptake pattern of PEG-*b*-PPS polymersomes seen in mice [121]. In mice, >80% of pDCs and 20-40% of cDCs were positive for PS signal. Additionally, effector T cell subpopulations were also positive for polymersome signal (**Figure 3-20d**). Some differences between the previous mouse study and this primate study do exist – in the work in mice, macrophages demonstrated a more modest uptake of polymersomes (~40%), while a significantly greater portion of the population internalized polymersomes here.

The liver is a major MPS organ and in mice there was considerable uptake of PEG-*b*-PPS polymersomes by immune cells in the liver. ~75% of macrophages (F4/80+ cells) in the liver of mice had taken up polymersomes 24 hours after IV injection. Cells in the liver of non-human primates also demonstrated uptake of polymersomes (**Figure 3-20e**). This uptake of polymersomes in CD45+ CD3- CD19- (non-lymphoid immune cells) becomes significant as a percent of the population when gating further for macrophages and monocytes in the liver (CD14+ CD16+ CD45+ CD3- CD19-). 25% of macrophages and monocytes in the liver were positive for polymersome signal, reaffirming the role the liver plays as a major MPS organ and route of clearance for nanoparticles such as polymersomes. This uptake is much lower than the uptake seen in mice previously. Uptake for other polymeric nanoparticles, such as PLGA nanoparticles administered to rats [213], is also typically much higher than 25%. Neither the PLGA study

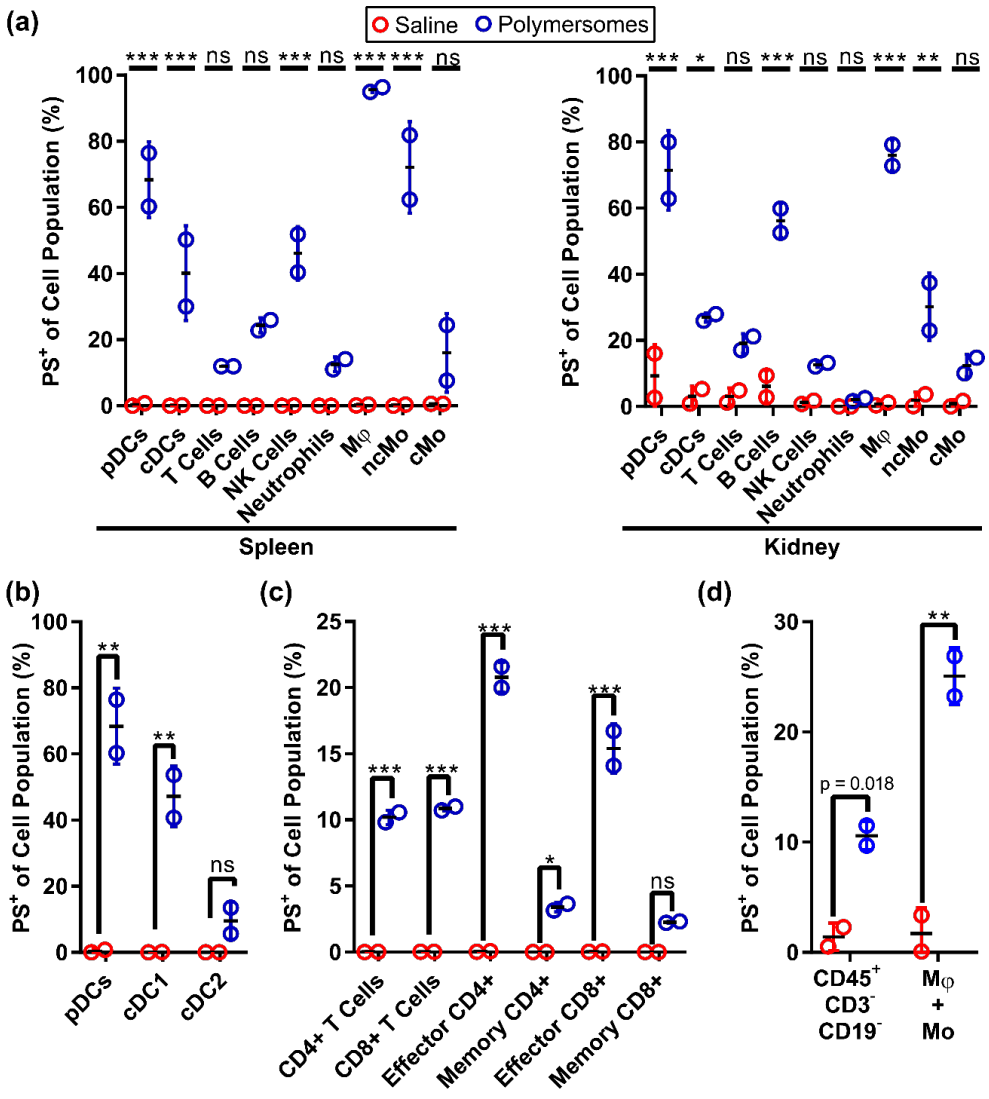

Figure 3-20. Characterization of polymersome uptake in *Macaca fascicularis* by flow cytometry. PS uptake in cells as a percentage of that cell population within the (a) spleen and (b) kidneys of NHPs after 4 weeks of administration, n=2 for each treatment error bars are s.d. Plasmacytoid dendritic cells (pDCs), classical dendritic cells (cDCs), T Cells, B Cells, NK Cells, Neutrophils, classical monocytes (cMo), non-classical monocytes (ncMo), macrophages (Mφ). PS uptake in (c) dendritic cell subsets and (d) T cell subsets within NHP spleens, n=2 error bars are s.d. (e), PS positive cells as a percentage of their immune cell population in non-T cell non-B cell immune cells (CD45+ CD3- CD19-) and macrophages and monocytes (CD45+ CD3- CD19- CD14+ CD49d+) in the NHP liver. n=2 error bars are s.d. Figure reprinted with permission from [173] © 2018 Springer.

nor the mouse study in Yi et al involved repeated administrations of nanoparticles, which was the case for this primate study and may account for some of the difference. Additionally, rodent and primate hepatic clearance rates often differ for small and macromolecular drugs, so it is possible that this difference also applies to nanocarriers [214, 215]. Due to a paucity of nanoparticle biodistribution studies comparing rodents and NHP, it is difficult to draw immediate conclusions as to the difference in uptake. Work using iron oxide nanoparticles found that their biodistribution in the liver of mice and NHP were similar up to 4 hours post injection [216], though these iron oxide nanoparticles were significantly smaller than the PEG-*b*-PPS polymersomes used in this study, making it difficult to draw a direct comparison. A similar study, using repeated administrations of MRI-contrast polymersomes, may provide more insight in the future.

Figure 3-20 displays polymersome uptake as measured by the percentage of polymersome-positive cells out of any particular cell population. What is not apparent from **Figure 3-20**, however, is the relative frequency of any given cell population. This can give an artificially inflated view of what populations contributed the most to nanocarrier uptake and clearance in a given organ. **Figure 3-21** therefore shows the uptake of polymersomes by each cell subset relative to total cell number. Classical monocytes in the spleen were a much larger fraction of the overall monocyte population compared to non-classical monocytes and took up more total polymersomes, shown by the red compared to blue in the middle pie chart of **Figure 3-21**, a much higher percentage (72% versus 16%) of non-classical monocytes were

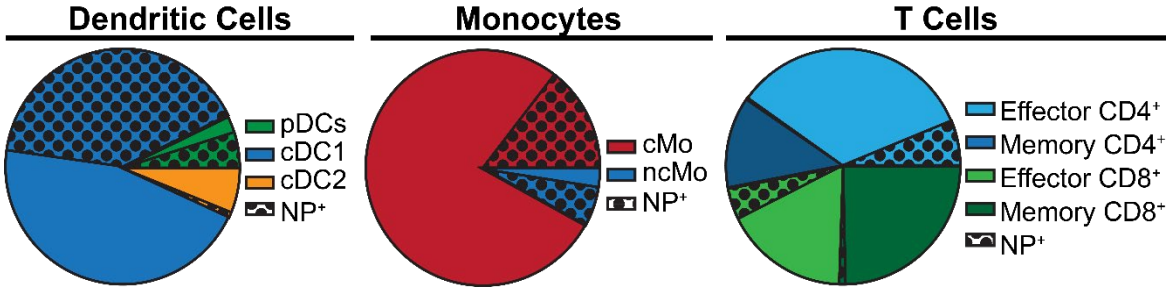

Figure 3-21. Scaled polymersome uptake by subpopulation size. Pie charts of cell subsets as a fraction of their parent cell type, labeled above the graphs. Overlaid dotted texture represents the fraction of those cells that were PS positive. Data only shown for the spleens of NHPs treated with polymersomes, mean value of n = 2 animals. Figure reprinted with permission from [173] © 2018 Springer.

targeted. As such, the dotted area (polymersome uptake positive) was larger for the classical monocytes compared to the non-classical. Of note, very low percentages of total T cell populations associated with polymersomes. Splenic plasmacytoid dendritic cells represented only 8.3% of the total dendritic cell population, but 68% were found to be positive for polymersomes. This was a 20% increase in the percentage of targeting over the other two dendritic cell subsets combined (**Figure 3-20c**), suggesting PEG-*b*-PPS polymersomes may be useful for delivery to and modulation of pDCs. By number of cells, however, cDC1s were delivered to in greater numbers.

3.4.10. Comparative Organ and Cell Population Biodistribution of Polymersomes and Bicontinuous Nanospheres in Mice

Polymersomes had, therefore, had their biodistribution analyzed in both mice and non-human primates. Micelles and filomicelles had both been characterized in mice as well. However, bicontinuous nanospheres had not yet been characterized *in vivo* in any model organism. As polymersomes had been characterized the most and was the most similar PEG-*b*-PPS nanocarrier to bicontinuous nanospheres, they were used in a comparative study examining the organ and cellular biodistribution of BCNs after IV administration in mice.

PEG-*b*-PPS polymer of f_{PEG} values that form PSs and BCNs (0.25 and 0.12, respectively) were synthesized and conjugated to DyLight 755 dye through a maleimide-thiol Michael addition. This fluorophore allows for IVIS quantification of nanocarrier uptake in the whole organ and allow the flow cytometric analysis of cell population uptake. These nanocarriers were administered by tail-vein injection and mice were sacked after 4 and 24 hours. The liver, spleen, lungs, and kidneys of mice were imaged ex vivo *via* IVIS imaging to determine uptake of PSs and BCNs (**Figure 3-22**). Representative fluorescence images of the organs 4 hours after IV injection show differences between BCN and PS distribution (**Figure 3-22a**). PSs show higher liver and lower spleen uptake compared to BCNs. The two morphologies show similar kidney uptake and BCNs show higher lung uptake than PSs. While it appears from the images that polymersomes did not have lung uptake, this is an artifact of the fluorescence being placed on a global scale rather than on a per-mouse scale, which is more informative with relation to comparative distribution

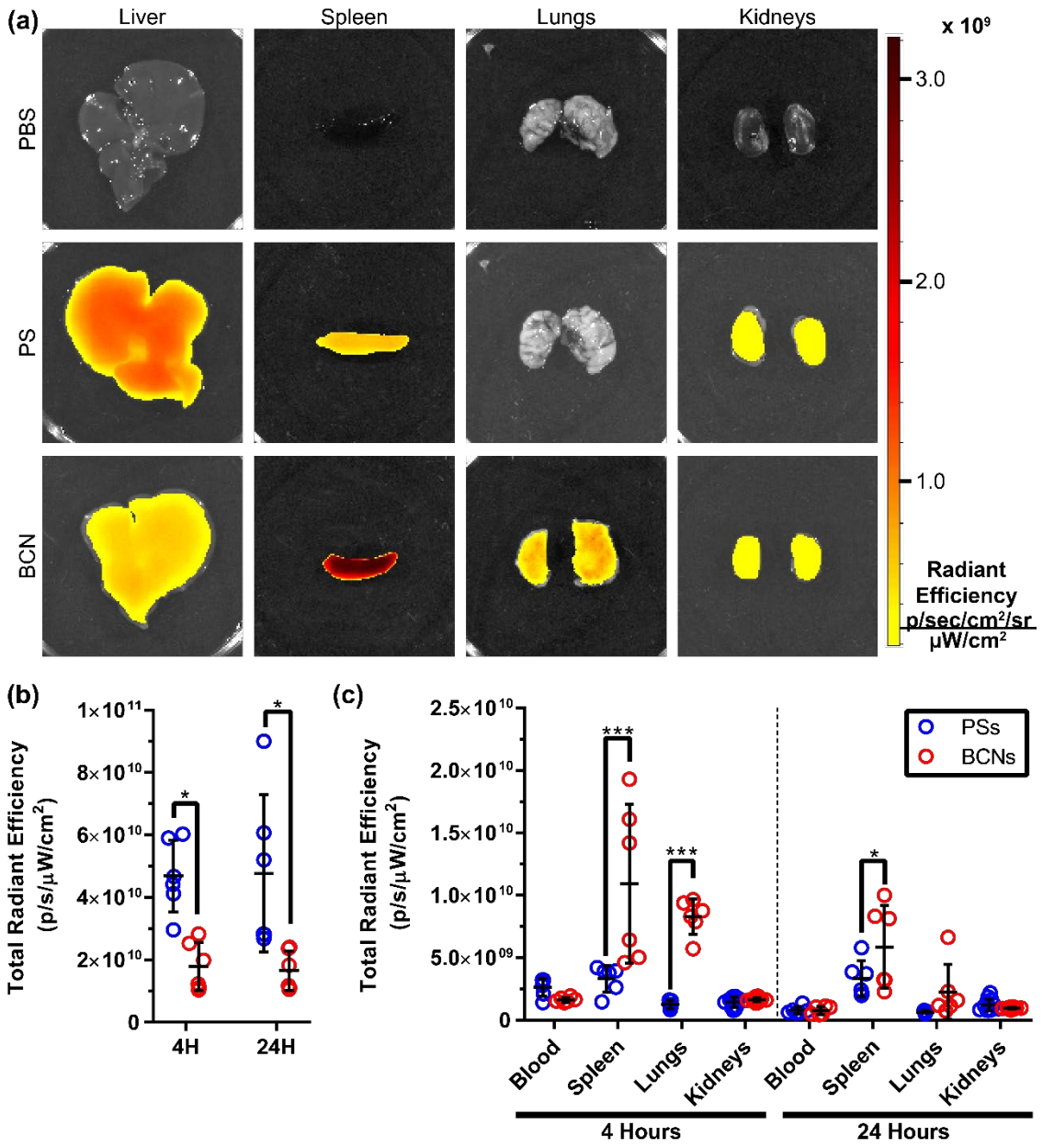

Figure 3-22. IVIS organ-level biodistribution of PSs and BCNs. (a) Representative IVIS images for mouse organs harvested 4 h post IV injection of PBS, PSs, or BCNs. Quantification of radiant efficiency of PS and BCN fluorescent signal in the (b) liver and (c) other organs at 4 and 24 h post IV injection. n = 6 for all organs, 12 points plotted for kidneys representing quantification for the right and left kidneys. Error bars = S.D., significance determined *via* Sidak's multiple comparisons test, * $p < 0.001$ and *** $p < 0.0001$. Adapted with permission from [222] © 2018 American Chemical Society.

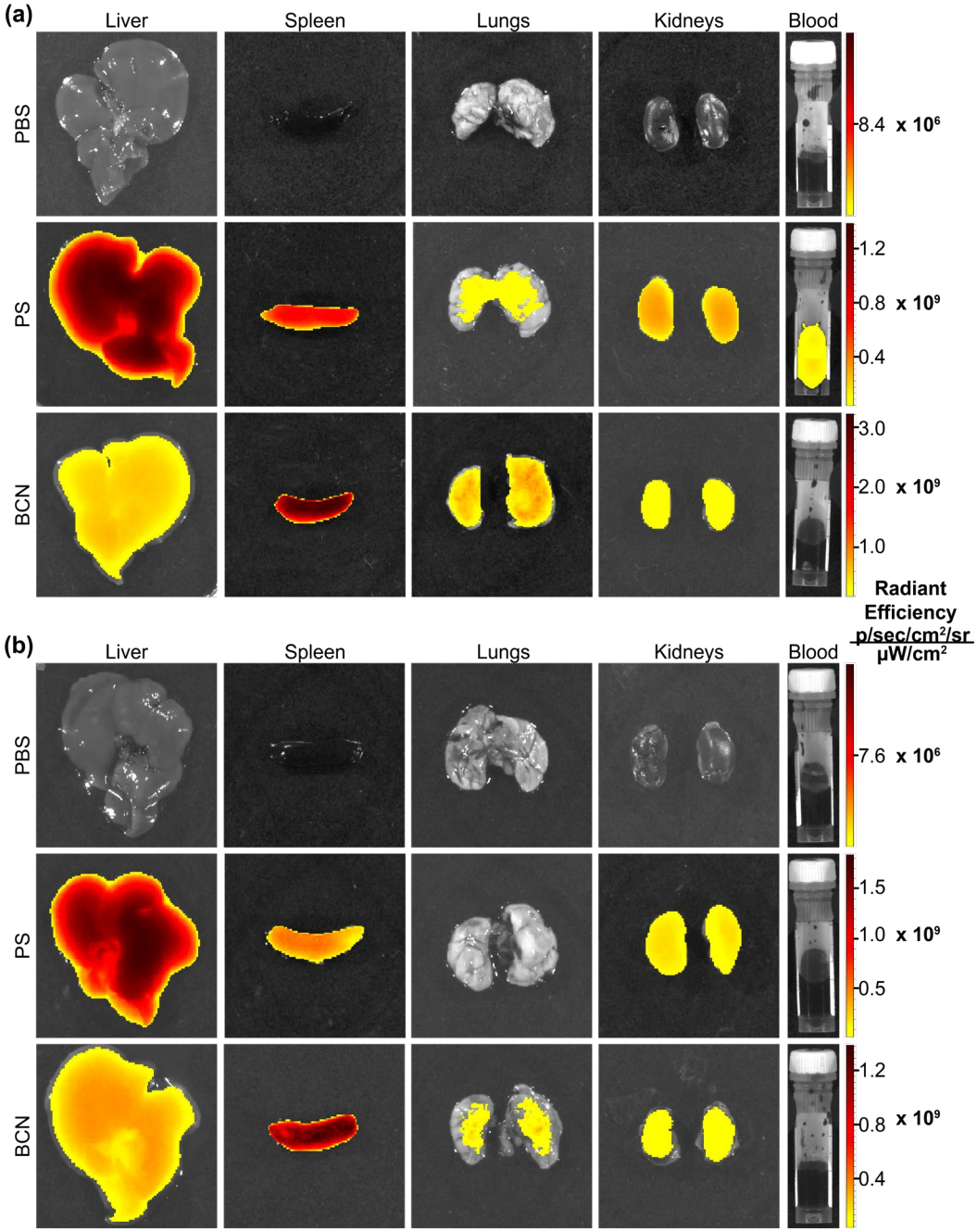

Figure 3-23. IVIS organ-level biodistribution of PSs and BCNs 4 and 24 H post IV injection. Representative IVIS images for organs harvested from a PBS, PS, or BCN treated mouse, (a) 4 h or (b) 24 h post IV injection. Each representative mouse is set to its own radiant efficiency scaling, displayed on the far right of each row. Adapted with permission from [222] © 2018 American Chemical Society.

between organs from a single mouse. Images scaled in this alternative fashion are available in **Figure 3-23**. Quantification of the radiant efficiency in the organs concur with the qualitative trend evidenced by the

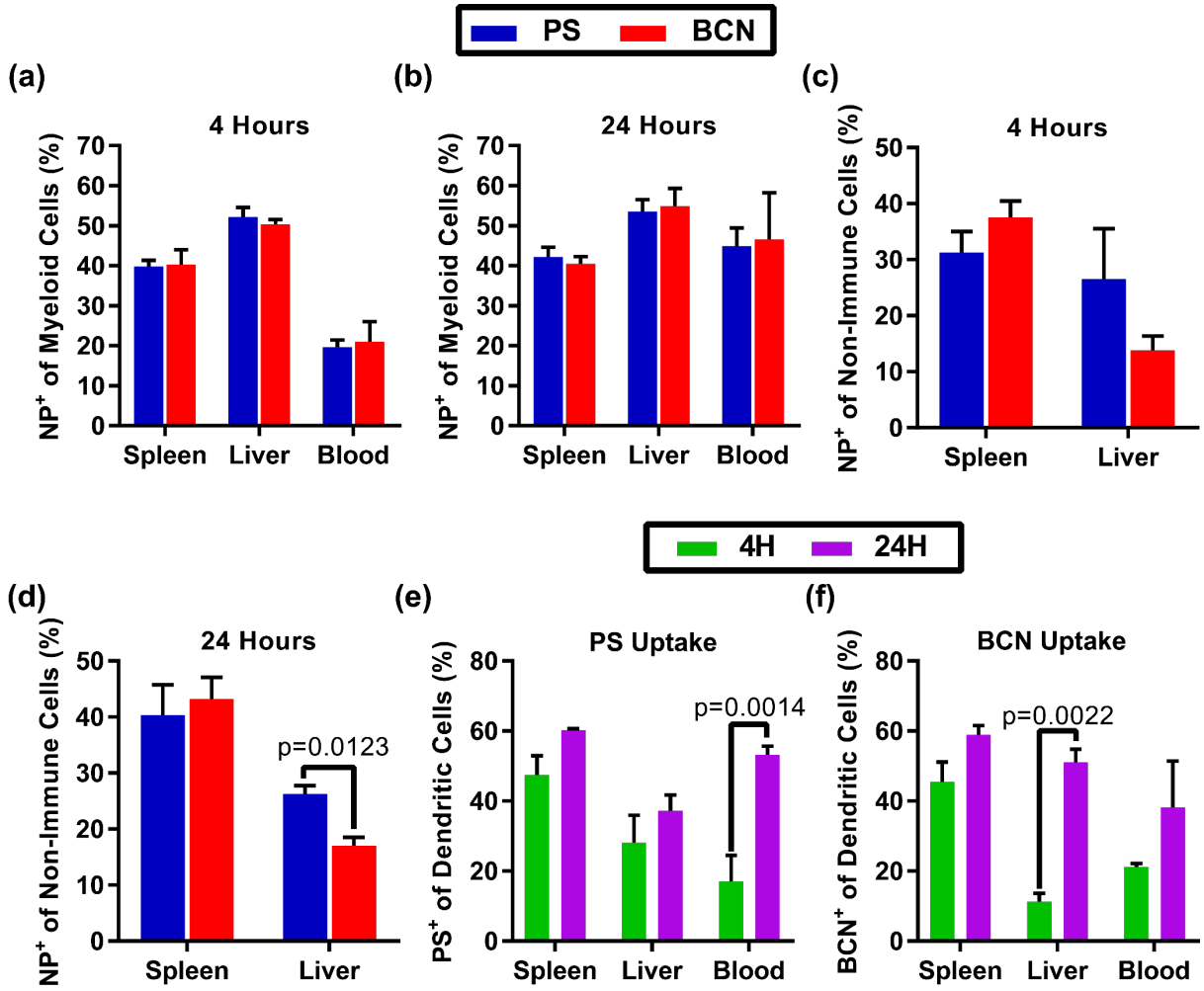

Figure 3-24. Flow cytometric assessment of cell population uptake of PSs and BCNs after IV injection. Nanoparticle uptake of PSs and BCNs by $CD45^+$ myeloid cells at (a) 4 h and (b) 24 h post IV injection and by $CD45^-$ cells at (c) 4 h and (d) 24 h post IV injection. Nanoparticle positive (NP^+) myeloid cells were identified as $CD45^+$ $CD3^-$ $CD19^-$ $NK1.1^-$$Ly\text{-}6G^-$. Dendritic cell (DC) uptake of (e) PSs and (f) BCNs, comparison of percentage of DCs that were nanoparticle positive at 4 vs 24 h post injection. Dendritic cells were identified as $CD45^+$ $CD3^-$ $CD19^-$ $NK1.1^-$ $Ly\text{-}6G^-$ $F4/80^-$ $CD11c^+$. For all graphs, significance determined using Holm–Sidak multiple *t*-tests, *p* values shown in graph. Error bars = S.E.M., *n* = 3. Adapted with permission from [222] © 2018 American Chemical Society.

IVIS images. PSs were taken up by the liver by a greater amount than BCNs at both timepoints (**Figure 3-22b**). BCNs were taken up by the spleen more than PSs at both timepoints and were present in the lungs more than PSs at the 4-hour timepoint, though this presence was transient (**Figure 3-22c**).

These organs have high levels of immune cells and I sought to uncover what immune cell populations were responsible for the uptake of BCNs. Flow cytometry of cells from the organs of IV injected mice revealed that large numbers of myeloid cells internalized BCNs and PSs in the spleen, liver, and blood of the mice at both 4 (**Figure 3-24a**) and 24 hours (**Figure 3-24b**). The percentage of myeloid cells positive for PSs or BCNs were not significantly different from one another. This lack of significant differences was borne out across different myeloid subpopulations as well (**Figure 3-25**). However, the organ-level data suggested that PSs were taken up more in the liver than BCNs. If so, what cell population was responsible for the difference? Examination of non-immune cells, likely a mix of liver sinusoidal endothelial cells and hepatocytes, revealed a significant increase in PS-positive cells compared to BCN-positive cells at 24 hours post-injection (**Figure 3-24c,d**). The largest changes over time occurred in the blood for PSs and the liver for BCNs, with large increases for each between the 4- and 24-hour timepoints. Overall, the clear trend from the PS and BCN cell population uptake was that the two morphologies showed very similar immune cell uptake (**Figure 3-26**).

3.4.11. Gradual SC Release of BCNs Tailored by MPLA Incorporation

The three other PEG-*b*-PPS morphologies besides BCNs had already had their biodistribution after subcutaneous injection characterized. I wanted to examine whether BCNs had significant uptake in the draining lymph nodes and/or spleen after subcutaneous injections. As a preliminary study, I injected fluorescent BCNs subcutaneously in mice and examined the gradual diminishment of fluorescent signal from the site of injection using IVIS. The rationale was to understand the kinetics of BCN diffusion from the site of injection to know when to sack the mice to examine uptake in the lymph nodes and spleen. Examination of the diffusion of micelles from the site of injection showed that 88% of micelle signal left the site of injection after 3 hours (**Figure 3-27**). Expecting a similar rate of diffusion, I examined the same release curve for BCNs. However, I found that BCNs left the site of injection much more slowly. After a

burst ‘release’ of 25% of signal in the first day, BCN signal at the site of injection was only diminished by

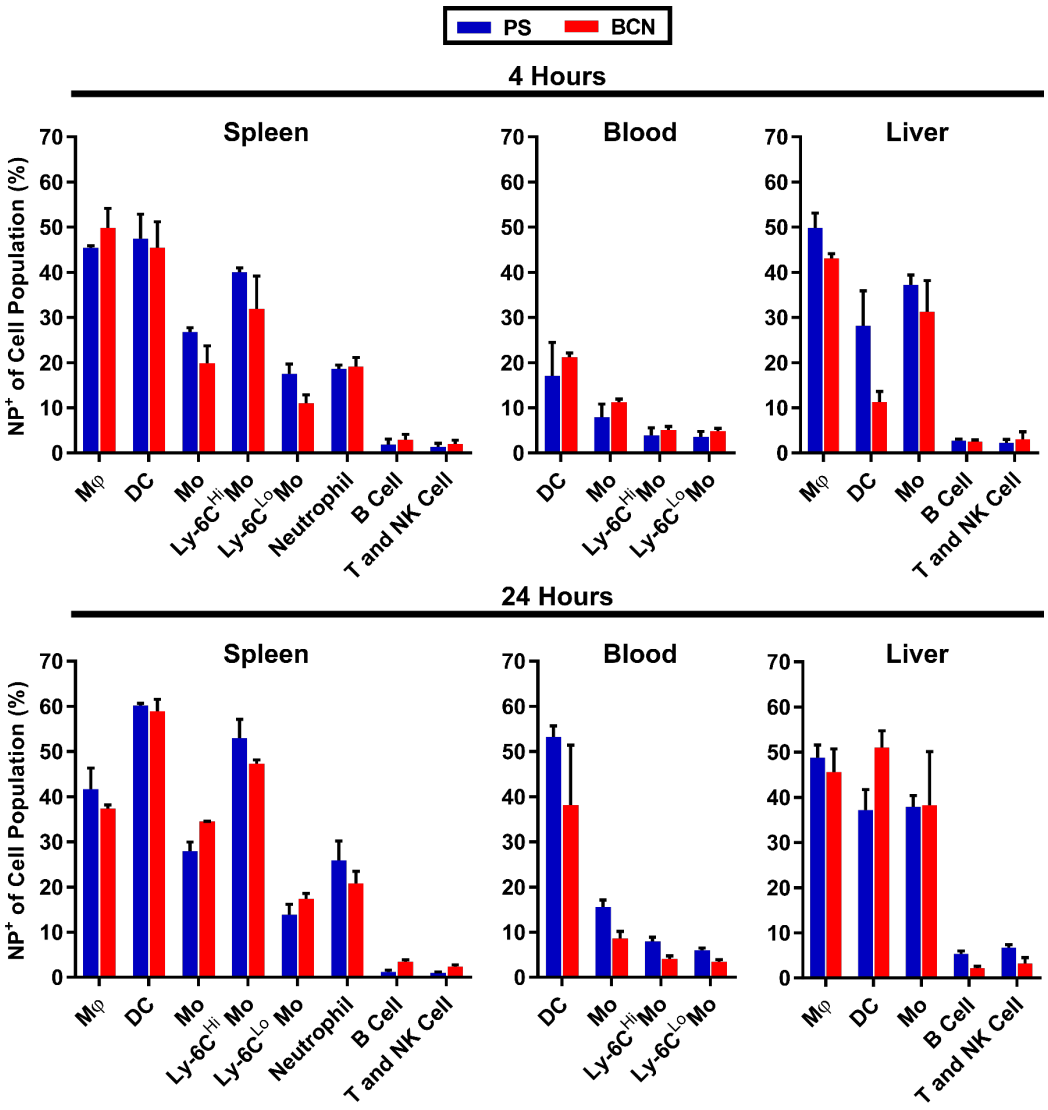

Figure 3-25. Flow cytometric assessment of full cell population uptake of PSs and BCNs 4 and 24 h post IV injection. Nanoparticle uptake of PSs and BCNs 4 and 24 h after IV injection in C57BL6J female mice, showing immune cell populations in the spleen, blood, and liver. N = 3, error bars = S.E.M. Mφ = macrophages ($CD45^+$ $CD3^-$ $CD19^-$ $NK1.1^-$ $Ly\text{-}6G^-$ $F4/80^+$), Mo = Monocytes ($CD45^+$ $CD3^-$ $CD19^-$ $NK1.1^-$ $Ly\text{-}6G^-$ $CD11b^+$ $CD11c^-$ $Ly\text{-}6C^{hi/lo}$), DCs = dendritic cells ($CD45^+$ $CD3^-$ $CD19^-$ $NK1.1^-$ $Ly\text{-}6G^-$ $F4/80^-$ $CD11c^+$ $CD8a^{+/-}$), neutrophils: $CD45^+$ $CD3^-$ $CD19^-$ $NK1.1^-$ $Ly\text{-}6G^+$, B cells: $CD45^+$ $CD19^+$, T and NK Cells: $CD45^+$ $CD19^-$ $NK1.1^{+/-}$ $CD3^{+/-}$. Adapted with permission from [222] © 2018 American Chemical Society.

43% 30 days after injection (**Figure 3-28,** red data points). This remarkably slow diffusion from the site of injection suggests that, by and large, BCNs are trapped at the site of injection, too large to effectively diffuse through the extracellular space. Gradual delivery of cargo over the course of a month has a number of potential applications, though it would often be beneficial to have some control over the rate of delivery. I hypothesized that if it is indeed the case that a bulk of the BCNs are unable to leave the site of injection, one way to speed up their departure would be the recruitment of immune cells. To test this hypothesis, I loaded BCNs with MPL, a TLR agonist and pro-inflammatory molecule. These MPL-BCNs were administered subcutaneously and their departure from the site of injection was measured, as before, by IVIS. As demonstrated by the green data points in **Figure 3-28**, incorporation of MPL led to an increased

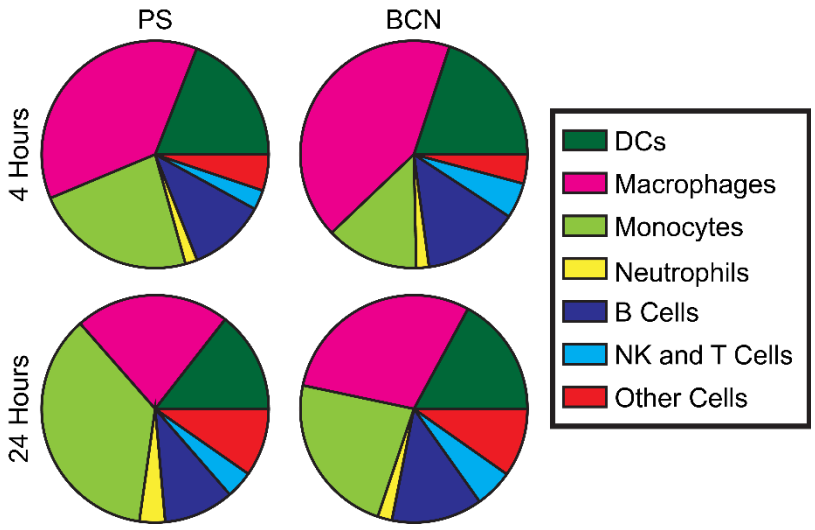

Figure 3-26. Population breakdown of PS and BCN positive cells in the spleen. Pie charts of all NP+ cells, divided into distinct populations. “Other Cells” represent all remaining NP+ cells not explicitly named in the legend, predominantly CD45– cells. Data shown are the average distribution from three mice per treatment group. Macrophages: CD45+ CD3– CD19– NK1.1– Ly-6G– F4/80+, monocytes: CD45+ CD3– CD19– NK1.1– Ly-6G– CD11b+ CD11c– Ly-6Chi/lo, dendritic cells: CD45+ CD3– CD19– NK1.1– Ly-6G– F4/80– CD11c+ CD8a+/–, neutrophils: CD45+ CD3– CD19– NK1.1– Ly-6G+, B cells: CD45+ CD19+, NK and T Cells: CD45+ CD19– NK1.1+/– CD3+/–. Adapted with permission from [222]

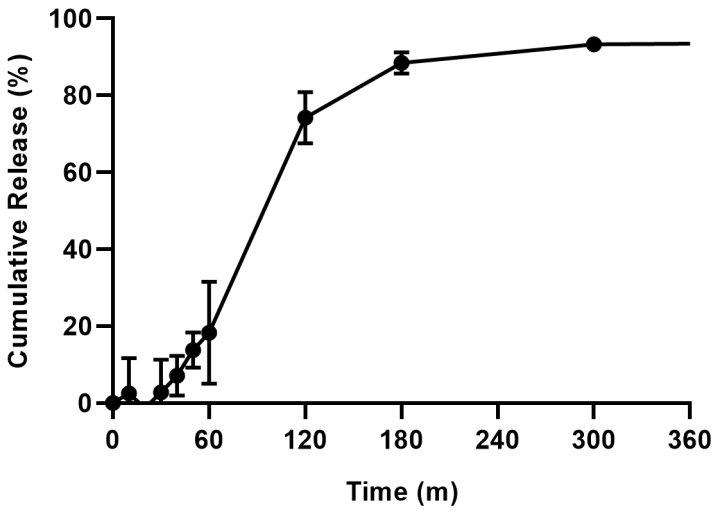

Figure 3-27. Cumulative release of MCs after subcutaneous administration in mice. BALB/c mice were injected with 100 uL of MCs in a scapular subcutaneous injection. MCs were loaded with DiR, n=6 mice for each data point, error bars = s.d.

rate of departure, resulting in more than double the amount of BCNs having left the injection site after one month.

3.5. Discussion

Flash nanoprecipitation has rarely been utilized to load hydrophilic cargo into nanoparticles. I was able to demonstrate that it is well-suited to the task of loading polymersomes with hydrophilic and hydrophobic cargoes, separately and simultaneously. The higher the logP value of the small molecule, the better it would load into the nanocarriers. For hydrophilic loading, macromolecules loaded better than the small molecule calcein. While the FNP process was able to cause some denaturation of protein cargo, this could be somewhat alleviated by loading the cargo from the reservoir rather than the aqueous syringe solution. While reservoir loading resulted in lower encapsulation efficiency, it also resulted in less protein denaturation. Even with syringe loading, alkaline phosphatase was able to exercise its enzymatic function after loading and release from polymersomes.

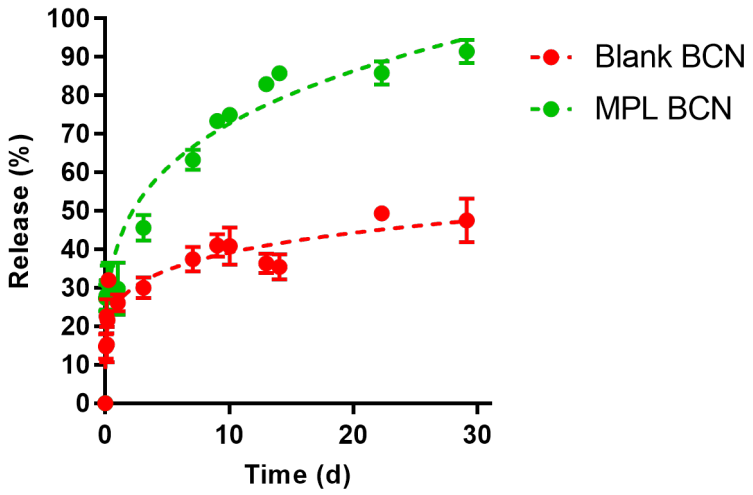

Figure 3-28. Cumulative release of BCNs with or without loaded MPL after subcutaneous administration in mice. BALB/c mice were injected with 100 uL of BCNs in a scapular subcutaneous injection. BCNs were either loaded with DiR or DiR and MPL. Release was tracked using IVIS and measured as a decrease in fluorescent signal from the site of injection. n=8 mice for each data point, error bars = s.d.

I found that BCNs were also able to be loaded with hydrophilic and hydrophobic cargoes by FNP. BCN loading followed the same general trend as PS loading, in that hydrophobic compounds loaded better than hydrophilic, and small hydrophilic molecules loading at a lower efficiency than larger hydrophilic macromolecules. Hydrophobic cargoes were retained within BCNs for longer than hydrophilic cargoes. Release of cargo from BCNs could be effected by oxidation of the BCNs, which shifted the aggregate structures from BCNs to micellar aggregates. BCNs, in the absence of an oxidative source, were stable for months at room temperature.

In a comparison between BCNs and PSs, I found that BCNs are able to load more hydrophobic cargo before becoming saturated. Also, I found that PSs were more susceptible to having their formation disrupted by high levels of hydrophobic cargo being present at the time of formation, suggesting that BCNs would be a better choice of morphology if very high levels of hydrophobic cargo need to be encapsulated. BCNs were also able to load a higher amount of hydrophilic cargo than PSs. Both BCNs and PSs were

able to deliver hydrophilic and hydrophobic cargo simultaneously to cells *in vitro*, a useful property of these morphologies that micelles and filomicelles cannot match. Subcellular localization of MCs, PSs, and BCNs all follow the same pattern of colocalization with the lysosome.

All PEG-*b*-PPS nanocarriers are non-immunogenic *in vitro* when incubated with immune cells sensitive to inflammatory molecules. Incorporation of a pro-inflammatory molecule (e.g. an adjuvant) and an antigen (e.g. a protein) within BCNs and PSs allowed for activation and antigen presentation by BMDCs. BCNs loaded with other adjuvants were able to stimulate cytokine secretion from myeloid cells *in vitro*. Different adjuvants should be able to induce different patterns of cytokine secretion. Elucidation of these patterns and rational combination of different adjuvants within BCNs could result in the development of stronger and more easily prototyped subunit vaccines.

Examination of PS uptake by immune cells in non-human primates revealed that PSs are internalized by largely the same groups between mice and NHP. Notable differences include increased macrophage uptake in NHP, somewhat lower cDC uptake in NHP, and lower myeloid uptake in the liver in NHP, compared to mice. Phagocytic cells such as monocytes, macrophages and dendritic cells understandably possessed high numbers of polymersome-positive cells. It is not clear, however, whether the signal seen in NK cells, T cell subsets, and B cells represents internalized polymersomes, or a cell-surface association of the polymersomes with the cells. These cells are not phagocytic or particularly macropinocytic. Elucidating the relationship between polymersomes and non-phagocytic cells may be achieved using recently developed PEG-*b*-PPS polymersomes with bioresponsive fluorescence that can detect internalization and subsequent degradation [217].

Organ-level biodistribution of BCNs and PSs after IV administration have a few notable differences. The reduced uptake by the liver and increased uptake by the spleen for BCNs compared to PSs could have a number of useful applications for immunomodulation. The spleen is an important secondary lymphoid organ, where many immune cells mature and can be activated [218]. Because of the presence of large numbers of immune cells, delivery to the spleen could be useful for eliciting strong humoral and cellular immune responses for vaccine and cancer immunotherapy applications [219]. Also, reduced liver clearance could allow for increased BCN accumulation in other tissues that are not a part of the MPS, such as the

vascular adventitia or the tumor microenvironment. BCNs also had increased accumulation in the lungs compared to PS at the 4-hour timepoint. The lungs are a highly vascularized tissue, and, in some cases, signal can be due to incomplete perfusion of the blood from the lungs. However, that is unlikely to be the explanation for this result in this case. First, there is little reason why mice injected with BCNs would consistently perfuse less effectively than those that were administered PSs. Second, BCN signal in the blood was actually lower than that for polymersomes at both timepoints, meaning that the signal in the lungs could not be accounted for by remaining blood. Long-term lung accumulation of nanoparticles is often considered dangerous if they are not cleared out by alveolar macrophages or are inappropriately internalized by mesothelial cells [220]. However, BCN single dropped at the 24-hour time point, suggesting that the lung accumulation was transient and not likely to have deleterious health implications. Delivery to lung immune cells, such as alveolar macrophages, could instead be a benefit of BCNs, as delivery to lung immune cells appears to be very important for establishment of strong immunity to respiratory diseases such as tuberculosis.

While BCNs and PSs have a number of similar characteristics, there are physical and structural differences that may help explain their organ-level differences in biodistribution. PSs are slightly smaller than BCNs, on average. Size is a major variable in relation to the biodistribution of nanoparticles in general. However, as noted, PSs demonstrated higher liver uptake than BCNs. Research with polystyrene nanoparticles showed a size dependent increase in accumulation in the liver, but the trend was reversed, with larger nanoparticles accumulating at higher levels in the liver [221]. Both PSs and BCNs are spherical, are made up of PEG-*b*-PPS, with PEG polymers of the same molecular weight. However, BCNs have higher surface area due to the presence of their aqueous channels, perhaps offering more opportunities for protein adsorption. Proteins that adsorb within channels, however, are unlikely to be available to bind to receptors for receptor-mediated uptake. PSs, possessing a single bilayer membrane, are fairly deformable [166]. This means PSs can squeeze through fenestrations that they would be excluded from if they were rigid spheres, given their diameter [222]. BCNs are most likely less deformable, as their bulk is made up of hydrophobic packed PPS chains. This difference in ability to pass through barriers may explain some of the biodistribution differences, with more polymersomes able to pass through the fenestrations within the liver.

BCNs and PSs showed very similar cell population uptake in mice. One exception is uptake by non-immune cells in the liver, which showed higher levels of PS uptake compared to BCNs. This may explain some of the difference seen between PS and BCN liver accumulation on the organ level. While the difference between PSs and BCNs in the non-immune cells appears modest, these cells make up a vast majority of the cells in the liver, and small percentage differences can result in very large organ-level differences. Monocytes and macrophages account for the bulk of nanocarrier uptake at the earlier 4-hour timepoint, but by 24 hours their share of uptake drops somewhat compared to other cell types. Despite being a minority of the cells in the spleen (~20%), myeloid cells account for a majority of the uptake of nanocarriers (~67-75%).

3.6. Acknowledgements

I would like to thank the hard work of Sharan Bobbala, who contributed a significant amount of time and effort to the characterization and utilization of bicontinuous nanospheres. Omar Osorio, the undergraduate student that worked with me, played a very important role in the acquisition of the encapsulation efficiency data for polymersomes formed by FNP. Yu-Gang Liu was indispensable for his help with *in vivo* experiments, particularly with IV injections and collection of organs after the sacking of mice.

3.7. Publication Information

Sections of this chapter have been published with the following citation information:

S. Yi, S. D. Allen, Y. G. Liu, B.Z. Ouyang, X. Li, P. Augsornworawat, E. B. Thorp, E. A. Scott. Tailoring nanostructure morphology for enhanced targeting of dendritic cells in atherosclerosis. ACS Nano 10 (12), 11290-11303. 2016. [121]

S. Allen, O. Osorio, Y.G. Liu, E. Scott. Facile assembly and loading of theranostic polymersomes *via* multi-impingement flash nanoprecipitation. Journal of Controlled Release, 262 91-103. 2017. [166]

S. Bobbala, S.D. Allen, E.A. Scott. Flash nanoprecipitation permits versatile assembly and loading of polymeric bicontinuous cubic nanospheres. Nanoscale 10 (11), 5078-5088. 2018. [148]

S.D. Allen, Y.G. Liu, S. Bobbala, L. Cai, P.I. Hecker, R. Temel, E.A. Scott. Polymersomes scalably fabricated *via* flash nanoprecipitation are non-toxic in non-human primates and associate with leukocytes in the spleen and kidney following intravenous administration. Nano Research 11(10), 5689-5703. 2018. [175]

S.D. Allen, S. Bobbala, N.B. Karabin, M. Modak, E.A. Scott. Benchmarking Bicontinuous Nanospheres against Polymersomes for *in vivo* Biodistribution and Dual Intracellular Delivery of Lipophilic and Water-Soluble Payloads. ACS Applied Materials & Interfaces 10 (40), 33857-33866. 2018. [223]

S.D. Allen, Y.G. Liu, T. Kim, S. Bobbala, S. Yi, X. Zhang, J. Choi, E.A. Scott. Celastrol-loaded PEG-*b*-PPS nanocarriers as an anti-inflammatory treatment for atherosclerosis. Biomaterials Science Advance Article. 2019. [224]

CHAPTER 4

In vivo Toxicity of Polymeric Nanocarriers in Murine and Non-Human Primate Models

4.1. Abstract

PEG-*b*-PPS nanocarriers have been utilized in mice for a number of studies and are clearly sufficiently non-toxic so as to not cause immediate harm to mice. However, prior to their use in humans, PEG-*b*-PPS nanocarriers would first need to undergo a much more rigorous examination of their toxicity *in vivo*, especially at higher and/or repeated doses. In this chapter, I demonstrate the lack of toxicity from repeated IV administrations of PEG-*b*-PPS polymersomes in mice and non-human primates. This work is a critical and necessary step toward clinical studies utilizing PEG-*b*-PPS nanocarriers in humans.

4.2. Introduction

Drugs administered *in vivo* exhibit toxic qualities above a given concentration and can cause cell death, tissue damage, and organ damage. In rare cases, non-drug excipients in the formulation may themselves have toxicological concerns [225]. Nanomaterials, due to their unique properties, have their own toxicological concerns [226]. As such, nanoparticles utilized as drug delivery vehicles must first have their own latent toxicology explored before they can be safely and effectively used to load and deliver drug cargo.

4.2.1. Traditional Metrics of Toxicity

Many toxicology studies begin with *in vitro* tests of cytotoxicity. Numerous different cell types can be dosed with formulations in a concentration series and the cells can be assessed for necrosis, apoptosis, changes in RNA and protein expression, and other morphological or functional changes [227]. In animals, there are many potential signs of toxicity. Animals may display behavioral changes, such as aversion to socializing or increased burrowing/hiding behavior. Animals may become lethargic or may display reduced appetence. Toxic effects are often associated with a loss in body weight in animals [228]. Blood can be drawn from animals and can be examined for changes in red and white blood cell counts. Additionally, serum can be tested for the presence of markers of tissue and organ damage. If animals die, or are

sacrificed, organs can be examined for gross morphological issues. Organs can also be sectioned for histology to examine if there are signs of necrosis, apoptosis, or microscopic morphological changes [229, 230]. Flow cytometry of blood or tissues can determine if there were large changes in cell populations or changes in expression of proteins within particular cell populations [231]. Examination of RNA expression through a number of techniques, such as in situ hybridization of histology sections, RT-PCR, or RNAseq of tissue [229], can help determine if there are deleterious changes in transcription upon administration of a potentially toxic compound. As with cells, animals can be administered increasingly large doses of formulation until animals begin dying upon administration to assess the LD50 of the formulation [232]. Many of these animal studies are performed using rodents, though they are sometimes performed on non-human primates or on other model organisms such as zebrafish or drosophila [233].

4.2.2. Nanotoxicology of Different Nanomaterials

Nanomaterials have an extremely wide range of impacts on biological systems. This is due to the fact that while nanomaterials share the common property of having at least one physical dimension within the size range of 1-1000 nm, they are otherwise a very diverse group of supramolecular aggregates. The PEG-*b*-PPS nanoparticles used in this dissertation are self-assembled aggregate structures formed from an amphiphilic diblock copolymer. Individual polymer chains vary in molecular weight from 3 to 7 kDa, making them small non-biodegradable macromolecules. Other polymeric nanoparticles may be made from polymers that have a larger molecular weight (e.g. >20 kDa) [234] or may be made from polymers that have hydrolysable bonds between monomers, making them biodegradable [235]. Not all polymeric nanoparticles are self-assembled aggregates. Dendrimer ‘unimolecular’ micelles are nanostructures formed from a single molecule, typically a highly branched hydrophobic polymer with each branch covalently attached to a hydrophilic polymer [236].

However, polymeric nanoparticles are just a single category of nanomaterial. Nanoparticles can also be created from metal oxides, noble metals, carbon, silica, etc. On a cellular level, nanoparticles can cause redox changes that can affect glutathione levels and mitochondrial function [237, 238]. Nanoparticles can produce reactive oxygen species that can cause significant cellular damage [239]. Nanoparticles can

interact with biological membranes can cause permeability [240]. High surface area and the presence of metal can allow for catalytic activity, some of which may be deleterious [241]. For metal nanoparticles, potentially toxic metal ions can leach out of the particles in the acidic environment of the lysosome [242]. These metal ions can have specific activities, e.g. displacing other metals in active sites of enzymes, or can have non-specific activities relating to redox balance or mitochondrial membrane depolarization. Nanoparticles can induce inflammation and the recruitment of inflammatory cells, which can themselves cause to tissue damage [229].

The morphology of nanoparticles can also affect their toxicity. Nanomaterials with high aspect ratios can cause frustrated phagocytosis when partially internalized by phagocytic cells [243]. These nanomaterials can also cause fibrosis in tissues and organs such as the lungs [244]. Large or unstable nanoparticles can aggregate in biological fluids, leading to the blockage of blood vessels [245]. Certain surface chemistries on nanoparticles can cause complement activation in mammalian serum, leading to the initiation of inflammatory immune responses [246].

4.2.3. Routes of Clearance for Nanomaterials

Even if nanomaterials are not immediately toxic, many treatments require repeated doses for therapeutic efficacy. It is important to consider how quickly and through what route nanomaterials are cleared from the body, which depends on the type of nanomaterial being considered. The main routes of clearance for materials are through the liver or through the kidneys [221]. Liver clearance requires uptake by hepatocytes, which can secrete nanomaterials *via* the biliary secretion pathway into the intestines [247]. Kidney clearance can filter aggregates directly from the blood, though there is a limit to the size of the filtrate that would exclude most nanoparticles from renal clearance (<6-8 nm) [221]. Nanomaterials that enter into other tissues would need to be broken down by resident macrophages and/or neutrophils or run the risk of remaining in the tissue long-term, which can lead to fibrosis. Even in cases where the nanoparticles can be broken down, their constituent parts may themselves be toxic [242].

4.2.4. PEG-*b*-PPS Toxicity

PEG-*b*-PPS nanocarriers are not cytotoxic to cells at a 2 mg/mL concentration after overnight incubation [191, 248]. This lack of cytotoxicity has been an important property of PEG-*b*-PPS nanocarriers, since their effective delivery to cells typically requires that cells do not die shortly after receiving cargo. PEG-*b*-PPS polymersomes, filomicelles, and micelles were administered to mice at concentrations ranging from 67 to 100 mg polymer per kg body weight (mg/kg) [121, 166, 191, 223]. A single dose of PEG-*b*-PPS nanocarriers at this concentration was not sufficient to cause any mice to die or suffer outward signs of toxicity. However, work has not yet been performing examining in more detail whether PEG-*b*-PPS nanocarriers exhibit any signs of toxicity at higher doses, repeated doses, or in other organisms. This chapter covers my work to address this deficiency in the toxicological characterization of PEG-*b*-PPS nanocarriers *in vivo*, particularly for polymersomes.

4.3. Materials and Methods

4.3.1. Animal Use

C57BL/6J female mice, 6-8 weeks old, were purchased from Jackson Laboratories. All mice were housed and maintained in the Center for Comparative Medicine at Northwestern University. All animal experimental procedures were performed according to protocols approved by the Northwestern University Institutional Animal Care and Use Committee (IACUC). Female cynomolgus monkeys (Macaca fascicularis) were used for the nonhuman primate study conducted at the University of Kentucky (UK). The four monkeys originated from Mauritius and were on average 4.8 years of age (range 4.5-4.9). The animals were housed in an AAALAC accredited facility under the care of the UK Division of Laboratory Animal Resources. All experiments were approved by the UK Institutional Animal Care and Use Committee.

4.3.2. Chemicals

Unless specifically denoted, all chemicals and reagents were purchased from Sigma Aldrich.

4.3.3. Cytokine and αPEG Antibody ELISAs

Monkey anti-PEG IgG and IgM ELISA kits were purchased from Life Diagnostics, Inc., and were used as supplied as per the manufacturer's instructions. Kits were confirmed by the manufacturer to recognize cynomolgus antibodies, and standard curves for quantification were calculated using anti-PEG lyophilized standards, as provided. Serum was diluted 1:100 for assaying, and absorbance values of HRP colorimetric activity were collected at 450 nm on a SpectraMax M3 plate reader.

4.3.4. Mouse and Primate Toxicity Studies

C57BL/6J mice were divided into 4 groups, n=4 per group, and were injected once a week for 4 weeks with 0 mg/mL, 6.67 mg/mL, 16.67 mg/mL, and 33.33 mg/mL formulations of polymersomes, at dosages of 0, 40, 100, and 200 mg/kg, respectively (approximately 100 µL of formulation per dose). Formulations were injected intravenously *via* the tail vein, while the mice were anesthetized by isoflurane. Prior to injection, the mass of each mouse was recorded. Food was weighed periodically to determine amount consumed, averaged amongst the mice in each cage. One week after the final injection, mice were weighed a final time before being euthanized by CO2. Organs (lungs, liver, kidney, and spleens) were collected and weighed.

Female cynomolgus monkeys fed Teklad 2050 global 20% protein primate diet were treated for 4 weeks with USP grade saline (n=2) or 20 mg/kg polymersomes (n=2). For injections, animals were fasted overnight and sedated with ketamine HCl (5-10 mg/kg IM). The vehicle and polymersomes were injected into the monkeys intravenously *via* the saphenous vein using a Harvard pump set at a rate of 1 ml/minute. Total injected volume was less than 5 ml. The monkeys were dosed once a week for 4 consecutive weeks. For weekly blood collection, animals were fasted overnight, sedated with ketamine HCl (5-10 mg/kg IM), and weighed. Blood samples were taken from the femoral vein. 7 ml of blood were collected once a week at treatment weeks -1, 0, 1, 2, 3, and 4. At weeks 0, 1, 2, and 3, blood was collected immediately before IV injection of vehicle or polymersomes. At week 4, blood was collected immediately before euthanasia. Blood was subjected to complete blood count (CBC) test and serum was analyzed using the Superchem test (ANTECH Diagnostics). Complement activity was assessed *via* standard sheep erythrocyte hemolytic (CH50) assay (Diamedix). Assay controls for complement activity: 'normal complement' human serum, 'low

complement' human serum, and 'high complement' human serum, were purchased from the assay vendor and were used as described when the assay was performed on NHP samples. After 4 weeks of treatment, the monkeys were euthanized.

4.4. Results

4.4.1. Lack of Mouse Weight/Appetence Changes

As mentioned in the introduction, PEG-*b*-PPS nanocarriers have been found to be non-toxic in mice. These studies evaluated the lack of toxicity simply by observing the survival of mice despite the injection of 100 mg/kg of PEG-*b*-PPS in a single dose [191] or 25 mg/kg/week in repeated administrations [132]. To examine if higher concentrations of PEG-*b*-PPS nanocarriers can be tolerated in mice, I injected C57BL/6 mice once a week for four weeks with PEG-*b*-PPS formulations at three concentrations: 40, 100, and 200 mg/kg. I found that mouse body weight did not decrease over the treatment period, relative to their baseline weight prior to treatment (**Figure 4-1a**). The only change in body weight was a statistically significant increase, by approximately 5%, in the body weight of the highest dose treatment mice. None of the treatments induced a change in appetence (**Figure 4-1b**), which indeed did not change at all over the entire course of the treatment regime (**Figure 4-2**).

4.4.2. Minor Changes to Mouse Organ Weights

Along with the overall body weight increase, there was also a statistically significant increase in the weight of mouse livers, relative to their body weight, in the mice treated at the top two polymersome concentration levels (**Figure 4-1c**). This increase in liver weight, on average 0.34 g, does not account for all of the body weight increase seen in (**Figure 4-1a**), on average 1.12 g. As decreases in body weight, not increases, are typically considered a sign of toxicity, the administration of high doses of PEG-*b*-PPS polymersomes was not considered to be particularly toxic, even when administered weekly for a month.

This data was considered strong enough to proceed with studies in non-human primates to help examine the biodistribution and safety of PEG-*b*-PPS in an organism with more similarities to human physiology.

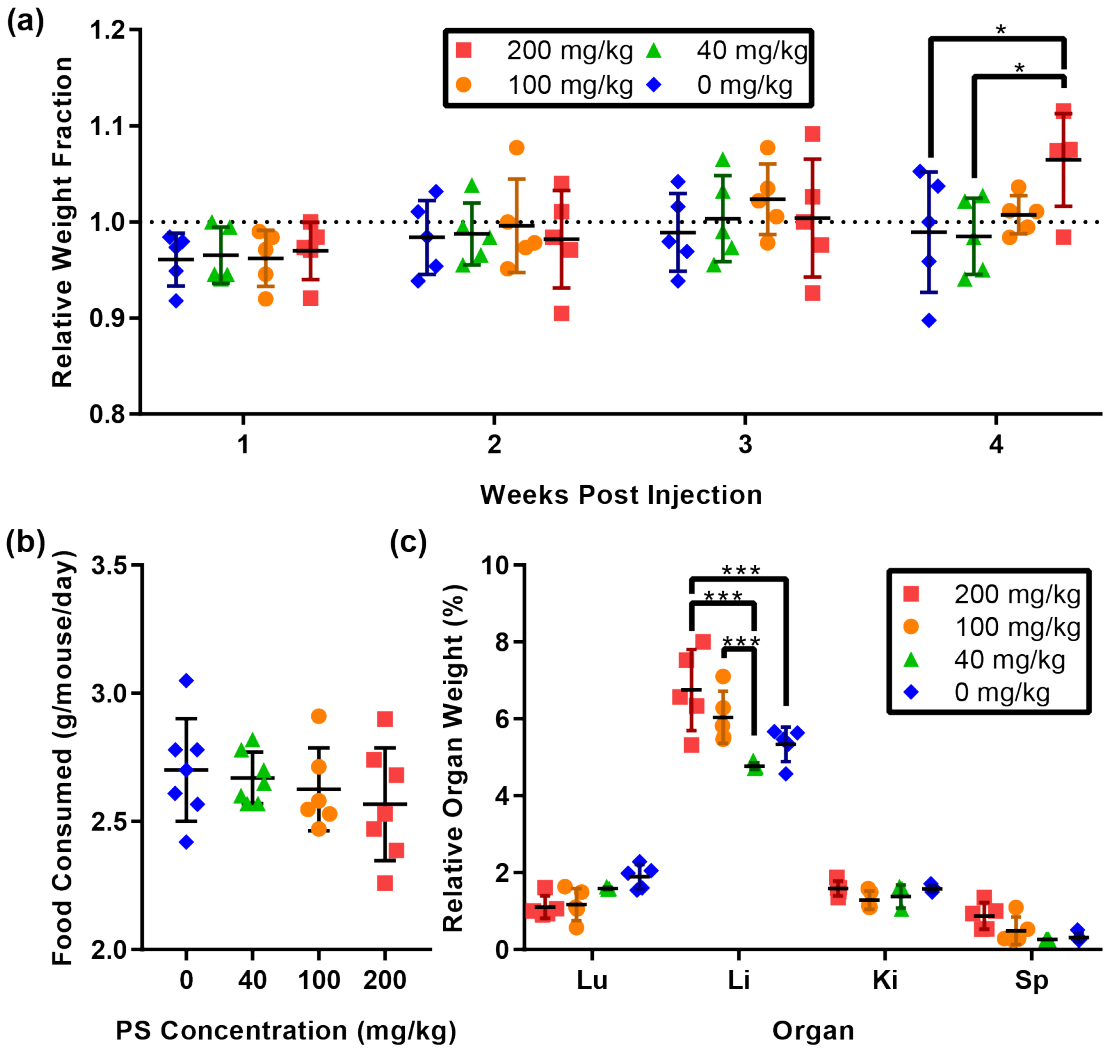

Figure 4-1. Concentration series of polymersome toxicity in mice. (a), Individual mouse weights, relative to initial weight at the start of polymersome administration, n=4 for each polymersome dose. Error bars are s.d. * $p < 0.01$, significance determined by Tukey's multiple comparisons test. (b), Mouse food consumption for the same treatment groups, n=7 error bars are s.d. (c), Organ weights, relative to total body weight prior to necropsy. Lu = lung, Li = liver, Ki = kidney, and Sp = spleen, n=4 error bars are s.d. *** $p < 0.0001$, significance determined by Tukey's multiple comparisons test. Figure reprinted with permission from [173] .

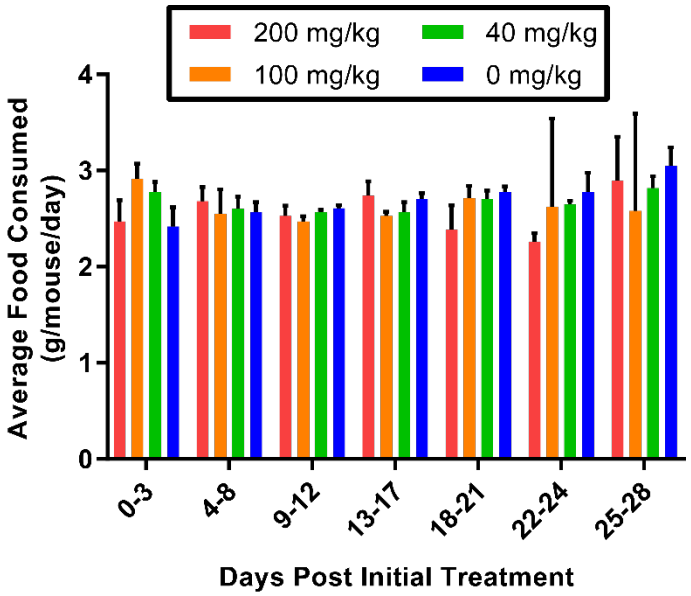

Figure 4-2. Mouse food consumption data separated by measurement interval. Mouse food consumption, averaged over 4- to 5-day intervals, with measurements beginning on the first day of polymersome administration. n=3, error bars = S.D. Figure reprinted with permission from [173] © 2018 Springer.

4.4.3. Lack of Issues in Comprehensive Blood Panel in Non-Human Primates

Cynomolgus monkeys were injected with either saline or 20 mg/kg PEG-*b*-PPS polymersomes once a week for a month. Blood was drawn from these monkeys and was tested for changes to blood cell counts and for the presence of organ damage markers (**Figure 4-3**). Red blood cell counts and white blood cell counts were within the normal range (shaded area in plots) for primates, regardless of whether they were treated with polymersomes or saline (**Figure 4-3a,b**). One monkey had a transient spike in their white blood cell count during the third week of injections, but the levels returned back to normal by the fourth week. Creatinine, a breakdown product of creatine phosphate in muscles, is cleared from the blood at a fairly steady rate. When kidney function is impaired, however, creatinine levels in the blood can rise, making it a good marker for kidney function [249]. Creatinine levels for all monkeys were well within the normal range for the entire treatment period (**Figure 4-3c**). Blood urea nitrogen (BUN) levels in the blood act as a proxy for both liver and kidney function. Urea is produced during protein digestion in the liver and is filtered

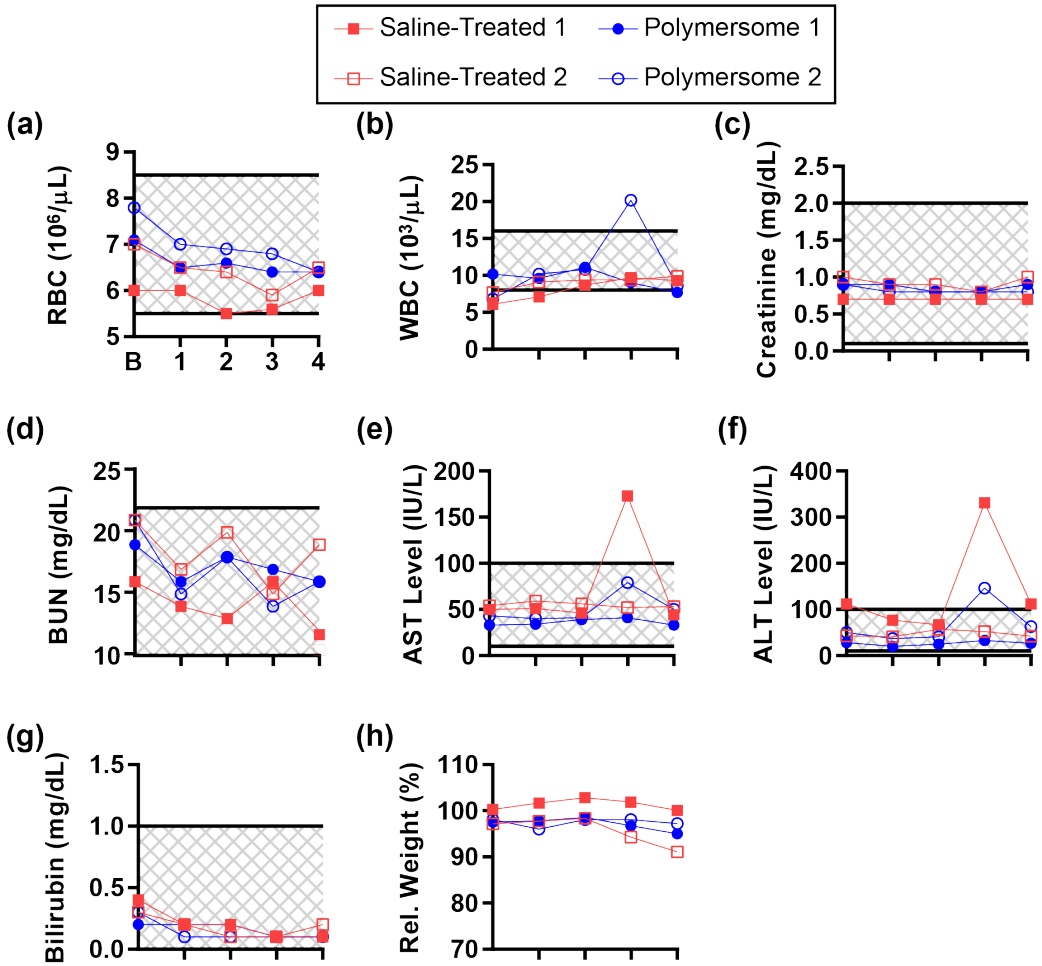

Figure 4-3. CBC, blood chemistry, and body weights of *Macaca fascicularis* over 4-week polymersome administration. Standard CBC and blood chemistry panel and relative body weights of NHPs over the course of 4-week polymersome I.V. administration. Cross-hatched areas in each graph represent standard 'healthy' ranges of values, n=2 for each treatment, saline-treated NHPs in red, polymersome-treated NHPs in blue, all individuals shown in graph. Body weights are represented as the relative body weight, as a percent of the average baseline weight for each animal. (a) RBC = red blood cell, (b) WBC = white blood cell, (c) creatinine, (d) BUN = blood urea nitrogen, (e) AST = aspartate aminotransferase, (f) ALT = alanine aminotransferase, (g) bilirubin, and (h) body weight relative to baseline value. X-axes for all graphs are as shown for the top left graph, beginning with the baseline value (B), and then the value at the time of each day post initial injection. Figure reprinted with permission from [173] © 2018 Springer.

out of blood by the kidneys. Lower than normal BUN levels can indicated liver damage or dysfunction, while higher than normal levels indicate kidney damage [249]. Again, BUN levels for all four monkeys were within the normal range, regardless of treatment (**Figure 4-3d**). Aspartate transaminase (AST) is a cytosolic and mitochondrial enzyme found in the liver, heart, skeletal muscle, kidneys, brain, and red blood cells. It is detectable in the blood in cases of damage to any of the organs it is found in, particularly the liver. A closely related biomarker for organ damage, alanine transaminase (ALT), is also found in several organs, but is most commonly found in the liver. Both are commonly used as biomarkers for liver damage when found in elevated levels in the blood [250]. One saline-treated and one polymersome-treated monkey each had a transient spike in their AST and ALT levels at week 3 (**Figure 4-3e,f**). The spike in AST for the polymersome-treated monkey was not sufficiently elevated to be considered abnormal. However, that is the same monkey that saw a spike in white blood cell levels at the same timepoint. Bilirubin is a product of heme metabolism, which occurs when macrophages phagocytose senescent or damaged red blood cells, typically in the spleen. Bilirubin is rapidly adsorbed to albumin upon entering the bloodstream. That albumin traffics to the liver, where it is endocytosed by hepatocytes and further processed for biliary secretion. Bilirubin is therefore a biomarker for both liver function and hemolysis, as either could result in increased bilirubin levels in serum [251]. Bilirubin levels in the non-human primates were stable and within normal range throughout the treatment window (**Figure 4-3g**). The monkeys showed no outward behavioral signs of distress during the month of weekly treatments and maintained a consistent body weight throughout the treatment period (**Figure 4-3h**).

4.4.4. Lack of Complement Activation or αPEG Antibody Generation in Non-Human Primates

Early in the process of translating liposomes into the clinic, it was found that PEGylating the liposomal surface helped to improve circulation time by reducing protein adsorption and liposomal clearance from the bloodstream [252]. However, it was soon thereafter found that some people possessed antibodies that appeared to be specific to PEG [253, 254]. The presence of these αPEG antibodies resulted in increased clearance of the PEGylated liposomes, and the administration of PEGylated liposomes could

induce the generation of αPEG antibodies. This meant that after the first administration, subsequent administrations would be cleared more quickly, undoubtedly deleteriously affecting the efficacy of the liposomal delivery system [255]. Since PEG-*b*-PPS nanocarriers are made up of a block copolymer that has PEG as one of its blocks, I wanted to determine whether treatment with PEG-*b*-PPS polymersomes could result in the generation of αPEG antibodies.

As both IgM and IgG antibodies have been generated through the administration of PEG-coated nanoparticles, my colleague Sharan Bobbala and I performed ELISA assays for both. We found that the polymersome-treated monkeys did not generate αPEG antibodies of neither the IgM nor the IgG isotype (**Figure 4-4a,b**). One monkey appeared to form IgG αPEG antibodies during the second week. However, this was a saline-treated monkey, so even if this signal is a true positive, the presence of signal could not be attributable to polymersome administration.

A number of nanoparticles have been reported to activate the complement protein C3, which can cause an inflammatory cascade [256]. To allay concerns about the potential for complement activation by the administered polymersomes, I performed an assay for complement activation using the collected primate serum and primed sheep erythrocytes. The assay revealed that there was no aberrant complement activity in any of the monkeys, including those treated with polymersomes, for the entire treatment period (**Figure 4-4c**).

4.5. Discussion

PEG-*b*-PPS polymersomes were non-toxic in both mice and non-human primates after repeated weekly doses. Mice did not demonstrate toxicity-induced weight loss or appetence loss even at very high cumulative doses of polymersomes. They did, however, demonstrate an increase in body and liver weight/size (liver hypertrophy and hepatomegaly).

Hepatomegaly alone is not a conclusive marker of adverse or non-adverse effect when seen after repeated administrations of a substance [257]. Also, even when used as a marker of toxicity, hepatomegaly is not consistent across species. Some drugs capable of inducing toxic liver hypertrophy in rodent models fail to demonstrate any apparent toxicity in other closely related models, such as guinea pigs and

marmosets, and vice versa [258]. As the liver is the organ with the largest population of phagocytes within the mononuclear phagocyte system (MPS), it would be expected to have the highest accumulation of administered nanocarriers [259]. It is likely, therefore, that the increase in liver weight is an adaptive response to the increased polymer burden within cells in the liver. This could be through an increase in

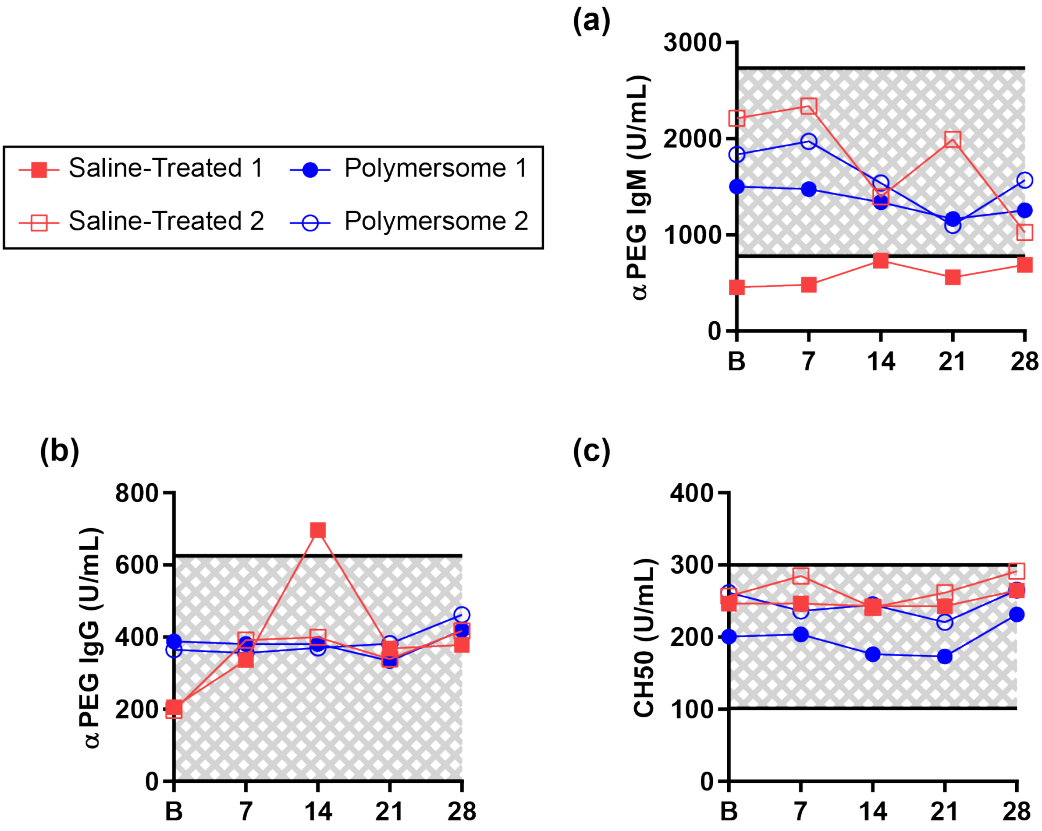

Figure 4-4. Anti-PEG antibody titers and complement activity in *Macaca fascicularis* serum. Serum from NHPs over the course of 4-week polymersome or saline I.V. administration was assayed for anti-PEG (a) IgM or (b) IgG antibodies *via* ELISA or (c) complement activity *via* sheep erythrocyte lysis assay. n=2 for each treatment, saline-treated NHPs in red, polymersome-treated NHPs in blue, all individuals shown in graph. Anti-PEG IgM and IgG antibodies and complement hemolytic activity (CH50) are all expressed as units per mL of serum, with cross-hatched areas representing normal ranges for naïve NHPs, as observed by the assay manufacturer. X-axis represents days post initial injection, B = baseline. Figure reprinted with permission from [173] © 2018 Springer.

absolute cell number or an increase in cell size, to accommodate additional peroxisomes and/or microsomes for degradation and clearance purposes [258].

PEG-*b*-PPS polymersome administration to non-human primates demonstrated a lack of toxicity as assessed by serum markers and behavioral observations. There was a transient spike in some of these markers at the third week of treatments. This spike was temporary, suggesting that it was not specific to polymersome treatment but was rather some unrelated issue. This is supported by the appearance of a similar spike in the AST and ALT serum levels of a saline-treated primate. The saline-treated primate spike was actually larger in magnitude than the spike in the ALT levels for the polymersome-treated primate. All together, this strongly suggests that the temporary elevations seen in **Figure 4-3b,e,f** are not indicative of polymersome toxicity in non-human primates.

The presence of αPEG antibodies could drastically affect the circulation time of PEG-*b*-PPS polymersomes, so it was important to uncover whether repeated administrations of PEG-*b*-PPS resulted in the generation of these antibodies. The molecular weight and packing/folding of PEG appears to play a role in whether antibodies are generated [255], which is a possible explanation for why neither IgG nor IgM αPEG antibodies were generated over the 4 week administration period. Naïve mice (i.e. mice with no detectable IgG or IgM αPEG antibodies) dosed with PEGylated liposomes generate αPEG IgM antibodies within two weeks and αPEG IgG antibodies within a month [260]. Therefore, the time window within which we were checking the primate serum for αPEG antibodies was sufficiently wide to observe these antibodies, were they present. A study with PEGylated nanoparticles administered at a dose 20x lower than the dose used here found robust αPEG antibody generation, demonstrating that our dose is more than high enough to generate these antibodies [261]. That the PEG-*b*-PPS polymersomes did not generate these antibodies is likely due to the conformation of the relatively small PEG utilized for the PEG-*b*-PPS polymer (MW = 750 g/mol).

An additional safety concern in nanoparticle intravenous administration is the activation of complement proteins, which has been documented for nanoparticulate systems such as PEGylated liposomes [262, 263]. Reassuringly, and in line with the observed maintenance of RBC levels, intravenous administration of PEG-*b*-PPS polymersomes did not change the hemolytic (CH50) activity of NHP serum, suggesting a

lack of complement protein activation. Overall, the lack of persistent clinical markers of organ damage in the serum, along with a lack of anti-PEG antibodies, and a lack of activated complement all point to a weekly dose of 20 mg/kg of polymersomes as non-toxic in NHP.

4.6. Acknowledgements

I would like to acknowledge the hard work of Yu-Gang Liu, who traveled with me to Kentucky in order to help collect and process tissue from the primates used in this chapter. I would also like to acknowledge the critical assistance of Lei Cai, Peter Hecker, and Ryan Temel, who housed, cared for, and treated the primates used in this study at the University of Kentucky. Also, I would like to acknowledge the help and expertise of Sharan Bobbala for his assistance with the ELISA assays.

4.7. Publication Information

Sections of this chapter have been published with the following citation information:

S.D. Allen, Y.G. Liu, S. Bobbala, L. Cai, P.I. Hecker, R. Temel, E.A. Scott. Polymersomes scalably fabricated *via* flash nanoprecipitation are non-toxic in non-human primates and associate with leukocytes in the spleen and kidney following intravenous administration. Nano Research 11(10), 5689-5703. 2018.

CHAPTER 5

In vivo Immunomodulation Using Anti-Inflammatory Nanocarriers

5.1. Abstract

There are a number of diseases and disorders for which immunomodulatory treatment would be beneficial. Many of the compounds that could perform this task have off-target effects or poor solubility, making this challenge one that nanocarrier-based drug delivery is well suited to address. My work and previous work in the lab have demonstrated that PEG-*b*-PPS nanocarriers are taken up by immune cells but are non-immunogenic unless loaded with immunostimulatory molecules. This suggests that PEG-*b*-PPS nanocarriers are a 'blank' slate immunogenically and could be loaded with immunosuppresive molecules to reduce immune and inflammatory responses in cases where they are deleterious. This application of PEG-*b*-PPS nanocarriers had been postulated but unexplored. This chapter addresses this deficiency, as I load and deliver *in vivo* rapamycin, an FDA-approved immunosuppressant, and celastrol, a small molecule anti-inflammatory molecule from Chinese herbal medicine. This work both demonstrates a legitimate treatment modality for atherosclerosis and lays the groundwork for a number of other applications for anti-inflammatory PEG-*b*-PPS therapeutics.

5.2. Introduction

This chapter concerns the proof of concept delivery of immunosuppressive compounds, first in healthy mice and afterwards in a disease model of atherosclerosis. To understand the concepts involved in nanocarrier delivery of immunosuppressive compounds, it is important to first know 1) what cells are typically inflammatory, 2) what signaling pathways are particularly implicated in inflammatory diseases such as atherosclerosis, 3) the ability of nanocarriers to interact with cells involved in atherosclerosis, 4) the characteristics and targets of the two compounds used in this chapter.

5.2.1. Inflammatory Cell Types

Nearly all immune cells are pro-inflammatory. The exceptions to this trend are M2 macrophages [67], tolerogenic dendritic cells [264], myeloid-derived suppressor cells [81], and regulatory T cells [77]. Details on all the immune cells relevant to these studies were covered in section 1.2.4. and **Table 1-3**. Nanocarrier-based therapeutic strategies can either focus on reducing the number of inflammatory cells in the site of injection, reducing their capacity to be inflammatory, or transition their phenotype from a pro-inflammatory phenotype to one of the anti-inflammatory phenotypes listed above. PEG-*b*-PPS nanocarriers are internalized the most by phagocytic cell types such as neutrophils, monocytes, macrophages, and dendritic cells. T cells, which can be critically important amplifiers of inflammatory signals, do not internalize PEG-*b*-PPS nanocarriers in large amounts. They can, however, have their phenotype modulated by myeloid cells that do internalize PEG-*b*-PPS nanocarriers, such as dendritic cells and macrophages.

5.2.2. Inflammatory Signaling in Disease

Cytokines, receptor-receptor binding between cells, and pathogen and damage associated molecular patterns all function as potential extracellular inflammatory signals. Cytokines are secreted signaling proteins produced for the purpose of modulating immune responses. Most of these are pro-inflammatory, with some of the most potent being TNF-α, IL-1β, IL-6, and IL-12 [265]. A few other cytokines can be anti-inflammatory. Anti-inflammatory cytokines can be classified as such either under all contexts, such as IL-10 [266], or under specific signaling contexts, such as TGF-β [267] and IL-4 [268]. Cytokines are often produced by the very cells and signaling pathways that they stimulate, leading to feedback loops that can have complex cross-talk to prevent runaway stimulation. There are many cytokines, many of which are poorly characterized, so I have summarized the current knowledge on the best characterized cytokines in **Table 5-1**.

Besides communicating *via* cytokines, antigen presenting cells can communicate directly with other cells, particularly T cells. This direct communication involves binding between cell membrane proteins on the antigen presenting cell and cell membrane receptor proteins on the T cells [269]. The particular proteins involved are CD80 and CD86 on APCs binding to CD28 or CTLA-4 on T cells, and CD40 on APCs binding to CD40L on T cells. MHCII and MHCI on APCs loaded with antigen also engage with the TCR on T cells

Table 5-1. Selected cytokines, their sources, and function.

Cytokine	Main Cellular Source	Main Activity
IL-1α	APCs	Pro-Inflammatory for APCs and T Cells
IL-1β	APCs	Pro-Inflammatory for APCs and T Cells
IL-2	Th1 Cells, NK Cells	Pro-Inflammatory for B Cells, T Cells, NK Cells
IL-4	Activated T Cells	B Cell Proliferation, Allergic Responses
IL-5	Th2 Cells, Mast Cells	Eosinophil Activation
IL-6	Th2 Cells, APCs	Pro-Inflammatory, Synergizes with IL-1 and TNF
IL-8	Macrophages	Attracts Neutrophils and T Cells
IL-10	Regulatory T Cells, Tolerogenic APCs	Anti-Inflammatory
IL-12	B Cells, Macrophages	Pro-Inflammatory, Stimulates IFN Secretion
IL-13	Th2 Cells	Appears Similar to IL-4 Function
IL-17	Th17 Cells	Pro-Inflammatory, Stimulates Cytokine Secretion and Homing by Macrophages and Neutrophils
IL-18	Macrophages	Pro-Inflammatory, Potent Stimuli for IFN Secretion by T cells and NK Cells
IFN-α	Macrophages, Neutrophils	Pro-Inflammatory, Activation of NK Cells and Macropahges
IFN-β	Macrophages, Neutrophils	Pro-Inflammatory, Activation of NK Cells and Macropahges
IFN-γ	Th1 Cells, NK Cells	Pro-Inflammatory, Stimulates APCs
TNF-α	Macrophages, NK Cells	Pro-Inflammatory, Promotes Cell Death
TNF-β	Th1 Cells	Pro-Inflammatory, Promotes NO Production, Cell Death, Phagocytosis
TGF-β	T Cells, Monocytes	Potentially Pro- or Anti-Inflammatory, Can Promote IL-1 but also Inhibit Proliferation

as a part of antigen-specific responses. CD80/CD86 engagement with CD28 is pro-inflammatory, while engagement with CTLA-4 is inhibitory and anti-inflammatory [270].

Pattern recognition receptors (PRRs) on and within innate immune cells are constitutively expressed and ready to detect molecular patterns indicating the presence of pathogens or damage, termed

pathogen-associated molecular patterns (PAMPs) and damage-associated molecular patterns (DAMPs) respectively [271]. When PRRs bind to PAMPs or DAMPs, they signal through pro-inflammatory pathways, stimulating cytokine secretion and the induction of pro-inflammatory cellular phenotypes. It is increasingly clear that a number of signals that bind to PRRs are not just from invading pathogens but can also be endogenous molecules aberrantly modified or located in compartments they should not have access to [272]. For example, low-density lipoprotein (LDL) is a natural nanoparticle consisting of a single apolipoprotein B-100 molecule and a collection of other proteins, fatty acids, and cholesterol. LDL functions as a delivery vehicle for fatty acids to cells throughout the body. When LDL accumulates in large amounts in the extracellular space without being internalized (i.e. if there are not enough cells to internalize and unload the LDL because there is too much accumulated LDL), the LDL can oxidize or become acetylated [273]. These modifications to LDL make it recognizable as a pro-inflammatory molecule by PRRs on innate immune cells, triggering an inflammatory response [274].

There are very high levels of cross-talk between the intracellular signaling pathways downstream of PRR and cytokine receptor engagement within inflammatory cells. One of the primary signaling pathways is the NF-κB signaling pathway. Cell surface PRRs such as TLR2 and TLR4 signal through MyD88, which eventually leads to the activation of IKKα and IKKβ, which inhibit IκK and prevent it from sequestering NF-κB in the cytoplasm [275]. NF-κB is then free to enter the nucleus where it can activate transcriptional targets such as IL-1, IL-6, and TNF-α. MyD88 can also activate JNK and MAPK signaling to activate AP-1, a transcription factor for many pro-survival and proliferation genes [276]. Endolysosomal PRRs such as TLR7 and TLR9 signal through TRIF and MyD88 to activate IRF3 and IRF7 transcription factors which largely target antiviral genes [277]. The JAK/STAT pathway is downstream of cytokine receptor engagement [278], though MyD88 can also be involved, providing crosstalk with the NF-κB pathway [279].

5.2.3. Nanocarrier Morphology-Based Passive Targeting to Atheroma

Atherosclerotic plaques (atheromas) begin to develop when vascular endothelial cells begin to take damage. This damage can be caused by disease or simply by wear-and-tear from high blood pressure. Damage to the endothelial cells results in the inappropriate transit of LDL particles from the bloodstream

into the arterial intima [280]. The damage to these cells also results in the expression of surface markers that help recruit immune cells to the site of damage. As the LDL accumulates in the arterial intima, it becomes modified by proteins and molecules in the extracellular environment. These modifications are most commonly oxidation and acetylation, forming oxidized or acetylated LDL (oxLDL and acLDL) [281, 282]. These modified LDL particles are recognized by receptors on vascular smooth muscle cells and resident macrophages, such as Scavenger Receptor A, MARCO, LOX-1, and CD36 [281, 283]. These cells internalize the LDL particles and attempt to unload the fatty acids and cholesterol and repackage them into apoAI particles [284]. If they are unsuccessful, cholesterol and fatty acid crystals and droplets may form within the cells, setting off inflammatory signaling pathways and phenotypically altering the cells into foam cells [285]. Foam cells are highly inflammatory and secrete many cytokines and chemokines. This results in the recruitment of more immune cells to the developing atheroma [286].

Because of the large number of immune cells involved in the progression of atherosclerosis, PEG-*b*-PPS nanocarriers have a number of ways that they could modulate the inflammatory environment in the atheroma (**Figure 5-1**). PEG-*b*-PPS nanocarriers could alter immune cells systemically (e.g. in the lymph nodes and spleen) to make those cells less likely to traffic to the atheroma and contribute to the inflammatory environment. This systemic anti-inflammatory effect would also reduce the levels of inflammatory cytokines in circulation. PEG-*b*-PPS nanocarriers could also directly travel to the atheroma, entering from the arterial lumen or from neovasculature that sometimes forms at the site of atheromas [287]. Work in our lab demonstrated that IV administration of PEG-*b*-PPS polymersomes resulted in the uptake of those polymersomes by cells within the atheroma of Ldlr-/- mice (**Figure 5-2**) [121]. Polymersomes were particularly internalized by DCs and macrophages in the atheroma (**Figure 5-2a**), both of which are typically pro-inflammatory in the atheroma microenvironment. While no therapeutic molecule was delivered in that study, it provided the proof of concept to use PEG-*b*-PPS nanocarriers for delivery to the atheroma in murine atherosclerosis.

5.2.4. Rapamycin Targets, Uses, and Effects

Rapamycin (also known as Sirolimus) is a macrolide hydrophobic molecule that binds to and inhibits a protein named (after the fact) mammalian target of rapamycin, or mTOR. Rapamycin was first isolated from *Streptomyces hygroscopicus*, a bacterium found in 1972 [288]. Originally developed as an anti-fungal compound, it was found to have anti-proliferative effects on T cells and B cells. mTOR forms complexes with several other proteins and these complexes, mTORC1 and mTORC2, act as kinases and activate a number of other proteins responsible for cell proliferation. Growth factors signal through cell membrane receptors, activating AKT, ERK, and IKKβ [289]. These proteins phosphorylate TSC1 and TSC2, which normally function to inhibit mTOR and the mTORC1 complex. Upon phosphorylation, TSC1 and TSC2 are inactivated, and mTOR can proceed to activate proliferation [290]. Notably, the involvement of IKKβ links the mTOR and NF-κB signaling pathways [291], providing an additional mechanism by which rapamycin can modulate inflammation (**Figure 5-3**).

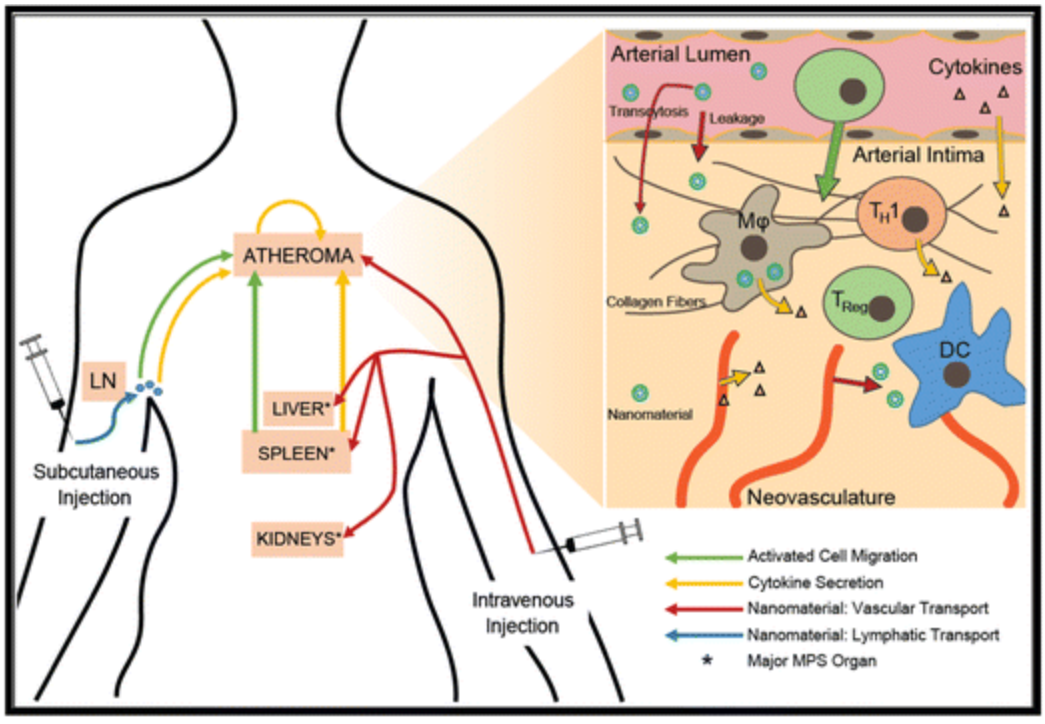

Figure 5-1. Multiple pathways to immunomodulation in atheroma by PEG-*b*-PPS nanocarriers. PEG-*b*-PPS nanocarriers can affect immunomodulation in the atheroma by changing cell migration (green), cytokine secretion (yellow), or by directly modulating cells in the atheroma. Reprinted with permission from [109] © 2016 American Chemical Society.

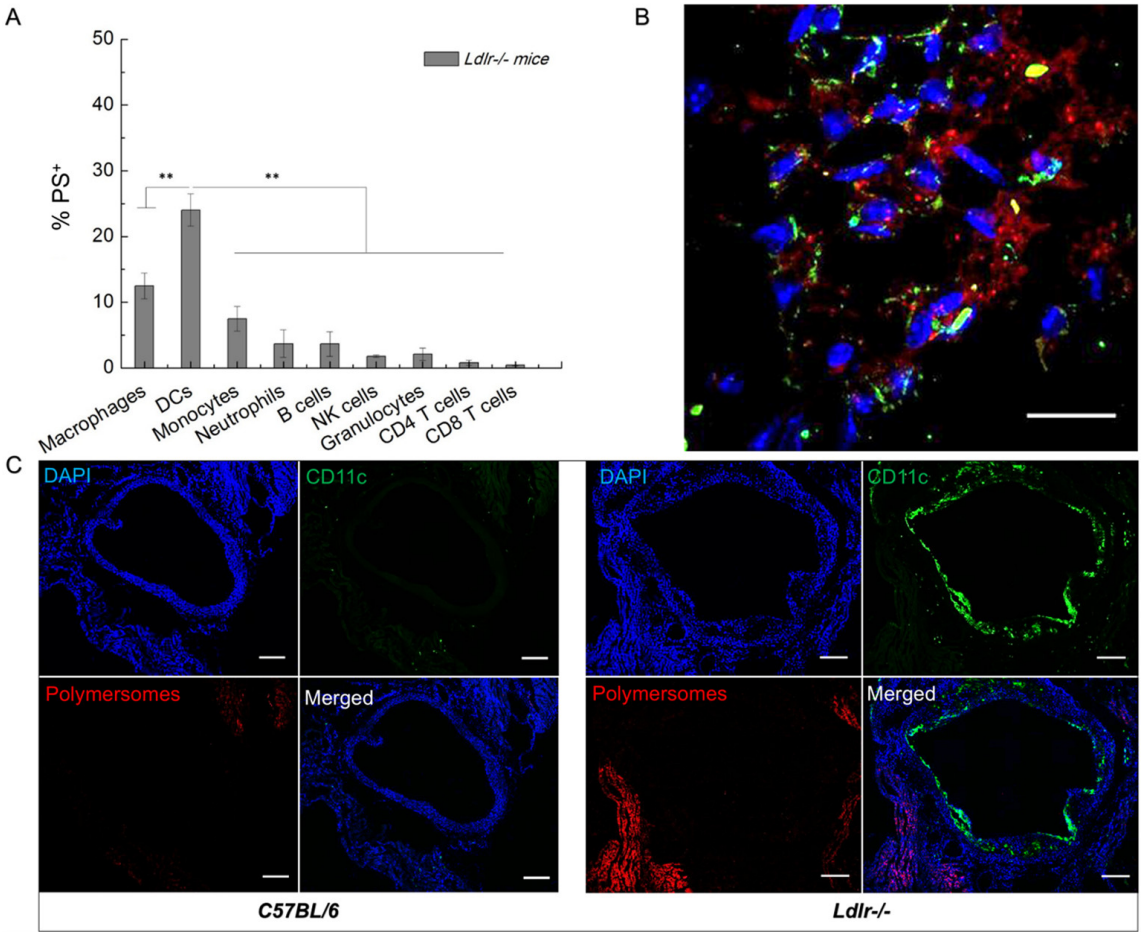

Figure 5-2. Polymersomes target aortic dendritic cells in atherosclerotic mice. (A) Distribution of polymersomes within immune cell populations in the aortas of atherosclerotic (Ldlr–/–) mice at 24 h post-injection, as analyzed by flow cytometry. N = 3 for each group; two independent experiments. Statistical significance: **p ≤ 0.005. (B) Spinning disk confocal fluorescence images (Z-stacks) of aortic tissue from an Ldlr–/– mouse after i.v. injection of Dylight 650-labeled PS 24 h prior to excision. The nuclei were stained with DAPI (blue); DCs were stained with Alexa 488 dye conjugated to anti-CD11c antibody (green); Dylight 650-labeled PS (red). Scale bar = 10 μm. (C) Confocal immunofluorescence images of aortas from C57BL/6 mice (left) and Ldlr–/– mice (right) following i.v. injection of PS-Dylight650 (red) 24 h prior to excision. Serial cross sections (5 μm thickness) were stained with DAPI (blue), and Alexa 488 dye conjugated antibodies against CD11c (green) for detection of DC. Scale bar = 50 μm. Adapted with permission from [121] © 2016 American Chemical Society.

Rapamycin is an FDA-approved drug for immunosuppression, particularly for preventing the rejection of kidney transplants [292]. It was originally believed that this immunosuppression is largely implemented by inhibiting the proliferation of T cells and B cells [293]. The anti-proliferative effects of rapamycin are not exclusive to immune cells and it can reduce cell division in other cell types, at times deleteriously [294]. As evidenced by **Figure 5-3**, reducing the proliferation of T cells and B cells directly is

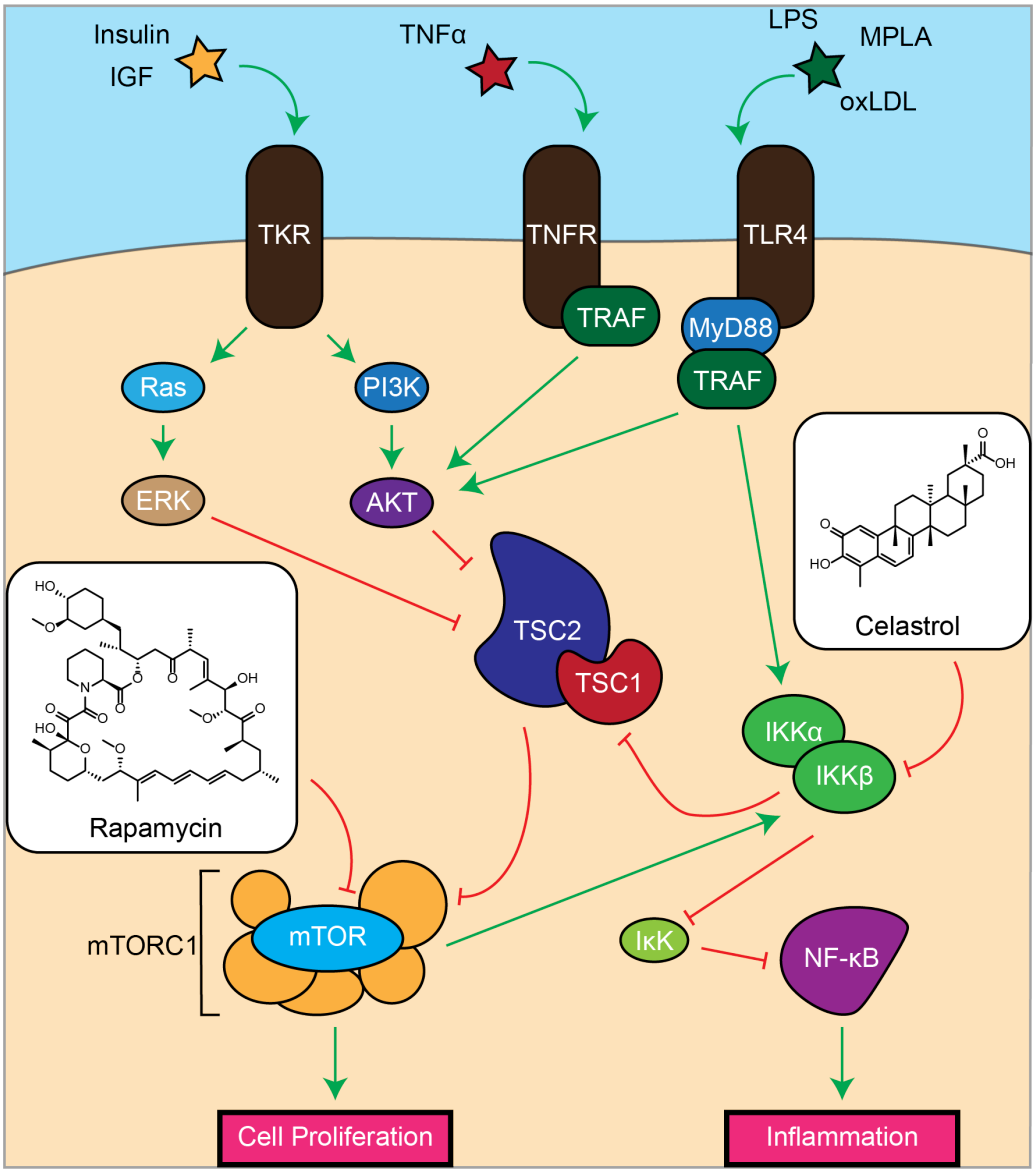

Figure 5-3. Crosstalk between the mTOR and NF-κB pathways and inhibition by rapamycin and celastrol. Green arrow indicate activation, red blunt arrows indicate inhibition.

not the only way rapamycin could function as an immunosuppressant [295]. Limiting the delivery of rapamycin to immune cells could help reduce some of the off-target anti-proliferative effects of the drug, making it a good candidate for PEG-*b*-PPS nanocarrier-based delivery.

5.2.5. Celastrol Targets, Uses, and Effects

Celastrol is a triterpenoid small molecule natural product extracted from a plant used in Chinese herbal medicine, *Tripterygium wilfordii* [296]. Unlike rapamycin, which targets mTOR specifically, celastrol appears to have many targets within cells [297]. Broadly, celastrol binds to available thiols, which appears to be important for its function [298]. Covalent binding to celastrol through a cysteine residue inhibits IKKβ [299]. IKKβ may also be indirectly inhibited by celastrol through celastrol binding to Nur77 [300], altering its interaction with TRAF2 [301]. Celastrol also inhibits HSP90, a molecular chaperone that assists in the folding and stability of other proteins [302]. Unlike HSP70, HSP90 is not involved in the initial folding of proteins but rather the final folding of specific proteins [303]. Inhibition of HSP90 therefore can affect a number of functions by inhibiting the normal functions of HSP90-client proteins. One such set of proteins is the IKKα-IKKβ complex, indicating that there is yet another way that celastrol can inhibit NF-κB signaling [304]. Celastrol is also able to induce the activation of heat shock response in cells. Celastrol can bind to Ssa1, an inhibitor of HSF1, which in turn activates HSP70 and other heat shock factor proteins [305]. HSP70 can promote cell survival and proteostasis while also inhibiting inflammatory signaling by inhibiting IKKβ and TRAF [306, 307]. Celastrol can also inhibit proteasomes [308], leading to an accumulation of unfolded proteins, which can result in the induction of the unfolded protein response, ER stress, and potentially apoptosis [309].

Celastrol is not FDA-approved as a drug for use in humans. It is currently investigated pre-clinically for use as a chemotherapeutic [310, 311], an anti-obesity therapeutic [312], a neuroprotectant [313, 314], and an anti-inflammatory compound [315]. In different cellular contexts, celastrol can be pro-apoptotic [316-318] or pro-survival [314, 319], making it difficult to predict what functional role celastrol will play in different organs and cell types. Systemic application of celastrol would therefore carry the risk of numerous off-target effects that are likely to be very patient-specific. Long-term use of celastrol at dosages where it is effective

(i.e. 1-2 mg/kg/day, I.P.) results in toxicity and organ damage in mice [320]. Thus, while Gu et al. demonstrated that daily administration of celastrol for 30 days can reduce plaque progression in an atherosclerotic mouse model, this administration regime is not sustainable or safe [321]. Celastrol has high cytotoxicity, with LD50 levels close to the effective inhibitory dose for NF-κB signaling [322]. Targeted delivery using nanocarriers may help alleviate these issues through specific delivery to the desired target cells *in vivo*.

5.3. Materials and Methods

5.3.1. Animal Use

C57BL/6 male mice, 6–8 weeks old, were purchased from Jackson Labs. All mice were housed and maintained in the Center for Comparative Medicine at Northwestern University. All animal experimental procedures were performed according to protocols approved by the Northwestern University Institutional Animal Care and Use Committee (IACUC).

Ldlr-/- female mice with a C57Bl/6 background, 4-5 weeks old, were purchased from Jackson Laboratories. All mice were housed and maintained in the Center for Comparative Medicine at Northwestern University. All animal experimental procedures were performed according to protocols approved by the Northwestern University Institutional Animal Care and Use Committee (IACUC), as supported by federal regulations, particularly the Public Health Service Policy on Humane Care and Use of Laboratory Animals.

5.3.2. Celastrol Micelle Characterization

For cryogenic transmission electron microscopy (cryoTEM), 4–5 μL of each formulation was applied to a 400-mesh lacy carbon copper grid. Specimens were then plunge-frozen with a Gatan Cryoplunge freezer. These specimens were imaged using a JEOL 3200FS transmission electron microscope operating at 300 keV at 4000× nominal magnification. All images were collected in vitreous ice using a total dose of ~10 e^{-} $Å^{-2}$ and a nominal defocus range of 2.0–5.0 μm.

Small angle X-ray scattering (SAXS) studies were performed at the DuPont-Northwestern-Dow Collaborative Access Team (DND-CAT) beamline at Argonne National Laboratory's Advanced Photon Source (Argonne, IL, USA) with 10 keV (wavelength λ = 1.24 Å) collimated X-rays. SAXS was performed on undiluted 15 mg mL^{-1} polymer formulations, as described previously. Model fitting was performed using SASView and the built-in polymer micelle model.

Dynamic light scattering (DLS) measurements were performed on 15 µg/mL polymer formulations using a Nano 300 ZS zetasizer (Malvern Panalytical, Malvern, UK), using the number average distribution for calculation of the mean diameter and polydispersity of the formulations.

Celastrol solubility, encapsulation efficiency, and loading capacity were all assessed *via* high performance liquid chromatography (HPLC) using a Thermo Scientific C18 reverse phase column with a dimethylformamide (DMF) mobile phase at 0.5 mL/min. Area under the curve quantification of celastrol absorbance at 280 nm was performed using Thermo Fisher Chromeleon 7 software. A celastrol standard curve was constructed, demonstrating good linearity between concentrations of 2 mg/mL to 12.5 µg/mL.

To determine the loading capacity of celastrol in micelles, defined here as the highest achievable mass of celastrol that can be stably loaded into 1 mg of micelles in 100 µL of 1xPBS, 1 mg of celastrol was added to 1 mg of PEG_{45}-*b*-PPS_{20}-benzyl polymer in 500 µL THF. THF was removed by vacuum desiccation and micelles were formed *via* thin film rehydration with 100 µL of 1xPBS. After micelles were formed, the solution was divided in two, with one half being purified *via* LH-20 lipophilic column filtration to remove unencapsulated celastrol and the other half being left as is. Both samples (column filtered and unfiltered) were then lyophilized and redissolved in 200 µL DMF and celastrol content was quantified *via* HPLC.

To determine the encapsulation efficiency of celastrol in micelles, defined as the percentage of the originally added celastrol mass that is stably encapsulated in micelles after filtration to remove unencapsulated celastrol, micelles were formed as described above with variable amounts of celastrol and subsequently filtered using an LH-20 column. Filtered micelles were lyophilized and redissolved in 200 µL DMF and celastrol content was quantified *via* HPLC.

To determine the solubility of celastrol in aqueous buffer, the standard saturation shake-flask method was employed. Briefly, 1 mg of celastrol was added to a glass vial along with 10 mL of 1xPBS. This solution was

heated to 37 °C, stirred for 6 hours, and then left unstirred for 18 hours. The PBS solution was centrifuged at 15,000 RCF to pellet insoluble celastrol aggregates and was subsequently lyophilized. The lyophilized powder was resuspended in 200 µL DMF and celastrol was quantified *via* HPLC.

Celastrol release from micelles into 1xPBS with or without oxidative trigger was determined as follows. Celastrol micelle formulations (500 µL) placed in Slide-A-Lyzer 10 K MWCO MINI dialysis tubes (15 mL tubes, ThermoFisher Scientific) with 13 mL 1xPBS. To each formulation was added either 100 µL of 500 µM H_2O_2 in water (Sigma Aldrich) or 100 µL of water. Tubes were placed on a shaker (250 rpm) and absorbance readings were obtained at regular intervals. Absorbance at 424 nm, an absorbance peak for celastrol, were taken using a SpectraMax M3 plate reader.

5.3.3. Chemicals

Unless specifically denoted, all chemicals and reagents were purchased from Sigma Aldrich.

5.3.4. RAW Blue Assay

NF-κB inhibition by celastrol was assayed using RAW Blue cells (supplied by Invivogen, raw-sp), a stably transfected cell line derived from RAW 264.7 macrophage-like cells, which contain the gene for secreted alkaline phosphatase (SEAP) downstream of the NF-κB promoter. Cells were seeded into a 96 well plate at 50,000 cells per well. NF-κB signaling was induced using 100 ng/mL LPS, with Cel-MC and free celastrol (0.1% THF in 1xPBS vehicle) added to the cells concurrent with LPS administration. All micelle formulations contained the same amount of polymer (15 mg/mL) but were loaded with variable amounts of celastrol, and free celastrol formulations were prepared to match the concentration of loaded celastrol within Cel-MC formulations. Free celastrol formulation were made by diluting celastrol stock solutions in THF with 1xPBS to reach the appropriate celastrol concentration and 0.1% THF in 1xPBS. Cells were incubated for 16 hours, as per assay instructions, before supernatant was collected for quantification of SEAP activity, as described by the manufacturer. Colorimetric quantification of SEAP activity was performed on an M3 plate reader (SpectraMax) at an absorbance wavelength of 630 nm.

5.3.5. RNAseq

RAW 264.7 cells were plated at $1x10^6$ cells per well of 6-well plates. Cells were treated with 100 ng/mL LPS to stimulate NF-κB signaling and were then treated in triplicate with one of the following: 1xPBS, 1 µg/mL celastrol in 0.1% THF/1xPBS, 1 ug/mL celastrol in 1 mg/mL micelle formulation in 1xPBS, 0.1% THF/1xPBS, or unloaded 'blank' micelles at 1 mg/mL in 1xPBS. Cells were treated for 2 or 6 hours to capture early and later transcriptional events. Cells were washed three times in 1xPBS before having their RNA extracted using a Qiagen RNeasy Mini Kit, as described by the manufacturer.

RNA samples were sent to Admera Health for RNA quality check using an Agilent Bioanalyzer 2100 Eukaryote Total RNA Pico Series II analysis. RNA samples that passed the quality check were used for library preparation (Lexogen QuantSeq 3' mRNA-Seq) and were sequenced (Illumina Platform 2x150 6-10M PE reads per sample). The RNA-Seq data was aligned and processed using Lexogen QuantSeq data package. Differential gene and pathway analysis utilized DE-Seq2 (https://bioconductor.org/packages/release/bioc/ html/DESeq2.html) and GSVA (http://bioconductor.org/packages /release/bioc/html/GSVA.html) using standard default parameters.

5.3.6. Anti-Inflammatory Rapamycin Administration

Formulations of rapamycin polymersomes and blank polymersomes were formed by flash nanoprecipitation using 20 mg of PEG_{17}-*b*-PPS_{36}-Thiol polymer, with or without 0.5 mg rapamycin, respectively, dissolved in THF. Sterile 1xPBS was used as the aqueous phase and reservoir solution. Fluorescently labeled polymersomes of both formulations were formed similarly, with the addition of 25 µg of DiD in the organic phase. A formulation of free rapamycin was made in a solution of 8% ethanol, 10% PEG (MW 300 g/mol), and 10% Tween 80 in 1xPBS. Briefly, rapamycin was dissolved in ethanol (3 mg/mL), and 31.2 µL was added to 1 mL of a solution of 10% PEG and 10% Tween 80 in 1xPBS (3.1% ethanol final, ~ 125 µg/mL rapamycin concentration). Vehicle was also injected without rapamycin, in which case 31.2 µL of pure ethanol was added to the 10% PEG 10% Tween 80 solution. Mice were injected subcutaneously, slightly anterior to the scapula, with 1 mg/kg doses of rapamycin, or equivalent injections of vehicle or blank polymersomes, N = 3 per treatment group. Injections were performed on days 1, 4 and 7, with the final set

of injections containing fluorescently labeled polymersomes, when applicable. Mice were sacked on day 8, and the draining (brachial) lymph nodes were collected, along with the spleens. Organs were mechanically homogenized in RPMI media and passed through a 70 μm cell strainer before being stained for flow cytometry.

Splenic cells were first treated with ACK lysis buffer for 5 min on ice before being spun down and resuspended in blocking buffer. Cells were stained with Zombie Aqua as a fixable live/dead stain and FcRs were blocked with anti-mouse CD16/CD32. Cells were stained with a cocktail of antibodies in three panels. Panel 1: anti-mouse CD45 FITC, anti-mouse CD3 APC-Cy7, anti-mouse CD4 PE-Cy5, anti-mouse CD8a PE-Cy7, anti-mouse CD19 Pacific Blue, anti-mouse CD49b PerCp-Cy5.5, and anti-mouse CD25 PE. Panel 2: anti-mouse CD11b PerCp-Cy5.5, anti-mouse CD11c Pacific Blue, anti-mouse I-A/I-E FITC, anti-mouse B220 PE, anti-mouse Gr-1 APC-Cy7, and anti-mouse CD8a PE-Cy7. Panel 3: anti-mouse CD11b PerCp-Cy5.5, anti-mouse CD11c Pacific Blue, anti-mouse F4/80 FITC, anti-mouse Ly-6C APC-Cy7, and anti-mouse Ly-6G PE-Cy7. After washes, cells were fixed by IC cell fixation buffer (Biosciences). Flow cytometry was performed with FACSDiva on a LSRII flow cytometer (BD Biosciences), with the APC channel used to detect the DiD loaded into polymersomes. Data was analyzed using Cytobank online software. Gating strategy available in Appendix A (**Figure A-5**).

5.3.7. Ldlr-/- Mouse Atherosclerosis Induction and Treatment

Ldlr-/- female mice were fed a normal diet until they were 2-3 months old, at which point they were switched to a high-fat diet (Tekklad TD 88137 42% calories from fat). Mice were fed a high-fat diet for 3 months prior to the beginning of treatment.

Four formulations were made for *in vivo* use: 15 mg/mL polymer blank micelle formulation, 15 mg/mL polymer 100 ng/mL celastrol micelle formulation, 200 ng/mL celastrol in a 1:1 DMSO:1xPBS formulation, and a vehicle control of 1:1 DMSO:1xPBS formulation. Both micelle formulations were injected intravenously (IV) *via* tail vein injection (100 μL per injection). The free celastrol and vehicle control formulations were injected intraperitoneally (IP) at 50 μL per injection. Injections were performed on high-fat diet mice (3 months on diet before the beginning of treatment) under isoflurane once a week for 18

weeks. Mice remained on high-fat diet for the duration of treatment. Mice were sacrificed one week after the end of treatment, and organs were harvested for flow cytometry or were mounted for histology.

5.3.8. Flow Cytometry of Celastrol Treated Ldlr-/- Mice

Organs collected from mice were processed for flow cytometry as described previously [121]. Blood was centrifuged to collect all blood cells. Red blood cells were subsequently lysed using ACK lysis buffer, resulting in a single cell suspension of blood immune cells. Spleens and lymph nodes were mechanically disrupted with a 70 μm nylon filter and a syringe plunger, to form a single cell suspension. Splenocytes were additionally treated with ACK lysis buffer to lyse red blood cells. The aortas were sliced into small pieces (~ 1 mm^2) and incubated at 37° C at 300 rpm for 30 minutes in an enzyme cocktail to free cells: 125 U/mL collagenase XI, 60 U/mL hyaluronidase I-S, 60 U/mL DNase I (Roche), and 450 U/mL collagenase I in HBSS buffer. The aorta pieces and buffer were then strained and mechanically disrupted through a 70 μm nylon filter with a syringe plunger.

All single cell suspensions were then incubated for 15 minutes in a blocking buffer containing a fixable viability dye, Zombie Aqua, and an FcR blocking antibody anti-CD16/32. Cells were then stained with one of two antibody panels. Panel 1: FITC anti-CD45, APC/Cy7 anti-CD3, PE anti-CD4, APC anti-CD8, Pacific Blue anti-CD19, PerCP/Cy5.5 anti-NK1.1. Panel 2: FITC anti-CD45, PerCP/Cy5.5 anti-CD11b, Pacific Blue anti-CD11c, PE/Cy5 anti-I-A/I-E, PE/Cy7 anti-F4/80, PE CD86, APC anti-Ly6C, APC/Cy7 anti-Ly6G. Cells were washed, fixed, and analyzed using a BD LSR II. Data was analyzed using Cytobank online software. The gating strategy is available in the supporting information (Appendix **Figure A-6**).

5.3.9. Histological Staining and Analysis

Aortas were carefully dissected from mice to preserve vascular structure and were trimmed and embedded in optimal cutting temperature (OCT) compound for frozen tissue sectioning. Aortas were serially sectioned into 10 μm thick slices, 8-10 sections per slide. Aortic cross sections were stained with Oil Red O, as described previously [323], for fluorescence imaging. Images were taken on a Leica DM6B

fluorescent microscope at 20x objective magnification with automated image stitching. Quantification of Oil Red O fluorescent staining was performed using a custom Python script.

5.4. Results

5.4.1. Subcutaneous Administration of Rapamycin Polymersomes

I have demonstrated in previous chapters the ability to form monodisperse PEG-*b*-PPS polymersomes using flash nanoprecipitation that are sterile. To demonstrate that these sterile polymersomes can be utilized for anti-inflammatory therapeutic purposes, I first sought to utilize them in healthy mice using an FDA-approved immunosuppressant. I chose rapamycin as it has low water solubility (logP = 6.18) and has a number of effects in a number of cell types, as discussed in section 5.2.4. I found previously that rapamycin was encapsulated into polymersomes easily, with an encapsulation efficiency of 65.6% (**Table 3-1**). Mechanistically, rapamycin is typically thought to be immunosuppressive by acting directly on T cells and B cells. PEG-*b*-PPS nanocarriers are not internalized by those cell types, however, raising questions of whether rapamycin would still function in its immunosuppressive capacity. PEG-*b*-PPS nanocarriers are internalized by phagocytic cell types after subcutaneous administration [191], a typical route of administration for free rapamycin [324]. I hypothesized that encapsulated rapamycin may be administered less frequently and at lower doses than normal, since it should be delivered more directly to immune cells and would be less likely to be degraded extracellularly. Rapamycin is normally administered daily at doses of 1.5-3 mg/kg/day in mice for sustained allograft survival [325-327]. As such, I administered rapamycin once every three days, at an effective average dose of 0.33 mg/kg/day.

At this reduced dose, free rapamycin was not able to alter T cell populations, while rapamycin-loaded polymersomes decreased T cell populations and CD8+ dendritic cells (**Figure 5-4a**). The only changes observed for free rapamycin-treated mice was a small increase in granulocytes (**Figure 5-5g,h**). The reduction of CD4+ and CD8+ T cells by rapamycin polymersome treatment saw an increase in the double negative T cell share of the T cell population (**Figure 5-4b**). This was due to an overall drop of T cells, particularly in the spleen (**Figure 5-4c**), not due to an increase in DN T cells. As mentioned previously,

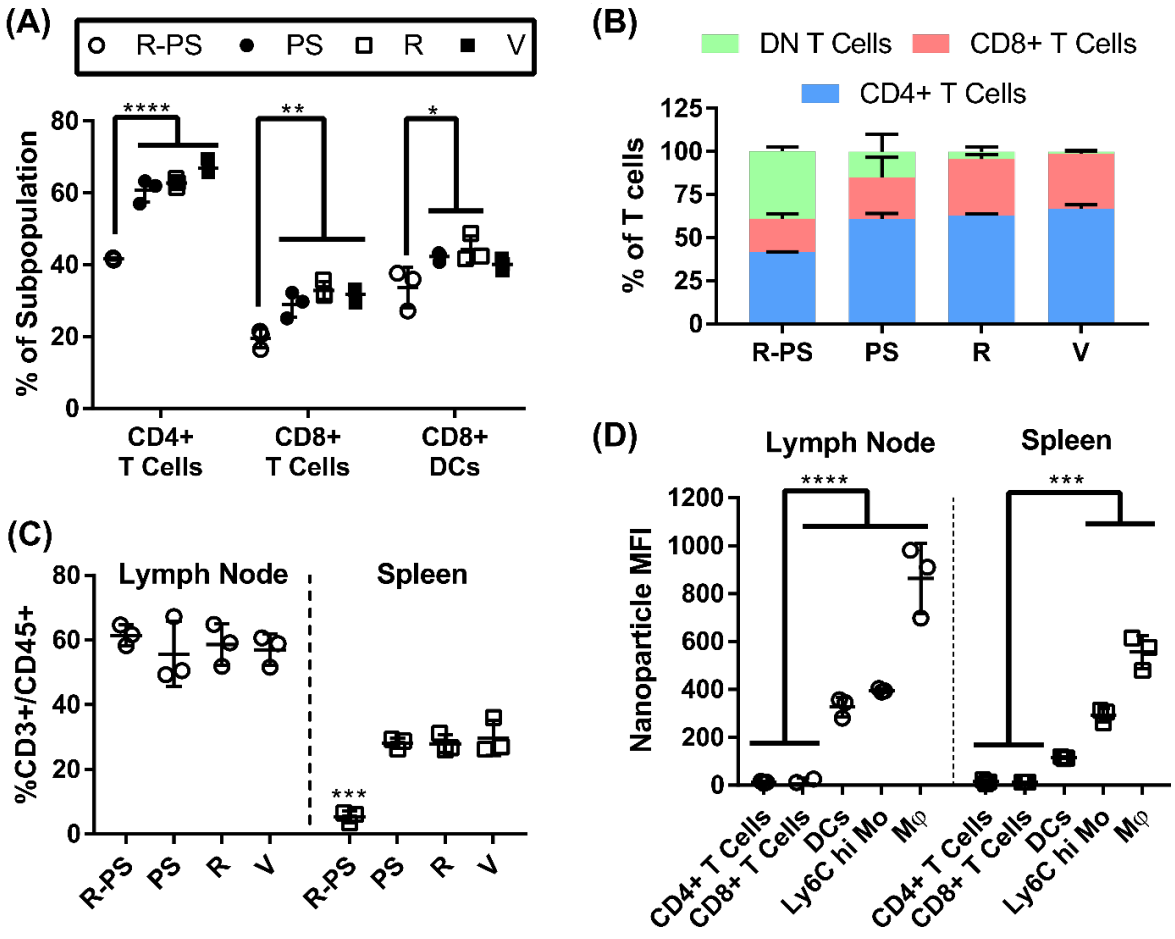

Figure 5-4. In vivo delivery of theranostic rapamycin/DiD-loaded polymersomes formed by flash nanoprecipitation. (A) Percentage of CD8 + T cells (CD45 + CD3 + CD4 − CD8 +) and CD4 + T cells (CD45 + CD3 + CD4 + CD8 −) within the total T cell population (CD45 + CD3 +) and percentage of CD8 + DCs (CD11c + I − A/I − E + CD8 +) within the total DC (CD11c +) population. Treatment groups were rapamycin polymersomes (R-PS), free rapamycin, blank polymersomes, and vehicle (PBS). (B) T cell subpopulations as a percent of total T cell population for all four treatment groups. (C) T cells in the spleen and lymph nodes, as a percentage of CD45 + cells. (D) Median fluorescence intensity of the polymersome channel for selected cell populations in the spleen and lymph nodes of mice administered rapamycin/DiD-loaded polymersomes. N = 3, statistical significance determined by Tukey's multiple comparisons test, *p < 0.05, **p < 0.01, ***p < 0.001, ****p < 0.0001. Reprinted with permission from [164] © 2017 Elsevier.

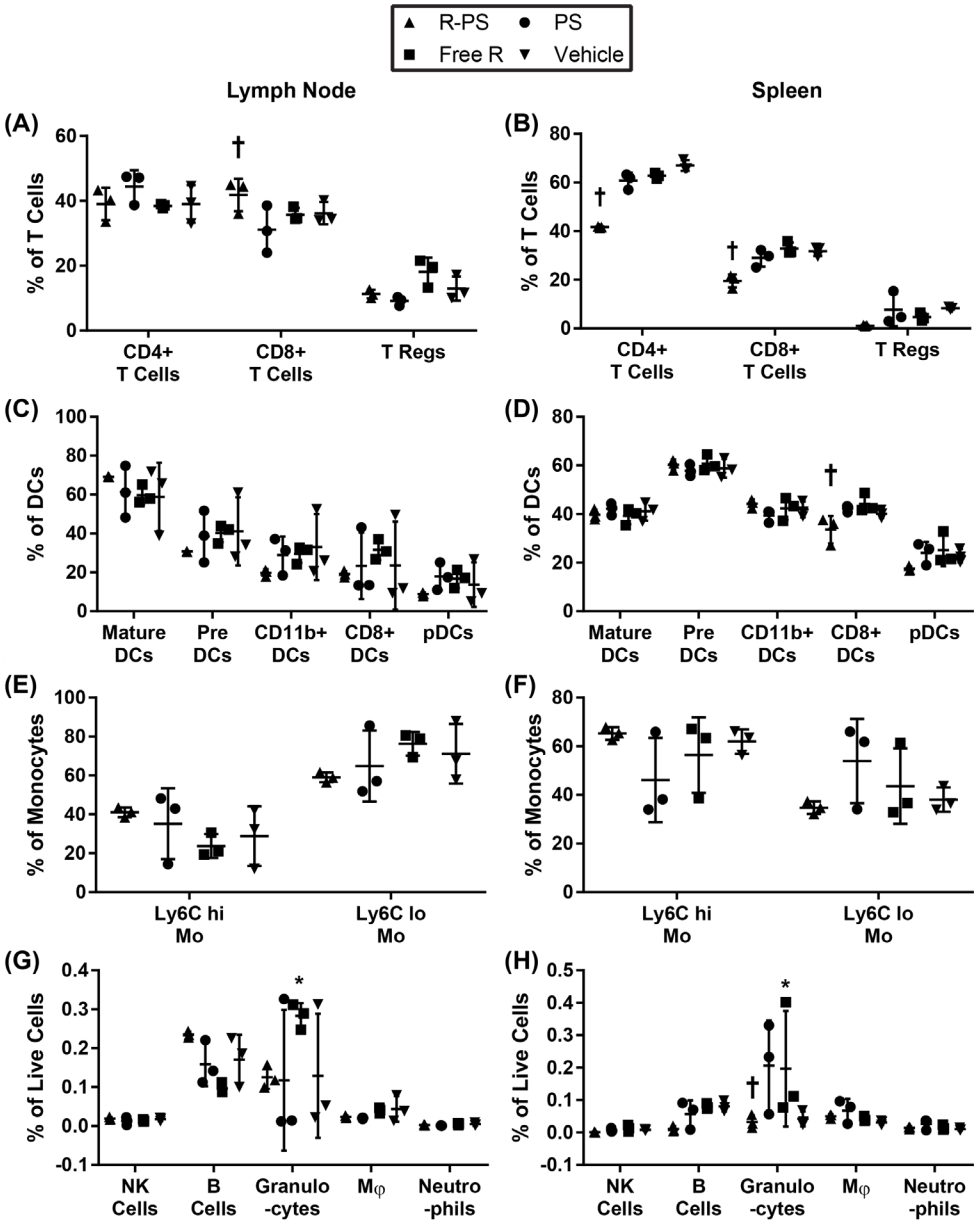

Figure 5-5. Additional in vivo effects of rapamycin polymersomes. Percentages of total live cells in the lymph nodes (A, C, E, G) and spleen (B, D, F, H) that are T cells, DCs, plasmacytoid DCs, monocytes, B cells, granulocytes, macrophages, and neutrophils. † indicates rapamycin polymersome treated populations that were significantly altered compared to blank polymersomes. * indicates free rapamycin treated populations that were significantly altered compared to vehicle, $p > 0.01$. Reprinted with permission from [164] © 2017 Elsevier.

this reduction in the number of T cells was not due to uptake of the rapamycin polymersomes by T cells themselves, but rather by the uptake of the rapamycin polymersomes by macrophages, monocytes, and dendritic cells in the lymph nodes and spleen (**Figure 5-4d**). Rapamycin is therefore able to exert an immunosuppressive effect on T cell numbers through antigen presenting cells, rather than only working directly on the T cells themselves.

5.4.2. Characterization of Celastrol Micelles

Having demonstrated that PEG-*b*-PPS nanocarriers are capable of acting as effective delivery vehicles for an anti-inflammatory drug, I sought to demonstrate the same in a disease model that features a pro-inflammatory pathology. Ldlr-/- mice develop atherosclerosis after 3 months on a high fat diet. The atherosclerotic plaques feature a number of inflammatory cell types, develop due to inflammatory signaling,

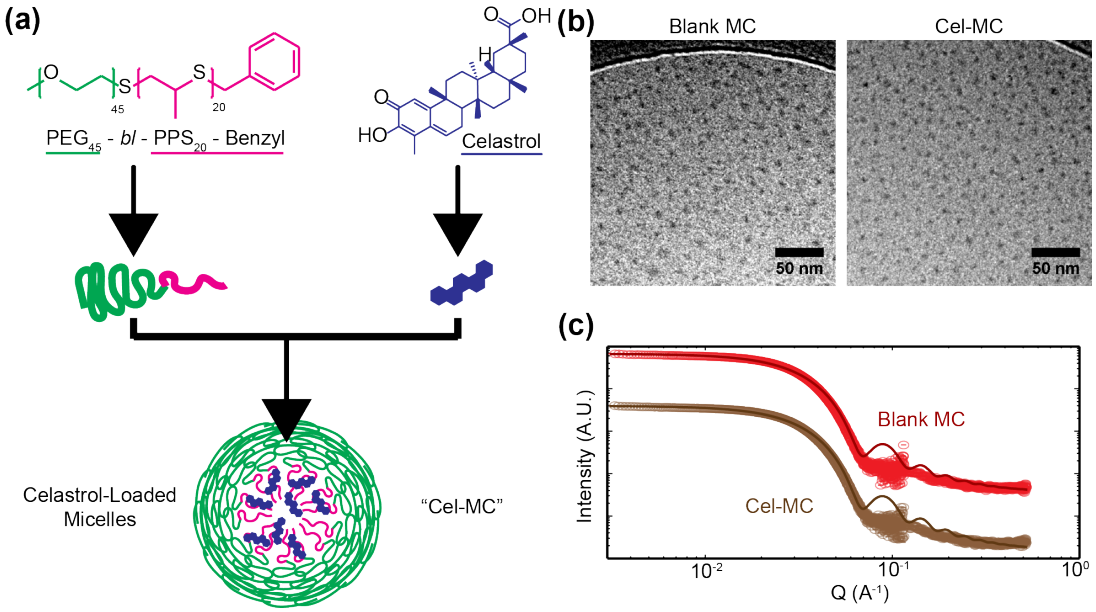

Figure 5-6. Size and morphological characterization of Blank MC and Cel-MC. (a) Schematic of polymer and celastrol chemical structures and a cartoon figure of an assembled micelle loaded with celastrol. (b) Cryogenic transmission electron micrographs of Blank MC and Cel-MC, scale bars = 50 nm. (c) Small angle x-ray scattering transformed data and polymer micelle model fits. Graphs are vertically offset for ease of visualization. Reproduced from [223] with permission from The Royal Society of Chemistry.

and demonstrate disease progression exacerbated by inflammatory signaling. This is particularly driven by NF-κB signaling. To target NF-κB signaling, I chose to utilize the small hydrophobic molecule celastrol, which inhibits NF-κB through a number of mechanisms, described in section 5.2.5. I loaded celastrol into micelles (**Figure 5-6**), which demonstrate broad uptake by immune cells after IV injection [121]. Micelles loaded with celastrol (Cel-MC) were morphologically indistinguishable from unloaded or 'blank' micelles by cryoTEM (**Figure 5-6b**) and SAXS modeling (**Figure 5-6c**). Celastrol micelles encapsulating different amounts of celastrol showed a slight relationship between amount of celastrol loaded and micelle size, indicating the slight increase in micelle diameter to incorporate the encapsulated celastrol in the hydrophobic volume (**Table 5-2**).

Celastrol demonstrated high encapsulation efficiency when loaded at 1 wt % with polymer (96.1 ± 0.8%) (**Figure 5-7a**). At higher weight percentages there was diminished encapsulation efficiency, though more celastrol was encapsulated overall. This relationship demonstrated diminishing returns (**Figure 5-7b**). At 70 wt%, encapsulation efficiency dropped to 31.1 ± 3.4%. The loading capacity of celastrol in micelles was 22% (2.2 mg celastrol in 10 mg polymer). Quantification of celastrol solubility in 1xPBS at 37 °C found that it was sparingly soluble, with 3.5 μg/mL detected in 1 mL 1xPBS. The highest concentration of PEG-*b*-PPS micelles that have been made is 200 mg/mL polymer. If loaded at the loading capacity of celastrol, that would result in 44 mg of celastrol solubilized per 1 mL 1xPBS, over 10,000 times higher than free celastrol. Celastrol loaded within micelles demonstrated very gradual release, with 8% released over 48 hours (**Figure 5-7c**). However, in the presence of oxidative species that cause the destabilization of PEG-*b*-PPS nanocarriers, celastrol was rapidly released, with 100% release at the 24-hour timepoint. This suggests that PEG-*b*-PPS nanocarriers should be able to prevent leakage of celastrol from the nanocarriers until they are taken up by cells and introduced to reactive oxygen species in the endolysosomal pathway.

5.4.3. *In vitro* Inhibition of NF-κB by Celastrol

Celastrol is known to inhibit NF-κB through a number of mechanisms. I wanted to determine whether the loading of celastrol into micelles deleteriously affected its ability to inhibit NF-κB, either by reducing its ability to access its targets by preventing the celastrol from leaving the nanocarrier,

inappropriately localizing celastrol to the endolysosomal pathway instead of the cytoplasm, or by stopping the activity of celastrol by binding any free thiol groups on the end of PEG-*b*-PPS polymer to celastrol. To

Table 5-2. Micelle diameter and polydispersity from dynamic light scattering and SAXS modelling. Reproduced from [223] with permission from The Royal Society of Chemistry.

	Celastrol Loaded (µg)	DLS Diameter (nm)	PdI	SAXS Model Diameter (nm)
Blank MC	0	15.5	0.045	17.9
Cel-MC	0.001	14.8	0.063	18.0
	0.1	16.4	0.053	20.2
	10	16.3	0.058	23.4
	1000	17.9	0.032	Not Performed

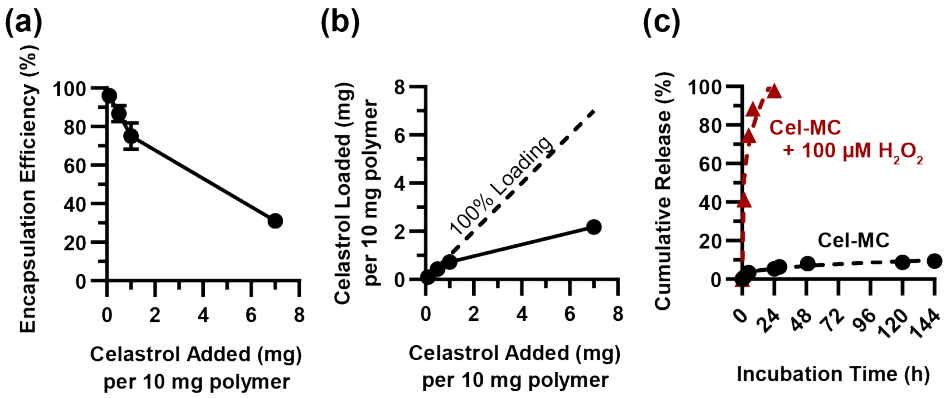

Figure 5-7. Encapsulation efficiency, loading capacity, and release of celastrol from micelles. (a) Encapsulation efficiency of celastrol in micelles when loaded at different starting amounts of celastrol. 'Celastrol Added' represents the amount of celastrol initially available to be loaded into 10 mg of polymer, n=3. (b) Loading capacity of celastrol in micelles. 'Celastrol Added' and 'Celastrol Loaded' represent the amount of celastrol initially available to be loaded into micelles and the amount of celastrol actually loaded into micelles, respectively, per 10 mg of polymer, n=3. (c) Cumulative release of celastrol from celastrol micelles into 1xPBS. Average values plotted on graph, error bars (S.D.) not visible due to low variability compared to y-axis scale, n=3.multiple comparisons test, *p < 0.05, **p < 0.01, ***p < 0.001, ****p < 0.0001. Reproduced from [223] with permission from The Royal Society of Chemistry.

test whether celastrol was still effective as an inhibitor, I utilized RAW Blue cells, which secrete alkaline phosphatase upon NF-κB stimulation, which can be triggered by LPS. While keeping the concentration of micelle polymer constant, a concentration series of encapsulated celastrol was delivered to RAW Blue cells. Matching concentrations of free celastrol were also used for comparison (**Figure 5-8a**). I found that at high concentrations of celastrol (>1 μg/mL), both free and encapsulated celastrol effectively inhibited NF-κB signaling. However, free celastrol stopped inhibiting NF-κB signaling at concentrations <0.1 μg/mL, with a

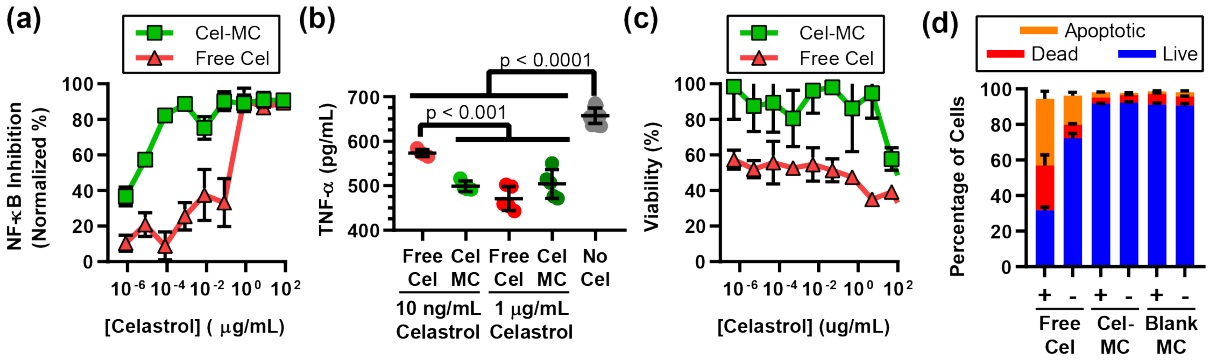

Figure 5-8. NF-κB inhibition, and cytotoxicity of Cel-MC in RAW 264.7 cells. (a) RAW Blue colorimetric assay of NF-κB expression at varying concentrations of celastrol. Y-axis is normalized such that 0% represents cells untreated with LPS and 100% represents cells treated with LPS but not treated with any celastrol. X-axis is on a log scale. n=4 (b) ELISA results for TNF-α secretion by RAW 264.7 cells treated with LPS and either free celastrol or Cel-MC. Celastrol treatments were at 10 ng/mL or 1 μg/mL concentrations. All data points shown on graph, n = 5 for treatment conditions, n = 12 for the LPS control. P values shown on graph are from Tukey's multiple comparison test. (c) RAW 264.7 cell viability with either free celastrol or Cel-MC treatment at varying concentrations of celastrol. Y-axis represents viability normalized by delivery vehicle or formulation, with 100% representing the mean viability of cells treated with vehicle but no celastrol, and 0% representing methanol-treated cells. X-axis is on a log scale. n = 4. (d) Stacked bar graph of RAW 264.7 viability split into three categories: live, dead, or apoptotic. Cells were either LPS treated (+) or not (-). n = 5 for each treatment group. For (a)-(d), error bars represent standard deviation. Reproduced from [223] with permission from The Royal Society of Chemistry.

half maximal effective concentration (EC50) of 0.2 μg/mL. Meanwhile micelle celastrol continued inhibiting NF-κB signaling at much lower concentrations, with an EC50 of 4.2 pg/mL, a concentration nearly 50,000 times lower. I also sought to examine the efficacy of inhibition by assessing the production and secretion of a pro-inflammatory cytokine downstream of NF-κB signaling, TNF-α. At concentrations where both free and encapsulated celastrol were found to inhibit NF-κB in RAW Blue cells, I found that they both effectively inhibited the secretion of TNF-α (**Figure 5-8b**). At 10 ng/mL celastrol, encapsulated celastrol inhibited TNF-α secretion as effectively as it had at 1 μg/mL, while free celastrol saw a reduced effect.

As mentioned previously, celastrol has a narrow therapeutic window due to cytotoxicity. Encapsulation in micelles appeared to drop the EC50, allowing for the use of celastrol at lower concentrations that may be less cytotoxic. To examine more closely the cytotoxicity of celastrol at the concentrations used in **Figure 5-8a**, I utilized the same RAW Blue cells and checked for viability. At high concentrations (>10 μg/mL), both celastrol micelles and free celastrol were cytotoxic to cells. However, at all lower concentrations, encapsulated celastrol was no longer cytotoxic (**Figure 5-8c**). In contrast, free celastrol was cytotoxic at all tested concentrations, though less so at lower concentrations. In further examination of the cell death, I found that free celastrol induced apoptosis in cells and that this induction of apoptosis was exacerbated by the presence of LPS (**Figure 5-8d**).

5.4.4. RNAseq of Free and Encapsulated Celastrol

Celastrol has a number of targets and potential pathways that it can affect. Given that I demonstrated that encapsulated and free celastrol have different EC50 values and different cytotoxicities, I wanted to ensure that encapsulation was not resulting in unintended changes in the transcriptional output of celastrol inhibition but was rather a result of improved delivery of celastrol to the cells. To interrogate this question, I utilized RNAseq on all mRNA produced by RAW 264.7 cells treated with LPS to stimulate NF-κB signaling. LPS-stimulated RAW 264.7 cells were treated with free or encapsulated celastrol (along with vehicle controls) at 1 μg/mL, the lowest concentration where both free and encapsulated celastrol inhibited NF-κB with minimized cytotoxicity, for 2 or 6 hours to capture early and later transcriptional bursts. Heatmap analysis of the 2084 genes that were differentially expressed due to treatment found that free and

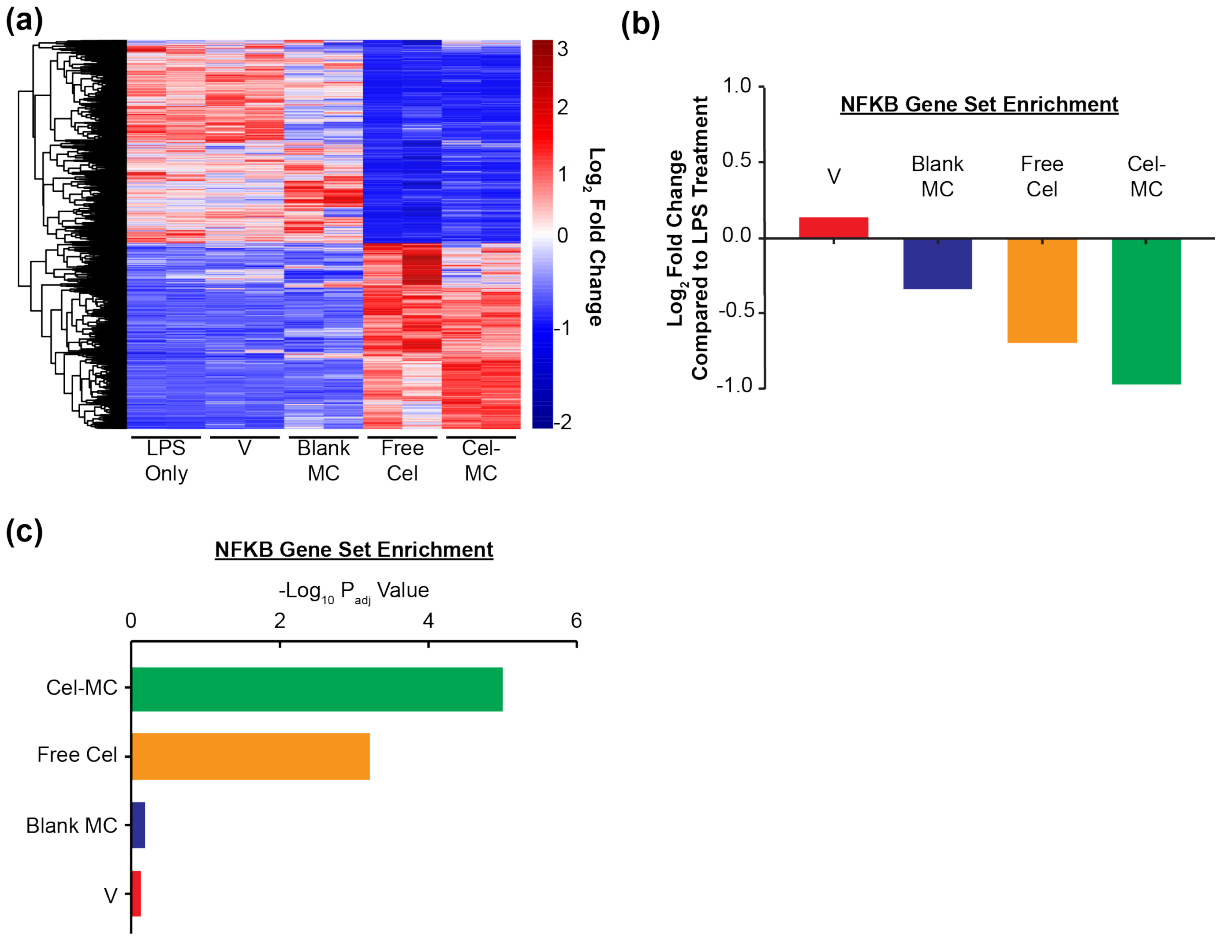

Figure 5-9. RNAseq analysis of transcriptional effects of free celastrol and Cel-MC treatment of LPS-stimulated RAW 264.7 cells. (a) Heatmap analysis of genes significantly affected by free celastrol. DE-Seq2 analysis identified 2649 genes significantly altered by free celastrol treatment of LPS-treated RAW 264.7 cells after 2 hours. Adjusted P-value (Padj)<0.1. This gene set was used to generate a heatmap with the following conditions: LPS-treated RAW 264.7 cells (LPS), LPS + celastrol vehicle (V), LPS + blank micelles (Blank MC), LPS + free celastrol (Free Cel), and LPS + Cel-MC (Cel-MC). Red and blue colors respectively represent genes that are overexpressed and underexpressed in that sample compared to the other cohorts. (b) Fold Change and (c) Padj of the NF-κB gene set. Gene set variation analysis of the NF-κB pathway in LPS-treated RAW 264.7 cells treated for 2 hours with vehicle (V), blank MC, free celastrol, or Cel-MC. Fold change is relative to RAW 264.7 cells treated with only LPS. Reproduced from [223] with permission from The Royal Society of Chemistry.

encapsulated celastrol had similar effects on transcription (**Figure 5-9a**). Notably pro-inflammatory genes il1b, tnf, and nfatc were downregulated while anti-inflammatory genes lrp1, irf7, and slpi were significantly upregulated (See appendix B for tables of up and downregulated genes). When examining the NF-κB gene set, both free and encapsulated celastrol inhibited transcription, though celastrol micelles inhibited transcription to a greater degree (**Figure 5-9b**) and more significantly (**Figure 5-9c**).

5.4.5. *In vivo* Alteration of Inflammatory Cell Types by Celastrol Micelles

After demonstrating that celastrol-loaded micelles could effectively inhibit inflammatory signaling *in vitro*, I sought to apply them to atherosclerosis, where inflammation initiates and exacerbates the development of atherosclerotic plaques. Previous work demonstrated that celastrol could help alleviate plaque burden in atherosclerotic mice, though the dosage of celastrol was too high and required daily IP administration – not at all useful for treatment in patients [321]. With an eye toward avoiding toxicity issues, I utilized a concentration of encapsulated celastrol, 100 ng/mL, that demonstrated good inhibition of NF-κB and low cytotoxicity *in vitro*. 10 μg/mL celastrol concentrations were toxic in mice (Figure 5-10), though Cel-MC formulations were less toxic than free celastrol formulations. Intriguingly, polymersome celastrol formulations were as toxic as free celastrol, significantly more toxic than Cel-MCs. This demonstrates that altering the morphology of the nanoparticle can result in different therapeutic outcomes (i.e. toxicity) while keeping the therapeutic concentration the same. Daily administrations are untenable and PEG-*b*-PPS nanocarriers have extended circulation times compared to unencapsulated cargoes, so I decided to perform weekly administrations of the celastrol micelles. I chose to perform IV administration, a route of administration that is tried-and-true for PEG-*b*-PPS nanocarriers and is more applicable to humans than IP injections. Free celastrol, due to the high organic solvent concentrations required to solubilize it, cannot be injected intravenously. Therefore, I injected it intraperitoneally, as is the standard in the field. Ldlr-/- mice were fed a high fat diet for 3 months prior to the start of treatment to initiate the development of atheromas. Treatment of the mice was performed for three months, longer than typical for celastrol treatments.

Toxicity is a consistent concern with celastrol treatment, so I checked for behavioral signs of toxicity, namely weight loss and loss of appetence. Celastrol treatment was well tolerated by the ldlr-/- mice. Mouse

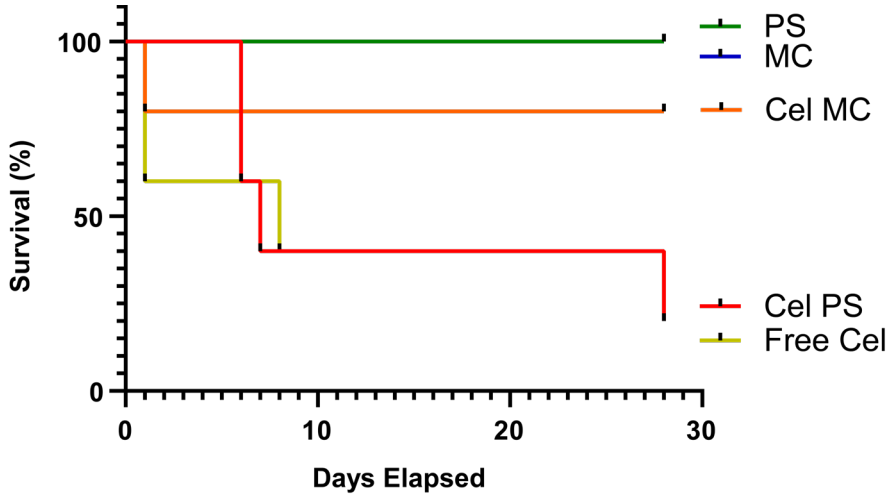

Figure 5-10. Mouse survival at 10 µg/mL celastrol doses. Kaplan Meier survival curves for mice (n=5 per treatment) treated once a week with 10 µg/mL celastrol formulations: celastrol polymersomes (Cel PS), celastrol micelles (Cel MC), or free celastrol (Free Cel). Also included are survival curves for blank polymersomes and blank micelles (PS and MC, respectively). Curves are significantly different (Mantel-Cox test, p = 0.0059).

body weight did not decrease over the course of treatment with neither free nor encapsulated celastrol (**Figure 5-10a**). Additionally, mice did not consume less food while treated with celastrol (**Figure 5-10b**). After three months of treatment, mice were sacrificed and organs were collected for histology and flow cytometry of immune cell populations.

Cel-MC significantly altered immune cell populations in the atheroma of the ldlr-/- mice, as assessed by flow cytometry. In contrast, free celastrol had a much more muted effect on immune cell populations, as can be visualized by the $\log_2$ fold change heatmap (**Figure 5-11a)**. There was no cell population where free celastrol resulted in a significant change in the population compared to a vehicle control. In contrast, there were a number of immune cell populations that were significantly altered by Cel-MC. Neutrophils associated with the atheroma and in the blood were significantly reduced by Cel-MC treatment (**Figure 5-11b,c**). Monocytes in the blood were also significantly reduced by Cel-MC treatment, though only compared to free celastrol (**Figure 5-11d**). Also reduced were NK cells in the atheroma (**Figure 5-11e**). There was an increase in NK cells in the spleen in mice treated with Cel-MC (**Figure 5-12a**). The

only significant findings for free celastrol was an increase in dendritic cells in atheroma and T cells in the spleen, but only when compared to Cel-MC treatment (**Figure 5-12b,c**).

5.4.6. *In vivo* Reduction of Atheroma Area by Celastrol Micelles

The relationship between inflammatory cell populations in the atheroma and overall disease prognosis in humans is not a settled question. As such, I sought to utilize a better-established criterion of successful treatment of atherosclerosis, namely the plaque staining area. This was established histologically using Oil Red O, a stain for lipid deposits. Representative images of Oil Red O staining demonstrate that Cel-MC treatment reduced the plaque staining area in ldlr-/- mice (**Figure 5-13a**). I quantified the plaque staining area and found that Cel-MC significantly decreased the staining area compared to the blank micelle vehicle control (**Figure 5-13b**).

5.5. Discussion

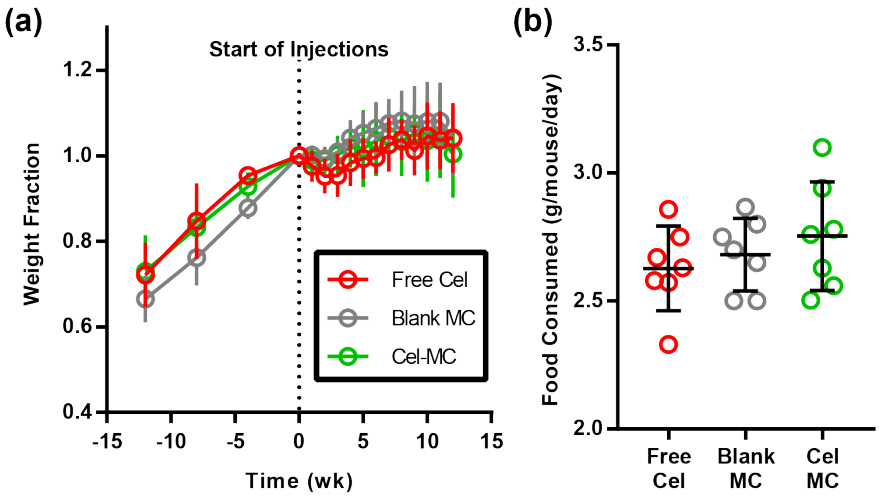

Figure 5-11. Mouse body weight and food consumption analysis. (a) Average mouse body weights in the weeks before and after the initiation of treatment with free celastrol, blank MC, and Cel-MC. N=8 for free celastrol and blank MC groups and n=9 for Cel-MC group. Error bars are standard deviation, x-axis time 0 is the initiation of treatment. (b) Average food consumed during treatment by mice within the three treatment groups, n=7 for all treatment groups, bars represent the mean and standard deviation. Reproduced from [223] with permission from The Royal Society of Chemistry.

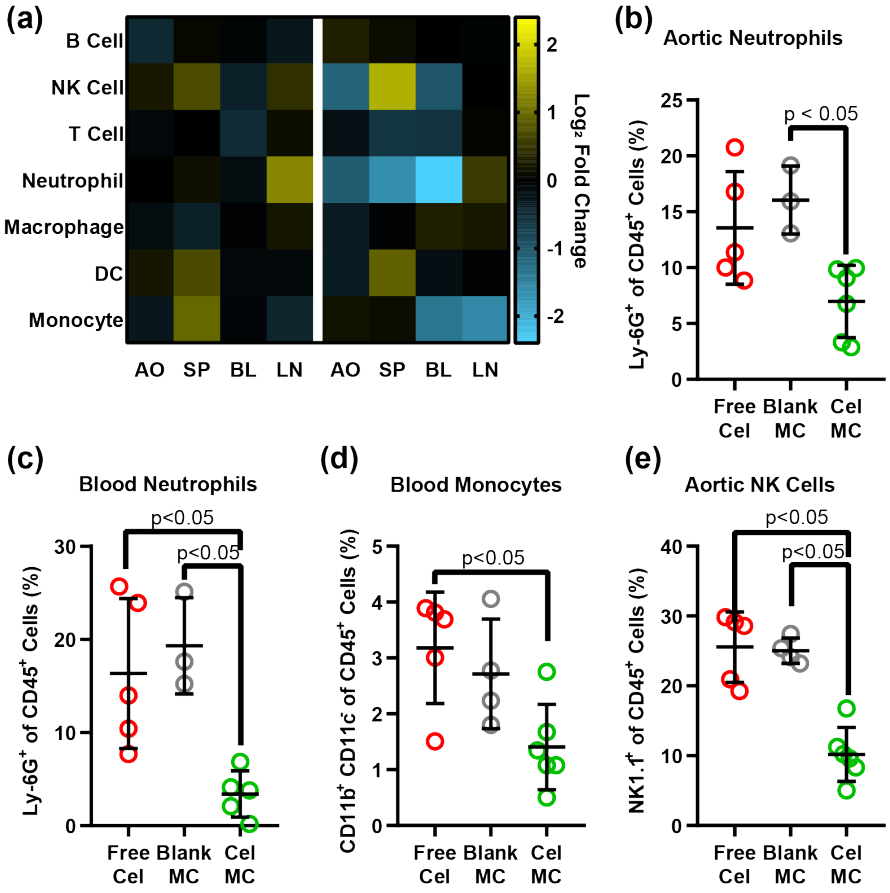

Figure 5-12. Flow cytometric analysis of changes in cell populations in Idlr-/- mice treated with free celastrol or Cel-MC. (a) Heatmap of fold change in cell populations. Each row represents an immune cell population, each column represents the organ from which the cells were isolated. Heatmap is on a log2 scale, with yellow representing a fold increase and blue representing a fold decrease in that cell population, compared to the Blank MC control. Cell population as a percent of all immune cells for a given population in a given organ are also provided for: (b) aortic neutrophils, (c) aortic NK cells, (d) blood monocytes, and (e) blood neutrophils. All significant p-values are displayed on their graphs, calculated using Dunn's multiple comparisons test. Cells were identified as follows: B cells – CD45+ CD19+, NK cells – CD45+ NK1.1+, T cells – CD45+ CD3+, Neutrophils – CD45+ Ly-6G+, Macrophages – CD45+ CD3- NK1.1- CD19- Ly-6G- F4/80+, Dendritic cells – CD45+ CD3- NK1.1- CD19- Ly-6G- F4/80- CD11c+, Monocytes – CD45+ CD3- NK1.1- CD19- Ly-6G- F4/80- CD11c- CD11b+ Ly-6C+. Reproduced from [223] with permission from The Royal Society of Chemistry.

Rapamycin loaded into polymersomes were able to reduce T cell populations in the spleen of C57Bl/6 mice, demonstrating a classic result of rapamycin treatment. Unlike typical rapamycin treatment, however, rapamycin polymersomes were administered at a lower dose (1 mg/kg every 3 days vs. 1.5-3 mg/kg/day) and less frequently. Rapamycin treatment is typically thought to reduce proliferation in T cells and B cells, resulting in its immunosuppressive effects. With rapamycin polymersomes, however, rapamycin was not able to exert its effects directly on T cells. As polymersomes are not internalized by T cells, but rather by phagocytic cells such as macrophages, monocytes, and dendritic cells, the change in T cell populations had to have been mediated by those cell populations. This robust response to rapamycin loaded in polymersomes suggests that the targeting intrinsic to the nanocarrier morphology allows for lower

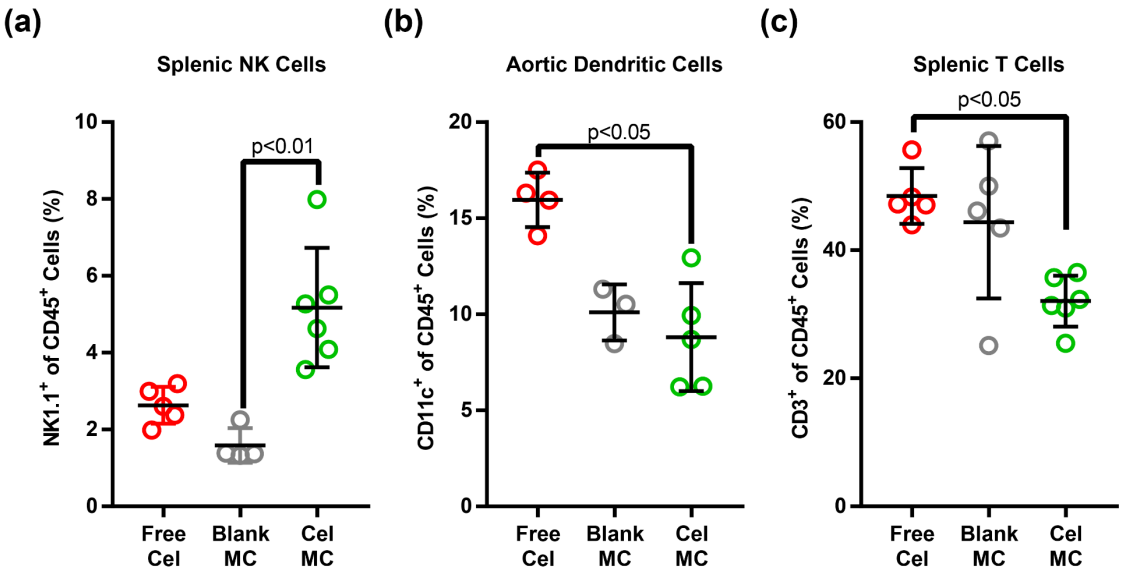

Figure 5-13. Additional changes in cell populations in ldlr-/- mice. Comparison of each cell population as a percent of CD45+ cells in that organ between free celastrol, blank MC, and Cel-MC treatments for (a) splenic NK cells, (b) aortic dendritic cells, and (c) splentic T cells. P values obtained using Dunn's multiple comparison test, n=6. Bars represent the mean and standard deviation. All data points shown on graphs. Reproduced from [223] with permission from The Royal Society of Chemistry.

concentrations and less frequent administrations for this drug. The targeting may also result in reduced off-target effects of rapamycin on non-immune cell types.

Celastrol did not drastically change the morphology of PEG-*b*-PPS micelles upon loading, even at very high concentrations of 70 wt %. Higher concentrations of celastrol resulted in small increases in the micelle diameter to accommodate the higher levels of celastrol. Celastrol loaded very effectively, with nearly 100% encapsulation efficiency at a weight percentage of 5 wt %. At maximum loading capacity, celastrol loaded at 22 wt %, though this is a cytotoxic concentration and is unnecessarily high for *in vitro* and *in vivo* use. Use of PEG-*b*-PPS to encapsulate celastrol results in significant improvement in the aqueous solubility of celastrol, over 10,000-fold. These Cel-MCs are very stable and demonstrate very little leakage of

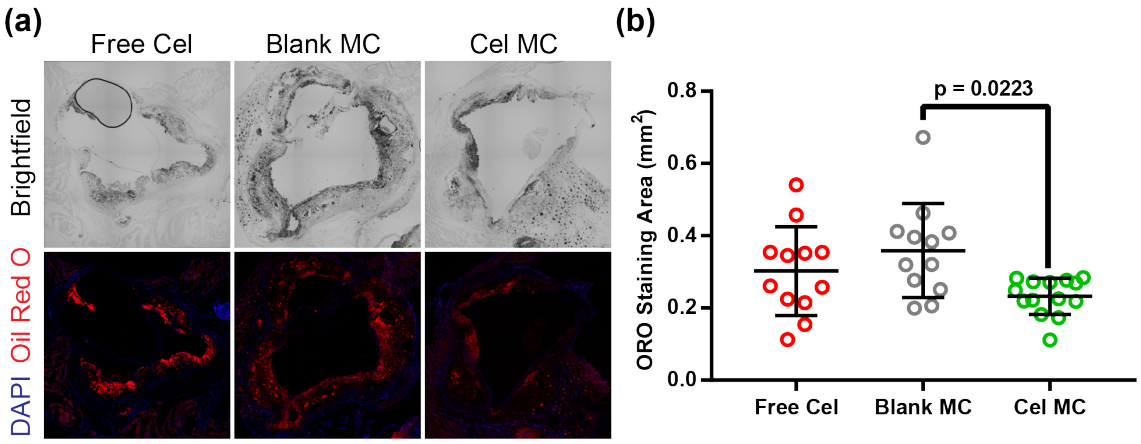

Figure 5-14. Oil Red O (ORO) analysis of plaque area in ldlr-/- mice treated with free celastrol or Cel-MC. (a) Representative fluorescence microscopy images of ORO stained, frozen aorta sections from free celastrol, blank MC or Cel-MC treated ldlr-/- mice. Top images represent brightfield microscopy, while bottom images were obtained with fluorescence microscopy of DAPI-stained nuclei (blue) and lipid-rich plaques (red). All images were acquired at 20x magnification. (b) Quantification of ORO staining area for free celastrol, Blank MC, and Cel MC treated aorta sections. P-value was calculated using Dunn's multiple comparisons test. Data points represent imaged sections from discrete portions along the length of the aorta, all data points shown on graph. Bars represent the mean and standard deviation, n = 12 for free celastrol, n = 11 for Blank MC, and n = 14 for Cel-MC. Reproduced from [223] with permission from The Royal Society of Chemistry.

celastrol in the absence of oxidation of PEG-*b*-PPS. As targeted delivery to immune cells is a significant benefit of PEG-*b*-PPS nanocarriers that would be largely neutralized if the cargo leaks out non-specifically, this was an important finding.

The encapsulation of celastrol in PEG-*b*-PPS micelles did not negatively affect its ability to inhibit NF-κB in inflammatory cells *in vitro*. In fact, Cel-MC demonstrated a lower EC50 and lower cytotoxicity than free celastrol *in vitro*, significantly expanding the therapeutic window of celastrol. The difference in EC50 is best explained by improved delivery of celastrol to the cells when encapsulated in micelles, compared to free celastrol being evenly diluted throughout the *in vitro* working volume. The difference in cytotoxicity is perhaps explained by the TNF-α ELISA data, which showed that while both free and encapsulated celastrol drastically reduce TNF-α secretion by RAW 264.7 cells, neither treatment completely eliminates the production and secretion of the cytokine. TNF-α is a potent inducer of apoptosis, a major mechanism by which celastrol induces cell death. Signaling by the low levels of TNF-α in the supernatant may have been sufficient to induce apoptosis in cells treated with free celastrol due to incomplete inhibition of pathways. Cel-MC treatment is not cytotoxic at most concentrations, perhaps due to more consistent or higher delivery of celastrol.

Both celastrol treatments downregulated transcription of pro-inflammatory genes and upregulated transcription of anti-inflammatory genes. Of the 2084 altered genes, the downregulation of the transcripts that result in IL-1β and TNF-α cytokines are particularly notable, especially because both are highly implicated in atherosclerosis development and progression. Cel-MC treatment induced greater change and at a higher degree of statistical significance in the transcription of NF-κB target genes, compared to free celastrol treatment.

Celastrol was administered to ldlr-/- mice at a much lower concentration than it is often administered, as many studies underestimate the long-term toxicity of celastrol administration by artificially reducing the duration of their studies. To avoid toxicity, celastrol was administered at a dose of 33 μg/kg/week. The reduced dose was not toxic to mice, evidenced by the lack of weight loss and lack of loss of appetence. This reduction in dose also resulted in a lack of positive result due to free celastrol administration. Celastrol encapsulated in micelles, however, was able to statistically alter immune cell populations, in the atheroma

and systemically. Neutrophils, a highly pro-inflammatory cell population, was significantly reduced in both the atheroma and blood. Neutrophils are implicated in amplifying the pro-inflammatory state of developing atheromas, particularly through NETosis and by inducing the death of vascular endothelial cells. Monocytes in the blood were also reduced, a potentially positive result as monocytes are frequently pro-inflammatory. NK cells are often pro-inflammatory as well, though their effects in atherosclerosis are not clear. As such, their reduction in atheromas due to Cel-MC treatment is not clearly a positive nor negative result. The decrease in NK cells in atheromas was matched by an increase in NK cells in the spleen of Cel-MC treated mice, an intriguing finding that suggests that Cel-MC treatment may alter the trafficking of NK cells to atheroma.

The reduction of plaque staining area by Cel-MC is a sign that Cel-MC treatment can affect change in the atherosclerotic plaque that can be relevant to human disease. It also suggests that changes in inflammatory cell populations in the atheroma and systemically can play an important role in plaque area regression. There are other potential markers of successful treatment of atherosclerosis, which are more prominently displayed in other models of atherosclerosis in other animal models. It would be instructive to pursue Cel-MC treatment in these other animal models of atherosclerosis to see what effect, if any, Cel-MC treatment may have on, for example, the formation of stable vs. unstable plaques.

In this chapter, I have demonstrated that PEG-*b*-PPS nanocarriers can very effectively serve as delivery vehicles for anti-inflammatory therapeutics to immune cell populations *in vivo*. Impressively, PEG-*b*-PPS nanocarriers allowed for less frequent administrations of the therapeutic at lower concentrations. This results in reduced off-target effects, such as toxicity, and suggests that more of the therapeutic is reaching the intended target cell populations.

5.6. Acknowledgements

I'd like to thank the assistance of Sijia Yi and Xiaohan Zhang in helping me with the histological staining of the atherosclerotic plaques. I also want to thank Taehyeung Kim and Jaehyuk Choi for their help with the interpretation and analysis of the RNAseq data. Sharan Bobbala was indispensable for his aid in performing

ELISA assays. Finally, I'd like to thank Yu-Gang Liu for his help in carefully collecting the aortas from diseased mice.

5.7. Publication Information

Sections of this chapter have been published with the following citation information:

S. Allen, O. Osorio, Y.G. Liu, E. Scott. Facile assembly and loading of theranostic polymersomes *via* multi-impingement flash nanoprecipitation. Journal of Controlled Release, 262 91-103. 2017. [166]

S.D. Allen, Y.G. Liu, T. Kim, S. Bobbala, S. Yi, X. Zhang, J. Choi, E.A. Scott. Celastrol-loaded PEG-*b*-PPS nanocarriers as an anti-inflammatory treatment for atherosclerosis. Biomaterials Science Advance Article. 2019. **[224]**

CHAPTER 6

Concluding Remarks and Future Directions

6.1. Concluding Remarks

The focus of this thesis was to expand the scientific understanding and clinical applicability of PEG-*b*-PPS nanocarriers. To that end, I have added a new fabrication technique to the repertoire of techniques for forming PEG-*b*-PPS nanocarriers, introduced a new PEG-*b*-PPS morphology, demonstrated the ability to load multiple hydrophilic and hydrophobic compounds in PEG-*b*-PPS nanocarriers, and demonstrated the usefulness of PEG-*b*-PPS nanocarriers for the delivery of anti-inflammatory therapeutics *in vivo*.

6.1.1. Rapid, Scalable, and Sterile Nanocarrier Formulation

The formation of PEG-*b*-PPS nanocarriers was previously done using thin film rehydration or solvent dispersion. While these techniques have been indispensable for nanocarrier self-assembly, neither one is able to successfully form the full range of morphologies or produce application-ready materials without the additional processing step of extrusion to enhance overall formulation quality, which increases the opportunity for endotoxin contamination. I found that flash nanoprecipitiation can be used to form PEG-*b*-PPS nanocarriers of all three of the previously found morphologies. I also found that there were several other exotic morphologies that were formed, including one that has been rarely explored in the polymer nanoparticle field – bicontinuous nanospheres. All of these nanocarriers could be formed rapidly in less than ten minutes. I showed that polymersomes could be made at a scaled-up volume for primate studies, and all morphologies can be made sterilely and absent of endotoxin contamination.

6.1.2. Polymersomes and Bicontinuous Nanospheres as Versatile Nanocarriers

I explored the formation and utility of a new PEG-*b*-PPS morphology, the bicontinuous nanosphere, compared to the polymersome, the most similar well-known morphology. I was able to show that BCNs and PSs are both able to encapsulate a diverse array of molecular cargoes, ranging in size and hydrophobicity. While both morphologies could load hydrophilic and hydrophobic cargoes simultaneously, BCNs were able

to encapsulate cargo more effectively than PSs and had a higher hydrophobic loading capacity, suggesting that they have a promising future as a drug delivery vehicle. In the first study of its kind in the field, I demonstrated that loaded BCNs administered *in vivo* are internalized by cells in different organs. I was able to compare this biodistribution of BCNs to PSs and show that BCNs and PSs have similar cellular uptake *in vivo* but different organ level biodistributions. Specifically, BCNs had reduced liver and increased splenic uptake compared to PSs, potentially due to differences in the deformability of BCNs compared to PSs.

PEG-*b*-PPS nanocarriers are non-toxic when administered *in vivo* and I was able to demonstrate this at higher concentrations of PSs than had previously been used in mice. I was also able to perform the first administration of PEG-*b*-PPs nanocarriers in non-human primates. These nanocarriers had similar uptake in non-human primates when compared to mice, and generally were non-toxic in both species at concentrations that are sufficient for therapeutic efficacy.

6.1.3. Anti-Inflammatory Nanocarrier Therapeutics

Previous work in the Hubbell and Scott labs have demonstrated that PEG-*b*-PPS nanocarriers can be used to deliver pro-inflammatory molecules to immune cells *in vivo*. It has also been demonstrated that PEG-*b*-PPS nanocarriers themselves are not immunogenic, opening up the possibility of their use as effective anti-inflammatory drug delivery vehicles as well. To demonstrate this, I utilized two anti-inflammatory compounds, rapamycin and celastrol, and loaded them in PEG-*b*-PPS polymersomes and micelles, respectively. In both cases, encapsulation in PEG-*b*-PPS nanocarriers allowed for fewer administrations and lower therapeutic concentrations to achieve the equivalent therapeutic effect as free therapeutic. Initially, rapamycin polymersomes were administered subcutaneously to healthy mice as a proof of concept and I found that it was able to exert an immunosuppressive effect by reducing T cell populations *in vivo*.

Celastrol micelles demonstrated an expanded therapeutic window compared to free celastrol by both reducing the effective inhibitory concentration and reducing the cytotoxicity of higher doses of celastrol. The encapsulation of celastrol into micelles did not affect its ability to inhibit NF-κB signaling and did not change its effects on transcription. When administered to atherosclerotic mice, celastrol micelles were non-

toxic and were able to significantly reduce inflammatory immune cell populations in the plaques, blood, and spleen. Additionally, celastrol micelle treatment reduced plaque size in the mice, suggesting that targeted anti-inflammatory intervention could be useful for alleviating atherosclerosis.

6.2. Future Directions

The work described in this dissertation represents a significant step toward clinical translation of PEG-*b*-PPS nanocarriers for drug delivery applications. As is always the case, all of these investigations have resulted in many more potential directions for further research. While I feel confident that I have comprehensively tested my hypotheses and addressed a number of questions, many more exciting questions remain. In this section, I will describe future experiments that I hope researchers will pursue in the interest of furthering our understanding of PEG-*b*-PPS nanocarriers.

6.2.1. Flow Rate and Mixed Solvent Variables for Flash Nanoprecipitation

I was able to demonstrate that flash nanoprecipitation can be used to form PEG-*b*-PPS nanocarriers. Flash nanoprecipitation as a technique has a number of input variables when using the CIJ mixer: flow rate, temperature, organic solvent, aqueous solvent, PEG-*b*-PPS polymer, reservoir volume, and impingement number. I was able to test a subset of these variables, such as the range of PEG-*b*-PPS polymers and impingement numbers. I was also able to explore, to a less comprehensive extent, the effect of reservoir volume, aqueous solvent, and organic solvent on nanocarrier formation and morphology. However, those three variables were only explored in the context of polymersome formation, rather than for all four stable morphologies. For example, how does reservoir volume affect the formation of bicontinuous nanospheres or filomicelles? I only explored the reservoir volume in 1 mL increments, which is relatively discretized. In my exploration of organic solvents, I focused on using THF and DMF as they are the two organic solvents that we primarily use to solubilize PEG-*b*-PPS. However, it is possible to use mixed solvent systems as well, which I have not explored at all. The only restriction on the choice of organic solvent is its miscibility in water. As such, systems that combine two or more of THF, DMF, methanol, ethanol, acetone, or acetonitrile are all viable options for probing deeper into this technique and

understanding the effect of organic solvent on nanocarrier formation, morphology, and cargo loading. Thorough examination of this variable could vastly expand the capacity of using FNP to load cargo that is not readily soluble in THF or DMF. Exploration of the aqueous solvent variable would involve a more theoretically grounded exploration of chaotropic and kosmotropic solutions. While I explored this question with a single chaotropic and several kosmotropic solutions, it was again only in the context of polymersomes. It is possible that changing the PEG interaction with water and hence its folding could alter the morphology of bicontinuous nanospheres and filomicelles. For example, BCNs formed in 1xPBS have a different diameter and polydispersity compared to those formed in water. This difference should be explored more comprehensively.

Flow rate and temperature were not explored in this dissertation. With help from a lab mate, Michael Vincent, we made an automated mechanical pump for the CIJ mixer that can control the flow rate with higher precision and accuracy than can be achieved by manual impingements. While some mechanical aspects still need to be refined to achieve reliable nanoparticle formation, this tool will enable rigorous exploration of the relationship between flow rate/force and nanocarrier morphology. Higher flow rates could, for example, result in more monodisperse polymersomes after a single impingement, instead of relying on multiple impingements at lower flow rates. Temperature and the kinetic energy that it imparts certainly plays a role in nanocarrier formation in general. In all of these studies, the temperature has been loosely held constant at the ambient room temperature. Formation of the nanocarriers at colder temperatures could result in more kinetic trapping of morphologies but could simultaneously result in more aggregation for aggregation-prone polymers such as those used for forming bicontinuous nanospheres. In its current configuration, temperature control of the CIJ mixer is difficult. However, more thoroughly investigating this variable could yield large dividends in developing a protocol for consistent formation of stable nanocarriers.

In addition to these variables relevant to the CIJ mixer, the unique geometry of a multi-inlet vortex mixer opens up an additional variable to investigate: the ability to manipulate four independent inlet streams. While more difficult to operate, it is easier to fabricate. The principle is the use of four inlet streams, which allows for the use of more than two solvents or the use of solvent ratios that aren’t the simple 1:1 ratio of the CIJ mixer. Tweaking these variables could result in the formation of different morphologies and could

potentially improve the encapsulation efficiencies of different cargoes by changing their solubility in the bulk solvent.

6.2.2. Therapeutic Applications for Bicontinuous Nanospheres

My exploration of using flash nanoprecipitation to form PEG-PPS nanostructures revealed a new morphology that is capable of loading hydrophilic and hydrophobic compounds throughout its bicontinuous membrane organization, improving upon both the capacity and efficiency of encapsulation compared to known nanostructures. These BCNs have a number of unique properties in addition to the enhanced loading that open up a range of potential applications. For example, BCNs demonstrate a very slow exit from the site of injection when administered subcutaneously, except when they are loaded with MPLA, which I found to increase the rate of BCN exit. Better understanding how MPLA affects this change would allow for the rational design and engineering of BCN delivery of compounds in a long-term sustained fashion. MPLA is a pro-inflammatory molecule and perhaps its stimulation of local immune cells was what resulted in more rapid uptake of BCNs by cells at the site of injection. A related idea is that the pro-inflammatory signal from MPLA resulted in the production and release of reactive oxygen species by immune cells recruited to the site of injection, leading to the breakdown of BCNs into smaller aggregate structures, e.g. smaller BCNs or micelles. The former can be explored by incorporating a different pro-inflammatory molecule, such as CL-429, into BCNs and tracking their exit from the site of injection. The latter could be explored by histologically assaying for the presence of inflammatory cells and reactive oxygen species, using ROS-reactive sensors and dyes or performing cryogenic scanning electron microscopy on the site of injection to attempt to observe morphological changes in BCNs due to local ROS. Alternatively, it is possible that MPLA incorporation alters the BCN in a structural way unrelated to the activity of MPLA itself. MPLA-loaded BCNs are slightly smaller in diameter than unloaded BCNs, perhaps leading to more rapid diffusion from the site of injection. It is unclear why MPLA reduces the size of BCNs. This could be explored by attempting to load molecularly similar cargo to MPLA that is divorced from the pro-inflammatory properties of MPLA. Alternatively, this could be explored by using BCNs of a matching diameter but loaded with a

completely different, immunologically-inert cargo. This would require trial and error to find an appropriate cargo to use.

Long term sustained release from a subcutaneous injection of BCNs has a number of useful therapeutic applications. One example is self-boosting single-shot vaccines, which can replace modern vaccination strategies that often require up to five doses to develop robust immunity. BCNs loaded with antigen and adjuvant could be administered subcutaneously, where they would gradually deliver the vaccine components to immune cells over the course of weeks. One aspect of this that would need to be explored is the possibility of developing T cell anergy, which has been observed in cases where too many vaccine attempts are made, and T cells become inactivated. Even if T cell anergy is observed, it could itself be a useful application of BCNs. BCNs could be loaded with an antigen for which the goal is to develop a tolerogenic response, and long-term gradual delivery could induce T cell anergy and tolerance.

BCNs are made of PEG-*b*-PPS polymer that contains a large number of propylene sulfide units. This suggests that BCNs may remain as stable nanocarriers for an extended period of time within the oxidative lysosomal environment compared to other PEG-*b*-PPS nanocarriers. This offers the interesting possibility that BCNs may be able to act as intracellular drug depots capable of gradually releasing drug from within the lysosome. This idea could be explored using a drug that induces an assayable readout in cells and observing the kinetics of that attribute. One example is latrunculin A (LatA), a drug that inhibits actin polymerization. LatA loaded BCNs could be administered to a cell type that normally possesses a clear ‘spread out’ or polarized morphology. Using a long-term imaging system, cells could be observed over time and compared to free latA or latA loaded into micelles, which should show a more rapid induction of a ‘balled up’ phenotype. Another option is to deliver an inhibitor of a signaling pathway, e.g. NF-κB, and attempt to periodically activate the pathway using an external stimulus. BCNs could be able to confer an inhibitory effect over a longer period of time than a different nanocarrier or free drug.

6.2.3. Rapamycin Polymersomes for Targeted Immunosuppression for Islet Transplantation

I utilized rapamycin loaded polymersomes as a proof of concept for the delivery of an anti-inflammatory FDA-approved drug *in vivo*. This work was as a proof of concept for the utilization of PEG-*b*-PPS nanocarriers as anti-inflammatory drug delivery vehicles and were therefore performed in healthy mice. However, there are a number of applications where rapamycin polymersomes could themselves be particularly useful. Generally, rapamycin is used to reduce transplant rejection. It has a mixed history as a therapeutic to reduce islet transplant rejection, mostly because rapamycin's anti-proliferative effect reduces the viability of the islet cells. As I demonstrated, rapamycin polymersomes are taken up by phagocytic cells and still exert an immunosuppressive effect. Islet cells are not phagocytic cells, and therefore would be expected to not internalize rapamycin polymersomes. This should reduce the toxicity of rapamycin for this application, while maintaining its immunosuppressive function. This work is actively being pursued by Jacqueline Burke, jointly advised by the Scott and Ameer labs. Her excellent work has already demonstrated that rapamycin polymersomes can extend diabetic mouse life after islet cell transplantation. This is an extremely exciting and promising application of this drug delivery technology.

6.2.4. Anti-Inflammatory Combinatorial Treatments for Atherosclerosis

Atherosclerosis is a complex disease with multiple contributing factors. One of the more successful therapeutic interventions for atherosclerosis is a combination of blood lipid-lowering drugs such as statins and blood pressure lowering drugs such as ACE inhibitors. Aside from some anti-inflammatory properties of statins, these two treatment approaches are orthogonal to the sort of anti-inflammatory treatment that I explored here in this dissertation. As such, it may be promising to administer celastrol micelles or another anti-inflammatory nanocarrier along with a statin and potentially an ACE inhibitor. In the mouse model of atherosclerosis, high blood pressure is typically less important than lipid levels from diet, so the statin approach may hold more relevance compared to the ACE inhibitor. An interesting question is whether the statin should be delivered in free form, or if it should itself be loaded into a nanocarrier. One of the main targets of statins is the liver, where they affect lipid/cholesterol metabolism. Loading of a statin in a nanocarrier would by default target the statin to immune cells, many of which would be in the liver. However, Kupffer cells may not be the optimal liver target cell population and as such encapsulation may reduce

statin efficacy. That said, statins are often administered orally and can result in severe and common side effects such as joint pain and gastrointestinal problems. Some of the most effective statins are also the more likely to cause side effects and, perhaps related, are also the most hydrophobic. As nanocarriers can help alleviate off-target effects, encapsulation may improve statin treatments as well. However, for that to be effective in this case, two independent projects would need to be explored first: oral delivery using PEG-*b*-PPS nanocarriers and active targeting of PEG-*b*-PPS nanocarriers.

6.2.5. Oral Delivery Using PEG-*b*-PPS Nanocarriers

PEG-*b*-PPS nanocarriers have been administered intravenously, subcutaneously, and intratracheally. The most popular route of administration in humans, however, is the oral route, which poses a number of challenges for drug delivery. The acidic environment of the stomach and the presence of a large number of catalytic enzymes and surfactant molecules result in difficult engineering problems for self-assembled nanocarriers. PEG-*b*-PPS nanocarriers are unlikely to be significantly affected by the pH in the stomach and do not contain bonds susceptible to catalysis by enzymes. However, as self-assembled structures, PEG-*b*-PPS nanocarriers can be sensitive to surfactants. Polymersomes, for example, readily release hydrophilic cargo upon incubation with 0.1% Triton X-100, a surfactant.

BCNs do not possess a vesicular membrane and appear to be more resistant to Triton-induced release of cargo. This may mean that BCNs are more likely to survive the gastrointestinal tract with cargo still loaded. This, however, is only one issue. The intestinal mucosa can easily trap nanocarriers before they can be internalized by intestinal epithelial cells or by immune cells surveilling Peyer patches. It is possible that trapped BCNs may gradually release their cargo in the mucosa and this localized release could be sufficient to provide therapeutic effect. However, cargo that needs to be protected and/or delivered in a targeted fashion on the other side of the intestinal epithelium will require a delivery vehicle that can transit through the mucosa. The efficacy of BCNs in this case is a completely open question, but one that could provide a significant boost in the effort to translate PEG-*b*-PPS nanocarriers to the clinic.

6.2.6. Active Targeting of PEG-*b*-PPS Nanocarriers

I relied on the passive targeting of PEG-*b*-PPS nanocarriers to immune cell populations based on their size and morphology. There are a number of potential applications, however, where PEG-*b*-PPS nanocarriers may need to deliver cargo to other cell types. Active targeting involves the attachment of a targeting moiety to the surface of the PEG-*b*-PPS nanocarriers. This can be achieved by synthesizing PEG-*b*-PPS polymer that has a reactive group on the PEG that can be conjugated to the targeting moiety. Work by Nicholas Karabin in the Scott lab has led to the successful modification of the PEG polymer to include a vinyl sulfone group, an azide group, or an amine group. All of these groups can react with common reactive groups on a number of molecules such as antibodies, other proteins, peptides, and nucleic acids. This system has the benefit of still being based on a diblock copolymer, which incorporates well into the rest of the nanoparticle aggregate. This should impart significant stability to the targeting moiety, reducing the odds that it will be pulled out of the nanocarrier. However, in its current state, the chemistry involved is complex and relatively low efficiency, reducing the reliability and maximum conjugation possible. Higher efficiency syntheses or better purification techniques could improve these issues.

Another method of incorporating a targeting moiety is to attach it to a PEG linker and lipid tail, essentially using a PEGylated lipid rather than a diblock copolymer. This chemistry is very well established, to the point that it can be purchased directly from a number of companies. However, it is unlikely to be as stably incorporated as the modified PEG-*b*-PPS option, as the lipid tail is not as hydrophobic as a PPS polymer chain. Also, there are likely limits to the amount of incorporation, due to the possibility of the construct forming its own micelles once concentrations reach the CMC of the construct. Work by Trevor Stack and Sijia Yi in the Scott lab has already demonstrated the efficacy of this system for targeting the uptake of nanocarriers *in vitro* and *in vivo*.

Increasing the specificity of the uptake of the nanocarriers is an important component of efficient and targeted delivery. However, an additional concern is avoiding inappropriate uptake. This will be increasingly important if there is an explicit goal to not deliver the cargo to macrophages, which are adept at internalizing PEG-*b*-PPS nanocarriers. One direction is to attempt to incorporate “don’t eat me” signals on the surface of nanocarriers. CD47 is the protein most commonly associated with self-recognition by immune cells, which inhibits phagocytosis of cells decorated with the protein. CD47 decorated nanocarriers

have been demonstrated by the Discher lab to reduce uptake by phagocytic cells. Successful surface conjugation of the CD47 extracellular domain could afford the same to PEG-*b*-PPS nanocarriers. Once successful, the next task would be to uncover the minimum CD47 density required to reduce uptake and test whether CD47 decoration is compatible with peptide or protein-based targeting.

6.2.7. Transcriptional Implications of Oxidation-Sensitive Nanocarriers

I performed RNAseq for my study on free and encapsulated celastrol. As a control I also performed RNAseq on LPS-stimulated RAW 264.7 cells that were incubated with blank micelles. The blank micelles demonstrated a small number of genes that were differentially regulated compared to the untreated LPS-stimulated cells. While PEG-*b*-PPS nanocarriers are largely considered a 'blank slate' delivery vehicle, it is entirely possible that PEG-*b*-PPS polymer itself could cause transcriptional changes in the cells. The PPS polymer is a sponge for oxidative species, able to accept two molecules of reactive oxygen species per unit of propylene sulfide. Rapid depletion of oxidative species by PPS in lysosomes could set off compensatory transcriptional programs. PEG-*b*-PPS nanocarriers could also potentially set off intracellular sensors for aggregation, though these are commonly pro-inflammatory, which is not a typical cellular response to PEG-*b*-PPS nanocarrier uptake. Also, PEG-*b*-PPS nanocarriers could set off transcriptional pathways to try to compensate for the increased endolysosomal burden caused by uptake of a large amount of gradually oxidizing polymer.

All of these questions could be explored in greater detail with a more controlled and in depth RNAseq experiment. RAW 264.7 cells or other cell populations (e.g. to expand clinical applicability, human PBMCs) could be incubated with all four morphologies of PEG-*b*-PPS nanocarrier without the interference of LPS stimulation. All these could be compared to RNA from untreated cells and pathway analysis could help determine whether there are any significant transcriptional implications of PEG-*b*-PPS uptake. If there is a clear transcriptional difference, it is possible that it could be exploited as an intrinsic benefit of using PEG-*b*-PPS nanocarriers for delivery to cells.

6.3. Curriculum Vitae

Sean Allen

PERSONAL INFORMATION

1649 W Wrightwood Ave Apt 1R, Chicago IL 60614 | 310-529-5517 | allen.sean.d@gmail.com

EDUCATION

PhD: Northwestern University, 2019, Interdisciplinary Biological Sciences, *Planned*

M.S.: San Francisco State University, 2013, Cell and Molecular Biology

B.A.: University of California, Berkeley, 2009, Molecular and Cellular Biology, Immunology Track

RESEARCH AND PROFESSIONAL EXPERIENCE

Intern – Genentech: June 2016-September 2016

PhD Candidate Researcher – Scott Lab, Northwestern University: 2014-Current

Graduate Student Researcher – Burrus Lab, San Francisco State University: 2010-2013

iGEM Undergraduate Researcher – Regenerative Sciences Institute Team: 2008

AWARDS, FELLOWSHIPS & GRANTS

2014-2016, NIH Biotechnology Training Grant, Northwestern University Administered Training Grant

2015, IBiS Travel Award, Grant for Travel Expenses to BMES Meeting 2015

2012, CSU Program for Education and Research in Biotechnology Student Travel Grant

HONORS, DISTINCTIONS

2016; NIH Biotechnology Training Grant Steering Committee Student Representative; Northwestern University

2011; Instructionally Related Research Award; San Francisco State University

PROFESSIONAL SOCIETY MEMBERSHIPS

2018-Current: American Heart Society Student Member

2014-Current: Biomedical Engineering Society Student Member

2011-2013: American Society for Cell Biology Student Member

2011-2013: Society for Developmental Biology Student Member

TEACHING

Jan 2016 – June 2016, Genetics and Molecular Biology, Teaching Assistant, Northwestern University

Sep 2014 – Dec 2014, Cell Biology, Teaching Assistant, Northwestern University

Sep 2014 – Dec 2014, Quantitative Biology, Grader, Northwestern University

Sep 2011 – Dec 2012, Introductory Biology Lab, Teaching Assistant, San Francisco State University

VOLUNTEERING AND OUTREACH

Bio Games Volunteer Assessor, Evanston Township High School, Feb 2018

Destination Imagination Appraiser, Destination Imagination Regional Tournament, Mar 2017

Graduate Student Volunteer, NU Science & Engineering Shadow Day, Feb 2016

Graduate Student Volunteer, NU Science & Engineering Shadow Day, Nov 2015

Outreach Volunteer, Northwestern University Biotechnology Day, Feb 2016

PUBLICATIONS

Sean Allen, Omar Osorio, Yu-Gang Liu, Evan Scott. Facile assembly and loading of theranostic polymersomes *via* multi-impingement flash nanoprecipitation. Journal of Controlled Release, 2017.

Sean Allen, Yu-Gang Liu, Sharan Bobbala, Lei Cai, Peter I. Hecker, Ryan Temel, Evan Scott. Polymersomes scalably fabricated *via* flash nanoprecipitation are non-toxic in non-human primates and associate with leukocytes in the spleen and kidney following intravenous administration. Nano Research, 2018.

Sean Allen, Michael Vincent, Evan Scott. Rapid, scalable assembly and loading of bioactive proteins and immunostimulants into diverse synthetic nanocarriers *via* flash nanoprecipitation. J. Vis. Exp., 2018.

Sean Allen, Sharan Bobbala, Nicholas Karabin, Mallika Modak, Evan Scott. Benchmarking bicontinuous nanospheres against polymersomes for *in vivo* biodistribution and dual intracellular delivery of lipophilic and water soluble payloads. ACS Appl. Mater. Interfaces, 2018.

Sean Allen, Yu-Gang Liu, Sharan Bobbala, Sijia Yi, Xiaohan Zhang, Evan Scott. Celastrol-loaded PEG-*b*-PPS nanocarriers as an anti-inflammatory treatment for atherosclerosis. Biomaterials Science, 2018.

Sean Allen, Sharan Bobbala, Nicholas Karabin, Evan Scott. On the Advancement of Polymeric Bicontinuous Nanospheres Toward Biomedical Applications. Nanoscale Horizons, 2018.

Sean Allen, Yu-Gang Liu, Evan Scott. Engineering Nanomaterials to Address Cell-Mediated Inflammation in Atherosclerosis. Regenerative Engineering and Translational Medicine, 2016.

Sharan Bobbala, *Sean Allen*, Evan Scott. Flash nanoprecipitation permits versatile assembly and loading of polymeric bicontinuous cubic nanospheres. Nanoscale, 2018.

Nicholas Karabin, *Sean Allen*, Emre Firlar, Tolou Shokuhfar, Evan Scott. Sustained Micellar Delivery *via* Inducible Transitions in Nanostructure Morphology. Nature Communications, 2018.

Sijia Yi, *Sean David Allen*, Yu-Gang Liu, Brian Zhou Ouyang, Xiaomo Li, Punn Augsornworawat, Edward Benjamin Thorp, Evan Alexander Scott. Tailoring nanostructure morphology for enhanced targeting of dendritic cells in atherosclerosis. ACS Nano, 2016.

SUBMITTED MANUSCRIPTS UNDER REVIEW OR REVISION

Sijia Yi, Xiaohan Zhang, Hussain Sangji, Yugang Liu, *Sean D. Allen*, Baixue Xiao, Sharan Bobbala, Cameron L. Braverman, Lei Cai, Peter I. Hecker, Ryan Temel, Samuel I. Stupp, Evan A. Scott. Targeted immunomodulation of dendritic cells *via* surface engineered polymersomes inhibits atherosclerosis. Nature Comm., 2019.

Indranil Roy, Sharan Bobbala, *Sean Allen*, Evan Scott, J. Fraser Stoddart. ExTzBox-Solubilized Chlorin for Photodynamic Therapy *In vitro*. Nature Chemistry, 2019.

Abhalaxmi Singh, Vikas Nandwana, Jonathan Rink, Soo-Ryoon Ryoo, Tzu Hung Chen, *Sean Allen*, Evan Scott, Leo Gordon, Colby Thaxton, Vinayak Dravid. Bio-mimetic magnetic nanostructures: A theranostic platform targeting lipid metabolism and immune response in lymphoma. ACS Nano, 2019.

CONFERENCE PRESENTATIONS AND ABSTRACTS

Anti-Inflammatory Nanotherapy Alters Immune Cell Composition and Reduces Lesion Area of Atherosclerotic Plaques in Ldlr-/- Mice; *Sean Allen*, Yugang Liu, Evan Scott. American Heart Association Scientific Sessions, Moderated Digital Poster, November 2018.

Rapid, Sterile, and Clinical-Scale Synthesis and Directed Self-Assembly of Block Copolymers for Applications in Nanomedicine; *Sean Allen*. Rising Stars of the Simpson Querrey Institute, Invited Talk, October 2018.

Rapid and scalable formation of soft nanostructures for immunomodulation using flash nanoprecipitation; Sean Allen. SPIE-MRSEC Student Seminar Series, Invited Talk, July 2018

NF-kB Inhibition *via* Celastrol-Loaded Nanocarriers Induces Distinct Changes in Atheroma-Resident Immune Cell Composition in Male vs. Female ldlr -/- Mice; *Sean Allen*, Yugang Liu, Evan Scott. ATVB/PVD 2018 Scientific Sessions Conference, Poster, May 2018.

Oxidation-Responsive Polymeric Bicontinuous Nanospheres for Drug and Vaccine Delivery; Sharan Bobbala, *Sean David Allen*, Evan Alexander Scott. NanoBio Collaborative International Conference, Abstract, Jan 2018

Targeted Inhibition of NF-kB in Mouse Models of Atherosclerosis Results in Sex-Dependent Immunomodulation; *Sean Allen*, Yu-Gang Liu, Evan Scott. Keystone Symposia on Molecular and Cellular Biology, Oral, Feb 2018

Celastrol-Loaded Nanocarriers for Targeted Therapeutic Inhibition of Inflammatory Cells; *Sean Allen*, Yu-Gang Liu, Evan Scott. Biomedical Engineering Society Annual Meeting, Oral, Oct 2017

Nanotheranostics Reveal Sex Dependent Inflammatory Responses in Mouse Models of Atherosclerosis; Yu-Gang Liu, *Sean David Allen*, Sijia Yi, Evan Alexander Scott. Biomedical Engineering Society Annual Meeting, Abstract, Oct 2017.

Facile Polymersome Assembly and Loading *via* Multi-Impingement Flash Nanoprecipitation; *Sean Allen*, Omar Osorio, Evan Alexander Scott. Society for Biomaterials Annual Meeting, Poster, April 2017

Dual Loading of Hydrophilic and Hydrophobic Molecules into Polymersomes *via* Flash Nanoprecipitation; *Sean Allen*, Omar Osorio, Evan Scott. Biomedical Engineering Society Annual Meeting, Poster, Oct 2016

Engineering Nanomaterial Morphology for Targeting Immune Cells in Naïve and Atherosclerotic Mice; Sijia Yi, Yu-Gang Liu, *Sean Allen*, Fanfan Du, Xiaomo Li, Brian Ouyang, Evan Scott. Biomedical Engineering Society Annual Meeting, Oral, Oct 2016.

Characterization of Indocyanine Green-Loaded Nanocarriers for the Targeting of Atherosclerotic Plaque-Resident Dendritic Cell Subsets; *Sean Allen*, Evan Scott. Biomedical Engineering Society Annual Meeting, Poster, Oct 2015

The Aggregate Structure of Self-Assembled Nanocarriers Specifies Their *In vivo* Uptake By Antigen Presenting Cell Subsets; Evan Scott, Presented by *Sean Allen*. Biomedical Engineering Society Annual Meeting, Oral, Oct 2014

Wntless is required for cell survival in the developing chick spinal cord; *Sean Allen*, Laura Burrus. American Society for Cell Biology Annual Meeting, Poster, Dec 2012

Characterization of a Wls knockdown in the developing chick spinal cord; *Sean Allen*, Laura Burrus. Society for Developmental Biology Annual Meeting, Poster, July 2012

PATENTS

Poly(ethylene glycol)-block-poly(propylene sulfide) Nanocarrier Platform for Enhanced Efficacy of Immunosuppressive Agents. Jacqueline Burke, Sijia Yi, Sean Allen, Evan Scott, Guillermo Ameer. Post-Disclosure, 2018.

Facile Assembly of Soft Nanoarchitectures and Co-Loading of Hydrophilic and Hydrophobic Molecules *via* Flash Nanoprecipitation. Evan Scott, Sean D. Allen. Provisional, 2017. US20180022878A1.

Nanostructure Enhanced Targeting (NSET) of Inflammatory Cells. Evan Scott, Sijia Yi, Sean D. Allen. Provisional, 2016. US20180028446A1.

REFERENCES

[1] G. Sessa, G. Weissmann, Phospholipid spherules (liposomes) as a model for biological membranes, J Lipid Res, 9 (1968) 310-318.

[2] T. Kunitake, Y. Okahata, M. Shimomura, S. Yasunami, K. Takarabe, Formation of stable bilayer assemblies in water from single-chain amphiphiles. Relationship between the amphiphile structure and the aggregate morphology, Journal of the American Chemical Society, 103 (1981) 5401-5413.

[3] J.A. Lucy, A.M. Glauert, Structure + Assembly of Macromolecular Lipid Complexes Composed of Globular Micelles, Journal of Molecular Biology, 8 (1964) 727-&.

[4] A. Akimoto, K. Dorn, L. Gros, H. Ringsdorf, H. Schupp, Polyreactions in Oriented Systems .23. Polymer Model Membranes, Angew Chem Int Edit, 20 (1981) 90-91.

[5] M.K. Pratten, J.B. Lloyd, G. Horpel, H. Ringsdorf, Micelle-Forming Block Copolymers - Pinocytosis by Macrophages and Interaction with Model Membranes, Makromol Chem, 186 (1985) 725-733.

[6] B.M. Discher, Y.Y. Won, D.S. Ege, J.C. Lee, F.S. Bates, D.E. Discher, D.A. Hammer, Polymersomes: tough vesicles made from diblock copolymers, Science, 284 (1999) 1143-1146.

[7] L. Leibler, Theory of Microphase Separation in Block Co-Polymers, Macromolecules, 13 (1980) 1602-1617.

[8] A.D. Bangham, Liposomes: the Babraham connection, Chem Phys Lipids, 64 (1993) 275-285.

[9] E. Rideau, R. Dimova, P. Schwille, F.R. Wurm, K. Landfester, Liposomes and polymersomes: a comparative review towards cell mimicking, Chem Soc Rev, 47 (2018) 8572-8610.

[10] S.Y. Kim, I.G. Shin, Y.M. Lee, C.S. Cho, Y.K. Sung, Methoxy poly(ethylene glycol) and epsilon-caprolactone amphiphilic block copolymeric micelle containing indomethacin. II. Micelle formation and drug release behaviours, J Control Release, 51 (1998) 13-22.

[11] I. Astafieva, X.F. Zhong, A. Eisenberg, Critical Micellization Phenomena in Block Polyelectrolyte Solutions, Macromolecules, 26 (1993) 7339-7352.

[12] Z.S. Gao, A. Eisenberg, A Model of Micellization for Block-Copolymers in Solutions, Macromolecules, 26 (1993) 7353-7360.

[13] S.C. Owen, D.P.Y. Chan, M.S. Shoichet, Polymeric micelle stability, Nano Today, 7 (2012) 53-65.

[14] M.L. Williams, R.F. Landel, J.D. Ferry, Temperature Dependence of Relaxation Mechanisms in Amorphous Polymers and Other Glass-Forming Liquids, Phys Rev, 98 (1955) 1549-1549.

[15] E. Lorenceau, A.S. Utada, D.R. Link, G. Cristobal, M. Joanicot, D.A. Weitz, Generation of polymerosomes from double-emulsions, Langmuir, 21 (2005) 9183-9186.

[16] Y.J. Men, F. Peng, Y.F. Tu, J.C.M. van Hest, D.A. Wilson, Methods for production of uniform small-sized polymersome with rigid membrane, Polym Chem-Uk, 7 (2016) 3977-3982.

[17] A.C. Apolinario, M.S. Magon, A. Pessoa, C.D. Rangel-Yagui, Challenges for the Self-Assembly of Poly(Ethylene Glycol)-Poly(Lactic Acid) (PEG-PLA) into Polymersomes: Beyond the Theoretical Paradigms, Nanomaterials-Basel, 8 (2018).

[18] D.E. Discher, F. Ahmed, Polymersomes, Annu Rev Biomed Eng, 8 (2006) 323-341.

[19] H. Bermudez, A.K. Brannan, D.A. Hammer, F.S. Bates, D.E. Discher, Molecular weight dependence of polymersome membrane structure, elasticity, and stability, Macromolecules, 35 (2002) 8203-8208.

[20] G. Srinivas, D.E. Discher, M.L. Klein, Self-assembly and properties of diblock copolymers by coarse-grain molecular dynamics, Nature Materials, 3 (2004) 638-644.

[21] G. Battaglia, A.J. Ryan, S. Tomas, Polymeric vesicle permeability: A facile chemical assay, Langmuir, 22 (2006) 4910-4913.

[22] R. Dimova, U. Seifert, B. Pouligny, S. Forster, H.G. Dobereiner, Hyperviscous diblock copolymer vesicles, Eur Phys J E, 7 (2002) 241-250.

[23] V. Kumar, R.K. Prud'Homme, Thermodynamic Limits on Drug Loading in Nanoparticle Cores, J Pharm Sci-Us, 97 (2008) 4904-4914.

[24] R. Gref, M. Luck, P. Quellec, M. Marchand, E. Dellacherie, S. Harnisch, T. Blunk, R.H. Muller, 'Stealth' corona-core nanoparticles surface modified by polyethylene glycol (PEG): influences of the corona (PEG chain length and surface density) and of the core composition on phagocytic uptake and plasma protein adsorption, Colloid Surface B, 18 (2000) 301-313.

[25] M. Muthukumar, C.K. Ober, E.L. Thomas, Competing interactions and levels of ordering in self-organizing polymeric materials, Science, 277 (1997) 1225-1232.

[26] R. Nagarajan, Molecular packing parameter and surfactant self-assembly: The neglected role of the surfactant tail, Langmuir, 18 (2002) 31-38.

[27] J.N. Israelachvili, Intermolecular and Surface Forces, 3rd Edition, Intermolecular and Surface Forces, 3rd Edition, (2011) 1-674.

[28] S.J. Holder, N.A.J.M. Sommerdijk, New micellar morphologies from amphiphilic block copolymers: disks, toroids and bicontinuous micelles, Polym Chem-Uk, 2 (2011) 1018-1028.

[29] Y.Y. Mai, A. Eisenberg, Self-assembly of block copolymers, Chemical Society Reviews, 41 (2012) 5969-5985.

[30] A. Napoli, N. Tirelli, G. Kilcher, J.A. Hubbell, New synthetic methodologies for amphiphilic multiblock copolymers of ethylene glycol and propylene sulfide, Macromolecules, 34 (2001) 8913-8917.

[31] E.V. Batrakova, A.V. Kabanov, Pluronic block copolymers: evolution of drug delivery concept from inert nanocarriers to biological response modifiers, J Control Release, 130 (2008) 98-106.

[32] K. Schillen, K. Bryskhe, Y.S. Mel'nikova, Vesicles formed from a poly(ethylene oxide)-poly(propylene oxide)-poly(ethylene oxide) triblock copolymer in dilute aqueous solution, Macromolecules, 32 (1999) 6885-6888.

[33] C. Booth, D. Attwood, Effects of block architecture and composition on the association properties of poly(oxyalkylene) copolymers in aqueous solution, Macromol Rapid Comm, 21 (2000) 501-527.

[34] A. Napoli, N. Tirelli, E. Wehrli, J.A. Hubbell, Lyotropic behavior in water of amphiphilic ABA triblock copolymers based on poly(propylene sulfide) and poly(ethylene glycol), Langmuir, 18 (2002) 8324-8329.

[35] S. Cerritelli, C.P. O'Neil, D. Velluto, A. Fontana, M. Adrian, J. Dubochet, J.A. Hubbell, Aggregation Behavior of Poly(ethylene glycol-bl-propylene sulfide) Di- and Triblock Copolymers in Aqueous Solution, Langmuir, 25 (2009) 11328-11335.

[36] I.V. Tetko, J. Gasteiger, R. Todeschini, A. Mauri, D. Livingstone, P. Ertl, V. Palyulin, E. Radchenko, N.S. Zefirov, A.S. Makarenko, V.Y. Tanchuk, V.V. Prokopenko, Virtual computational chemistry laboratory - design and description, J Comput Aid Mol Des, 19 (2005) 453-463.

[37] N. Tirelli, M.P. Lutolf, A. Napoli, J.A. Hubbell, Poly(ethylene glycol) block copolymers, J Biotechnol, 90 (2002) 3-15.

[38] J.M. Harris, Introduction to biomedical and biotechnical applications of polyethylene glycol., Abstr Pap Am Chem S, 213 (1997) 21-Poly.

[39] A. Abuchowski, J.R. McCoy, N.C. Palczuk, T. van Es, F.F. Davis, Effect of covalent attachment of polyethylene glycol on immunogenicity and circulating life of bovine liver catalase, J Biol Chem, 252 (1977) 3582-3586.

[40] Q.A. Yu, Y.X. Zhang, H.W. Wang, J. Brash, H. Chen, Anti-fouling bioactive surfaces, Acta Biomater, 7 (2011) 1550-1557.

[41] J.M. Harris, N.E. Martin, M. Modi, Pegylation - A novel process for modifying pharmacokinetics, Clin Pharmacokinet, 40 (2001) 539-551.

[42] V.C.F. Mosqueira, P. Legrand, J.L. Morgat, M. Vert, E. Mysiakine, R. Gref, J.P. Devissaguet, G. Barratt, Biodistribution of long-circulating PEG-grafted nanocapsules in mice: Effects of PEG chain length and density, Pharmaceut Res, 18 (2001) 1411-1419.

[43] A. Napoli, M. Valentini, N. Tirelli, M. Muller, J.A. Hubbell, Oxidation-responsive polymeric vesicles, Nat Mater, 3 (2004) 183-189.

[44] N.B. Karabin, S. Allen, H.K. Kwon, S. Bobbala, E. Firlar, T. Shokuhfar, K.R. Shull, E.A. Scott, Sustained micellar delivery *via* inducible transitions in nanostructure morphology, Nat Commun, 9 (2018) 624.

[45] A.E. Vasdekis, E.A. Scott, C.P. O'Neil, D. Psaltis, J.A. Hubbell, Precision intracellular delivery based on optofluidic polymersome rupture, ACS Nano, 6 (2012) 7850-7857.

[46] U. Bulbake, S. Doppalapudi, N. Kommineni, W. Khan, Liposomal Formulations in Clinical Use: An Updated Review, Pharmaceutics, 9 (2017).

[47] H.I. Chang, M.K. Yeh, Clinical development of liposome-based drugs: formulation, characterization, and therapeutic efficacy, Int J Nanomedicine, 7 (2012) 49-60.

[48] C.L. Ventola, Progress in Nanomedicine: Approved and Investigational Nanodrugs, P T, 42 (2017) 742-755.

[49] J.M. Caster, A.N. Patel, T. Zhang, A. Wang, Investigational nanomedicines in 2016: a review of nanotherapeutics currently undergoing clinical trials, Wiley Interdiscip Rev Nanomed Nanobiotechnol, 9 (2017).

[50] J.I. Hare, T. Lammers, M.B. Ashford, S. Puri, G. Storm, S.T. Barry, Challenges and strategies in anti-cancer nanomedicine development: An industry perspective, Adv Drug Deliv Rev, 108 (2017) 25-38.

[51] N.M. La-Beck, A.A. Gabizon, Nanoparticle Interactions with the Immune System: Clinical Implications for Liposome-Based Cancer Chemotherapy, Front Immunol, 8 (2017) 416.

[52] J.S. Lee, M. Ankone, E. Pieters, R.M. Schiffelers, W.E. Hennink, J. Feijen, Circulation kinetics and biodistribution of dual-labeled polymersomes with modulated surface charge in tumor-bearing mice: comparison with stealth liposomes, J Control Release, 155 (2011) 282-288.

[53] A.D. Bangham, R.W. Horne, Negative Staining of Phospholipids and Their Structural Modification by Surface-Active Agents as Observed in the Electron Microscope, J Mol Biol, 8 (1964) 660-668.

[54] K. Yu, A. Eisenberg, Bilayer morphologies of self-assembled crew-cut aggregates of amphiphilic PS-b-PEO diblock copolymers in solution, Macromolecules, 31 (1998) 3509-3518.

[55] L.F. Zhang, A. Eisenberg, Multiple Morphologies of Crew-Cut Aggregates of Polystyrene-B-Poly(Acrylic Acid) Block-Copolymers, Science, 268 (1995) 1728-1731.

[56] J. Karlsson, H.J. Vaughan, J.J. Green, Biodegradable Polymeric Nanoparticles for Therapeutic Cancer Treatments, Annu Rev Chem Biomol Eng, 9 (2018) 105-127.

[57] A.C. Anselmo, S. Mitragotri, Nanoparticles in the clinic, Bioeng Transl Med, 1 (2016) 10-29.

[58] J. Shi, P.W. Kantoff, R. Wooster, O.C. Farokhzad, Cancer nanomedicine: progress, challenges and opportunities, Nat Rev Cancer, 17 (2017) 20-37.

[59] H.K. Ahn, M. Jung, S.J. Sym, D.B. Shin, S.M. Kang, S.Y. Kyung, J.W. Park, S.H. Jeong, E.K. Cho, A phase II trial of Cremorphor EL-free paclitaxel (Genexol-PM) and gemcitabine in patients with advanced non-small cell lung cancer, Cancer Chemother Pharmacol, 74 (2014) 277-282.

[60] T. Boehm, C.C. Bleul, The evolutionary history of lymphoid organs, Nat Immunol, 8 (2007) 131-135.

[61] L.C. Davies, S.J. Jenkins, J.E. Allen, P.R. Taylor, Tissue-resident macrophages, Nat Immunol, 14 (2013) 986-995.

[62] S. Gordon, P.R. Taylor, Monocyte and macrophage heterogeneity, Nat Rev Immunol, 5 (2005) 953-964.

[63] X.B. Ding, S.Q. Jin, Y. Tong, X. Jiang, Z.X. Chen, S.Y. Mei, L.M. Zhang, T.R. Billiar, Q. Li, TLR4 signaling induces TLR3 up-regulation in alveolar macrophages during acute lung injury, Sci Rep-Uk, 7 (2017).

[64] K. Kugathasan, E.K. Roediger, C.L. Small, S. McCormick, P.C. Yang, Z. Xing, CD11c+antigen presenting cells from the alveolar space, lung parenchyma and spleen differ in their phenotype and capabilities to activate naive and antigen-primed T cells, Bmc Immunol, 9 (2008).

[65] T.A. Wynn, A. Chawla, J.W. Pollard, Macrophage biology in development, homeostasis and disease, Nature, 496 (2013) 445-455.

[66] L. Chavez-Galan, M.L. Olleros, D. Vesin, I. Garcia, Much more than M1 and M2 macrophages, there are also CD169(+) and TCR+ macrophages, Frontiers in Immunology, 6 (2015).

[67] C.D. Mills, Anatomy of a discovery: M1 and M2 macrophages, Frontiers in Immunology, 6 (2015).

[68] K. Liddiard, P.R. Taylor, Understanding Local Macrophage Phenotypes In Disease: Shape-shifting macrophages, Nat Med, 21 (2015) 119-120.

[69] R.M. Steinman, Z.A. Cohn, Identification of a novel cell type in peripheral lymphoid organs of mice. I. Morphology, quantitation, tissue distribution, J Exp Med, 137 (1973) 1142-1162.

[70] R.M. Steinman, The dendritic cell system and its role in immunogenicity, Annu Rev Immunol, 9 (1991) 271-296.

[71] M. Guilliams, F. Ginhoux, C. Jakubzick, S.H. Naik, N. Onai, B.U. Schraml, E. Segura, R. Tussiwand, S. Yona, Dendritic cells, monocytes and macrophages: a unified nomenclature based on ontogeny, Nat Rev Immunol, 14 (2014) 571-578.

[72] O.P. Joffre, E. Segura, A. Savina, S. Amigorena, Cross-presentation by dendritic cells, Nat Rev Immunol, 12 (2012) 557-569.

[73] M. Colonna, G. Trinchieri, Y.J. Liu, Plasmacytoid dendritic cells in immunity, Nat Immunol, 5 (2004) 1219-1226.

[74] M. Swiecki, M. Colonna, The multifaceted biology of plasmacytoid dendritic cells, Nat Rev Immunol, 15 (2015) 471-485.

[75] W. Chen, X. Liang, A.J. Peterson, D.H. Munn, B.R. Blazar, The indoleamine 2,3-dioxygenase pathway is essential for human plasmacytoid dendritic cell-induced adaptive T regulatory cell generation, J Immunol, 181 (2008) 5396-5404.

[76] G. Penna, S. Amuchastegui, N. Giarratana, K.C. Daniel, M. Vulcano, S. Sozzani, L. Adorini, 1,25-Dihydroxyvitamin D3 selectively modulates tolerogenic properties in myeloid but not plasmacytoid dendritic cells, J Immunol, 178 (2007) 145-153.

[77] V.K. Raker, M.P. Domogalla, K. Steinbrink, Tolerogenic Dendritic Cells for Regulatory T Cell Induction in Man, Front Immunol, 6 (2015) 569.

[78] B.K. Stansfield, D.A. Ingram, Clinical significance of monocyte heterogeneity, Clin Transl Med, 4 (2015) 5.

[79] A.V. Misharin, C.M. Cuda, R. Saber, J.D. Turner, A.K. Gierut, G.K. Haines, 3rd, S. Berdnikovs, A. Filer, A.R. Clark, C.D. Buckley, G.M. Mutlu, G.R. Budinger, H. Perlman, Nonclassical Ly6C(-) monocytes drive the development of inflammatory arthritis in mice, Cell Rep, 9 (2014) 591-604.

[80] J. Wang, L. Yang, L. Yu, Y.Y. Wang, R. Chen, J. Qian, Z.P. Hong, X.S. Su, Surgery-induced monocytic myeloid-derived suppressor cells expand regulatory T cells in lung cancer, Oncotarget, 8 (2017) 17050-17058.

[81] D.I. Gabrilovich, Myeloid-Derived Suppressor Cells, Cancer Immunol Res, 5 (2017) 3-8.

[82] M. Ouzounova, E. Lee, R. Piranlioglu, A. El Andaloussi, R. Kolhe, M.F. Demirci, D. Marasco, I. Asm, A. Chadli, K.A. Hassan, M. Thangaraju, G. Zhou, A.S. Arbab, J.K. Cowell, H. Korkaya, Monocytic and granulocytic myeloid derived suppressor cells differentially regulate spatiotemporal tumour plasticity during metastatic cascade, Nat Commun, 8 (2017) 14979.

[83] D.C. Dale, L. Boxer, W.C. Liles, The phagocytes: neutrophils and monocytes, Blood, 112 (2008) 935-945.

[84] V. Brinkmann, U. Reichard, C. Goosmann, B. Fauler, Y. Uhlemann, D.S. Weiss, Y. Weinrauch, A. Zychlinsky, Neutrophil extracellular traps kill bacteria, Science, 303 (2004) 1532-1535.

[85] C. Nathan, Neutrophils and immunity: challenges and opportunities, Nat Rev Immunol, 6 (2006) 173-182.

[86] M. Herant, V. Heinrich, M. Dembo, Mechanics of neutrophil phagocytosis: experiments and quantitative models, J Cell Sci, 119 (2006) 1903-1913.

[87] T.N. Mayadas, X. Cullere, C.A. Lowell, The multifaceted functions of neutrophils, Annu Rev Pathol, 9 (2014) 181-218.

[88] K.E. O'Connell, A.M. Mikkola, A.M. Stepanek, A. Vernet, C.D. Hall, C.C. Sun, E. Yildirim, J.F. Staropoli, J.T. Lee, D.E. Brown, Practical murine hematopathology: a comparative review and implications for research, Comp Med, 65 (2015) 96-113.

[89] J.A. Nemzek, G.L. Bolgos, B.A. Williams, D.G. Remick, Differences in normal values for murine white blood cell counts and other hematological parameters based on sampling site, Inflamm Res, 50 (2001) 523-527.

[90] E.G. Engleman, C.J. Benike, F.C. Grumet, R.L. Evans, Activation of human T lymphocyte subsets: helper and suppressor/cytotoxic T cells recognize and respond to distinct histocompatibility antigens, J Immunol, 127 (1981) 2124-2129.

[91] M.H. Andersen, D. Schrama, P. Thor Straten, J.C. Becker, Cytotoxic T cells, J Invest Dermatol, 126 (2006) 32-41.

[92] S.P. Schoenberger, R.E. Toes, E.I. van der Voort, R. Offringa, C.J. Melief, T-cell help for cytotoxic T lymphocytes is mediated by CD40-CD40L interactions, Nature, 393 (1998) 480-483.

[93] P. Bhat, G. Leggatt, N. Waterhouse, I.H. Frazer, Interferon-gamma derived from cytotoxic lymphocytes directly enhances their motility and cytotoxicity, Cell Death Dis, 8 (2017) e2836.

[94] B.C. Sheu, W.C. Chang, S.C. Huang, New era of regulatory T cells in tumor immunity: insights in cancer immunotherapy, J Formos Med Assoc, 109 (2010) 1-3.

[95] S.M. Kaech, E.J. Wherry, R. Ahmed, Effector and memory T-cell differentiation: implications for vaccine development, Nat Rev Immunol, 2 (2002) 251-262.

[96] S. Nonoyama, D. Hollenbaugh, A. Aruffo, J.A. Ledbetter, H.D. Ochs, B cell activation *via* CD40 is required for specific antibody production by antigen-stimulated human B cells, J Exp Med, 178 (1993) 1097-1102.

[97] F.D. Batista, N.E. Harwood, The who, how and where of antigen presentation to B cells, Nat Rev Immunol, 9 (2009) 15-27.

[98] C.S. Park, Y.S. Choi, How do follicular dendritic cells interact intimately with B cells in the germinal centre?, Immunology, 114 (2005) 2-10.

[99] A. Lanzavecchia, Antigen-specific interaction between T and B cells, Nature, 314 (1985) 537-539.

[100] S. Crotty, P. Felgner, H. Davies, J. Glidewell, L. Villarreal, R. Ahmed, Cutting edge: long-term B cell memory in humans after smallpox vaccination, J Immunol, 171 (2003) 4969-4973.

[101] G. Trinchieri, Biology of natural killer cells, Adv Immunol, 47 (1989) 187-376.

[102] M.A. Cooper, T.A. Fehniger, M.A. Caligiuri, The biology of human natural killer-cell subsets, Trends Immunol, 22 (2001) 633-640.

[103] T. Kambayashi, T.M. Laufer, Atypical MHC class II-expressing antigen-presenting cells: can anything replace a dendritic cell?, Nat Rev Immunol, 14 (2014) 719-730.

[104] Y. Chen, J. Cai, Q. Xu, Z.W. Chen, Atomic force bio-analytics of polymerization and aggregation of phycoerythrin-conjugated immunoglobulin G molecules, Mol Immunol, 41 (2004) 1247-1252.

[105] D.M. Belnap, N.H. Olson, N.M. Cladel, W.W. Newcomb, J.C. Brown, J.W. Kreider, N.D. Christensen, T.S. Baker, Conserved features in papillomavirus and polyomavirus capsids, J Mol Biol, 259 (1996) 249-263.

[106] W. Zhang, S. Cao, J.L. Martin, J.D. Mueller, L.M. Mansky, Morphology and ultrastructure of retrovirus particles, AIMS Biophys, 2 (2015) 343-369.

[107] J.P. Lim, P.A. Gleeson, Macropinocytosis: an endocytic pathway for internalising large gulps, Immunol Cell Biol, 89 (2011) 836-843.

[108] M. Elsabahy, K.L. Wooley, Design of polymeric nanoparticles for biomedical delivery applications, Chem Soc Rev, 41 (2012) 2545-2561.

[109] S. Allen, Y.G. Liu, E. Scott, Engineering nanomaterials to address cell-mediated inflammation in atherosclerosis, Regen Eng Transl Med, 2 (2016) 37-50.

[110] D.E. Owens, 3rd, N.A. Peppas, Opsonization, biodistribution, and pharmacokinetics of polymeric nanoparticles, Int J Pharm, 307 (2006) 93-102.

[111] D.A. Hume, Differentiation and heterogeneity in the mononuclear phagocyte system, Mucosal Immunol, 1 (2008) 432-441.

[112] A. Chow, B.D. Brown, M. Merad, Studying the mononuclear phagocyte system in the molecular age, Nat Rev Immunol, 11 (2011) 788-798.

[113] M. Longmire, P.L. Choyke, H. Kobayashi, Clearance properties of nano-sized particles and molecules as imaging agents: considerations and caveats, Nanomedicine (Lond), 3 (2008) 703-717.

[114] H.S. Choi, W. Liu, P. Misra, E. Tanaka, J.P. Zimmer, B. Itty Ipe, M.G. Bawendi, J.V. Frangioni, Renal clearance of quantum dots, Nat Biotechnol, 25 (2007) 1165-1170.

[115] H.J. Cho, J.W. Park, I.S. Yoon, D.D. Kim, Surface-modified solid lipid nanoparticles for oral delivery of docetaxel: enhanced intestinal absorption and lymphatic uptake, Int J Nanomedicine, 9 (2014) 495-504.

[116] J.S. Patton, Mechanisms of macromolecule absorption by the lungs, Adv Drug Deliver Rev, 19 (1996) 3-36.

[117] S. Cai, Q. Yang, T.R. Bagby, M.L. Forrest, Lymphatic drug delivery using engineered liposomes and solid lipid nanoparticles, Adv Drug Deliv Rev, 63 (2011) 901-908.

[118] A. Sharma, U.S. Sharma, Liposomes in drug delivery: progress and limitations, Int J Pharmaceut, 154 (1997) 123-140.

[119] S. Cerritelli, A. Fontana, D. Velluto, M. Adrian, J. Dubochet, P. De Maria, J.A. Hubbell, Thermodynamic and kinetic effects in the aggregation behavior of a poly(ethylene glycol-b-propylene sulfide-b-ethylene glycol) ABA triblock copolymer, Macromolecules, 38 (2005) 7845-7851.

[120] Y.M. Chen, J.Z. Du, M. Xiong, H.X. Guo, H. Jinnai, T. Kaneko, Perforated block copolymer vesicles with a highly folded membrane, Macromolecules, 40 (2007) 4389-4392.

[121] S.J. Yi, S.D. Allen, Y.G. Liu, B.Z. Ouyang, X.M. Li, P. Augsornworawat, E.B. Thorp, E.A. Scott, Tailoring Nanostructure Morphology for Enhanced Targeting of Dendritic Cells in Atherosclerosis, Acs Nano, 10 (2016) 11290-11303.

[122] J.R. Howse, R.A.L. Jones, G. Battaglia, R.E. Ducker, G.J. Leggett, A.J. Ryan, Templated formation of giant polymer vesicles with controlled size distributions, Nature Materials, 8 (2009) 507-511.

[123] C.P. O'Neil, T. Suzuki, D. Demurtas, A. Finka, J.A. Hubbell, A Novel Method for the Encapsulation of Biomolecules into Polymersomes *via* Direct Hydration, Langmuir, 25 (2009) 9025-9029.

[124] B.K. Johnson, R.K. Prud'homme, Flash NanoPrecipitation of Organic Actives and Block Copolymers using a Confined Impinging Jets Mixer, Australian Journal of Chemistry, 56 (2003) 1021-1024.

[125] B.K. Johnson, W. Saad, R.K. Prud'homme, Nanoprecipitation of Pharmaceuticals Using Mixing and Block Copolymer Stabilization, in: Polymeric Drug Delivery II, American Chemical Society, 2006, pp. 278-291.

[126] A.J. Mahajan, D.J. Kirwan, Nucleation and Growth-Kinetics of Biochemicals Measured at High Supersaturations, J Cryst Growth, 144 (1994) 281-290.

[127] W.S. Saad, R.K. Prud'homme, Principles of nanoparticle formation by flash nanoprecipitation, Nano Today, 11 (2016) 212-227.

[128] Y. Liu, K. Kathan, W. Saad, R.K. Prud'homme, Ostwald ripening of beta-carotene nanoparticles, Phys Rev Lett, 98 (2007).

[129] J. Han, Z.X. Zhu, H.T. Qian, A.R. Wohl, C.J. Beaman, T.R. Hoye, C.W. Macosko, A simple confined impingement jets mixer for flash nanoprecipitation, J Pharm Sci-Us, 101 (2012) 4018-4023.

[130] Y. Liu, C.Y. Cheng, Y. Liu, R.K. Prud'homme, R.O. Fox, Mixing in a multi-inlet vortex mixer (MIVM) for flash nano-precipitation, Chem Eng Sci, 63 (2008) 2829-2842.

[131] E.A. Scott, A. Stano, M. Gillard, A.C. Maio-Liu, M.A. Swartz, J.A. Hubbell, Dendritic cell activation and T cell priming with adjuvant- and antigen-loaded oxidation-sensitive polymersomes, Biomaterials, 33 (2012) 6211-6219.

[132] A. Stano, E.A. Scott, K.Y. Dane, M.A. Swartz, J.A. Hubbell, Tunable T cell immunity towards a protein antigen using polymersomes vs. solid-core nanoparticles, Biomaterials, 34 (2013) 4339-4346.

[133] Z.X. Zhu, Flash Nanoprecipitation: Prediction and Enhancement of Particle Stability *via* Drug Structure, Mol Pharmaceut, 11 (2014) 776-786.

[134] M.D. Nichols, E.A. Scott, D.L. Elbert, Factors affecting size and swelling of poly(ethylene glycol) microspheres formed in aqueous sodium sulfate solutions without surfactants, Biomaterials, 30 (2009) 5283-5291.

[135] B.E. McKenzie, J.F. de Visser, H. Friedrich, M.J.M. Wirix, P.H.H. Bomans, G. de With, S.J. Holder, N.A.J.M. Sommerdijk, Bicontinuous Nanospheres from Simple Amorphous Amphiphilic Diblock Copolymers, Macromolecules, 46 (2013) 9845-9848.

[136] I.D.M. Azmi, S.M. Moghimi, A. Yaghmur, Cubosomes and hexosomes as versatile platforms for drug delivery, Ther Deliv, 6 (2015) 1347-1364.

[137] J. Barauskas, M. Johnsson, F. Johnson, F. Tiberg, Cubic phase nanoparticles (Cubosome): Principles for controlling size, structure, and stability, Langmuir, 21 (2005) 2569-2577.

[138] I. Amar-Yuli, E. Wachtel, E. Ben Shoshan, D. Danino, A. Aserin, N. Garti, Hexosome and hexagonal phases mediated by hydration and polymeric stabilizer, Langmuir, 23 (2007) 3637-3645.

[139] S. Engelskirchen, R. Maurer, O. Glatter, Effect of glycerol addition on the internal structure and thermal stability of hexosomes prepared from phytantriol, Colloid Surface A, 391 (2011) 95-100.

[140] Y.D. Dong, I. Larson, T. Hanley, B.J. Boyd, Bulk and dispersed aqueous phase behavior of phytantriol: Effect of vitamin E acetate and F127 polymer on liquid crystal nanostructure, Langmuir, 22 (2006) 9512-9518.

[141] X. Shi, T. Peng, Y. Huang, L. Mei, Y. Gu, J. Huang, K. Han, G. Li, C. Hu, X. Pan, C. Wu, Comparative studies on glycerol monooleate- and phytantriol-based cubosomes containing oridonin in vitro and in vivo, Pharm Dev Technol, 22 (2017) 322-329.

[142] M. Malmsten, Soft drug delivery systems, Soft Matter, 2 (2006) 760-769.

[143] A. Chemelli, M. Maurer, R. Geier, O. Glatter, Optimized loading and sustained release of hydrophilic proteins from internally nanostructured particles, Langmuir, 28 (2012) 16788-16797.

[144] A. Yaghmur, O. Glatter, Characterization and potential applications of nanostructured aqueous dispersions, Adv Colloid Interface Sci, 147-148 (2009) 333-342.

[145] W. Leesajakul, M. Nakano, A. Taniguchi, T. Handa, Interaction of cubosomes with plasma components resulting in the destabilization of cubosomes in plasma, Colloid Surface B, 34 (2004) 253-258.

[146] B.E. Mkenzie, S.J. Holder, N.A.J.M. Sommerdijk, Assessing internal structure of polymer assemblies from 2D to 3D CryoTEM: Bicontinuous micelles, Current Opinion in Colloid & Interface Science, 17 (2012) 343-349.

[147] B.E. McKenzie, H. Friedrich, M.J.M. Wirix, J.F. de Visser, O.R. Monaghan, P.H.H. Bomans, F. Nudelman, S.J. Holder, N.A.J.M. Sommerdijk, Controlling Internal Pore Sizes in Bicontinuous Polymeric Nanospheres, Angewandte Chemie International Edition, 54 (2015) 2457-2461.

[148] S. Bobbala, S.D. Allen, E.A. Scott, Flash nanoprecipitation permits versatile assembly and loading of polymeric bicontinuous cubic nanospheres, Nanoscale, 10 (2018) 5078-5088.

[149] Y. La, C. Park, T.J. Shin, S.H. Joo, S. Kang, K.T. Kim, Colloidal inverse bicontinuous cubic membranes of block copolymers with tunable surface functional groups, Nat Chem, 6 (2014) 534-541.

[150] S.A. Barnhill, N.C. Bell, J.P. Patterson, D.P. Olds, N.C. Gianneschi, Phase Diagrams of Polynorbornene Amphiphilic Block Copolymers in Solution, Macromolecules, 48 (2015) 1152-1161.

[151] Y. La, T.H. An, T.J. Shin, C. Park, K.T. Kim, A Morphological Transition of Inverse Mesophases of a Branched-Linear Block Copolymer Guided by Using Cosolvents, Angewandte Chemie-International Edition, 54 (2015) 10483-10487.

[152] Z.X. Lin, S.H. Liu, W.T. Mao, H. Tian, N. Wang, N.H. Zhang, F. Tian, L. Han, X.L. Feng, Y.Y. Mai, Tunable Self-Assembly of Diblock Copolymers into Colloidal Particles with Triply Periodic Minimal Surfaces, Angewandte Chemie-International Edition, 56 (2017) 7135-7140.

[153] A. Cho, Y. La, T.J. Shin, C. Park, K.T. Kim, Structural Requirements of Block Copolymers for Self-Assembly into Inverse Bicontinuous Cubic Mesophases in Solution, Macromolecules, 49 (2016) 4510-4519.

[154] S.J. Holder, G. Woodward, B. McKenzie, N.A.J.M. Sommerdijk, Semi-crystalline block copolymer bicontinuous nanospheres for thermoresponsive controlled release, Rsc Adv, 4 (2014) 26354-26358.

[155] O.R. Monaghan, P.H.H. Bomans, N.A.J.M. Sommerdijk, S.J. Holder, Controlling the melting transition of semi-crystalline self-assembled block copolymer aggregates: controlling release rates of ibuprofen, Polym Chem-Uk, 8 (2017) 5303-5316.

[156] A.L. Parry, P.H.H. Bomans, S.J. Holder, N.A.J.M. Sommerdijk, S.C.G. Biagini, Cryo Electron Tomography Reveals Confined Complex Morphologies of Tripeptide-Containing Amphiphilic Double-Comb Diblock Copolymers, Angewandte Chemie-International Edition, 47 (2008) 8859-8862.

[157] H.K. He, K. Rahimi, M.J. Zhong, A. Mourran, D.R. Luebke, H.B. Nulwala, M. Moller, K. Matyjaszewski, Cubosomes from hierarchical self-assembly of poly(ionic liquid) block copolymers, Nature Communications, 8 (2017).

[158] K. Hales, Z.Y. Chen, K.L. Wooley, D.J. Pochan, Nanoparticles with tunable internal structure from triblock copolymers of PAA-b-PMA-b-PS, Nano Lett, 8 (2008) 2023-2026.

[159] T.H. An, Y. La, A. Cho, M.G. Jeong, T.J. Shin, C. Park, K.T. Kim, Solution Self-Assembly of Block Copolymers Containing a Branched Hydrophilic Block into Inverse Bicontinuous Cubic Mesophases, Acs Nano, 9 (2015) 3084-3096.

[160] A. Cho, Y. La, S. Jeoung, H.R. Moon, J.H. Ryu, T.J. Shin, K.T. Kim, Mix-and-Match Assembly of Block Copolymer Blends in Solution, Macromolecules, 50 (2017) 3234-3243.

[161] M.G. Jeong, K.T. Kim, Covalent Stabilization of Inverse Bicontinuous Cubic Structures of Block Copolymer Bilayers by Photodimerization of Indene Pendant Groups of Polystyrene Hydrophobic Blocks, Macromolecules, 50 (2017) 223-234.

[162] Y. Kang, A. Pitto-Barry, M.S. Rolph, Z. Hua, I. Hands-Portman, N. Kirby, R.K. O'Reilly, Use of complementary nucleobase-containing synthetic polymers to prepare complex self-assembled morphologies in water, Polym Chem-Uk, 7 (2016) 2836-2846.

[163] X.L. Lyu, A.Q. Xiao, W. Zhang, P.P. Hou, K.H. Gu, Z.H. Tang, H.B. Pan, F. Wu, Z.H. Shen, X.H. Fan, Head-Tail Asymmetry as the Determining Factor in the Formation of Polymer Cubosomes or Hexasomes in a Rod-Coil Amphiphilic Block Copolymer, Angewandte Chemie-International Edition, 57 (2018) 10132-10136.

[164] H.-K. Liu, L.-J. Ren, H. Wu, Y.-L. Ma, S. Richter, M. Godehardt, C. Kübel, W. Wang, Unraveling the Self-Assembly of Heterocluster Janus Dumbbells into Hybrid Cubosomes with Internal Double-Diamond Structure, Journal of the American Chemical Society, (2018).

[165] B.E. McKenzie, F. Nudelman, P.H.H. Bomans, S.J. Holder, N.A.J.M. Sommerdijk, Temperature-Responsive Nanospheres with Bicontinuous Internal Structures from a Semicrystalline Amphiphilic Block Copolymer, Journal of the American Chemical Society, 132 (2010) 10256-10259.

[166] S. Allen, O. Osorio, Y.G. Liu, E. Scott, Facile assembly and loading of theranostic polymersomes *via* multi-impingement flash nanoprecipitation, Journal of Controlled Release, 262 (2017) 91-103.

[167] B.E. McKenzie, J.F. de Visser, G. Portale, D. Hermida-Merino, H. Friedrich, P.H.H. Bomans, W. Bras, O.R. Monaghan, S.J. Holder, N.A.J.M. Sommerdijk, The evolution of bicontinuous polymeric nanospheres in aqueous solution, Soft Matter, 12 (2016) 4113-4122.

[168] J. Cui, J.P. Xu, Y.T. Zhu, W. Jiang, Shear Flow Controlled Morphological Polydispersity of Amphiphilic ABA Triblock Copolymer Vesicles, Langmuir, 29 (2013) 15704-15710.

[169] Z.P. Yang, X.L. Chen, Z. Xu, M.N. Xiao, L.Z. Hong, T. Ngai, Shear-Assisted Fabrication of Block Copolymer Agglomerates with Various Morphologies in Viscous Medium, Langmuir, 33 (2017) 2829-2836.

[170] S.M. Gruner, R.P. Lenk, A.S. Janoff, M.J. Ostro, Novel Multilayered Lipid Vesicles - Comparison of Physical Characteristics of Multilamellar Liposomes and Stable Plurilamellar Vesicles, Biochemistry-Us, 24 (1985) 2833-2842.

[171] P.O. Magalhaes, A.M. Lopes, P.G. Mazzola, C. Rangel-Yagui, T.C.V. Penna, A. Pessoa, Methods of endotoxin removal from biological preparations: a review, J Pharm Pharm Sci, 10 (2007) 388-404.

[172] P. Malyala, M. Singh, Endotoxin limits in formulations for preclinical research, J Pharm Sci-Us, 97 (2008) 2041-2044.

[173] R.E. Lewis, G.L. Liao, K. Young, C. Douglas, D.P. Kontoyiannis, Macrophage Reporter Cell Assay for Screening Immunopharmacological Activity of Cell Wall-Active Antifungals, Antimicrob Agents Ch, 58 (2014) 1738-1743.

[174] S. Allen, M. Vincent, E. Scott, Rapid, Scalable Assembly and Loading of Bioactive Proteins and Immunostimulants into Diverse Synthetic Nanocarriers *via* Flash Nanoprecipitation, J Vis Exp, (2018).

[175] S.D. Allen, Y.G. Liu, S. Bobbala, L. Cai, P.I. Hecker, R. Temel, E.A. Scott, Polymersomes scalably fabricated *via* flash nano-precipitation are non-toxic in non-human primates and associate with leukocytes in the spleen and kidney following intravenous administration, Nano Res, 11 (2018) 5689-5703.

[176] S.D. Allen, S. Bobbala, N.B. Karabin, E.A. Scott, On the advancement of polymeric bicontinuous nanospheres toward biomedical applications, Nanoscale Horizons, (2019).

[177] J. Mondal, A. Yethiraj, Driving Force for the Association of Amphiphilic Molecules, J Phys Chem Lett, 2 (2011) 2391-2395.

[178] G.S. Kwon, M. Naito, K. Kataoka, M. Yokoyama, Y. Sakurai, T. Okano, Block copolymer micelles as vehicles for hydrophobic drugs, Colloids and Surfaces B: Biointerfaces, 2 (1994) 429-434.

[179] Z.P. Zhang, S.S. Feng, The drug encapsulation efficiency, in vitro drug release, cellular uptake and cytotoxicity of paclitaxel-loaded poly(lactide)-tocopheryl polyethylene glycol succinate nanoparticles, Biomaterials, 27 (2006) 4025-4033.

[180] S.L. Hao, Y.Z. Wang, B.C. Wang, J. Deng, X. Liu, J.Y. Liu, Rapid preparation of pH-sensitive polymeric nanoparticle with high loading capacity using electrospray for oral drug delivery, Mat Sci Eng C-Mater, 33 (2013) 4562-4567.

[181] G. Kwon, M. Naito, M. Yokoyama, T. Okano, Y. Sakurai, K. Kataoka, Block copolymer micelles for drug delivery: loading and release of doxorubicin, Journal of Controlled Release, 48 (1997) 195-201.

[182] Y. Mi, J. Zhao, S.S. Feng, Vitamin E TPGS prodrug micelles for hydrophilic drug delivery with neuroprotective effects, Int J Pharmaceut, 438 (2012) 98-106.

[183] X.Y. Ke, V.W.L. Ng, R.J. Ono, J.M.W. Chan, S. Krishnamurthy, Y. Wang, J.L. Hedrick, Y.Y. Yang, Role of non-covalent and covalent interactions in cargo loading capacity and stability of polymeric micelles, Journal of Controlled Release, 193 (2014) 9-26.

[184] F. Ahmed, R.I. Pakunlu, A. Brannan, F. Bates, T. Minko, D.E. Discher, Biodegradable polymersomes loaded with both paclitaxel and doxorubicin permeate and shrink tumors, inducing apoptosis in proportion to accumulated drug, Journal of Controlled Release, 116 (2006) 150-158.

[185] H.M.G. Barriga, M.N. Holme, M.M. Stevens, Cubosomen: die nächste Generation intelligenter Lipid-Nanopartikel?, Angewandte Chemie, 0.

[186] X. Xu, M.A. Khan, D.J. Burgess, Predicting hydrophilic drug encapsulation inside unilamellar liposomes, Int J Pharm, 423 (2012) 410-418.

[187] G. Battaglia, A.J. Ryan, Pathways of polymeric vesicle formation, J Phys Chem B, 110 (2006) 10272-10279.

[188] L. Messager, J. Gaitzsch, L. Chierico, G. Battaglia, Novel aspects of encapsulation and delivery using polymersomes, Curr Opin Pharmacol, 18 (2014) 104-111.

[189] M. Frey, S. Bobbala, N. Karabin, E. Scott, Influences of nanocarrier morphology on therapeutic immunomodulation, Nanomedicine (Lond), (2018).

[190] Z. Cheng, A. Al Zaki, J.Z. Hui, V.R. Muzykantov, A. Tsourkas, Multifunctional nanoparticles: cost versus benefit of adding targeting and imaging capabilities, Science, 338 (2012) 903-910.

[191] D.J. Dowling, E.A. Scott, A. Scheid, I. Bergelson, S. Joshi, C. Pietrasanta, S. Brightman, G. Sanchez-Schmitz, S.D. Van Haren, J. Ninkovic, D. Kats, C. Guiducci, A. de Titta, D.K. Bonner, S. Hirosue, M.A. Swartz, J.A. Hubbell, O. Levy, Toll-like receptor 8 agonist nanoparticles mimic immunomodulating effects of the live BCG vaccine and enhance neonatal innate and adaptive immune responses, J Allergy Clin Immunol, 140 (2017) 1339-1350.

[192] L. Talamini, M.B. Violatto, Q. Cai, M.P. Monopoli, K. Kantner, Z. Krpetic, A. Perez-Potti, J. Cookman, D. Garry, P.S. C, L. Boselli, B. Pelaz, T. Serchi, S. Cambier, A.C. Gutleb, N. Feliu, Y. Yan, M. Salmona, W.J. Parak, K.A. Dawson, P. Bigini, Influence of Size and Shape on the Anatomical Distribution of Endotoxin-Free Gold Nanoparticles, ACS Nano, 11 (2017) 5519-5529.

[193] S.T. Reddy, A. Rehor, H.G. Schmoekel, J.A. Hubbell, M.A. Swartz, In vivo targeting of dendritic cells in lymph nodes with poly(propylene sulfide) nanoparticles, J Control Release, 112 (2006) 26-34.

[194] M.B. Lutz, N. Kukutsch, A.L. Ogilvie, S. Rossner, F. Koch, N. Romani, G. Schuler, An advanced culture method for generating large quantities of highly pure dendritic cells from mouse bone marrow, J Immunol Methods, 223 (1999) 77-92.

[195] T.J. Chen, N. Kotecha, Cytobank: providing an analytics platform for community cytometry data analysis and collaboration, Curr Top Microbiol Immunol, 377 (2014) 127-157.

[196] M. Massignani, I. Canton, T. Sun, V. Hearnden, S. Macneil, A. Blanazs, S.P. Armes, A. Lewis, G. Battaglia, Enhanced fluorescence imaging of live cells by effective cytosolic delivery of probes, PLoS One, 5 (2010) e10459.

[197] K.M. Pustulka, A.R. Wohl, H.S. Lee, A.R. Michel, J. Han, T.R. Hoye, A.V. McCormick, J. Panyam, C.W. Macosko, Flash nanoprecipitation: particle structure and stability, Mol Pharm, 10 (2013) 4367-4377.

[198] B. Maherani, E. Arab-Tehrany, A. Kheirolomoom, D. Geny, M. Linder, Calcein release behavior from liposomal bilayer; influence of physicochemical/mechanical/structural properties of lipids, Biochimie, 95 (2013) 2018-2033.

[199] S.F. van Dongen, M. Nallani, J.J. Cornelissen, R.J. Nolte, J.C. van Hest, A three-enzyme cascade reaction through positional assembly of enzymes in a polymersome nanoreactor, Chemistry, 15 (2009) 1107-1114.

[200] S. Rameez, H. Alosta, A.F. Palmer, Biocompatible and biodegradable polymersome encapsulated hemoglobin: a potential oxygen carrier, Bioconjug Chem, 19 (2008) 1025-1032.

[201] D.R. Arifin, A.F. Palmer, Polymersome encapsulated hemoglobin: a novel type of oxygen carrier, Biomacromolecules, 6 (2005) 2172-2181.

[202] H. Lomas, M. Massignani, K.A. Abdullah, I. Canton, C. Lo Presti, S. MacNeil, J. Du, A. Blanazs, J. Madsen, S.P. Armes, A.L. Lewis, G. Battaglia, Non-cytotoxic polymer vesicles for rapid and efficient intracellular delivery, Faraday Discuss, 139 (2008) 143-159; discussion 213-128, 419-120.

[203] J.P. Horwitz, J. Chua, M. Noel, J.T. Donatti, J. Freisler, Substrates for cytochemical demonstration of enzyme activity. II. Some dihalo-3-indolyl phosphates and sulfates, J Med Chem, 9 (1966) 447.

[204] A. Rehor, J.A. Hubbell, N. Tirelli, Oxidation-sensitive polymeric nanoparticles, Langmuir, 21 (2005) 411-417.

[205] C. de Gracia Lux, S. Joshi-Barr, T. Nguyen, E. Mahmoud, E. Schopf, N. Fomina, A. Almutairi, Biocompatible polymeric nanoparticles degrade and release cargo in response to biologically relevant levels of hydrogen peroxide, J Am Chem Soc, 134 (2012) 15758-15764.

[206] G.B. Ray, I. Chakraborty, S.P. Moulik, Pyrene absorption can be a convenient method for probing critical micellar concentration (cmc) and indexing micellar polarity, J Colloid Interf Sci, 294 (2006) 248-254.

[207] M.J. Geisow, P.D. Hart, M.R. Young, Temporal Changes of Lysosome and Phagosome Ph during Phagolysosome Formation in Macrophages - Studies by Fluorescence Spectroscopy, J Cell Biol, 89 (1981) 645-652.

[208] S.B. Shang, D. Kats, L. Cao, E. Morgun, D. Velluto, Y. He, Q.C. Xu, C.R. Wang, E.A. Scott, Induction of Mycobacterium Tuberculosis Lipid-Specific T Cell Responses by Pulmonary Delivery of Mycolic Acid-Loaded Polymeric Micellar Nanocarriers, Frontiers in Immunology, 9 (2018).

[209] S.R. Bonam, C.D. Partidos, S.K.M. Halmuthur, S. Muller, An Overview of Novel Adjuvants Designed for Improving Vaccine Efficacy, Trends Pharmacol Sci, 38 (2017) 771-793.

[210] P. Sahdev, L.J. Ochyl, J.J. Moon, Biomaterials for nanoparticle vaccine delivery systems, Pharm Res, 31 (2014) 2563-2582.

[211] S. Bobbala, S. Hook, Is There an Optimal Formulation and Delivery Strategy for Subunit Vaccines?, Pharm Res, 33 (2016) 2078-2097.

[212] W.R. Heath, G.T. Belz, G.M. Behrens, C.M. Smith, S.P. Forehan, I.A. Parish, G.M. Davey, N.S. Wilson, F.R. Carbone, J.A. Villadangos, Cross-presentation, dendritic cell subsets, and the generation of immunity to cellular antigens, Immunol Rev, 199 (2004) 9-26.

[213] J.K. Park, T. Utsumi, Y.E. Seo, Y. Deng, A. Satoh, W.M. Saltzman, Y. Iwakiri, Cellular distribution of injected PLGA-nanoparticles in the liver, Nanomedicine, 12 (2016) 1365-1374.

[214] Y. Huh, D.E. Smith, M.R. Feng, Interspecies scaling and prediction of human clearance: comparison of small- and macro-molecule drugs, Xenobiotica, 41 (2011) 972-987.

[215] C. Vaure, Y. Liu, A comparative review of toll-like receptor 4 expression and functionality in different animal species, Front Immunol, 5 (2014) 316.

[216] P.A. Chiarelli, R.A. Revia, Z.R. Stephen, K. Wang, M. Jeon, V. Nelson, F.M. Kievit, J. Sham, R.G. Ellenbogen, H.P. Kiem, M. Zhang, Nanoparticle Biokinetics in Mice and Nonhuman Primates, ACS Nano, 11 (2017) 9514-9524.

[217] F. Du, Y.G. Liu, E.A. Scott, Immunotheranostic Polymersomes Modularly Assembled from Tetrablock and Diblock Copolymers with Oxidation-Responsive Fluorescence, Cell Mol Bioeng, 10 (2017) 357-370.

[218] V. Bronte, M.J. Pittet, The Spleen in Local and Systemic Regulation of Immunity, Immunity, 39 (2013) 806-818.

[219] J.G. Cyster, Chemokines and cell migration in secondary lymphoid organs, Science, 286 (1999) 2098-2102.

[220] Y. Song, X. Li, X. Du, Exposure to nanoparticles is related to pleural effusion, pulmonary fibrosis and granuloma, Eur Respir J, 34 (2009) 559-567.

[221] F. Alexis, E. Pridgen, L.K. Molnar, O.C. Farokhzad, Factors affecting the clearance and biodistribution of polymeric nanoparticles, Mol Pharmaceut, 5 (2008) 505-515.

[222] A.L. Palange, R. Palomba, I.F. Rizzuti, M. Ferreira, P. Decuzzi, Deformable Discoidal Polymeric Nanoconstructs for the Precise Delivery of Therapeutic and Imaging Agents, Mol Ther, 25 (2017) 1514-1521.

[223] S.D. Allen, S. Bobbala, N.B. Karabin, M. Modak, E.A. Scott, Benchmarking Bicontinuous Nanospheres against Polymersomes for in Vivo Biodistribution and Dual Intracellular Delivery of Lipophilic and Water-Soluble Payloads, Acs Appl Mater Inter, 10 (2018) 33857-33866.

[224] S.D. Allen, Y.G. Liu, T. Kim, S. Bobbala, S. Yi, X. Zhang, J. Choi, E.A. Scott, Celastrol-loaded PEG-b-PPS nanocarriers as an anti-inflammatory treatment for atherosclerosis, Biomater Sci, (2019).

[225] L.A. Buckley, S. Salunke, K. Thompson, G. Baer, D. Fegley, M.A. Turner, Challenges and strategies to facilitate formulation development of pediatric drug products: Safety qualification of excipients, Int J Pharmaceut, 536 (2018) 563-569.

[226] A. Nel, T. Xia, L. Madler, N. Li, Toxic potential of materials at the nanolevel, Science, 311 (2006) 622-627.

[227] Y. Jin, S. Kannan, M. Wu, J.X. Zhao, Toxicity of luminescent silica nanoparticles to living cells, Chem Res Toxicol, 20 (2007) 1126-1133.

[228] W.P. Hoffman, D.K. Ness, R.B.L. van Lier, Analysis of rodent growth data in toxicology studies, Toxicol Sci, 66 (2002) 313-319.

[229] W.S. Cho, M.J. Cho, J. Jeong, M. Choi, H.Y. Cho, B.S. Han, S.H. Kim, H.O. Kim, Y.T. Lim, B.H. Chung, J. Jeong, Acute toxicity and pharmacokinetics of 13 nm-sized PEG-coated gold nanoparticles, Toxicol Appl Pharm, 236 (2009) 16-24.

[230] H. Nishimori, M. Kondoh, K. Isoda, S. Tsunoda, Y. Tsutsumi, K. Yagi, Histological analysis of 70-nm silica particles-induced chronic toxicity in mice, Eur J Pharm Biopharm, 72 (2009) 626-629.

[231] J.R. Haskins, P. Rowse, R. Rahbari, F.A. de la Iglesia, Thiazolidinedione toxicity to isolated hepatocytes revealed by coherent multiprobe fluorescence microscopy and correlated with multiparameter flow cytometry of peripheral leukocytes, Arch Toxicol, 75 (2001) 425-438.

[232] C. Ispas, D. Andreescu, A. Patel, D.V. Goia, S. Andreescu, K.N. Wallace, Toxicity and developmental defects of different sizes and shape nickel nanoparticles in zebrafish, Environ Sci Technol, 43 (2009) 6349-6356.

[233] H. Olson, G. Betton, D. Robinson, K. Thomas, A. Monro, G. Kolaja, P. Lilly, J. Sanders, G. Sipes, W. Bracken, M. Dorato, K. Van Deun, P. Smith, B. Berger, A. Heller, Concordance of the toxicity of pharmaceuticals in humans and in animals, Regul Toxicol Pharmacol, 32 (2000) 56-67.

[234] J.A. Opsteen, R.P. Brinkhuis, R.L.M. Teeuwen, D.W.P.M. Lowik, J.C.M. van Hest, "Clickable" polymersomes, Chem Commun, (2007) 3136-3138.

[235] G.Y. Liu, C.J. Chen, J. Ji, Biocompatible and biodegradable polymersomes as delivery vehicles in biomedical applications, Soft Matter, 8 (2012) 8811-8821.

[236] H.X. Xu, J. Xu, X.Z. Jiang, Z.Y. Zhu, J.Y. Rao, J. Yin, T. Wu, H.W. Liu, S.Y. Liu, Thermosensitive unimolecular micelles surface-decorated with gold nanoparticles of tunable spatial distribution, Chem Mater, 19 (2007) 2489-2494.

[237] Y. Pan, A. Leifert, D. Ruau, S. Neuss, J. Bornemann, G. Schmid, W. Brandau, U. Simon, W. Jahnen-Dechent, Gold nanoparticles of diameter 1.4 nm trigger necrosis by oxidative stress and mitochondrial damage, Small, 5 (2009) 2067-2076.

[238] W. Gao, K. Xu, L. Ji, B. Tang, Effect of gold nanoparticles on glutathione depletion-induced hydrogen peroxide generation and apoptosis in HL7702 cells, Toxicol Lett, 205 (2011) 86-95.

[239] V. Sharma, D. Anderson, A. Dhawan, Zinc oxide nanoparticles induce oxidative DNA damage and ROS-triggered mitochondria mediated apoptosis in human liver cells (HepG2), Apoptosis, 17 (2012) 852-870.

[240] J. Chen, J.A. Hessler, K. Putchakayala, B.K. Panama, D.P. Khan, S. Hong, D.G. Mullen, S.C. Dimaggio, A. Som, G.N. Tew, A.N. Lopatin, J.R. Baker, M.M. Holl, B.G. Orr, Cationic nanoparticles induce nanoscale disruption in living cell plasma membranes, J Phys Chem B, 113 (2009) 11179-11185.

[241] L.K. Limbach, P. Wick, P. Manser, R.N. Grass, A. Bruinink, W.J. Stark, Exposure of engineered nanoparticles to human lung epithelial cells: influence of chemical composition and catalytic activity on oxidative stress, Environ Sci Technol, 41 (2007) 4158-4163.

[242] S. Sabella, R.P. Carney, V. Brunetti, M.A. Malvindi, N. Al-Juffali, G. Vecchio, S.M. Janes, O.M. Bakr, R. Cingolani, F. Stellacci, P.P. Pompa, A general mechanism for intracellular toxicity of metal-containing nanoparticles, Nanoscale, 6 (2014) 7052-7061.

[243] D.M. Brown, I.A. Kinloch, U. Bangert, A.H. Windle, D.M. Walter, G.S. Walker, C.A. Scotchford, K. Donaldson, V. Stone, An in vitro study of the potential of carbon nanotubes and nanofibres to induce inflammatory mediators and frustrated phagocytosis, Carbon, 45 (2007) 1743-1756.

[244] K. Donaldson, F. Murphy, A. Schinwald, R. Duffin, C.A. Poland, Identifying the pulmonary hazard of high aspect ratio nanoparticles to enable their safety-by-design, Nanomedicine, 6 (2011) 143-156.

[245] D. Kim, H. El-Shall, D. Dennis, T. Morey, Interaction of PLGA nanoparticles with human blood constituents, Colloids Surf B Biointerfaces, 40 (2005) 83-91.

[246] S.M. Moghimi, J. Szebeni, Stealth liposomes and long circulating nanoparticles: critical issues in pharmacokinetics, opsonization and protein-binding properties, Prog Lipid Res, 42 (2003) 463-478.

[247] Y.N. Zhang, W. Poon, A.J. Tavares, I.D. McGilvray, W.C.W. Chan, Nanoparticle-liver interactions: Cellular uptake and hepatobiliary elimination, Journal of Controlled Release, 240 (2016) 332-348.

[248] K.Y. Dane, C. Nembrini, A.A. Tomei, J.K. Eby, C.P. O'Neil, D. Velluto, M.A. Swartz, L. Inverardi, J.A. Hubbell, Nano-sized drug-loaded micelles deliver payload to lymph node immune cells and prolong allograft survival, Journal of Controlled Release, 156 (2011) 154-160.

[249] L.R. Narasimhan, W. Goodman, C.K.N. Patel, Correlation of breath ammonia with blood urea nitrogen and creatinine during hemodialysis, P Natl Acad Sci USA, 98 (2001) 4617-4621.

[250] L.L. Schiavon, J.L.N. Schiavon, R.J. Carvalho, J.P. Sampaio, V.P. Lanzoni, A.E.B. Silva, M.L.G. Ferraz, Simple blood tests as noninvasive markers of liver fibrosis in hemodialysis patients with chronic hepatitis C virus infection, Hepatology, 46 (2007) 307-314.

[251] P. Cales, F. Oberti, S. Michalak, I. Hubert-Fouchard, M.C. Rousselet, A. Konat, Y. Gallois, C. Ternisien, A. Chevailler, F. Lunel, A novel panel of blood markers to assess the degree of liver fibrosis, Hepatology, 42 (2005) 1373-1381.

[252] A.L. Klibanov, K. Maruyama, V.P. Torchilin, L. Huang, Amphipathic Polyethyleneglycols Effectively Prolong the Circulation Time of Liposomes, Febs Lett, 268 (1990) 235-237.

[253] J.K. Armstrong, G. Hempel, S. Koling, L.S. Chan, T. Fisher, H.J. Meiselman, G. Garratty, Antibody against poly(ethylene glycol) adversely affects PEG-asparaginase therapy in acute lymphoblastic leukemia patients, Cancer-Am Cancer Soc, 110 (2007) 103-111.

[254] A.W. Richter, E. Akerblom, Polyethylene-Glycol Reactive Antibodies in Man - Titer Distribution in Allergic Patients Treated with Monomethoxy Polyethylene-Glycol Modified Allergens or Placebo, and in Healthy Blood-Donors, Int Arch Aller a Imm, 74 (1984) 36-39.

[255] Q. Yang, S.K. Lai, Anti-PEG immunity: emergence, characteristics, and unaddressed questions, Wires Nanomed Nanobi, 7 (2015) 655-677.

[256] F. Chen, G. Wang, J.I. Griffin, B. Brenneman, N.K. Banda, V.M. Holers, D.S. Backos, L. Wu, S.M. Moghimi, D. Simberg, Complement proteins bind to nanoparticle protein corona and undergo dynamic exchange in vivo, Nat Nanotechnol, 12 (2017) 387-393.

[257] A.P. Hall, C.R. Elcombe, J.R. Foster, T. Harada, W. Kaufmann, A. Knippel, K. Kuttler, D.E. Malarkey, R.R. Maronpot, A. Nishikawa, T. Nolte, A. Schulte, V. Strauss, M.J. York, Liver hypertrophy: a

review of adaptive (adverse and non-adverse) changes--conclusions from the 3rd International ESTP Expert Workshop, Toxicol Pathol, 40 (2012) 971-994.

[258] B.G. Lake, J.G. Evans, T.J. Gray, S.A. Korosi, C.J. North, Comparative studies on nafenopin-induced hepatic peroxisome proliferation in the rat, Syrian hamster, guinea pig, and marmoset, Toxicol Appl Pharmacol, 99 (1989) 148-160.

[259] K. Ray, Liver: Clearance of nanomaterials in the liver, Nat Rev Gastroenterol Hepatol, 13 (2016) 560.

[260] X. Wang, T. Ishida, H. Kiwada, Anti-PEG IgM elicited by injection of liposomes is involved in the enhanced blood clearance of a subsequent dose of PEGylated liposomes, J Control Release, 119 (2007) 236-244.

[261] W. Yang, S.J. Liu, T. Bai, A.J. Keefe, L. Zhang, J.R. Ella-Menye, Y.T. Li, S.Y. Jiang, Poly(carboxybetaine) nanomaterials enable long circulation and prevent polymer-specific antibody production, Nano Today, 9 (2014) 10-16.

[262] J. Szebeni, L. Baranyi, S. Savay, M. Bodo, D.S. Morse, M. Basta, G.L. Stahl, R. Bunger, C.R. Alving, Liposome-induced pulmonary hypertension: properties and mechanism of a complement-mediated pseudoallergic reaction, Am J Physiol-Heart C, 279 (2000) H1319-H1328.

[263] J. Szebeni, L. Baranyi, S. Savay, J. Milosevits, R. Bunger, P. Laverman, J.M. Metselaar, G. Storm, A. Chanan-Khan, L. Liebes, F.M. Muggia, R. Cohen, Y. Barenholz, C.R. Alving, Role of complement activation in hypersensitivity reactions to doxil and HYNICPEG liposomes: Experimental and clinical studies, J Liposome Res, 12 (2002) 165-172.

[264] M.C. Takenaka, F.J. Quintana, Tolerogenic dendritic cells, Semin Immunopathol, 39 (2017) 113-120.

[265] C.A. Dinarello, Proinflammatory cytokines, Chest, 118 (2000) 503-508.

[266] S.S. Iyer, G.H. Cheng, Role of Interleukin 10 Transcriptional Regulation in Inflammation and Autoimmune Disease, Crit Rev Immunol, 32 (2012) 23-63.

[267] S. Sanjabi, L.A. Zenewicz, M. Kamanaka, R.A. Flavell, Anti-inflammatory and pro-inflammatory roles of TGF-beta, IL-10, and IL-22 in immunity and autoimmunity, Current Opinion in Pharmacology, 9 (2009) 447-453.

[268] E.A. Woodward, C.M. Prele, S.E. Nicholson, T.B. Kolesnik, P.H. Hart, The anti-inflammatory effects of interleukin-4 are not mediated by suppressor of cytokine signalling-1 (SOCS1), Immunology, 131 (2010) 118-127.

[269] A. Grakoui, S.K. Bromley, C. Sumen, M.M. Davis, A.S. Shaw, P.M. Allen, M.L. Dustin, The Immunological Synapse: A Molecular Machine Controlling T Cell Activation, Journal of Immunology, 194 (2015) 221-227.

[270] V. Vasilevko, A. Ghochikyan, M.J. Holterman, M.G. Agadjanyan, CD80 (B7-1) and CD86 (B7-2) are functionally equivalent in the initiation and maintenance of CD4+ T-cell proliferation after activation with suboptimal doses of PHA, DNA Cell Biol, 21 (2002) 137-149.

[271] D.L. Tang, R. Kang, C.B. Coyne, H.J. Zeh, M.T. Lotze, PAMPs and DAMPs: signal 0s that spur autophagy and immunity, Immunological Reviews, 249 (2012) 158-175.

[272] H. Bjorkbacka, V.V. Kunjathoor, K.J. Moore, S. Koehn, C.M. Ordija, M.A. Lee, T. Means, K. Halmen, A.D. Luster, D.T. Golenbock, M.W. Freeman, Reduced atherosclerosis in MyD88-null mice links elevated serum cholesterol levels to activation of innate immunity signaling pathways, Nat Med, 10 (2004) 416-421.

[273] M.O. Pentikäinen, K. Öörni, M. Ala-Korpela, P.T. Kovanen, Modified LDL – trigger of atherosclerosis and inflammation in the arterial intima, Journal of Internal Medicine, 247 (2000) 359-370.

[274] L.J. van Tits, R. Stienstra, P.L. van Lent, M.G. Netea, L.A. Joosten, A.F. Stalenhoef, Oxidized LDL enhances pro-inflammatory responses of alternatively activated M2 macrophages: a crucial role for Kruppel-like factor 2, Atherosclerosis, 214 (2011) 345-349.

[275] E. Andreakos, S.M. Sacre, C. Smith, A. Lundberg, S. Kiriakidis, T. Stonehouse, C. Monaco, M. Feldmann, B.M. Foxwell, Distinct pathways of LPS-induced NF-kappa B activation and cytokine production in human myeloid and nonmyeloid cells defined by selective utilization of MyD88 and Mal/TIRAP, Blood, 103 (2004) 2229-2237.

[276] M. Karin, Z.G. Liu, E. Zandi, AP-1 function and regulation, Curr Opin Cell Biol, 9 (1997) 240-246.

[277] N. Wang, H.W. Liang, K. Zen, Molecular mechanisms that influence the macrophage M1-M2 polarization balance, Frontiers in Immunology, 5 (2014).

[278] M.H. Kaplan, STAT signaling in inflammation, JAKSTAT, 2 (2013) e24198.

[279] S. Janssens, R. Beyaert, A universal role for MyD88 in TLR/IL-1R-mediated signaling, Trends Biochem Sci, 27 (2002) 474-482.

[280] H. Bommel, F. Kleefeldt, A. Zernecke, S. Ghavampour, N. Wagner, S. Kuerten, S. Ergun, Visualization of endothelial barrier damage prior to formation of atherosclerotic plaques, Histochem Cell Biol, 148 (2017) 117-127.

[281] A. Pirillo, G.D. Norata, A.L. Catapano, LOX-1, OxLDL, and atherosclerosis, Mediators Inflamm, 2013 (2013) 152786.

[282] S.C. Landers, J.C. Lewis, acLDL binding and endocytosis by macrophages and macrophage foam cells in situ, Exp Mol Pathol, 59 (1993) 38-50.

[283] P. Libby, P.M. Ridker, G.K. Hansson, A. Leducq Transatlantic Network on, Inflammation in atherosclerosis: from pathophysiology to practice, J Am Coll Cardiol, 54 (2009) 2129-2138.

[284] H. Tavori, Y.R. Su, P.G. Yancey, I. Giunzioni, A.J. Wilhelm, J.L. Blakemore, M. Zabalawi, M.F. Linton, M.G. Sorci-Thomas, S. Fazio, Macrophage apoAI protects against dyslipidemia-induced dermatitis and atherosclerosis without affecting HDL, J Lipid Res, 56 (2015) 635-643.

[285] D.A. Chistiakov, A.A. Melnichenko, V.A. Myasoedova, A.V. Grechko, A.N. Orekhov, Mechanisms of foam cell formation in atherosclerosis, J Mol Med (Berl), 95 (2017) 1153-1165.

[286] S. Bekkering, J. Quintin, L.A. Joosten, J.W. van der Meer, M.G. Netea, N.P. Riksen, Oxidized low-density lipoprotein induces long-term proinflammatory cytokine production and foam cell formation *via* epigenetic reprogramming of monocytes, Arterioscler Thromb Vasc Biol, 34 (2014) 1731-1738.

[287] K. Wang, D. Pan, A.H. Schmieder, A. Senpan, S.D. Caruthers, G. Cui, J.S. Allen, H. Zhang, B. Shen, G.M. Lanza, Atherosclerotic neovasculature MR imaging with mixed manganese-gadolinium nanocolloids in hyperlipidemic rabbits, Nanomedicine, 11 (2015) 569-578.

[288] S.N. Sehgal, H. Baker, C. Vezina, Rapamycin (AY-22,989), a new antifungal antibiotic. II. Fermentation, isolation and characterization, J Antibiot (Tokyo), 28 (1975) 727-732.

[289] D.F. Lee, M.C. Hung, All roads lead to mTOR - Integrating inflammation and tumor angiogenesis, Cell Cycle, 6 (2007) 3011-3014.

[290] D.C. Fingar, J. Blenis, Target of rapamycin (TOR): an integrator of nutrient and growth factor signals and coordinator of cell growth and cell cycle progression, Oncogene, 23 (2004) 3151-3171.

[291] Y. Zhang, R.G. Lapidus, P. Liu, E.Y. Choi, S. Adediran, A. Hussain, X. Wang, X. Liu, H.C. Dan, Targeting IkappaB Kinase beta/NF-kappaB Signaling in Human Prostate Cancer by a Novel IkappaB Kinase beta Inhibitor CmpdA, Mol Cancer Ther, 15 (2016) 1504-1514.

[292] R.N. Saunders, M.S. Metcalfe, M.L. Nicholson, Rapamycin in transplantation: a review of the evidence, Kidney Int, 59 (2001) 3-16.

[293] A.W. Thomson, H.R. Turnquist, G. Raimondi, Immunoregulatory functions of mTOR inhibition, Nat Rev Immunol, 9 (2009) 324-337.

[294] T. Berney, A. Secchi, Rapamycin in islet transplantation: friend or foe?, Transpl Int, 22 (2009) 153-161.

[295] E.K. Geissler, The influence of mTOR inhibitors on immunity and the relationship to post-transplant malignancy, Transplant Res, 2 (2013) S2.

[296] A. Salminen, M. Lehtonen, T. Paimela, K. Kaarniranta, Celastrol: Molecular targets of Thunder God Vine, Biochem Biophys Res Commun, 394 (2010) 439-442.

[297] J. Hansen, J. Palmfeldt, S. Vang, T.J. Corydon, N. Gregersen, P. Bross, Quantitative proteomics reveals cellular targets of celastrol, PLoS One, 6 (2011) e26634.

[298] A. Trott, J.D. West, L. Klaic, S.D. Westerheide, R.B. Silverman, R.I. Morimoto, K.A. Morano, Activation of heat shock and antioxidant responses by the natural product celastrol: transcriptional signatures of a thiol-targeted molecule, Mol Biol Cell, 19 (2008) 1104-1112.

[299] J.H. Lee, T.H. Koo, H. Yoon, H.S. Jung, H.Z. Jin, K. Lee, Y.S. Hong, J.J. Lee, Inhibition of NF-kappa B activation through targeting I kappa B kinase by celastrol, a quinone methide triterpenoid, Biochem Pharmacol, 72 (2006) 1311-1321.

[300] D. Zhang, Z. Chen, C. Hu, S. Yan, Z. Li, B. Lian, Y. Xu, R. Ding, Z. Zeng, X.K. Zhang, Y. Su, Celastrol binds to its target protein *via* specific noncovalent interactions and reversible covalent bonds, Chem Commun (Camb), 54 (2018) 12871-12874.

[301] M. Hu, Q. Luo, G. Alitongbieke, S. Chong, C. Xu, L. Xie, X. Chen, D. Zhang, Y. Zhou, Z. Wang, X. Ye, L. Cai, F. Zhang, H. Chen, F. Jiang, H. Fang, S. Yang, J. Liu, M.T. Diaz-Meco, Y. Su, H. Zhou, J. Moscat, X. Lin, X.K. Zhang, Celastrol-Induced Nur77 Interaction with TRAF2 Alleviates Inflammation by Promoting Mitochondrial Ubiquitination and Autophagy, Mol Cell, 66 (2017) 141-153 e146.

[302] H. Hieronymus, J. Lamb, K.N. Ross, X.P. Peng, C. Clement, A. Rodina, M. Nieto, J. Du, K. Stegmaier, S.M. Raj, K.N. Maloney, J. Clardy, W.C. Hahn, G. Chiosis, T.R. Golub, Gene expression signature-based chemical genomic prediction identifies a novel class of HSP90 pathway modulators, Cancer Cell, 10 (2006) 321-330.

[303] J. Li, J. Buchner, Structure, function and regulation of the hsp90 machinery, Biomed J, 36 (2013) 106-117.

[304] A. Salminen, T. Paimela, T. Suuronen, K. Kaarniranta, Innate immunity meets with cellular stress at the IKK complex: regulation of the IKK complex by HSP70 and HSP90, Immunol Lett, 117 (2008) 9-15.

[305] Y. Wang, P.A. Gibney, J.D. West, K.A. Morano, The yeast Hsp70 Ssa1 is a sensor for activation of the heat shock response by thiol-reactive compounds, Mol Biol Cell, 23 (2012) 3290-3298.

[306] Y.G. Weiss, Z. Bromberg, N. Raj, J. Raphael, P. Goloubinoff, Y. Ben-Neriah, C.S. Deutschman, Enhanced heat shock protein 70 expression alters proteasomal degradation of IkappaB kinase in experimental acute respiratory distress syndrome, Crit Care Med, 35 (2007) 2128-2138.

[307] H. Chen, Y. Wu, Y. Zhang, L. Jin, L. Luo, B. Xue, C. Lu, X. Zhang, Z. Yin, Hsp70 inhibits lipopolysaccharide-induced NF-kappaB activation by interacting with TRAF6 and inhibiting its ubiquitination, Febs Lett, 580 (2006) 3145-3152.

[308] H. Yang, D. Chen, Q.C. Cui, X. Yuan, Q.P. Dou, Celastrol, a triterpene extracted from the Chinese "Thunder of God Vine," is a potent proteasome inhibitor and suppresses human prostate cancer growth in nude mice, Cancer Res, 66 (2006) 4758-4765.

[309] A. Fribley, C.Y. Wang, Proteasome inhibitor induces apoptosis through induction of endoplasmic reticulum stress, Cancer Biol Ther, 5 (2006) 745-748.

[310] S. Boridy, P.U. Le, K. Petrecca, D. Maysinger, Celastrol targets proteostasis and acts synergistically with a heat-shock protein 90 inhibitor to kill human glioblastoma cells, Cell Death Dis, 5 (2014) e1216.

[311] Y.T. Xiao, J. Liu, M.Y. Guo, H.G. Zhou, J. Jin, J.M. Liu, Y. Liu, Z.J. Zhang, C.Y. Chen, Synergistic combination chemotherapy using carrier-free celastrol and doxorubicin nanocrystals for overcoming drug resistance, Nanoscale, 10 (2018) 12639-12649.

[312] J. Liu, J. Lee, M.A. Salazar Hernandez, R. Mazitschek, U. Ozcan, Treatment of obesity with celastrol, Cell, 161 (2015) 999-1011.

[313] A.M. Chow, I.R. Brown, Induction of heat shock proteins in differentiated human and rodent neurons by celastrol, Cell Stress Chaperones, 12 (2007) 237-244.

[314] A. Petrovic, J. Kaur, I. Tomljanovic, A. Nistri, M. Mladinic, Pharmacological induction of Heat Shock Protein 70 by celastrol protects motoneurons from excitotoxicity in rat spinal cord in vitro, Eur J Neurosci, (2018).

[315] A.C. Allison, R. Cacabelos, V.R.M. Lombardi, X.A. Alvarez, C. Vigo, Celastrol, a potent antioxidant and anti-inflammatory drug, as a possible treatment for Alzheimer's disease, Prog Neuro-Psychoph, 25 (2001) 1341-1357.

[316] H.F. Lin, M.J. Hsieh, Y.T. Hsi, Y.S. Lo, Y.C. Chuang, M.K. Chen, S.Y. Chien, Celastrol-induced apoptosis in human nasopharyngeal carcinoma is associated with the activation of the death receptor and the mitochondrial pathway, Oncol Lett, 14 (2017) 1683-1690.

[317] B. Ren, H. Liu, H. Gao, S.T. Liu, Z.H. Zhang, A.M. Fribley, M.U. Callaghan, Z.X. Xu, Q.H. Zeng, Y.L. Li, Celastrol induces apoptosis in hepatocellular carcinoma cells *via* targeting ER-stress/UPR, Oncotarget, 8 (2017) 93039-93050.

[318] Y.Y. Yan, H. Bi, W. Zhang, Q. Wen, H. Liu, J.X. Li, H.Z. Zhang, Y.X. Zhang, J.S. Li, Downregulation and subcellular distribution of HER2 involved in MDA-MB-453 breast cancer cell apoptosis induced by lapatinib/celastrol combination, J Buon, 22 (2017) 644-651.

[319] S. Sharma, R. Mishra, B.L. Walker, S. Deshmukh, M. Zampino, J. Patel, M. Anamalai, D. Simpson, I.S. Singh, S. Kaushal, S. Kaushal, Celastrol, an oral heat shock activator, ameliorates multiple animal disease models of cell death, Cell Stress Chaperon, 20 (2015) 185-201.

[320] S.R. Chen, Y. Dai, J. Zhao, L. Lin, Y. Wang, Y. Wang, A Mechanistic Overview of Triptolide and Celastrol, Natural Products from Tripterygium wilfordii Hook F, Front Pharmacol, 9 (2018) 104.

[321] L. Gu, W. Bai, S. Li, Y. Zhang, Y. Han, Y. Gu, G. Meng, L. Xie, J. Wang, Y. Xiao, L. Shan, S. Zhou, L. Wei, A. Ferro, Y. Ji, Celastrol prevents atherosclerosis *via* inhibiting LOX-1 and oxidative stress, PLoS One, 8 (2013) e65477.

[322] G. Sethi, K. SeokAhn, M.K. Pandey, B.B. Aggarwal, Celastrol, a novel triterpene, potentiates TNF-induced apoptosis and suppresses invasion of tumor cells by inhibiting NF-kappa B-regulated gene products and TAK1-mediated NF-kappa B activation, Blood, 109 (2007) 2727-2735.

[323] R. Koopman, G. Schaart, M.K.C. Hesselink, Optimisation of oil red O staining permits combination with immunofluorescence and automated quantification of lipids, Histochemistry and Cell Biology, 116 (2001) 63-68.

[324] X.D. Li, K. Garcia, Z.F. Sun, Z.G. Xiao, Temporal Regulation of Rapamycin on Memory CTL Programming by IL-12, Plos One, 6 (2011).

[325] T.S. Ikonen, J.F. Gummert, N. Serkova, M. Hayase, Y. Honda, Y. Kobayase, B. Hausen, P.G. Yock, U. Christians, R.E. Morris, Efficacies of sirolimus (rapamycin) and cyclosporine in allograft vascular disease in non-human primates: trough levels of sirolimus correlate with inhibition of progression of arterial intimal thickening, Transpl Int, 13 Suppl 1 (2000) S314-320.

[326] R.S. Poston, M. Billingham, E.G. Hoyt, J. Pollard, R. Shorthouse, R.E. Morris, R.C. Robbins, Rapamycin reverses chronic graft vascular disease in a novel cardiac allograft model, Circulation, 100 (1999) 67-74.

[327] A. Xiong, L. Duan, J. Chen, Z. Fan, F. Zheng, Z. Tan, F. Gong, M. Fang, Flt3L combined with rapamycin promotes cardiac allograft tolerance by inducing regulatory dendritic cells and allograft autophagy in mice, PLoS One, 7 (2012) e46230.

APPENDIX A

Flow Cytometry Gating Strategies

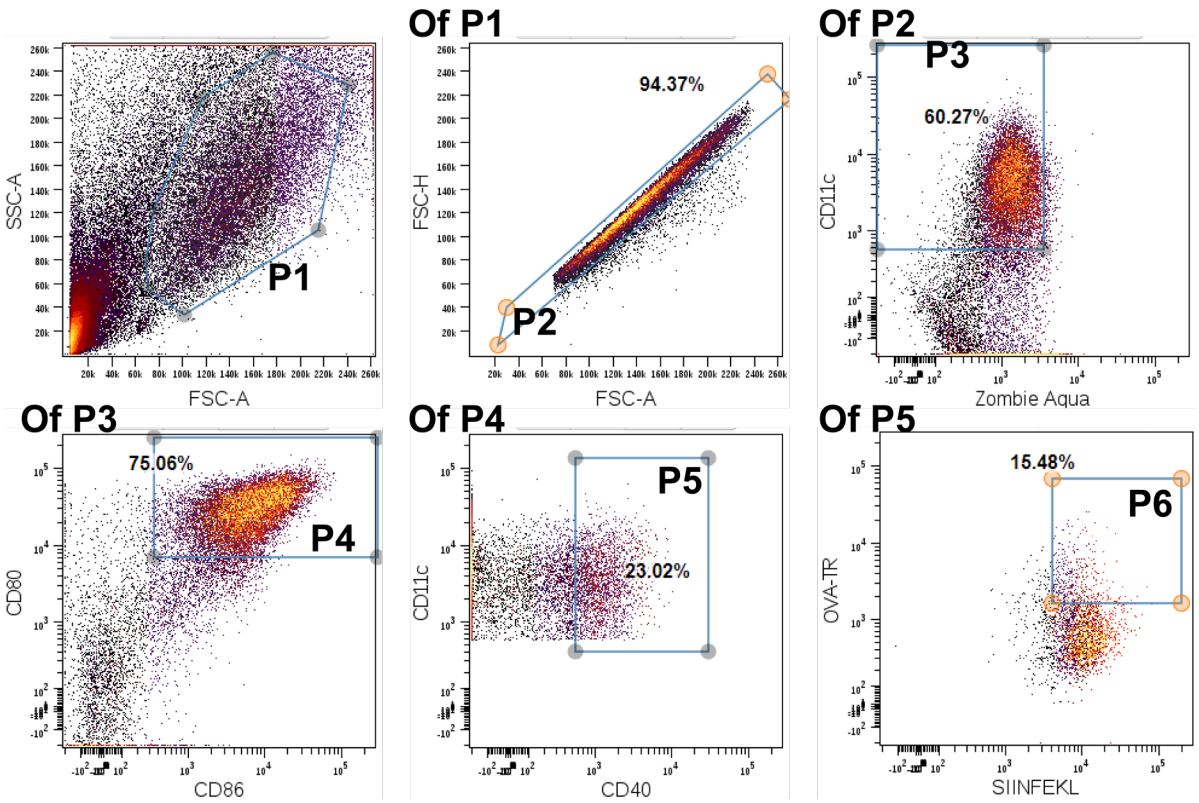

Figure A-1. Gating strategy for flow cytometry data shown in Figure 3-10. BMDCs were gated on FSC and SSC to exclude debris and FSC-A vs H to exclude doublets. DCs were selected in P3, then were gated for activation in P4 and P5 before being gated for SIINFEKL display on MHC I and ovalbumin uptake within cells. Representative dot plots are shown. Adapted from [146] with permission from The Royal Society of Chemistry.

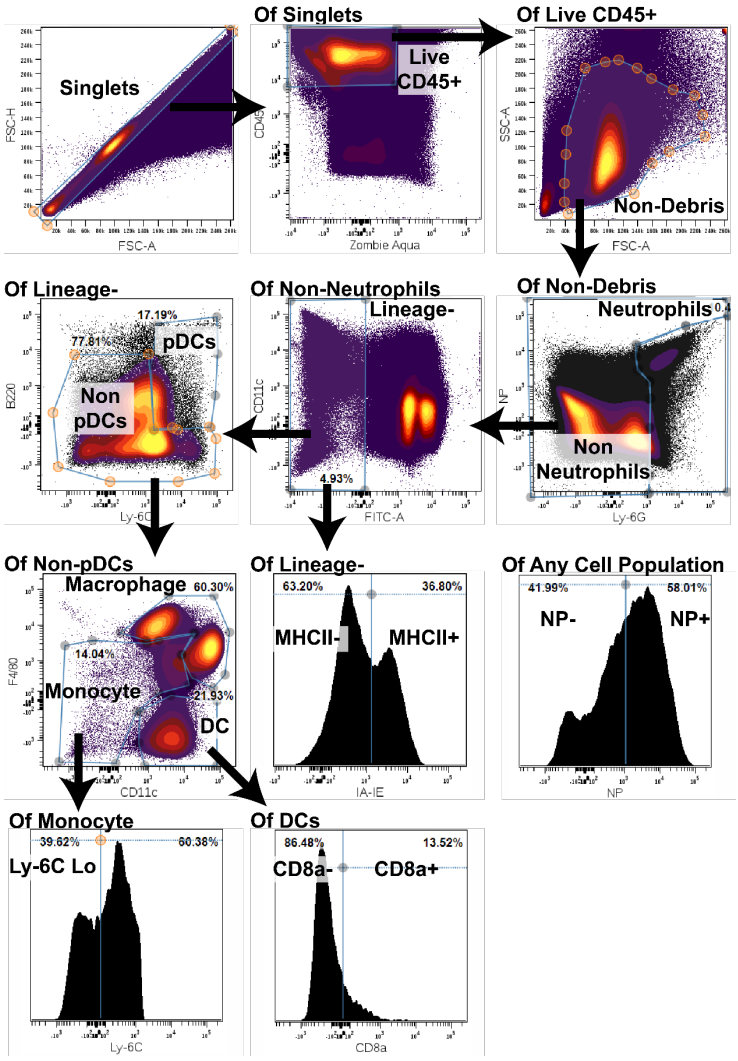

Figure A-2. Gating strategy for flow cytometry data shown in Figure 3-16. Cells collected from mouse organs were gated into immune cell subpopulations and were assessed for uptake of PSs or BCNs. Representative dot plots shown. Adapted with permission from [222] © 2018 American Chemical Society.

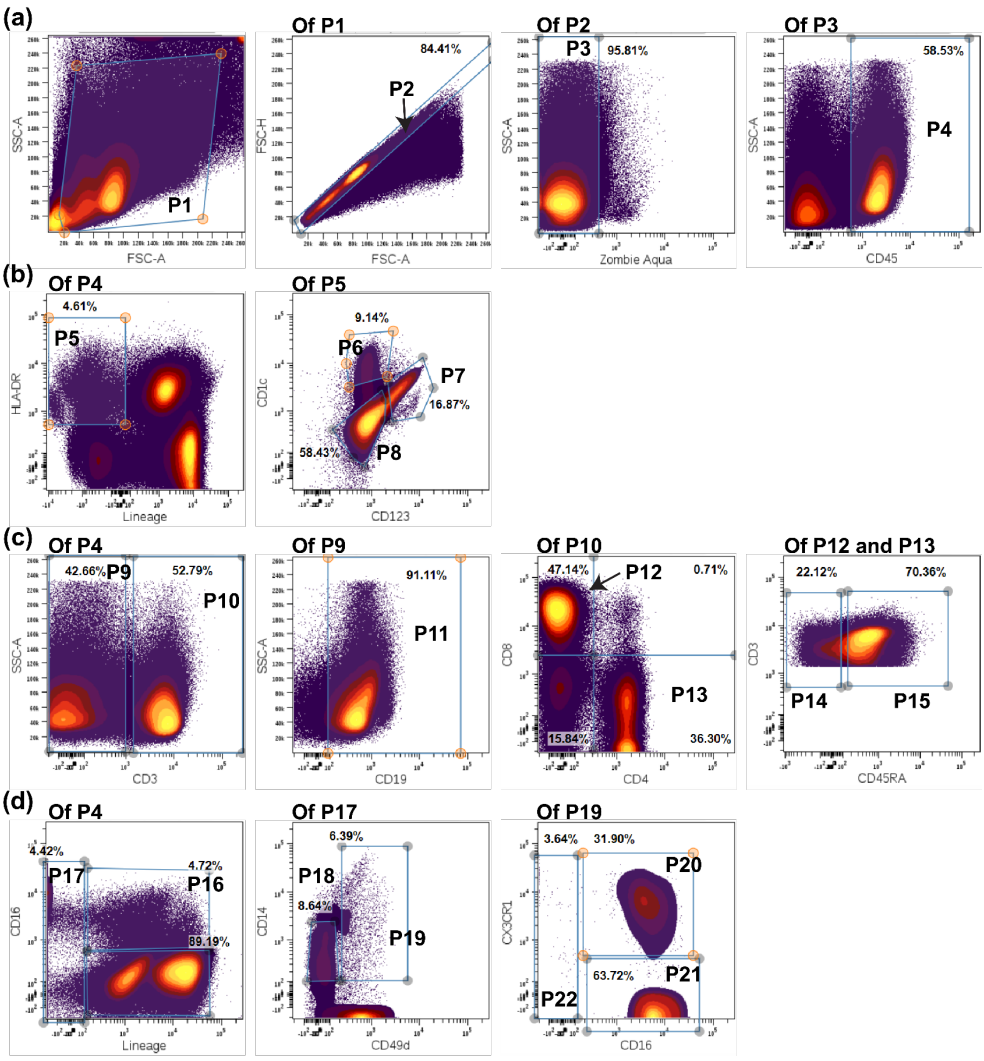

Figure A-3. Gating strategy for flow cytometry data shown in Figure 3-13, panel 1. Cells collected from non-human primate organs were gated into immune cell subpopulations and were assessed for uptake of PSs. Representative dot plots shown. Figure reprinted with permission from [173] © 2018 Springer.

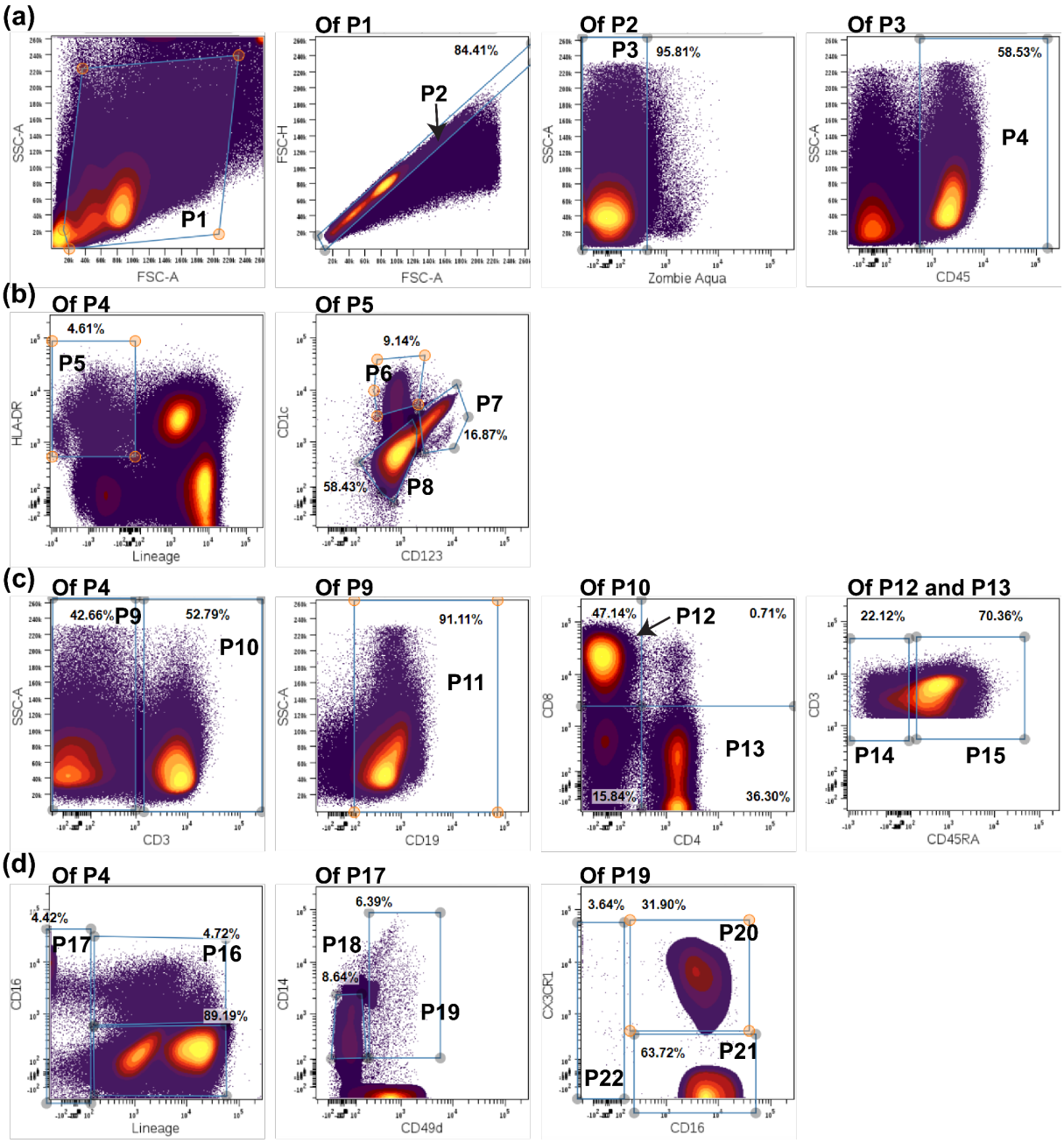

Figure A-4. Gating strategy for flow cytometry data shown in Figure 3-13, panel 2. Cells collected from non-human primate organs were gated into immune cell subpopulations and were assessed for uptake of PSs. Representative dot plots shown. Figure reprinted with permission from [173] © 2018 Springer.

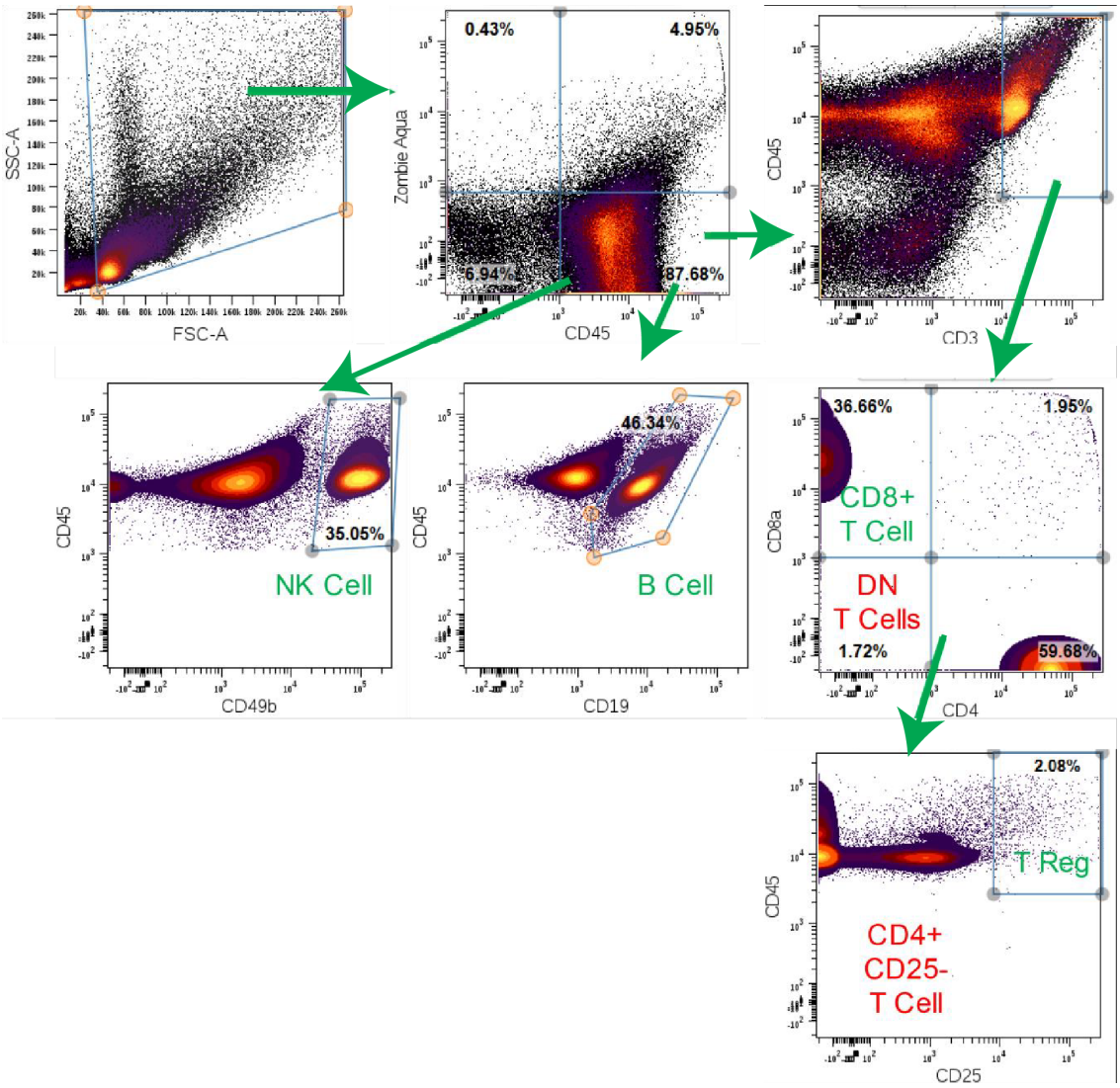

Figure A-5. Gating strategy for flow cytometry data shown in Figure 5-4. Gating strategy for immune cells isolated from mouse spleen to identify NK cells, B cells, CD4+ T cells, CD8+ T cells, 'double negative' (DN) T cells, and regulatory T cells. All plots shown are representative gating strategies for cells, in this case from the spleen of a vehicle treated mouse. Reprinted with permission from [164]

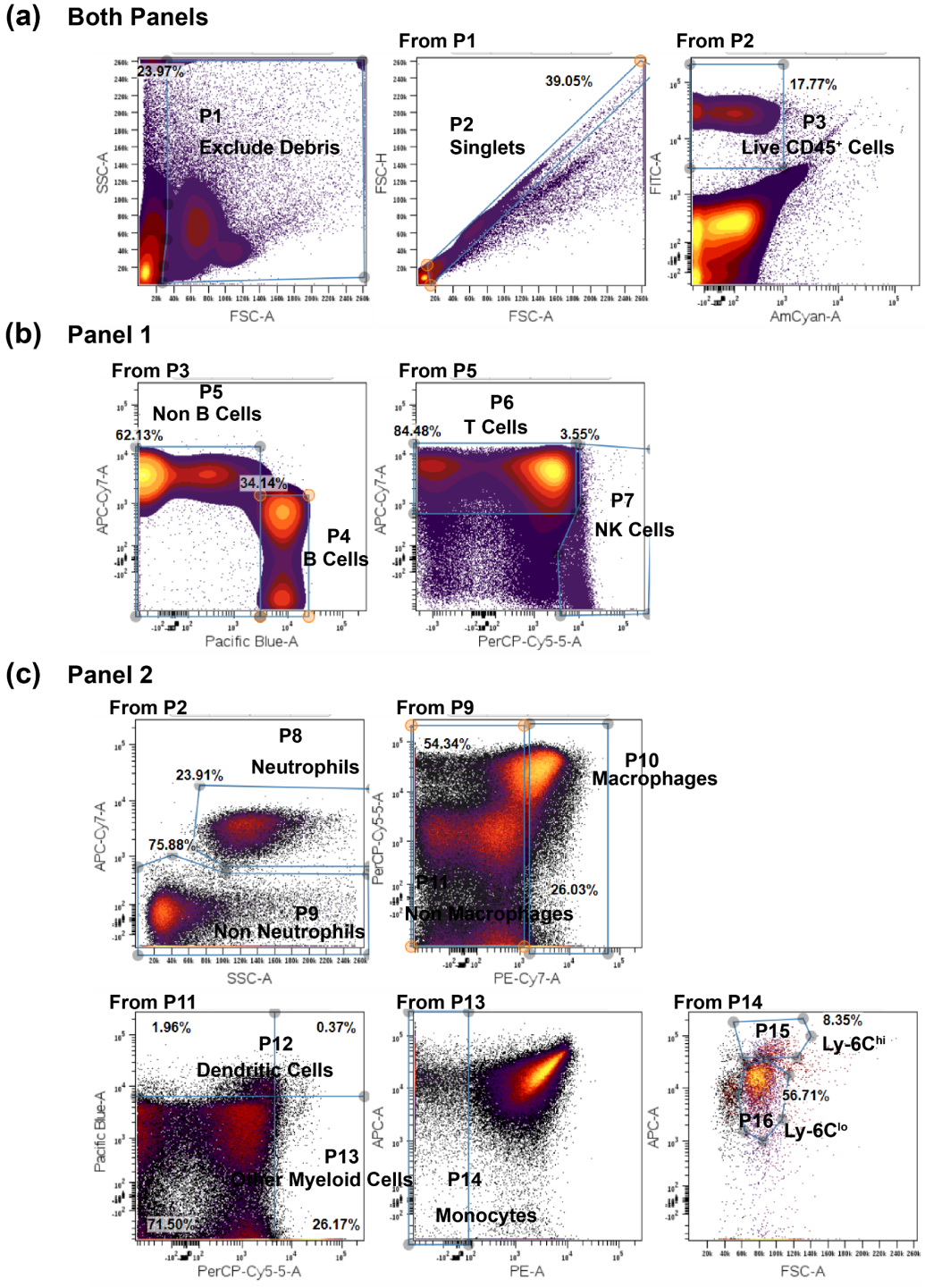

Figure A-6. Gating strategy for flow cytometry data shown in Figure 5-11. Representative contour plots for the gating of cells from Ldlr-/- mice. Reproduced from [223] with permission from The Royal Society of Chemistry.

APPENDIX B

RNAseq DESeq2 Tables

Table B-1. RNAseq DESeq2 top 100 results for LPS vs. free celastrol treatments.

symbol	description	baseMean	log2FoldChange	stat	padj
Pclaf	PCNA clamp associated factor [Source:MGI Symbol;Acc:MGI:1915276]	534.8923	-4.59733	-16.6926	1.52E-58
Top2a	topoisomerase (DNA) II alpha [Source:MGI Symbol;Acc:MGI:98790]	794.9518	-3.65207	-15.3953	9.00E-50
Birc5	baculoviral IAP repeat-containing 5 [Source:MGI Symbol;Acc:MGI:1203517]	441.504	-4.08538	-14.3304	4.81E-43
D17H6S56E-5	NA	2824.241	-3.66666	-14.3023	5.41E-43
Fdps	farnesyl diphosphate synthetase [Source:MGI Symbol;Acc:MGI:104888]	438.1781	-3.09901	-12.1772	8.41E-31
Tuba1b	tubulin, alpha 1B [Source:MGI Symbol;Acc:MGI:107804]	3262.109	-2.86863	-11.9838	7.36E-30
Pttg1	pituitary tumor-transforming gene 1 [Source:MGI Symbol;Acc:MGI:1353578]	197.2771	-4.27185	-11.9488	9.62E-30
Ppp1r15a	protein phosphatase 1, regulatory (inhibitor) subunit 15A [Source:MGI Symbol;Acc:MGI:1927072]	361.6796	3.828206	11.88927	1.72E-29
Lig1	ligase I, DNA, ATP-dependent [Source:MGI Symbol;Acc:MGI:101789]	893.6232	-3.37074	-11.6177	3.80E-28
Mcm7	minichromosome maintenance complex component 7 [Source:MGI Symbol;Acc:MGI:1298398]	271.5301	-3.474	-11.5467	7.84E-28
Plk1	polo-like kinase 1 [Source:MGI Symbol;Acc:MGI:97621]	251.3773	-3.71523	-11.3917	4.27E-27
Ndrg1	N-myc downstream regulated gene 1 [Source:MGI Symbol;Acc:MGI:1341799]	405.8646	2.962301	11.37646	4.67E-27
Jun	jun proto-oncogene [Source:MGI Symbol;Acc:MGI:96646]	224.0666	3.261816	11.20922	2.89E-26
Mcm5	minichromosome maintenance complex component 5 [Source:MGI Symbol;Acc:MGI:103197]	305.8131	-3.34458	-11.1404	5.83E-26
Acat2	acetyl-Coenzyme A acetyltransferase 2 [Source:MGI Symbol;Acc:MGI:87871]	149.1672	-3.70416	-11.1304	6.08E-26

Cdca8	cell division cycle associated 8 [Source:MGI Symbol;Acc:MGI:1196274]	284.2127	-2.96738	-11.0633	1.21E-25
Rgs1	regulator of G-protein signaling 1 [Source:MGI Symbol;Acc:MGI:1354694]	566.6225	3.72119	10.89181	7.58E-25
Ccnb1	cyclin B1 [Source:MGI Symbol;Acc:MGI:88302]	137.7699	-4.25184	-10.8475	1.16E-24
Cyp51	cytochrome P450, family 51 [Source:MGI Symbol;Acc:MGI:106040]	360.1578	-2.77106	-10.8396	1.20E-24
Bcl6b	B cell CLL/lymphoma 6, member B [Source:MGI Symbol;Acc:MGI:1278332]	110.1932	-5.38856	-10.8327	1.23E-24
Ska1	spindle and kinetochore associated complex subunit 1 [Source:MGI Symbol;Acc:MGI:1913718]	174.8582	-3.70753	-10.779	2.10E-24
Dnmt1	DNA methyltransferase (cytosine-5) 1 [Source:MGI Symbol;Acc:MGI:94912]	290.9421	-2.80568	-10.5043	3.83E-23
Cks1b	CDC28 protein kinase 1b [Source:MGI Symbol;Acc:MGI:1889208]	312.6278	-2.75528	-10.4075	1.02E-22
Tubb4b	tubulin, beta 4B class IVB [Source:MGI Symbol;Acc:MGI:1915472]	1096.887	-2.43779	-10.3858	1.23E-22
Mki67	antigen identified by monoclonal antibody Ki 67 [Source:MGI Symbol;Acc:MGI:106035]	256.2802	-3.46735	-10.2057	7.65E-22
Cdk1	cyclin-dependent kinase 1 [Source:MGI Symbol;Acc:MGI:88351]	298.6122	-3.26246	-10.1585	1.19E-21
Egr1	early growth response 1 [Source:MGI Symbol;Acc:MGI:95295]	280.6426	3.261784	9.957046	8.89E-21
Tsc22d1	TSC22 domain family, member 1 [Source:MGI Symbol;Acc:MGI:109127]	184.8368	-3.63013	-9.93234	1.10E-20
Spc25	SPC25, NDC80 kinetochore complex component, homolog (S. cerevisiae) [Source:MGI Symbol;Acc:MGI:1913692]	103.0694	-3.74063	-9.87506	1.88E-20
Odc1	ornithine decarboxylase, structural 1 [Source:MGI Symbol;Acc:MGI:97402]	677.1365	-2.39671	-9.8283	2.90E-20
Tacc3	transforming, acidic coiled-coil containing protein 3 [Source:MGI Symbol;Acc:MGI:1341163]	88.72908	-4.19984	-9.81422	3.22E-20

Angptl6	angiopoietin-like 6 [Source:MGI Symbol;Acc:MGI:1917976]	132.833	3.745992	9.791001	3.93E-20
Fam20c	family with sequence similarity 20, member C [Source:MGI Symbol;Acc:MGI:2136853]	297.8249	3.185674	9.696422	9.67E-20
Pbk	PDZ binding kinase [Source:MGI Symbol;Acc:MGI:1289156]	84.66335	-5.11437	-9.6688	1.23E-19
Pmf1	polyamine-modulated factor 1 [Source:MGI Symbol;Acc:MGI:1914287]	292.1891	-3.09782	-9.59787	2.38E-19
Arl4c	ADP-ribosylation factor-like 4C [Source:MGI Symbol;Acc:MGI:2445172]	187.6723	3.02434	9.502018	5.84E-19
Rfc5	replication factor C (activator 1) 5 [Source:MGI Symbol;Acc:MGI:1919401]	277.3161	-2.9149	-9.45126	9.25E-19
Ube2c	ubiquitin-conjugating enzyme E2C [Source:MGI Symbol;Acc:MGI:1915862]	357.1045	-3.0081	-9.38844	1.60E-18
Ccnd2	cyclin D2 [Source:MGI Symbol;Acc:MGI:88314]	139.8245	3.109667	9.345603	2.33E-18
Ncapd2	non-SMC condensin I complex, subunit D2 [Source:MGI Symbol;Acc:MGI:1915548]	116.0901	-3.27013	-9.30174	3.44E-18
Rrm2	ribonucleotide reductase M2 [Source:MGI Symbol;Acc:MGI:98181]	70.84197	-4.4628	-9.29481	3.59E-18
Ccl9	chemokine (C-C motif) ligand 9 [Source:MGI Symbol;Acc:MGI:104533]	1663.396	-2.51161	-9.29104	3.63E-18
Snhg9	small nucleolar RNA host gene 9 [Source:MGI Symbol;Acc:MGI:1920724]	212.8585	-2.76477	-9.0555	3.16E-17
Rsrp1	arginine/serine rich protein 1 [Source:MGI Symbol;Acc:MGI:106498]	131.6112	3.187001	8.961611	7.27E-17
Syce2	synaptonemal complex central element protein 2 [Source:MGI Symbol;Acc:MGI:1919096]	137.8468	-2.83943	-8.956	7.48E-17
Ccna2	cyclin A2 [Source:MGI Symbol;Acc:MGI:108069]	72.66925	-4.06079	-8.94739	7.91E-17
Lmnb1	lamin B1 [Source:MGI Symbol;Acc:MGI:96795]	396.1902	-2.2335	-8.94027	8.27E-17
Plk2	polo-like kinase 2 [Source:MGI Symbol;Acc:MGI:1099790]	193.6306	3.047476	8.871199	1.51E-16

Smc2	structural maintenance of chromosomes 2 [Source:MGI Symbol;Acc:MGI:106067]	236.1926	-2.52625	-8.85833	1.66E-16
Hspa1b	heat shock protein 1B [Source:MGI Symbol;Acc:MGI:99517]	106.4798	4.50342	8.854272	1.69E-16
Snrpd1	small nuclear ribonucleoprotein D1 [Source:MGI Symbol;Acc:MGI:98344]	901.9515	-2.12699	-8.80679	2.53E-16
Bbc3	BCL2 binding component 3 [Source:MGI Symbol;Acc:MGI:2181667]	733.9894	2.351006	8.800702	2.62E-16
Ptma	prothymosin alpha [Source:MGI Symbol;Acc:MGI:97803]	3570.808	-2.30457	-8.77857	3.13E-16
Sirpa	signal-regulatory protein alpha [Source:MGI Symbol;Acc:MGI:108563]	581.8386	2.284799	8.766347	3.43E-16
Syne3	spectrin repeat containing, nuclear envelope family member 3 [Source:MGI Symbol;Acc:MGI:2442408]	223.4139	-2.34541	-8.74833	3.95E-16
Hirip3	HIRA interacting protein 3 [Source:MGI Symbol;Acc:MGI:2142364]	110.8297	-2.85893	-8.68943	6.53E-16
Scd1	stearoyl-Coenzyme A desaturase 1 [Source:MGI Symbol;Acc:MGI:98239]	84.06425	-3.39894	-8.68479	6.69E-16
Cenpa	centromere protein A [Source:MGI Symbol;Acc:MGI:88375]	101.8817	-3.70219	-8.59563	1.43E-15
Gla	galactosidase, alpha [Source:MGI Symbol;Acc:MGI:1347344]	61.31107	4.218962	8.560888	1.91E-15
Msrb1	methionine sulfoxide reductase B1 [Source:MGI Symbol;Acc:MGI:1351642]	237.6718	2.435194	8.554478	1.98E-15
Tk1	thymidine kinase 1 [Source:MGI Symbol;Acc:MGI:98763]	81.19266	-3.25744	-8.50754	2.93E-15
Cox6a2	cytochrome c oxidase subunit *via* polypeptide 2 [Source:MGI Symbol;Acc:MGI:104649]	57.57384	4.463789	8.498728	3.11E-15
Fcgr1	Fc receptor, IgG, high affinity I [Source:MGI Symbol;Acc:MGI:95498]	102.0654	3.076153	8.429011	5.57E-15
Spc24	SPC24, NDC80 kinetochore complex component, homolog (S.	104.8381	-3.25101	-8.42658	5.60E-15

	cerevisiae) [Source:MGI Symbol;Acc:MGI:1914879]				
Nusap1	nucleolar and spindle associated protein 1 [Source:MGI Symbol;Acc:MGI:2675669]	139.8719	-3.09197	-8.42231	5.72E-15
Mcm3	minichromosome maintenance complex component 3 [Source:MGI Symbol;Acc:MGI:101845]	234.8506	-2.37992	-8.41294	6.10E-15
Tubb5	tubulin, beta 5 class I [Source:MGI Symbol;Acc:MGI:107812]	1896.514	-2.01764	-8.40697	6.32E-15
Fnip1	folliculin interacting protein 1 [Source:MGI Symbol;Acc:MGI:2444668]	180.0499	2.51443	8.389363	7.24E-15
Zfand2a	zinc finger, AN1-type domain 2A [Source:MGI Symbol;Acc:MGI:2140729]	59.47997	4.827317	8.385558	7.37E-15
Cenpe	centromere protein E [Source:MGI Symbol;Acc:MGI:1098230]	110.5302	-2.79686	-8.35849	9.14E-15
Mir6516	microRNA 6516 [Source:MGI Symbol;Acc:MGI:5562736]	84.16074	-3.03081	-8.3171	1.28E-14
Rrm1	ribonucleotide reductase M1 [Source:MGI Symbol;Acc:MGI:98180]	111.3718	-2.93149	-8.31075	1.33E-14
Tiparp	TCDD-inducible poly(ADP-ribose) polymerase [Source:MGI Symbol;Acc:MGI:2159210]	82.75969	3.56851	8.228946	2.61E-14
Aurka	aurora kinase A [Source:MGI Symbol;Acc:MGI:894678]	129.8021	-2.67697	-8.15235	4.86E-14
Cenpf	centromere protein F [Source:MGI Symbol;Acc:MGI:1313302]	108.4889	-2.80896	-8.13818	5.40E-14
Mafb	v-maf musculoaponeurotic fibrosarcoma oncogene family, protein B (avian) [Source:MGI Symbol;Acc:MGI:104555]	83.99214	3.538081	8.092865	7.73E-14
Ppil1	peptidylprolyl isomerase (cyclophilin)-like 1 [Source:MGI Symbol;Acc:MGI:1916066]	124.3104	-2.48673	-8.04947	1.09E-13
S100a4	S100 calcium binding protein A4 [Source:MGI Symbol;Acc:MGI:1330282]	21162.49	-2.14533	-8.01727	1.40E-13
1700017B05Rik	RIKEN cDNA 1700017B05 gene	288.5839	3.083393	7.98048	1.86E-13

	[Source:MGI Symbol;Acc:MGI:1921461]				
Rpa2	replication protein A2 [Source:MGI Symbol;Acc:MGI:1339939]	182.5286	-2.75827	-7.96226	2.13E-13
Dnajc9	DnaJ heat shock protein family (Hsp40) member C9 [Source:MGI Symbol;Acc:MGI:1915326]	79.21108	-2.99107	-7.9505	2.32E-13
Tnf	tumor necrosis factor [Source:MGI Symbol;Acc:MGI:104798]	3971.652	-1.90981	-7.94747	2.34E-13
Dgkg	diacylglycerol kinase, gamma [Source:MGI Symbol;Acc:MGI:105060]	50.04727	3.999435	7.93091	2.65E-13
Cbx5	chromobox 5 [Source:MGI Symbol;Acc:MGI:109372]	156.62	-2.33633	-7.84475	5.22E-13
Dbi	diazepam binding inhibitor [Source:MGI Symbol;Acc:MGI:94865]	1125.408	-1.75881	-7.79202	7.84E-13
Ier5	immediate early response 5 [Source:MGI Symbol;Acc:MGI:1337072]	1434.115	1.91308	7.788717	7.95E-13
Fads1	fatty acid desaturase 1 [Source:MGI Symbol;Acc:MGI:1923517]	299.6574	-2.2161	-7.78662	7.99E-13
Pqlc1	PQ loop repeat containing 1 [Source:MGI Symbol;Acc:MGI:1914193]	140.8221	2.835665	7.778745	8.41E-13
Mrpl18	mitochondrial ribosomal protein L18 [Source:MGI Symbol;Acc:MGI:1914931]	233.1693	-2.11503	-7.77708	8.43E-13
Cenpw	centromere protein W [Source:MGI Symbol;Acc:MGI:1913561]	125.5612	-2.46464	-7.76598	9.10E-13
Racgap1	Rac GTPase-activating protein 1 [Source:MGI Symbol;Acc:MGI:1349423]	88.06902	-2.75885	-7.74192	1.09E-12
Gins2	GINS complex subunit 2 (Psf2 homolog) [Source:MGI Symbol;Acc:MGI:1921019]	87.06565	-2.84088	-7.73672	1.11E-12
Grwd1	glutamate-rich WD repeat containing 1 [Source:MGI Symbol;Acc:MGI:2141989]	173.0384	-2.16624	-7.73607	1.11E-12
Ncapg	non-SMC condensin I complex, subunit G [Source:MGI Symbol;Acc:MGI:1930197]	54.31061	-3.43357	-7.68847	1.60E-12
Acod1	aconitate decarboxylase 1 [Source:MGI Symbol;Acc:MGI:103206]	1020.53	-2.34549	-7.65087	2.13E-12

Impact	impact, RWD domain protein [Source:MGI Symbol;Acc:MGI:1098233]	96.93094	2.901377	7.61789	2.72E-12
Stard4	StAR-related lipid transfer (START) domain containing 4 [Source:MGI Symbol;Acc:MGI:2156764]	53.51499	-3.80561	-7.61258	2.80E-12
Zbtb32	zinc finger and BTB domain containing 32 [Source:MGI Symbol;Acc:MGI:1891838]	192.2375	-2.44337	-7.60716	2.89E-12
Cpeb4	cytoplasmic polyadenylation element binding protein 4 [Source:MGI Symbol;Acc:MGI:1914829]	87.88448	2.675864	7.600743	3.01E-12
Nfatc1	nuclear factor of activated T cells, cytoplasmic, calcineurin dependent 1 [Source:MGI Symbol;Acc:MGI:102469]	108.4624	-2.62693	-7.57709	3.58E-12

Table B-1. RNAseq DESeq2 top 100 results for LPS vs. free celastrol treatments.

symbol	description	baseMean	log2FoldChange	stat	padj
Pclaf	PCNA clamp associated factor [Source:MGI Symbol;Acc:MGI:1915276]	439.7541	-3.82946	-19.6113	1.29E-81
Fam20c	family with sequence similarity 20, member C [Source:MGI Symbol;Acc:MGI:2136853]	676.3304	4.284542	18.89963	5.99E-76
Arl4c	ADP-ribosylation factor-like 4C [Source:MGI Symbol;Acc:MGI:2445172]	374.334	3.941582	17.64581	3.81E-66
Top2a	topoisomerase (DNA) II alpha [Source:MGI Symbol;Acc:MGI:98790]	660.4016	-3.20216	-17.3266	7.72E-64
Cdk1	cyclin-dependent kinase 1 [Source:MGI Symbol;Acc:MGI:88351]	232.2638	-4.20897	-16.0776	6.37E-55
Zc3hav1	zinc finger CCCH type, antiviral 1 [Source:MGI Symbol;Acc:MGI:1926031]	484.5924	2.907216	15.95867	3.69E-54
Ube2c	ubiquitin-conjugating enzyme E2C [Source:MGI Symbol;Acc:MGI:1915862]	278.3889	-3.84416	-15.8913	9.49E-54
Jun	jun proto-oncogene [Source:MGI Symbol;Acc:MGI:96646]	278.3108	3.410248	15.81301	2.93E-53
D17H6S56E-5	NA	2426.374	-2.77403	-15.6597	2.97E-52

Fcgr3	Fc receptor, IgG, low affinity III [Source:MGI Symbol;Acc:MGI:95500]	369.9621	3.621748	15.65069	3.11E-52
Pttg1	pituitary tumor-transforming gene 1 [Source:MGI Symbol;Acc:MGI:1353578]	159.4047	-4.05476	-15.4478	6.78E-51
Angptl6	angiopoietin-like 6 [Source:MGI Symbol;Acc:MGI:1917976]	205.5368	4.22473	15.35368	2.68E-50
Tuba1b	tubulin, alpha 1B [Source:MGI Symbol;Acc:MGI:107804]	2793.142	-2.43983	-15.2412	1.40E-49
Birc5	baculoviral IAP repeat-containing 5 [Source:MGI Symbol;Acc:MGI:1203517]	369.1581	-3.29854	-15.1483	5.40E-49
Msrb1	methionine sulfoxide reductase B1 [Source:MGI Symbol;Acc:MGI:1351642]	346.0242	2.907991	14.80345	9.07E-47
Cks1b	CDC28 protein kinase 1b [Source:MGI Symbol;Acc:MGI:1889208]	249.3711	-3.17469	-14.5296	4.83E-45
Mcm7	minichromosome maintenance complex component 7 [Source:MGI Symbol;Acc:MGI:1298398]	225.6127	-3.11173	-14.2634	2.14E-43
Lmnb1	lamin B1 [Source:MGI Symbol;Acc:MGI:96795]	318.0021	-2.63178	-14.2099	4.36E-43
Ndrg1	N-myc downstream regulated gene 1 [Source:MGI Symbol;Acc:MGI:1341799]	399.688	2.753709	14.03706	4.82E-42
Plk1	polo-like kinase 1 [Source:MGI Symbol;Acc:MGI:97621]	207.1091	-3.36895	-14.0259	5.37E-42
Odc1	ornithine decarboxylase, structural 1 [Source:MGI Symbol;Acc:MGI:97402]	567.8112	-2.34291	-13.9614	1.27E-41
Fdps	farnesyl diphosphate synthetase [Source:MGI Symbol;Acc:MGI:104888]	377.6692	-2.49397	-13.8542	5.44E-41
Gpnmb	glycoprotein (transmembrane) nmb [Source:MGI Symbol;Acc:MGI:1934765]	6521.519	2.71647	13.57884	2.32E-39
Ier5	immediate early response 5 [Source:MGI Symbol;Acc:MGI:1337072]	1920.577	2.311004	13.41714	2.00E-38
Lgals3	lectin, galactose binding, soluble 3 [Source:MGI Symbol;Acc:MGI:96778]	5762.091	1.998459	13.33815	5.57E-38
Ppp1r15a	protein phosphatase 1, regulatory (inhibitor)	310.9635	3.375816	13.19369	3.68E-37

	subunit 15A [Source:MGI Symbol;Acc:MGI:1927072]				
Ccnb1	cyclin B1 [Source:MGI Symbol;Acc:MGI:88302]	109.6404	-4.52363	-13.1173	9.75E-37
Cyb5r1	cytochrome b5 reductase 1 [Source:MGI Symbol;Acc:MGI:1919267]	2399.214	2.687248	13.02598	3.13E-36
Tubb5	tubulin, beta 5 class I [Source:MGI Symbol;Acc:MGI:107812]	1604.378	-2.00779	-12.9377	9.58E-36
Cdca8	cell division cycle associated 8 [Source:MGI Symbol;Acc:MGI:1196274]	243.7486	-2.47673	-12.8097	4.86E-35
Acat2	acetyl-Coenzyme A acetyltransferase 2 [Source:MGI Symbol;Acc:MGI:87871]	124.258	-3.18382	-12.8023	5.18E-35
Dnmt1	DNA methyltransferase (cytosine-5) 1 [Source:MGI Symbol;Acc:MGI:94912]	246.1641	-2.52011	-12.7617	8.47E-35
H2afz	H2A histone family, member Z [Source:MGI Symbol;Acc:MGI:1888388]	907.2927	-1.93647	-12.7358	1.15E-34
Tsc22d1	TSC22 domain family, member 1 [Source:MGI Symbol;Acc:MGI:109127]	147.4274	-3.92279	-12.7049	1.65E-34
Ctsd	cathepsin D [Source:MGI Symbol;Acc:MGI:88562]	13213.01	2.559807	12.69837	1.75E-34
S100a4	S100 calcium binding protein A4 [Source:MGI Symbol;Acc:MGI:1330282]	18202.77	-1.97618	-12.5303	1.43E-33
Sphk2	sphingosine kinase 2 [Source:MGI Symbol;Acc:MGI:1861380]	494.2137	2.797616	12.34292	1.46E-32
Bbc3	BCL2 binding component 3 [Source:MGI Symbol;Acc:MGI:2181667]	867.625	2.485288	12.20415	7.89E-32
Mki67	antigen identified by monoclonal antibody Ki 67 [Source:MGI Symbol;Acc:MGI:106035]	213.8409	-3.03619	-12.1738	1.12E-31
Grina	glutamate receptor, ionotropic, N-methyl D-aspartate-associated protein 1 (glutamate binding) [Source:MGI Symbol;Acc:MGI:1913418]	311.671	2.483154	12.13255	1.81E-31
Slc25a37	solute carrier family 25, member 37 [Source:MGI Symbol;Acc:MGI:1914962]	479.4801	2.409227	12.11827	2.10E-31
Mafb	v-maf musculoaponeurotic fibrosarcoma oncogene family, protein B (avian)	126.7874	3.991051	12.05787	4.27E-31

	[Source:MGI Symbol;Acc:MGI:104555]				
Atp5g3	ATP synthase, H+ transporting, mitochondrial F0 complex, subunit C3 (subunit 9) [Source:MGI Symbol;Acc:MGI:2442035]	1041.633	-2.20298	-11.9397	1.74E-30
Serpine1	serine (or cysteine) peptidase inhibitor, clade E, member 1 [Source:MGI Symbol;Acc:MGI:97608]	81.70593	-4.07987	-11.8882	3.16E-30
Bcl6b	B cell CLL/lymphoma 6, member B [Source:MGI Symbol;Acc:MGI:1278332]	89.48327	-4.44064	-11.8492	4.92E-30
Pld4	phospholipase D family, member 4 [Source:MGI Symbol;Acc:MGI:2144765]	326.3579	2.238377	11.84391	5.13E-30
Mcm3	minichromosome maintenance complex component 3 [Source:MGI Symbol;Acc:MGI:101845]	197.7256	-2.30164	-11.705	2.61E-29
Egr1	early growth response 1 [Source:MGI Symbol;Acc:MGI:95295]	250.165	2.871113	11.66521	4.08E-29
Ccnd2	cyclin D2 [Source:MGI Symbol;Acc:MGI:88314]	145.1333	2.987053	11.58392	1.04E-28
Ska1	spindle and kinetochore associated complex subunit 1 [Source:MGI Symbol;Acc:MGI:1913718]	146.6138	-3.09736	-11.5518	1.48E-28
Csf3	colony stimulating factor 3 (granulocyte) [Source:MGI Symbol;Acc:MGI:1339751]	150.8891	-3.93608	-11.5495	1.49E-28
Cdc20	cell division cycle 20 [Source:MGI Symbol;Acc:MGI:1859866]	119.0829	-3.77619	-11.5327	1.78E-28
Syne3	spectrin repeat containing, nuclear envelope family member 3 [Source:MGI Symbol;Acc:MGI:2442408]	183.7414	-2.48238	-11.4811	3.17E-28
Tacc3	transforming, acidic coiled-coil containing protein 3 [Source:MGI Symbol;Acc:MGI:1341163]	71.17607	-4.24986	-11.4048	7.50E-28
Fcgr1	Fc receptor, IgG, high affinity I [Source:MGI Symbol;Acc:MGI:95498]	125.0171	3.220478	11.39082	8.65E-28
Cenpa	centromere protein A [Source:MGI Symbol;Acc:MGI:88375]	78.64428	-5.15438	-11.3367	1.58E-27
Rnf149	ring finger protein 149 [Source:MGI Symbol;Acc:MGI:2677438]	1019.917	1.872586	11.29732	2.39E-27

Tubb4b	tubulin, beta 4B class IVB [Source:MGI Symbol;Acc:MGI:1915472]	986.5893	-1.83517	-11.2977	2.39E-27
Cd300lf	CD300 molecule like family member F [Source:MGI Symbol;Acc:MGI:2442359]	117.9467	3.075997	11.29292	2.47E-27
Ncapd2	non-SMC condensin I complex, subunit D2 [Source:MGI Symbol;Acc:MGI:1915548]	94.0997	-3.33567	-11.2466	4.11E-27
Rsad2	radical S-adenosyl methionine domain containing 2 [Source:MGI Symbol;Acc:MGI:1929628]	2657.137	2.349978	11.22715	5.04E-27
Mcm6	minichromosome maintenance complex component 6 [Source:MGI Symbol;Acc:MGI:1298227]	85.34668	-3.19869	-11.2076	6.19E-27
Cse1l	chromosome segregation 1-like (S. cerevisiae) [Source:MGI Symbol;Acc:MGI:1339951]	143.0023	-2.56521	-11.198	6.79E-27
Mdm2	transformed mouse 3T3 cell double minute 2 [Source:MGI Symbol;Acc:MGI:96952]	2862.971	2.139994	11.15762	1.05E-26
Cd74	CD74 antigen (invariant polypeptide of major histocompatibility complex, class II antigen-associated) [Source:MGI Symbol;Acc:MGI:96534]	249.2129	2.954076	11.15257	1.10E-26
Ptma	prothymosin alpha [Source:MGI Symbol;Acc:MGI:97803]	3118.51	-1.96597	-11.1273	1.44E-26
Tmpo	thymopoietin [Source:MGI Symbol;Acc:MGI:106920]	117.6822	-2.639	-11.0752	2.54E-26
Dut	deoxyuridine triphosphatase [Source:MGI Symbol;Acc:MGI:1346051]	90.37427	-3.04553	-11.0693	2.67E-26
Klf6	Kruppel-like factor 6 [Source:MGI Symbol;Acc:MGI:1346318]	1244.232	2.337937	11.05446	3.11E-26
Aurka	aurora kinase A [Source:MGI Symbol;Acc:MGI:894678]	103.6357	-3.08659	-11.0352	3.80E-26
Rrm1	ribonucleotide reductase M1 [Source:MGI Symbol;Acc:MGI:98180]	88.99015	-3.31674	-10.9918	6.06E-26
Mcm5	minichromosome maintenance complex	268.8307	-2.41308	-10.9778	6.98E-26

	component 5 [Source:MGI Symbol;Acc:MGI:103197]				
Pbxip1	pre B cell leukemia transcription factor interacting protein 1 [Source:MGI Symbol;Acc:MGI:2441670]	410.1182	2.27183	10.8898	1.82E-25
Pbk	PDZ binding kinase [Source:MGI Symbol;Acc:MGI:1289156]	69.28989	-4.10891	-10.8679	2.28E-25
Kif23	kinesin family member 23 [Source:MGI Symbol;Acc:MGI:1919069]	92.66219	-3.36004	-10.8469	2.83E-25
Ccl9	chemokine (C-C motif) ligand 9 [Source:MGI Symbol;Acc:MGI:104533]	1423.024	-2.24301	-10.8445	2.83E-25
Racgap1	Rac GTPase-activating protein 1 [Source:MGI Symbol;Acc:MGI:1349423]	68.40843	-3.63856	-10.8446	2.83E-25
Fads1	fatty acid desaturase 1 [Source:MGI Symbol;Acc:MGI:1923517]	252.0727	-2.19443	-10.8143	3.89E-25
Ccnl1	cyclin L1 [Source:MGI Symbol;Acc:MGI:1922664]	458.7551	1.872236	10.80583	4.21E-25
Mcrip1	MAPK regulated corepressor interacting protein 1 [Source:MGI Symbol;Acc:MGI:2384752]	235.9748	2.247922	10.78069	5.47E-25
Cenpf	centromere protein F [Source:MGI Symbol;Acc:MGI:1313302]	87.89191	-3.01951	-10.7618	6.63E-25
1700017B05Rik	RIKEN cDNA 1700017B05 gene [Source:MGI Symbol;Acc:MGI:1921461]	323.1608	3.086686	10.73714	8.55E-25
Amz1	archaelysin family metallopeptidase 1 [Source:MGI Symbol;Acc:MGI:2442258]	317.4323	2.159055	10.68773	1.44E-24
Snrpd1	small nuclear ribonucleoprotein D1 [Source:MGI Symbol;Acc:MGI:98344]	788.2128	-1.85379	-10.6853	1.46E-24
Hexa	hexosaminidase A [Source:MGI Symbol;Acc:MGI:96073]	860.3216	1.61416	10.6169	2.98E-24
Rrm2	ribonucleotide reductase M2 [Source:MGI Symbol;Acc:MGI:98181]	56.25446	-4.74266	-10.6174	2.98E-24
Cox6a2	cytochrome c oxidase subunit *via* polypeptide 2 [Source:MGI Symbol;Acc:MGI:104649]	82.60045	4.7733	10.60893	3.21E-24

Nfatc1	nuclear factor of activated T cells, cytoplasmic, calcineurin dependent 1 [Source:MGI Symbol;Acc:MGI:102469]	87.40414	-2.94305	-10.5653	5.06E-24
Dcstamp	dendrocyte expressed seven transmembrane protein [Source:MGI Symbol;Acc:MGI:1923016]	95.9493	-3.03654	-10.5593	5.30E-24
Gcc1	golgi coiled coil 1 [Source:MGI Symbol;Acc:MGI:1921625]	103.4025	3.012203	10.5588	5.30E-24
Nusap1	nucleolar and spindle associated protein 1 [Source:MGI Symbol;Acc:MGI:2675669]	114.8401	-3.05438	-10.5319	6.97E-24
Hpgds	hematopoietic prostaglandin D synthase [Source:MGI Symbol;Acc:MGI:1859384]	283.588	2.453023	10.46803	1.36E-23
Slc6a8	solute carrier family 6 (neurotransmitter transporter, creatine), member 8 [Source:MGI Symbol;Acc:MGI:2147834]	199.0107	2.586092	10.43115	1.98E-23
Hirip3	HIRA interacting protein 3 [Source:MGI Symbol;Acc:MGI:2142364]	92.41911	-2.69706	-10.4253	2.09E-23
Map1lc3b	microtubule-associated protein 1 light chain 3 beta [Source:MGI Symbol;Acc:MGI:1914693]	162.4842	2.339065	10.37184	3.62E-23
Fam129a	family with sequence similarity 129, member A [Source:MGI Symbol;Acc:MGI:2137237]	248.0253	2.197231	10.36485	3.85E-23
Scd1	stearoyl-Coenzyme A desaturase 1 [Source:MGI Symbol;Acc:MGI:98239]	68.94706	-3.23359	-10.3609	3.97E-23
Atg2a	autophagy related 2A [Source:MGI Symbol;Acc:MGI:1916291]	308.957	2.728327	10.35975	3.98E-23
Rgs1	regulator of G-protein signaling 1 [Source:MGI Symbol;Acc:MGI:1354694]	342.4001	2.702461	10.34749	4.48E-23
Ccna2	cyclin A2 [Source:MGI Symbol;Acc:MGI:108069]	56.80467	-5.05898	-10.3032	7.03E-23